



TECHNISCHE
UNIVERSITÄT
DARMSTADT

Eulerian-Lagrangian Approach for Modeling and Simulations of Turbulent Reactive Multi-Phase Flows under Gas Turbine Combustor Conditions

Vom Fachbereich Maschinenbau
An der Technische Universität Darmstadt

zur

Erlangung des Grades eines Doktor-Ingenieurs (Dr.-Ing.)
genehmigte

Dissertation

Vorgelegt von

Dipl.-Ing. Mouldi Chrigui

aus Medenine/Tunesien

Referent	Prof. Dr.-Ing. Johannes Janicka
Co-referent	Prof. Dr.-Ing. Hans-Jörg Bauer
Co-referent	Prof. Dr. rer. nat. Amsini Sadiki
Date of submission	02.09.2005
Date of examination	23.11.2005

Darmstadt 2005

D17

Acknowledgments

The present work has been done during my scientific fellowship in the Institute of Energy and Power Plant Technology, Darmstadt University of Technology.

First I would like to thank my supervisor, the head of the department Prof. Dr.-Ing. Johannes Janicka, for giving me the opportunity of promotion and for providing me with the optimum work conditions. I also would like to thank Prof. Dr. Amsini Sadiki for his excellent guidance and constant encouragement. His enthusiasm and patience have been a source of inspiration throughout the course of this work.

Many thanks are due to Prof. Dr.-Ing. Hans-Jörg Bauer for his interest and taking over the referee process.

I would like to thank Dr.-Ing. Ruud Egels, Dr.-Ing. Thomas Schilling and Dipl.-Ing. Leif Rackwitz from the company Rolls Royce Deutschland for the successful cooperation and useful professional discussions.

I thank Dr. rer.-nat. Andreas Dreizler for the cooperation work in SFB568-Project part A4 and for the discussion about some experimental measuring conditions

My appreciations are also extended to a number of my colleagues for useful discussions and suggestions as well as their technical and moral support during my time in Darmstadt. In particular I would like to thank Dr.-Ing. Bernd Groh, Dr.-Ing. Erich Wachter, Dipl.-Ing Bernhard Wegner, Dipl.-Ing. Felix Flemming, and my office mate, M.S. Rajani Akula.

Last, but not least, I would like to thank my wife Chedia for having much patience and constant faith in me.

Mouldi Chrigui

Darmstadt, September 2005

Contents

1	Introduction	1
1.1	Motivation	1
1.2	State of the art.....	3
1.3	Objectives	10
1.4	Outlines of the thesis.....	11
2	Turbulent reacting multiphase flows basics	13
2.1	PDF approach.....	13
2.2	Eulerian-Eulerian approach.....	15
2.3	Eulerian-Lagrangian approach	16
2.3.1	Continuous phase description	17
2.3.2	Dispersed phase description	23
2.4	Combustion	28
2.4.1	Chemical kinetics	28
2.4.2	Non-premixed flame.....	32
2.4.3	Premixed flame	35
2.4.4	Partially premixed flame	37
3	Eulerian-Lagrangian modeling approach	40
3.1	Turbulence modeling for non-reacting flows.....	40
3.1.1	First order turbulence modeling	40
3.1.2	Second order turbulence modeling	43
3.2	Carrier phase and two way coupling	47
3.2.1	Turbulence modulation modeling.....	48
3.2.2	Thermodynamically modulation modeling	50
3.2.3	Dispersion modeling	53
3.3	Spray evaporation modeling	56
3.3.1	Concept of the droplet evaporation models	56
3.3.2	The Uniform Temperature model.....	58
3.3.3	The Non-equilibrium evaporation model	60
3.3.4	Turbulence-droplets interaction regimes.....	62
3.4	Turbulent spray combustion modeling.....	63
3.4.1	Mixture fraction and its variance	64
3.4.2	Turbulent combustion modeling based on primitive variables	67
3.4.3	Turbulence modeling for reacting flows	70
4	Numerical procedure	73

4.1	Numerical method for the gas phase	73
4.1.1	Finite volume method	74
4.1.2	Boundary conditions	82
4.1.3	Solvers	88
4.2	Numerical method for the dispersed phase	90
4.2.1	Solving the equation of motion and time discretization	90
4.2.2	Statistical sampling	91
4.3	Eulerian-Lagrangian coupling	92
4.3.1	Steady state coupling	93
4.3.2	Under-relaxations of source terms	94
5	Models validation	96
5.1	Configuration and numerical Set up	96
5.2	Flow conditions	97
5.3	Results and discussions	99
5.3.1	Standard modulation model	99
5.3.2	Crowe modulation model	101
5.3.3	Thermodynamically consistent modulation model	101
5.3.4	Particle fluctuations	102
5.3.5	Some remarks	103
6	Applications	105
6.1	Isothermal swirling particulate two-phase flow	106
6.1.1	Flow conditions	107
6.1.2	Results and discussions	109
6.1.3	Some remarks	113
6.2	Spray issuing into a co-flowing heated air-stream	113
6.2.1	Configuration description	113
6.2.2	Flow conditions	114
6.2.3	Results and discussions	117
6.3	Spray combustion in complex configuration: gas turbine engine combustor	129
6.3.1	Configuration description	130
6.3.2	Flow conditions	131
6.3.3	Results and discussion	133
7	Conclusion	151
8	Bibliography	154

Nomenclature

Latin symbols

Symbol	Dimension	Definition
A_{fj}	-	Pre-exponential frequency factor in Arrhenius law for elementary reaction j
B_M	-	Spalting mass transfer number
B_T	-	Spalting heat transfer number
c	$J/(Kg K)$	Specific heat capacity of the droplet
c_p	$J/(kg.K)$	Specific heat capacity by constant pressure
C_W	-	Resistance coefficient
C_w	-	Drag coefficient
$C_{\varepsilon,3}^{k-\varepsilon}$	-	Constant model for the turbulence modulation of the k- ε model
$C_{\varepsilon,3}^{RS}$	-	Constant model for the turbulence modulation of the RSM model
D	s^{-1}	Diffusion term within skalar transport equation
D_d	m	Particle diameter
E_j	J/kg	Activation energy in Arrhenius law for elementary reaction j
E_ω	m^3/s^2	Turbulent kinetic enrgy density
\vec{F}	N	Force
\vec{g}/g_i	m/s^2	Gravity acceleration vector / Cartesian components
\dot{H}	J/s	Enthalpy rate
h_v	J	Latent heat of vaporization
k	m^2s^{-2}	Turbulent kinetic energy
K_{fj}/K_{bj}	-	Forward / backward rates of reaction j
k_ω	$1/m$	Wave number
L	m	Characteristic length scale
Le	-	Lewis number
l_t	m	Turbulent length scale
L_δ	m	Reaction zone thickness
$\dot{m}_{p,v}$	Kg/s	Droplet evaporation rate

n_j	-	Temperature exponent in Arrhenius law for elementary reaction j
N_p	-	number of real particles represented by one numerical parcel
p	Pa	Static pressure
Pr	-	Prandtl number
P_φ	-	Probability density function of variable φ
\dot{Q}_l	j/s	Heat flux rate penetrating into the droplet interior
R	$J/(kg.K)$	Universal gas constant
Re	-	Reynolds number
Re_p	-	Particle Reynolds number
$r_{f,j}, r_{b,j}$	mol/s	Forward/backward rates of progress of reaction j
r_j	mol/s	Rate of progress of reaction j
s	-	Stoichiometric ratio
Sc	-	Molecular Schmidt number
Sh	-	Sherwood number
s_L	m/s	Laminar burning velocity
St	-	Stokes number
$S_{\psi,p,s}$	<i>Variable ψ dependent</i>	Source term of the variable ψ for a non-evaporating droplet
$S_{\psi,p,v}$	<i>Variable ψ dependent</i>	Source term of the variable ψ due to evaporation
T	K	temperature
t	s	time
T_{avg}	K	Average combustor exit temperature
T_{inl}	K	Average combustor inlet temperature
T_t	s	Turbulent time scale
\vec{u} / u_i	m/s	Velocity vector / Cartesian components
V	m^3	Volume
$V_{i,j,k}$	m^3	Volume of the cell ijk
W_k	Kg/mol	Molecular weight
x_i	m	Cartesian coordinates
y_k	-	Mass fraction of species k
z	-	Mixture fraction
Z_L	-	Mass loading

Greek symbols

Symbol	Dimension	Definition
$\dot{\omega}_{kj}$	Kg/s	Mass reaction rate of species k in reaction j
Γ_{ψ}	-	Molecular diffusion coefficient of a general scalar quantity ψ
Π_{ij}	m^2/s^3	Pressure-strain correlation tensor (Cartesian components)
α_p	-	Volume fraction
β_j	J/mole	Activation energy of species k in reaction j
χ	1/s	Skalar dissipation rate
δ	m	Flame thickness
δ_{ij}	-	Cartesian components of unit tensor (Kronecker delta)
ε	m^2/s^3	Turbulent kinetic energy dissipation rate
ϕ	-	Equivalence ratio
η_k	m	Kolmogorov length scale
λ	J/(s.K.m)	Thermal conductivity
μ / μ_t	Kg/(m.s)	Dynamic molecular / turbulent viscosity
ν / ν_t	m^2/s	kinematic molecular / turbulent viscosity
ν_k, ν'_k, ν''_k	-	Stoichiometric coefficients for species k
ρ	Kg/m^3	density
σ_{φ}	m	Turbulent Schmidt/Prandtl number for the variable φ
τ_p	s	Particle relaxation time
ψ	-	General scalar quantity

Operators

Operator	Definition
$\overline{(\cdot)}$	Reynolds averaging
$\widetilde{(\cdot)}$	Favre averaging
\sum	Sum
Δ	difference
$\vec{(\cdot)}$	Vector
$(\cdot)'$	Reynolds fluctuation
$(\cdot)''$	Favre fluctuation

Indices

Symbol	Definition
∞	Infinity
p	Particle / droplet
$(.)_F$	Fuel
$(.)_O$	Oxidiser
ref	Reference
$(.)_v$	Vapor

Abbreviations

Abbreviation	Definition
<i>ASM</i>	Algebraic Reynolds Stress Model
<i>CDS</i>	Central Difference Scheme
<i>CFD</i>	Computational Fluid Dynamics
<i>CV</i>	Control Volume
<i>EASM</i>	Explicit Algebraic Reynolds Stress Model
<i>E-E</i>	Eulerian-Eulerian
<i>E-L</i>	Eulerian-Lagrangian
<i>ILD</i>	Intrinsic Low Dimensional Manifolds
<i>LDA</i>	Laser Doppler Anemometry
<i>LRR</i>	Launder-Reece-Rodi pressure strain formulation/ model
<i>PDA</i>	Phase Doppler Anemometry
<i>PDF</i>	Probability Density Function
<i>RANS</i>	Reynolds Averaging based numerical Simulation
<i>RHS</i>	Right Hand Side
<i>RMS</i>	Root Mean Square
<i>RQL</i>	Rich Burn-Quick Quench-Lean Burn
<i>RRD</i>	Rolls Royce Deutschland
<i>RSM</i>	Reynolds Stress Model
<i>RTDF</i>	Radial Temperature Distribution Factor
<i>SIP</i>	Strongly Implicit Pressure
<i>UDS</i>	Upwind Difference Scheme
<i>URANS</i>	Unsteady RANS
<i>UTM</i>	Uniform Temperature Model
<i>ZFK</i>	Zeldovich Frank Kamenetsky von Karman theory

1 Introduction

1.1 Motivation

The energy generation over the world remains primarily due to the fossil fuel. Over 80% of all the energy production is manufactured by combustion (Coal, Gas, Oil) [1]. During the last decades a high attempts have been paid towards the renewable energy. Among the most important of these sources one can mention solar, and wind. They are characterized by their environmental cleanliness and their virtual inexhaustibility. In most cases, however, they are not suitable for large-scale power generation as well as relative costliness to build and maintain. Despite its known disadvantages, combustion remains the cheapest and the most direct way to produce energy. It is therefore important to seek for improvements of combustion processes in order to promote the efficiency of the energy conversion. For optimization purposes, numerical simulations aid in the development and improvement of fundamental flow models or practical flow and combustion devices in different engineering applications. Today's numerical CFD (Computational Fluid Dynamics) tools provide user-friendly capabilities, handling complex geometry, comprehensive virtual modeling and powerful visualization features for predicting many types of fluid flow and heat transfer phenomena. Deeper understanding of the underlying physical phenomena controlling various processes makes it easier to optimize current processes, and to design improved or completely new processes.

The multiphase aspect of fluid flow is very complex as it involves the movements of many individual particles and their interaction with the fluid flow, turbulence, mass transfer between fluid and particulate phase, heat transfer between the phases and their surrounding phase and interaction between the individual particles themselves. The situation becomes more complicated when the particles have changed their physical state and enter to the combustion zone. They are heated and ignited releasing hot combustible gases that burn in the gas phase. The rate of modification of physical state from solid to gaseous phase (rate of droplet evaporation), as well as droplets spatial distribution and injection characteristics are key parameters for fuel air mixture preparation and homogenization. They form together a particular importance for combustion. In the context of a combustion chamber design, an accurate determination of droplet and vapor spatial distribution, and a reliable control of the interaction between the spray with the surrounding turbulent gas flow are prerequisites. If the mixing of air and fuel is not perfect then there will be partially unburned fuel. Obviously, the mixture will greatly affect the efficiency of the energy extraction. If the mixture does not have enough oxygen present during combustion, it will not burn completely. When combustion takes place in an oxygen starved environment, the present oxygen will be insufficient to

fully oxidize the carbon atoms into carbon dioxide (CO₂). Thus carbon atoms will be born with only one oxygen atom carbon monoxide (CO). Controlling the mixture of fuel and air contributes to the reduction of the exhaust gaseous emission.

However, due to the complex nature of the spray atomization, vaporization and combustion processes, many practical devices designs are based upon the trial-and-error approach [2], which is very expensive. Hence, research and industry are concentrating their efforts on combustion technologies that reduce exhaust emissions, achieve more economical use of fuels, and longer lifetime of engineering devices. Specific aspects of fuel-air mixing are used in LPP¹ or RQL² combustor concept. The fuel droplets are completely vaporized in the RQL zone. Consequently, the molecular mixing of fuel and air that minimizes stoichiometric burning (and the associated local heat release that leads to fixation of atmospheric nitrogen) is desired. The LPP combustion concept aims to reduce NO_x emissions principally by reducing the peak flame temperatures inside an engine.

The progression of combustion is strongly dependent on the rate of strain in the fluid since this directly affects the fuel/air interfacial area, and diffusion of heat and chemical species. The strain itself is influenced by the presence of droplets, their dispersion and evaporation due to the modification of mass flow, turbulence intensity and flow velocities. Depending on the magnitude, strain can either increase or decrease the progression of a given reaction. The exchange of mass, momentum, and energy between the droplets and the surrounding gas phase in the combustion chamber are critical features of the combustion processes. The droplets characteristics influence the spray vaporization, which in turn influence the combustion performance [105]. The rate of combustion will be affected by the rate of vaporization. Droplet trajectories affect the local vaporization rates, and droplet drag affects drop trajectories.

In order to consider all of the above mentioned technical and physical phenomena in modeling and simulation strategies, one realizes that industrial combustion devices like gas turbine combustors or internal combustion engines require various sub-models to well predict the spray combustion and therefore to ameliorate the industrial combustion systems. The formulation of advanced robust and accurate sub-models with their consistent implementation into numerical tools is of great importance.

¹ Lean Premixed Prevaporized

² Rich Burn Quench

1.2 State of the art

Turbulent reactive multiphase flows have been investigated by several researchers many years ago. However, since this topic is multifaceted and exhibits wide physical phenomena, many researchers have focused their work on specific aspects. I will therefore introduce first the classification of multiphase flows. Then I will outline the turbulence modulation and droplets evaporation. At last I will focus on the multiphase combustion issues.

Classification of multiphase flows

For a better classification of multiphase flows, first I am going to pay attention to the main interaction processes in such flows. In general, different classes of interaction can be distinguished, depending primarily on particle volume fraction. According to Sato [3], Elghobashi [5] and Crowe et al. [6], for particle volume fractions less than 10^{-6} , particle motion is influenced by continuous phase properties but there is practically no feedback from the dispersed phase. This is known as “one-way coupling”. For particle volume fractions in the range from 10^{-6} to approximately 10^{-3} , feedback of the dispersed phase on the properties of the continuous phase fluid dynamics also must be taken into account (“two-way coupling”). This regime is termed “diluted” and the effect of the feedback mechanism is called “turbulence modification”. A dense flow is characterized by particle volume fractions higher than 10^{-3} . In addition, for dense flows particle-particle interactions have to be taken into consideration. This is known as “four-way coupling”.

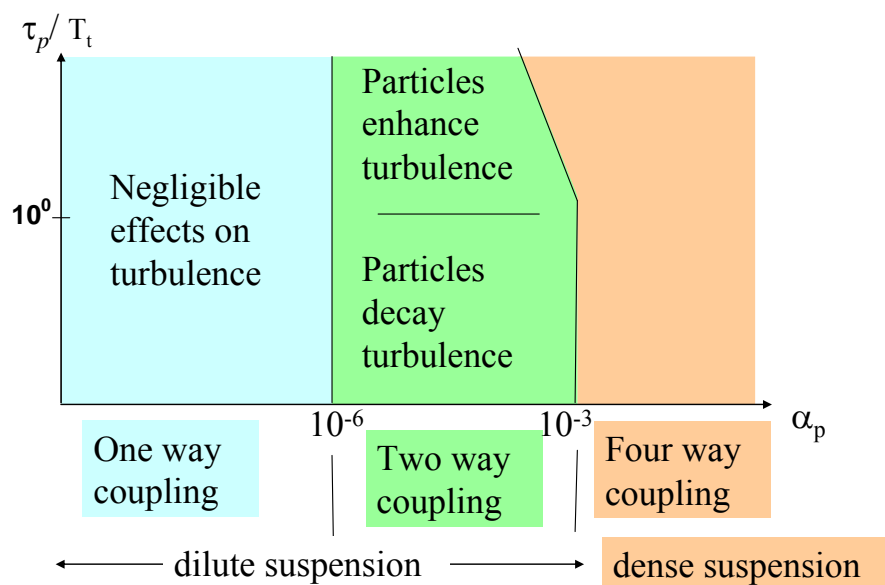


Figure 1.1: classification of turbulent multiphase coupling

Figure 1.1 shows the different coupling types and the effect of particles diameter, represented by the Stokes number which will be explained later, on the turbulence enhancement or decay.

In a different analysis Hetsroni [28] introduced a particle Reynolds number (see Sect. 2.3.2.1) to classify turbulence modification. The particle Reynolds number is proportional to particle diameter and the slip velocity between continuous and dispersed phase. In this view, turbulence production is due to detachment of eddies created in the wake of the particles (vortex shedding). Production of turbulent kinetic energy is expected for values of $Re_p > 400$.

Theoretically, the description of one-way coupling is simple because the flow field of the continuous phase in the absence of a feedback mechanism can be computed as a single phase flow. Particle motion is determined in a post-processing step. However, in technical applications particle volume fractions are generally high. Consequently, turbulence modification has to be taken into account and included in a proper mathematical description of turbulent two-phase flows. Therefore, a fully two way coupling with respect to turbulence modulation has to be accounted for.

Turbulence modulation

The impact of turbulence modification on the fluid dynamics of the continuous phase is not yet clearly understood. In the work by Elghobashi and Truesdell [7], Michaelides and Stock [8], Owen [9], Parthasarthy and Faeth [10] and [11], dissipation or production of turbulent kinetic energy of the continuous phase were reported. For specific configurations, the effective viscosity of the carrier phase is changed, wakes are generated and an increase of velocity gradients is stated. In the case of dense flow, particle-particle as well as particle-wall interactions have been observed. Numerically, the effect of particles on the carrier flow turbulence were investigated in detail by Varaksin and Zaichik [12], based on a RANS approach, while Lei et al. [13] considered an LES-approach. So far, experimental investigations regarding turbulence modification have focused on flows in vertical pipes (Chandok and Pei [14] ; Meada et al. [15] ; Durst [16] ; Tsuji et al. [17]) and turbulent jets (Modarress et al. [18]; Solomon et al. [19], [20]; Mostafa et al. [21]; Park and Chen [22] , [23]). In addition, Schreck and Kleis [24] reported on modification of grid-generated turbulence in a solid-liquid two-phase flow, where a monotonic increase of dissipation rate with particle loading was found. However, particle sizes were not varied by Schreck and Kleis.

In the work by Gore et al. [25], most the data available up to 1989 were reviewed and analyzed. For a qualitative classification of turbulence modification, the ratio of particle diameter (D_p) to turbulent length scale l_t was proposed as a criterion whether turbulent kinetic energy of the continuous phase is dissipated ($D_p/l_t < 0.1$) or produced ($D_p/l_t > 0.1$). In an ostensive view, sufficiently small particles partly follow the turbulent flow

and therefore “consume” kinetic energy. Large particles do not follow the turbulent flow field due to their high inertia. These particles generate turbulent kinetic energy because they act as obstacles that create wakes. This analysis has been supported for small particles in a two-phase channel flow by Kulick et al. [26] but is in contradiction to experimental findings by Hardalupas et al. [27].

In order to account for the turbulence modulation, Crowe developed in his work [87] a model which was based on the energy balance. The Crowe modulation model, as used within this thesis has over predicted the turbulence enhancement and is usually productive. Lain and Sommerfeld [92] proposed in their paper a “consistent” Lagrangian-formulation and results have been evaluated and compared with data from the standard terms. In the “consistent” terms all the forces in the particle equation of motion are included with the aim of influencing the turbulent quantities. Thus the so called wake induced turbulence is accounted for. Unfortunately the standard and consistent terms provide similar values in the investigated particle-laden flows.

Droplets evaporation

To account for the mass and heat transfer, various droplet vaporization models have been suggested [43] - [47]. They require physical description of the gas phase around the droplet and the transport processes inside the droplet (liquid phase) as well as the interfacial interactions of the two-phases. Depending on how the transport inside the droplet is described, the liquid phase models can be classified in four groups:

- a The infinite diffusion model,
- b The pure diffusion model,
- c The vortex model, and,
- d The simplified model,
- e The thin skin model.

The infinite diffusion model assumes that the transport processes of mass and heat occur so quickly that the physical properties and the chemical composition are always uniform inside the droplet. The pure diffusion model assumes that the transport is dominated by the molecular diffusion and that the property distribution is spherically symmetrical. The vortex models describe the droplet as unsteady and axisymmetric. The vortex motion inside the droplet is described by additional vorticity and stream function equations or analytical solutions including therefore the effects of both diffusion and convection. The simplified vortex model (equivalent to the effective diffusion models as compromise between (a) and (b)) attempts to account for the primary phenomena of droplet vaporization with less computational cost (compared with the vortex models).

In recent works, some numerical calculations have been carried out in which the effects of the presence of particles/droplets have been pointed out. They deal mostly with 2-D numerical codes in which the evaporation process description has been included (see [43] and [44]). In many cases, only the standard $k-\varepsilon$ model has been coupled to evaporation models, in particular to equilibrium evaporation models [44]. The implication of non equilibrium models has been accomplished in [30].

In his work, Berlemont et al. [45] investigated the effects of turbulence influence on mass and heat transfer. However, the used configuration was only 2D. Diverse parameter studies have been carried out; however there are relatively few experimental results on the effects of turbulence characteristics on spray evaporation and combustion [47]. The effect of turbulence on vaporization, mixing and combustion of liquid-fuel sprays has been experimentally investigated in [46]. Non-reacting and reacting spray jets in a duct with square cross-section have been chosen. Authors realized that the turbulence strongly affected the evaporation rate. With the increase of evaporation rate, the mixing of gaseous fuel and air becomes a controlling process of combustion. In [47], the experimental results suggest that the turbulence modifies the mass transfer from liquid droplets in dependence on a defined vaporization Damkohler number. An accurate capture of turbulent fluctuations is therefore decisive for better prediction of these phenomena. In this connection, the so-called turbulence modulation can no longer be neglected.

Faeth [41] considered in his work a simple approach to compute the evaporation and combustion of sprays. He applied the D2 model which has been widely used to describe the evaporation of fuel droplets. In this model droplets are heated till boiling temperature without any mass transfer. Then an evaporation period at an almost constant temperature takes place. This model is suitable in case of small heating period time compared to the droplet life time. The second type of evaporation models is the Uniform Temperature model (UT model) which neglects the mass transport inside the droplet. Here the temperature variation in the interior of the droplet is homogenous. It has an unsteady behavior and it is accompanied with mass transition [42]. Both models do not consider any temperature gradient at the interior of the droplet. Therefore they do not need more computing time. A recent review of evaporation models is given in [35].

With regard to technical applications environments, all models mentioned above are developed into low pressure conditions, i.e. $p_{atm} \leq p < 10$ bars. Oefelein et al. [29] tried to show the differences between classical low-pressure and high-pressure evaporation models. They mentioned that the subsequent (high pressure) drop regression process is different from that in the subcritical (low-pressure) state. All these models can be classified as equilibrium based models. Prommersberger et al. [32] built an experimental setup where evaporation of free falling monodisperse droplets was investigated at high pressure; he then compared the

experimental results with numerical calculations based on some equilibrium droplet evaporation models. The convective transport of heat and mass at the droplet surface was calculated according to the film theory of Abramson and Sirignano [33] accounting for the molar mass fraction through the Clausius-Clapeyron equation. He determined the best correspondence with experiments fit with conduction limit model of Law and Sirignano [33], which assumes a diffusive heat and mass transport within the droplet. Due to its high computational time consumption, this model was not considered in this paper.

Miller et al. performed in [30] an evaluation of existing evaporation models which are applicable to describe droplets having various diameters at a low pressure. Of particular interest was the vaporization of small single-component of water, benzene, decane, heptane and hexane droplets in high temperature environments as found in many spray mixing and spray combustion processes. He realized that non-equilibrium effects became significant when the initial droplet diameter is less than 50 μm and, that these effects are enhanced with increasing slip velocity. Thereby, they used the non-equilibrium model by Langmuir-Knudsen [31]. The results agreed most favorably with a wide variety of experimental results. In [43], the investigation was focused on the study of spray evaporation in turbulent flow using the equilibrium evaporation model. Indeed the numerical computing had two-dimensional.

Multicomponent droplets are often captured using the rapid mixing model which assumes equilibrium evaporation of the droplet comparable with a batch distillation process [138]. The model delivers reasonable results for slow evaporation processes, when droplet internal heat conduction and diffusion has not a major effect on the internal temperature and concentration profiles. The second type of multicomponent droplets is the diffusion limit model where the temperature and concentration distribution inside the droplet are determined using a discretization scheme to capture the heat conduction and mass diffusion. The disadvantage of this model is the enormous computational time [138].

Particles/Droplets dispersion

In the Lagrangian particle tracking approach, as it is the case within this thesis, the instantaneous fluid velocity is unknown. However, the Eulerian approach for the turbulent fluid phase gives mean velocities and turbulent parameters that can be used to model the instantaneous fluid velocity. Additional work has been done to deal with turbulent droplet dispersion and its effect on phase transfer. So different dispersion models have been suggested [93]. The way to account for the stochastic process for the fluctuating velocity plays a significant role in describing the essential spray properties. It was shown recently [54] that the so-called modified particle Langevin model is able to well reproduce the anisotropic turbulence and vortex structures responsible for turbulent dispersion. Sommerfeld used in his work [93] random walk models.

In fact, for formulations, e.g. random walk model, that do not model the vortex structure, spurious distribution of droplets leading to droplet immigration in regions with low turbulence intensity has been observed. To avoid such a behavior, a drift term has been introduced in [55]. Liu et al. [107] used a Langevin equation model for the instantaneous fluid velocity with a Reynolds stress model for the continuous phase. They got reliable results for the average velocities and fluctuations in a particle laden swirl flow. Melheim et al. [108] used a stochastic process for the fluctuating velocity “Particle Langevin equation model” to model the vortex structure in a particle laden mixing layer. They showed that the numerical results agree reasonably well with the PIV measurements.

Other aspects of particles/droplets dispersion were observed in the four way coupling. Indeed, the particle velocity fluctuations and the number density of the dispersed phase within a control volume are key parameter to develop stochastic models for particle collisions [106]. The dispersion of droplets influences also the trajectory of the dispersed phase. Thus it impacts some chemical processes i.e. evaporation, which depend on the droplet history. It is therefore very important to account for in a proper way the dispersion i.e. the effect of turbulence on droplets distribution.

Spray combustion modeling

Focused on the fuel preparation in gas turbine combustors, the performance, the stability and emissions of the combustors depend strongly on the fuel-air mixing processes, which in turn are determined by the turbulent dispersion, the evaporation of liquid fuel droplets and the related interaction phenomena with the turbulent carrier phase.

A systematic consideration of the effect of the turbulent interactions between gas and droplets in internal combustion engines is rather rare [35], although the turbulence is one of the major factors controlling droplet dispersion, formation of particle/droplets high concentration regions and thus spray flame structure [36], [37], [38], [39] and [40]. Available results for these configurations are usually limited to those of the experiments of turbulence augmentation by additional injections of air or gaseous fuel without investigating deeply the nature of the interaction process. From these studies, it is well-known that the turbulence-droplet interaction can strongly influence the mixing processes and the spray combustion as well (see [48] and cited references therein).

With regard to numerical simulations, the consideration of all these effects along with a fully two-way coupling and related interphase transport modifications in numerical models used for turbulence and vaporization either in RANS-(here Reynolds Averaging based Numerical Simulation) context [36], [49] and [50] or in large eddy simulation ([51], [52] and [53]) is not complete or not physically sufficient. However, RANS-based calculations are state of the art in many engineering design applications because of their economically computational costs.

Furthermore, many substantial theoretical and experimental works have been done concerning turbulent reacting gas flows. Related to one phase flow, many researches, among others, combustion are well known. Borghi [57] applied the Reynolds Averaged Navier Stokes (RANS) calculations to simulate the nonpremixed turbulent combustion. The turbulent parameters/variables (velocities, temperature, etc.) are averaged and calculated from equations which rely on turbulence and turbulent combustion models. However, one of the limitations of RANS is the lack of accuracy in capturing unsteady large scales mixing controlling many properties of combustion chambers. Pope [58] and Lindstedt et al. [59] have shown in their work that PDF methods offer an important advantage over other methods where chemical reactions appear in closed form in the PDF equations. As a consequence, realistic combustion chemistry can be incorporated without the need for closure approximations pertaining to reactions. Deken and Peters [56] have used the G-equation to model the turbulent flame front propagation by implementing the Flamelet model in a CFD code. The advantage of this combustion model is the decoupling of the chemistry from the turbulent flow.

However, it turns out for turbulent reactive sprays that fundamental understandings of the combustion processes are lacking due to the complexity of the problem. Faeth [41] and Law et al. [33] have reviewed the status of spray combustion. Réveillon and Vervisch [60] applied a three dimensional direct numerical simulations (DNS) to simulate the spray vaporization and combustion. Closures were proposed for the source terms appearing in the transport equation for the fluctuations of the mixture fraction. They are based on a simple One Droplet Model utilized to express the conditional mean of the turbulent vaporization rate. The simulations, however, are limited to clusters of droplets due to high computational costs. Mashayek [62] investigated evaporating and reacting fuel droplets in forced turbulent flows. He realized that the combustion process is significantly affected by the rate of evaporation. The fuel vapor participates in the chemical reaction almost immediately after its production. A strong correlation is observed between the droplet concentration and the reaction rate. The results are also used to discuss the temporal evolution of the mean temperatures and the mean mass fractions, as well as the role of the preferential distribution of the droplets. Hollmann and Gutheil [50] developed a flamelet model for turbulent spray diffusion flames. In their work a laminar spray flame has been studied. It appeared that the used model predict all principal results of the experiment. The major advantage of the use of a laminar spray flame library versus a laminar gas flame library is the generality of the approach. There is no need for artificially introducing a cut-off temperature to correctly predict the cold flame regime where vaporizing droplets are present. Sankaran and Menon [109] studied the spray combustion in swirling flows using LES. They found that the global behavior of the spray combustion such as droplet dispersion and turbulence modification by the particles are all captured reasonably well in

the simulations. Results show that increase in swirl increases vortex breakdown and spray dispersion which in turn leads to enhanced fuel-air mixing.

Moreover, the major problem for turbulent reactive multiphase flows underlies the difficulty of providing experimental data close to the liquid injection where the spray is very dense. Nevertheless, this is the most important region for the computation because it represents the boundary conditions for the inlets. Sommerfeld et al. [43] investigated the spray evaporation in a sudden-expansion pipe with an expansion ratio of 3 experimentally. The Boundary conditions of the dispersed phase have been produced at an axial position of 5 mm far away from the nozzle exit.

1.3 Objectives

The aim of this work is to develop robust and accurate mathematical integral models to study the physics of turbulent reacting multiphase flows. It aims also at validating and applying them for the simulation of complex industrial configurations. The models are developed in the frame of statistical turbulence modeling within the Eulerian Lagrangian approach. They include different sub-models of turbulence, dispersion, evaporation, combustion as well as different interaction processes. The work is therefore structured in five tasks such as:

- Focus on the interaction between solid particles and turbulence seeking correct prediction of the turbulent quantities in two phase flows. The comparison of turbulence properties with and without a dispersed phase is used to deduce the feedback of the dispersed phase on the continuous phase.

Based on a thermodynamically consistent approach, a modulation model that accounts for the particle-induced turbulence modification in the calculation of the turbulent kinetic energy will be involved. Its prediction of performance will be compared to experimental data as well as results of other existing modulation models.

- Achievement of the coupling between the Eulerian and Lagrangian codes for the computation of two-phase flows problems.
- Integration of evaporation models within the Lagrangian code. Thereby equilibrium and non-equilibrium models will be used.
- Consideration of the spray combustion in the frame of non-premixed flame using Eulerian-Lagrangian procedure.
- Design of a complete reacting spray model consisting of turbulence modulation, equilibrium/non-equilibrium evaporation, second order turbulence, equilibrium/Flamelet chemistry and Mixture fraction / PDF approach to describe the spray combustion of a high complex industrial combustion chamber.

From the last point one derives statements not only about the combined sub-models describing the physics but also about the faced numerical problems to solve a complex system of coupled partial differential equations.

In order to achieve all of the above mentioned objectives, four different configurations with diverse complexity have been investigated. The first configuration, a vertical laden channel flow provides basic experimental results to validate the turbulence modulation models, whereas the second configuration consisting of a swirling particulate two-phase flow serves for the validation of the dispersion model. The third configuration deals with droplets evaporation and comparison between equilibrium and non-equilibrium models. The fourth one represents a high complex industrial gas turbine configuration (BR 710) by Rolls Royce where all the complex processes are occurring, i.e. turbulence, turbulence modulation, dispersion, evaporation, combustion, etc.

1.4 Outlines of the thesis

This section outlines the framework underlying the calculations of turbulent reactive multiphase flows on which the work in this thesis is based. A starting point is the introduction which contains a discussion of motivation, state of the art and objectives. This part aims at providing an idea about the confronted difficulties in earlier works done by other researchers. It aims also at revealing some still open problems that researchers encountered in the academia or industry.

Chapter 2 describes the turbulent reacting multiphase flows. First an overview of used procedures to numerically describe multiphase flows is summarized. Thereafter different combustion process is presented. The governing equations for both phases are given and discussed in the same chapter.

Chapter 3 sets the theoretical basis of the modeling approach in the frame of Eulerian Lagrangian procedure. This chapter reviews a wide range of mathematical approaches. They are turbulence modulation modeling, dispersion modeling, spray evaporation and spray combustion modeling.

Chapter 4 introduces the numerical procedure used. First the numerical method for the gas phase is presented, followed by a description of the discretization procedure for the dispersed phase. Additionally, the coupling of the Eulerian and the Lagrangian codes, and the problems confronted by the convergence of fully two ways coupling will be discussed.

Chapter 5 presents the test case used to validate different modulation models. Experimental data concerning turbulent kinetic energy are taken as a scale to highlight the differences between all used models for the description of the turbulence modulation

Chapter 6 contains three different applicable configurations. The first one consists of a swirling particulate two-phase flow where the dispersed phase is composed by solid particles. The second configuration deals with spray evaporation. The last configuration consists of a complex geometry of gas turbine combustor. The main idea behind this is to ascertain the combustion using Eulerian Lagrangian procedure in the frame of RANS and investigate the effect of modulation modeling as well as evaporation models on the development of combustion process for industrial purposes. Finally, Chapter 7 summarizes the contents of this thesis and suggests some possible directions for future research.

2 Turbulent reacting multiphase flows basics

The numerical methods used in solving the dispersed multi-phase flow are basically separated into three categories:

- The Eulerian Lagrangian method, where the trace of each particle is followed by the gas phase and the characteristics of the individual particle which are computed,
- The two-fluid method. Here, the particle phase and carrier phase are considered as continuum,
- The Probability Density Function (PDF) method. It describes a turbulent spray by the joint statistical properties of the gas phase properties and the droplet properties.

2.1 PDF approach

In the PDF approach the non-continuous phase is thought of as a cloud of material elements, whose behavior is driven by a probability function depending on velocity, temperature, mass of droplets and the velocity, temperature and species concentration of gas phases seen by droplets. The joint-PDF transport equation describes the unsteady evolution and convection by the velocity mean field in the physical space, and describes the PDF evolution in the phase space. For this purpose some conditional average over the phase space due to dispersion, phase change, heat transfer of droplets, and the momentum, heat, and mass transport of gas particles seen by droplets have to be modeled.

The joint PDF transport equation of turbulent gas-droplet flows is given by (2.1) [64].

The variable $\left\langle S \Big|_{V_{pi}, \theta_p, M_p, V_{gi,p}, \theta_{g,p}, \xi_{g,p}} \right\rangle$ denotes the conditional average of S over the space. The variables V_{pi} , θ_p , M_p , $V_{gi,p}$, $\theta_{g,p}$ and $\xi_{g,p}$ are the corresponding variables for the velocity, temperature, mass of droplets and the velocity, temperature, and species concentration of gas phase seen by the droplets in the phase space respectively. The RHS of (2.1) represents the shift of the joint-PDF in the phase space due to dispersion, phase change, heat transfer of droplets, and the momentum, heat, and mass transport of gas phase seen by droplets, respectively.

The gas phase equations combined with the turbulence modeling are Reynolds time-averaged in Eulerian coordinates and are solved using the Finite Volume method. The PDF model of the dispersed phase is solved using a Lagrangian approach in the phase space. Based on the properties

2. Turbulent reacting multiphase flows basics

of PDF, the averaged value of a generalized variable, as a function of phase-space, can be obtained by integration in the phase space [64].

$$\begin{aligned}
 \frac{\partial P}{\partial t} + V_{pi} \frac{\partial P}{\partial x_i} = & - \frac{\partial}{\partial V_{pi}} \left[P \left\langle S_{up,i} \middle| V_{pi}, \theta_p, M_p, V_{gi,p}, \theta_{g,p}, \xi_{g,p} \right\rangle \right] \\
 & - \frac{\partial}{\partial M_p} \left[P \left\langle S_{mp} \middle| V_{pi}, \theta_p, M_p, V_{gi,p}, \theta_{g,p}, \xi_{g,p} \right\rangle \right] \\
 & - \frac{\partial}{\partial \theta_p} \left[P \left\langle S_{hp} \middle| V_{pi}, \theta_p, M_p, V_{gi,p}, \theta_{g,p}, \xi_{g,p} \right\rangle \right] \\
 & - \frac{\partial}{\partial V_{gi,p}} \left[P \left\langle S_{ug,i} \middle| V_{pi}, \theta_p, M_p, V_{gi,p}, \theta_{g,p}, \xi_{g,p} \right\rangle \right] \\
 & - \frac{\partial}{\partial \theta_{g,p}} \left[P \left\langle S_{hg} \middle| V_{pi}, \theta_p, M_p, V_{gi,p}, \theta_{g,p}, \xi_{g,p} \right\rangle \right] \\
 & - \frac{\partial}{\partial \xi_{g,p}} \left[P \left\langle S_{yg} \middle| V_{pi}, \theta_p, M_p, V_{gi,p}, \theta_{g,p}, \xi_{g,p} \right\rangle \right]
 \end{aligned} \tag{2.1}$$

During the PDF simulation, trial particles/droplets are distributed uniformly in the physical computational domain. One should perform a random function for the arrangement of the dispersed phase, so that the number of particles in every cell is kept almost constant during all the iterations. Each particle has random-set values of its spatial position, velocity, diameter, temperature, and the gas properties seen by it. These variables of particles and properties seen by it change their value and obey stochastic equations which are solved by integration in a certain time step [65].

Particle calculation is achieved for one or several time steps, and over a period of every time step, the droplet-averaged properties in each cell are calculated by an ensemble average of the number of particles existing in it. Accordingly, the source term is added to the gas-phase equations and the process iterates until convergence.

The advantage of the PDF approach over the Eulerian-Lagrangian approach lies on the ability to provide more detailed and accurate droplets statistics at any location of the flow field, whereas the Eulerian-Lagrangian approach (see below) gives a very little information in the low droplet concentration regions. The advantage of the PDF approach over the traditional Eulerian-Eulerian approach (see below) is that the former can easily treat the droplets with different initial sizes, temperatures, and velocities. It gives also more accurate particle statistics, for cases where the particle behavior in a low-particle-concentration area is important, without additional cost [64].

The drawback of this model is that it needs much more computation time than the two-fluids or Lagrangian models. The use of PDF necessitates solving the full-droplet PDF even in regions where there are very few

droplets that have little influence on the overall solution. This causes needless additional effort and expenses.

2.2 Eulerian-Eulerian approach

The classical two-fluid models have been the subject of many publications either in the mathematics community [66] or in the engineering one [65]. The Eulerian-Eulerian (E-E) approach treats both phases as continua. The behavior of dispersed and gas phase is characterized by using the partial differential Navier-Stokes equations which describe the flow of (incompressible) fluid. Eulerian-Eulerian approach is more suitable in case of dense two-phase flow, e.g. the volume fraction of both phases is greater than 10^{-3} . Indeed the assumption that dispersed phase is continuous phase become more realistic and using a Lagrangian approach needs a lot of computational time.

Compared to Eulerian-Lagrangian procedure, the Eulerian-Eulerian approach has the advantages of less computational costs. So it is more time effective. Such schemes lend themselves more naturally to parallel computing and transient flow calculations. The reason behind this is that parallel numerical computation is achieved by arranging fluid-blocks to CPU and not particles. The multiple dispersed phases have similar transport equations as the gas phase which makes the implementation not very complex. The coupling between two phases is easily done and the convergence criteria can be clearly defined [65].

The difficulties of Eulerian-Eulerian approach are the modeling of turbulent diffusion of the dispersed phase and the closure of the interface exchange terms in momentum equations. The last one (momentum transfer between phases) is generally included in a drag term determined by the local slip velocity between phases. The determination of droplet/particle concentration at certain physical point is calculated by its volume fraction which is solved for all phases. The volume fraction underlies the law that the sum of all volume fractions in every point is unity. In the Eulerian-Eulerian approach one should make the assumptions that all phases are considered incompressible. We should suppose as well the pressure field generated for all phases are single unless additional modeling effort is required in particular if the multiphase flows consider phase transitions e.g. vaporization. The following are additional complex problems to solve while using E-E for the multi-phase flow:

- Fluctuations of the dispersed phases [65],
- Particle wall interaction [110],
- Boundary conditions,
- Numerical diffusion [111].

The major drawback of the Eulerian-Eulerian approach is the inability to capture the polydispersion in size of the spray (different diameters, density ...). One should therefore treat every class of particles diameter as a separate phase. Thus the advantage of less computational costs becomes not realistic, due to the fact that every class of particles has to be treated separately [135].

2.3 Eulerian-Lagrangian approach

The third procedure to solve two-phase flow is to use the combined Eulerian-Lagrangian models (E-L), which treat the fluid as a continuum and the particles (dispersed phase) as discrete entities [44], [55], [93] and [112]. The Eulerian framework is used to formulate the carrier-phase transport equations as will be described later. The Navier Stokes equations provides a solution to the transport problem over a fixed computational grid, while the particles models involve solving the Lagrangian equations. The path of a large number of particles, bubbles or droplets is tracked throughout the flow field based on a force balance on each entity [44].

The E-L method is suited for dense as well as dense multi-phase flows. Nevertheless the computing time is increasing with the number of considered parcels, i.e. the more the flow is dense, the more the tracked particle is high. The modeling of fluid particle interaction, droplet evaporation, collision, wall interaction etc. is physically concrete and clear, making it as main advantages of E-L approach [54].

Most Eulerian-Lagrangian approaches are hybrid methods that divide the solution of the transport problem into two steps [136]. The first step consists of the computation of the Eulerian part while the second step uses the Lagrangian approach to solve the dispersed portion. The algorithm alternates repeatedly between the two steps till reaching convergence criteria of the coupling between the phases. The coupling is performed via source terms calculated for each variable at every control volume [44]. Most works from the literature using the E-L approach neglect the volume change of the continuous phase due to the presence of particles/droplets [55], [114]. The transport equations are solved with the constant volume of the cell as well. This hypothesis becomes critical in region with high concentration, e.g. nozzle outlet zone. The second assumption often used while solving two-phase flow with E-L approach is that a numerical parcel does not represent only one real particle but it represents a set of real particles [113]. The aim behind this assumption is to reduce the computational time. However this may produce very poor numerical results due to poor statistics.

The statistical mean values of the dispersed phase require high number of parcels. This leads to high computational costs making it a draw back of the Eulerian-Lagrangian approach. In order to get the fluid properties on the parcel location one uses different spatial interpolation algorithms e.g.

linear, quadratic, cubic, spline etc. This has a significant effect on the accuracy of the Eulerian-Lagrangian approach. It can deliver different results of the dispersed phase properties [67]. Complex geometries postulate the use of multiblock concept for the grid generation. This results in long and complex searching algorithm for every new parcel location. that is extremely time consuming. Compared to Eulerian-Eulerian, the Eulerian-Lagrangian approach has also the disadvantage of being more difficult to run on parallel computer, because of the discrete treatment of particle allowing it to move in all blocks of the physical domain [93].

Despite all difficulties and problems mentioned above the Eulerian-Lagrangian approach remains the most popular model to solve multiphase flows [61]. This procedure will be adapted within this work. So it will be analyzed and discussed in the next chapter.

2.3.1 Continuous phase description

The description of the continuous phase is based on laws of continuum mechanics, namely the balance equation of mass, momentum, energy, etc.

2.3.1.1 Fundamental equations

For the description of the continuous phase, the Eulerian approach has been used. The general equation for the carrier phase describing the transport of a physical variable ψ is given by:

$$\frac{\partial \rho \psi}{\partial t} + \frac{\partial (\rho u_j \psi)}{\partial x_j} = \frac{\partial}{\partial x_j} \left(\Gamma_\psi \frac{\partial \psi}{\partial x_j} \right) + S_\psi + S_{\psi,p,s} + S_{\psi,p,y}, \quad (2.2)$$

where the variables Γ_ψ and S_ψ are summarized in Table 2.1 for the carrier phase variables.

The equation of mass conservation corresponds to the substitution of ψ by 1 in the equation (2.2). This law states that the mass of an isolated system remains usually constant independently of all process where this system is involved in.

For the case $\psi = u_i$, (2.2) produce the Navier Stokes transport equation for a Newtonian fluid, which states that the amount of momentum remains constant within a considered control volume. Momentum is neither created nor destroyed, but only changed through the action of forces as described by Newton's law of motion.

2. Turbulent reacting multiphase flows basics

ψ	Γ_ψ	S_ψ
1	-	-
u_i	μ	$\frac{\partial}{\partial x_j} \left(\mu \frac{\partial u_i}{\partial x_j} - \frac{2}{3} \frac{\partial u_k}{\partial x_k} \delta_{ij} \right) - \frac{\partial p}{\partial x_i} - \rho g_i$
y	$\frac{\mu}{Sc}$	0
T	$\frac{\mu}{Pr}$	0

Table 2.1: Viscosity and source term for the carrier phase variables

The variable μ denotes the viscosity, δ_{ij} the Kronecker tensor and \vec{g} the gravity acceleration vector.

In multiphase flows the transport of many scalars is involved, e.g. energy, vapor concentration, species, etc. The general form of transport equation for the temperature ($\psi = T$) and for the vapor concentration ($\psi = y$) is also governed by (2.2). Here, the quantity Sc denotes the Schmitt number, whereas Pr represents the Prandtl number.

The variables $S_{\psi,p,s}$ and $S_{\psi,p,v}$ represent the source terms due to the presence of particles/droplets. $S_{\psi,p,v}$ denotes the evaporation source terms of the transported species in case of mass transfer, whereas $S_{\psi,p,s}$ represents the source terms for solid particle (without mass transition). These source terms will be expressed in detail later.

2.3.1.2 Averaging technique

For engineering purposes, it is not necessary to consider in detail all the small scale fluctuations that occur in the flow particularly if it is high turbulent. For this reason, one has worked with averaged values which are, from the engineering point of view, sufficient for design and optimization purposes. In RANS context one usually decomposes a variable φ to a mean value part and a fluctuation part:

$$\varphi = \overline{\varphi} + \varphi' \quad (2.3)$$

where the bar indicates a linear averaging operator and φ' denotes the fluctuation characterized by $\overline{\varphi'} = 0$. The mean value part is defined by:

$$\overline{\varphi} = \frac{1}{T} \int_0^T \varphi dt \quad (2.4)$$

2.3 Eulerian-Lagrangian approach

Other averaging possibility is to define $(\bar{\quad})$ to be an average over an infinite ensemble of actions (ensemble averaging). This is more used while analyzing the measurement results. This means one measure for example the velocity u for each an infinity of experiments and obtain \bar{u} by averaging over the ensemble. Some properties of time or ensemble averaging are:

$$\begin{aligned} \overline{(f + g)} &= \bar{f} + \bar{g}, \\ \overline{af} &= a\bar{f}, \text{ where } a \text{ constant,} \\ \overline{\bar{f}} &= \bar{f}, \\ \overline{f'g} &= 0 \end{aligned} \quad (2.5)$$

Applying the Reynolds averaging (2.3), to equations of mass, momentum and scalar yields to:

$$\frac{\partial \bar{\rho}}{\partial t} + \frac{\partial (\bar{\rho} u_i)}{\partial x_i} = \bar{S}_{1,p,v}, \quad (2.6)$$

$$\frac{\partial (\bar{\rho} u_i)}{\partial t} + \frac{\partial (\bar{\rho} u_j u_i)}{\partial x_j} = \bar{\rho} g_i - \frac{\partial \bar{p}}{\partial x_i} + \frac{\partial}{\partial x_j} \left(\mu \frac{\partial \bar{u}_i}{\partial x_j} - \overline{\rho u_i' u_j'} \right) + \bar{S}_{u_i,p,s} + \bar{S}_{u_i,p,v}, \quad (2.7)$$

$$\frac{\partial (\bar{\rho} y)}{\partial t} + \frac{\partial (\bar{\rho} u_j y)}{\partial x_j} = \frac{\partial}{\partial x_j} \left(\bar{\rho} \Gamma \frac{\partial \bar{y}}{\partial x_j} - \overline{\rho u_j' y'} \right) + \bar{S}_{y,p,s} + \bar{S}_{y,p,v}, \quad (2.8)$$

$$\frac{\partial (\bar{\rho} T)}{\partial t} + \frac{\partial (\bar{\rho} u_j T)}{\partial x_j} = \frac{\partial}{\partial x_j} \left(\bar{\rho} \Gamma \frac{\partial \bar{T}}{\partial x_j} - \overline{\rho u_j' T'} \right) + \bar{S}_{T,p,s} + \bar{S}_{T,p,v}, \quad (2.9)$$

In flows with large density variation, e.g. combustion, the Reynolds averaging described above produces some more unclosed terms, thus a density weighted average, the so-called Favre average, is often preferred:

$$\varphi = \tilde{\varphi} + \varphi'', \quad (2.10)$$

with

$$\tilde{\varphi} = \frac{\overline{\rho \varphi}}{\bar{\rho}} \quad (2.11)$$

The tilde ($\tilde{\quad}$) denotes the Favre average and ($''$) marks the Favre fluctuation of the quantity. The important properties of this averaging technique are:

$$\begin{aligned}\overline{f''} &\neq 0, \\ \overline{\rho f} &= \overline{\rho} \tilde{f}, \\ \overline{\rho f''} &= 0.\end{aligned}\tag{2.12}$$

In case of Favre averaging, equations for mass, momentum and scalar yields to.

$$\frac{\partial \overline{\rho}}{\partial t} + \frac{\partial (\overline{\rho u_i})}{\partial x_j} = \tilde{S}_{1,p,v},\tag{2.13}$$

$$\frac{\partial (\overline{\rho u_i})}{\partial t} + \frac{\partial (\overline{\rho u_j u_i})}{\partial x_j} = \overline{\rho} g_i - \frac{\partial \overline{p}}{\partial x_i} + \frac{\partial}{\partial x_j} \left(\mu \frac{\partial \tilde{u}_i}{\partial x_j} - \overline{\rho u_i'' u_j''} \right) + \tilde{S}_{u_i,p,s} + \tilde{S}_{u_i,p,v},\tag{2.14}$$

$$\frac{\partial (\overline{\rho y})}{\partial t} + \frac{\partial (\overline{\rho u_j y})}{\partial x_j} = \frac{\partial}{\partial x_j} \left(\overline{\rho \Gamma} \frac{\partial \tilde{y}}{\partial x_j} - \overline{\rho u_j'' y''} \right) + \tilde{\omega}_y + \tilde{S}_{y,p,s} + \tilde{S}_{y,p,v},\tag{2.15}$$

$$\frac{\partial (\overline{\rho T})}{\partial t} + \frac{\partial (\overline{\rho u_j T})}{\partial x_j} = \frac{\partial}{\partial x_j} \left(\overline{\rho \Gamma} \frac{\partial \tilde{T}}{\partial x_j} - \overline{\rho u_j'' T''} \right) + \tilde{\omega}_T + \tilde{S}_{T,p,s} + \tilde{S}_{T,p,v},\tag{2.16}$$

In case of large Reynolds number, the molecular viscosity and diffusion coefficient are very small, therefore they can be neglected.

In the equations (2.7)-(2.8) and (2.14)-(2.15) some new terms arise, namely the unclosed Reynolds stress tensor $\overline{u_i'' u_j''} / \overline{u_i'' u_j''}$ and the turbulent transport terms $\overline{u_j'' y''} / \overline{u_j'' y''}$, which have to be modeled as it will be shown in chapter 3. The third type of unclosed terms is the mean chemical source term in the averaged equation of mass fraction which has to be closed within a combustion model. The last type of unclosed quantities is the particles/droplets source terms which in turn will be explained in details later.

2.3.1.3 Turbulent scales

The turbulence consists of a superposition of eddies of ever-smaller sizes. The rate at which the turbulent kinetic energy is transferred from bigger eddies to smaller eddies is called the dissipation rate ε . The energy cascade, however, can not be extended infinitely because of the viscous forces. The smaller an eddy, the greater the velocity gradient inside the eddy and the greater the viscous stress that counteracts the eddying

2.3 Eulerian-Lagrangian approach

motion. Consequently, there is a statistical lower limit of the smallest eddy size that corresponds to a minimum scale of turbulence and a maximum frequency in the turbulent motion. At this limit the kinetic energy of the fluctuating motion dissipates completely into the internal energy of the flow. The length scale of such smallest eddies is called Kolmogorov scale and is defined as

$$\eta_k = \frac{\nu^{3/4}}{\varepsilon^{1/4}}. \quad (2.17)$$

The corresponding Kolmogorov time scale is

$$\tau_k = \frac{\nu^{1/2}}{\varepsilon^{1/2}}. \quad (2.18)$$

The major part of the turbulent kinetic energy is contained in the large but not the largest eddies. The large eddies are, therefore, often called energy containing eddies. The length and time scales of those eddies are further important scales. The size of the energy containing eddies depends on the geometry of a spatial domain. It depends also on the local intensity of turbulence. This size can be related (it is not exactly the same) to the integral turbulent length scale that can be determined from the two-point spatial correlation function for statistically steady (time independent) turbulence

$$R_{ij}^L(x, x + \Delta x) = \frac{\overline{u_i'(x)u_j'(x + \Delta x)}}{\sqrt{\overline{u_i'^2(x)}}\sqrt{\overline{u_i'^2(x + \Delta x)}}}. \quad (2.19)$$

as

$$L_{ij}(x) = \frac{1}{2} \int_{-\infty}^{+\infty} R_{ij}^L(x, x + \Delta x) d(\Delta x). \quad (2.20)$$

Here, L_{ij} denotes the length scale tensor. For homogeneous isotropic turbulence the integral length scale is independent of the direction and is given by

$$l_i = \frac{1}{3} L_{ii} \quad (2.21)$$

The two-point velocity correlation function for homogeneous isotropic turbulence and the corresponding integral turbulent length scale are schematically shown in Figure 2.1.

The corresponding time scale can be determined from the known time correlation function

$$R_{ij}^T(x, t, t + \Delta t) = \frac{\overline{u_i'(t)u_j'(t + \Delta t)}}{\sqrt{\overline{u_i'^2(t)}}\sqrt{\overline{u_i'^2(t + \Delta t)}}}, \quad (2.22)$$

2. Turbulent reacting multiphase flows basics

as

$$T_{ij}^L(x) = \frac{1}{2} \int_{-\infty}^{+\infty} R_{ij}^T(x, t, t + \Delta t) d(\Delta t) \quad (2.23)$$

Assuming isotropy and homogeneity leads to

$$T_t = \frac{1}{3} T_{ii} \quad (2.24)$$

Qualitatively the integral turbulent time scale can be interpreted as an averaged inverse rotational frequency of the typical big eddy appearing in the spatial location x .

Though turbulence in practical flows is neither isotropic nor homogeneous, the idealized integral length scale (2.21) provides at least coarse quantitative information about spatial correlation and sizes of typical energy containing eddies in turbulent flows. Qualitatively the integral turbulent length scale can be interpreted as an averaged radius of the typical big eddy appearing in the spatial location x .

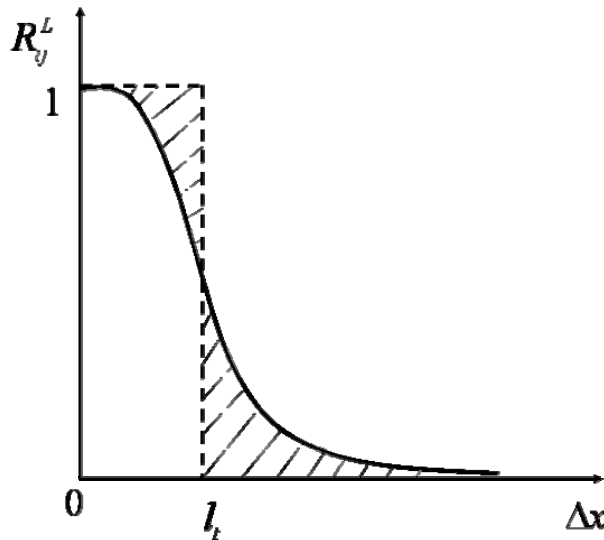


Figure 2.1: Two-point velocity correlation function versus the distance between two point Δx for homogeneous isotropic turbulence

The turbulent kinetic energy spectrum obtained from the Fourier transformation of the spatial isotropic two-point correlation function R_{ij}^L is schematically plotted in Figure 2.2. $E_\omega(k_\omega)$ is the kinetic energy density per wave number k_ω or the inverse turbulent length scale. The maximal values of $E_\omega(k_\omega)$ correspond to the energy containing scales that are

2.3 Eulerian-Lagrangian approach

related to the turbulent length scale l_t . Eddies of size smaller than the energy containing eddies build the inertial subrange. As it was shown by Kolmogorov, the energy transfer from large to small scales within the inertial subrange is independent on the scale size and is followed by the $\sim k_\omega^{-5/3}$. At the right side of the inertial subrange the wave number corresponding to the Kolmogorov scale η_k is located.

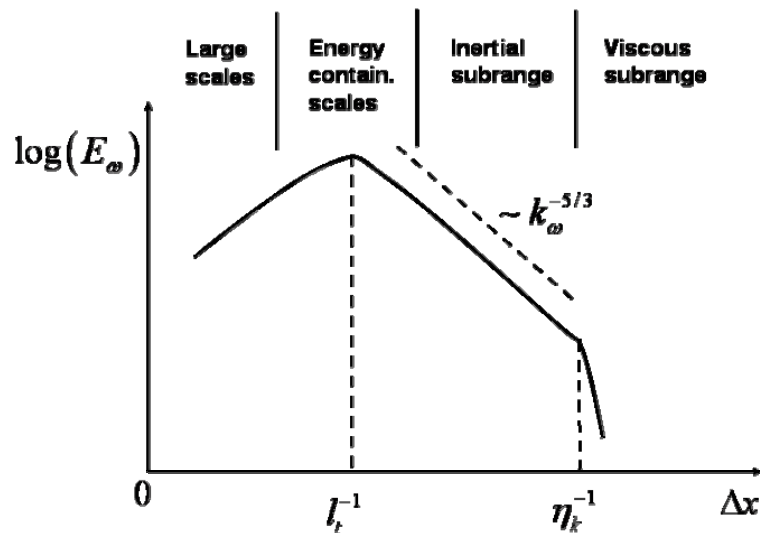


Figure 2.2: Two-point velocity correlation function versus the distance between two point Δx for homogeneous isotropic turbulence

2.3.2 Dispersed phase description

As mentioned before, the dispersed phase, within this thesis, is described using a Lagrangian procedure, where all numerical particles/droplets are tracked by solving the equation of motion. For that purpose, some relevant parameters have to be introduced.

2.3.2.1 Relevant parameters characterizing the dispersed phase

Volume fraction: It describes the amount of dispersed phase volume within the gas phase. The volume fraction is used to characterize the level of interaction between the different phases. It is defined by:

2. Turbulent reacting multiphase flows basics

$$\alpha_p = \frac{\sum_{l=1}^n V_{p,l}}{\delta V}, \quad (2.25)$$

where $V_{p,l}$ denotes the volume of particle l within the considered control volume δV . The summation is done over all existent particle n . The continuous phase volume fraction is defined in a similar way:

$$\alpha = \frac{\delta V}{\delta V}, \quad \text{with: } \alpha + \alpha_p = 1 \quad (2.26)$$

Mass loading: It is defined by:

$$Z_L = \frac{\dot{m}_p}{\dot{m}}, \quad (2.27)$$

where \dot{m}_p represents the particles mass flux, while \dot{m} represents the mass flux of the continuous phase.

Particle Reynolds number: it was revealed to be an important parameter to characterize the effect of dispersed phase on the turbulence variation of carrier gas. It is defined by:

$$\text{Re}_p = \frac{\rho D_p |U - u_p|}{\mu}, \quad (2.28)$$

where ρ , μ and U represent the density, viscosity and absolute velocity of the continuous phase, respectively, D_p is the particle diameter while u_p denotes the absolute velocity of dispersed phase.

Particle relaxation time defines the ability of a given particle to react to the carrier gas. The particle relaxation time yields the time taken by a particle to respond on the fluid velocity modification. It is defined by:

$$\tau_p = \frac{\rho_p D_p^2}{18\mu} \quad (2.29)$$

where ρ_p , D_p and μ are particle density, particle diameter and fluid dynamic viscosity, respectively.

Stokes number: measures the inertia of one particle. It is defined as the ratio of the particle relaxation time to the turbulent integral time scale. The Stokes number is important in case of separation and particle deposition.

$$St = \frac{\tau_p}{T_t} \quad (2.30)$$

where T_t denotes the turbulent integral time scale. defined in (2.23) and (2.24)

2.3.2.2 Equation of motion for particles

The particle dynamics is described according to the Basset-Boussinesq-Oseen equation, "BBO-equation" [68]. In this work, a spherical, small, non deformable and non rotating particle is considered. The equation of motion illustrates the second law of Newton which mentions that the sum of forces acting upon a mass provides their acceleration. The particles trajectories are then deduced from the equation of motion. Tchen [69] introduced in his dissertation (1945) the relative velocity for the description of motion and formulated the equation (2.31) by making the following assumptions:

1. Distance between particles should be long compared to particle diameter.
2. No particle wall interaction.
3. Particle-Reynolds-Number should be very small $Re_p \ll 1$.
4. Particle diameter should be very small compared to characteristic length scale $D_p / 2L \ll 1$.

$$\underbrace{\rho_p \frac{\pi}{6} D_p^3 \frac{du_{p,i}}{dt}}_I = \underbrace{3\pi\mu\rho(u_i - u_{p,i})}_{II} + \underbrace{\frac{1}{2}\rho \frac{\pi}{6} \frac{d(u_i - u_{p,i})}{dt}}_{III} - \underbrace{\frac{\pi}{6} D_p^3 \frac{\partial P}{\partial x_i}}_{IV} + \underbrace{\frac{\pi}{6} D_p^3 (\rho_p - \rho) g_i}_V + \underbrace{\frac{3}{2} D_p^2 \sqrt{\pi\rho\mu} \int_{t_0}^t \frac{d(u_i - u_{p,i})}{d\tau} \frac{1}{\sqrt{t-\tau}} d\tau}_{VI} \quad (2.31)$$

For turbulent multiphase flows, the above mentioned assumptions are dismissed and can not be satisfied. Particularly points 3 and 4 cause serious limitations for real industrial processes. For cases of high particle Reynolds number, $Re_p \gg 1$, the non linear convective terms within the equation of motion are not negligible. However a theoretical derivation for the particle equation of motion under consideration of such conditions is still an open question and only some empirical function fitted to experimental results are available. The influence of convective terms are modeled by Hansell et al. [70] by adding terms *III* and *VI* which represent the added mass force and the basset force, respectively.

Part *I* describes the inertia of a particle, which describes the resistance of mass to change the velocities and direction. Part *II* describes the drag force which appears when even there is a relative motion between the particle and the fluid. It is opposite to the direction of motion of the

2. Turbulent reacting multiphase flows basics

particle relative to the liquid, and is basically due to frictional effects. The drag force is often dominating the motion of particle. Part *III* states the added mass force which considers the additional effects acting on the structure of particle for the case of unsteady motion of bodies or unsteady flow around the objects. The added mass force accounts for the drag variation induced by the particle velocities modification or acceleration/deceleration of the carrier gas. Part *IV* denotes the pressure gradient which applies a force on the particle and acts in the same direction as the pressure gradient itself. This force becomes important when the carrier gas density is higher compared to the density of the dispersed phase, which is not the case in this work, therefore it is neglected. The pressure gradient is often derived from the velocity gradient of the gas phase and set to:

$$-\frac{\partial p}{\partial x_i} = \rho \frac{du_i}{dt} \quad (2.32)$$

Part *V* states the buoyancy and gravitation forces. Buoyancy is based on the Archimedes' principle. It is important in case of high fluid density and particle volume. Part *VI* denotes the Basset term representing an unsteady force exerted on a particle due to acceleration of relative velocity between particle and fluid.

For different types of two-phase flow, there are some characteristics estimating Basset force on a particle. For the bubble-liquid two-phase flow, the Basset force can be neglected when the perturbation frequency of the fluid flow is small or has a large value. For liquid (or solid) particle-gas two-phase flow, neglecting Basset force is reasonable. But for the other two-phase flows, the magnitude of Basset force is determined by some actual conditions such as; the particle size, ratio of the fluid density to the particle, the flow characteristic time and the relaxation time of the particle, acceleration of relative velocity, etc.

The implementation of new modification for the drag force (Part *II*) [70] and the substitution of equation (2.32) describing the pressure gradient in (2.31) yields to:

$$\begin{aligned} \underbrace{\frac{du_{p,i}}{dt}}_I &= \underbrace{\frac{3 C_w}{4 D_p} \frac{\rho}{\rho_p} (u_i - u_{p,i}) \left| \vec{u}_i - \vec{u}_{p,i} \right|}_{II} + \underbrace{\frac{1}{2} \frac{\rho}{\rho_p} C_{VM} \frac{d(u_i - u_{p,i})}{dt}}_{IV} \\ &+ \underbrace{\frac{\rho}{\rho_p} \frac{\partial u_i}{\partial t}}_{III} + \underbrace{\frac{(\rho_p - \rho)}{\rho_p} g_i}_V + \underbrace{\frac{9}{D_p} \frac{\rho}{\rho_p} \sqrt{\frac{v}{\pi}} C_B \int_{i0}^t \frac{d(u_i - u_{p,i})}{d\tau} \frac{1}{\sqrt{t - \tau}} d\tau}_{VI} \quad (2.33) \end{aligned}$$

The correlation factors C_w , C_{VM} and C_B represent the coefficient for drag, added mass and Basset force, respectively, and are determined based on

2.3 Eulerian-Lagrangian approach

empirical functions fitted to experimental data. These correlations approve the use of equation (2.33) for high particle Reynolds number. The drag coefficient C_w is used to model the complex dependencies between the particle and the flow conditions. C_w is not constant and depends on relative velocities, viscosities of the dispersed phase and carrier phase, the shape of particle and, the roughness of particle's surface. Morsi and Alexander [71] published in their work (1972) formulations for the drag coefficient depending on the particle Reynolds number. Clift et al. [72] suggested some new correlations for the calculation of C_w limiting thus the error to 5% compared to experimental results. The drag coefficient used within this work is determined for a spherical, not deformable particle by the standard equation [93]:

$$C_w = \frac{24}{\text{Re}_p} \left(1 + \frac{1}{6} \text{Re}_p^{2/3} \right) \quad \text{Re}_p \leq 1000 \quad (2.34)$$

$$C_w = 0.44 \quad \text{Re}_p \geq 1000 \quad (2.35)$$

The particle Reynolds number is calculated using the equation (2.28). The other correlation terms C_{VM} and C_B are used according to the work of Odar and Hamilton [73]:

$$C_{VM} = 2.1 - \frac{0.132 A_c^2}{(1 + 0.12 A_c^2)} \quad (2.36)$$

$$C_B = 0.48 + \frac{0.52 A_c^3}{(1 + A_c^3)}, \quad (2.37)$$

where A_c represents an acceleration factor which can be determined by:

$$A_c = \frac{\left| \frac{d(\vec{u} - \vec{u}_p)}{dt} \right|}{|\vec{u} - \vec{u}_p|^2} D_p. \quad (2.38)$$

The particle equation of motion, in fact, should account for the effect of other physical phenomena which influence the path of particle and not considered in equation (2.33), e. g. the Magnus and Saffman forces [55]. The first one is a result of rotation of the particle, inducing 'lift' (differential pressures) perpendicular to the direction of the motion (i.e., the 'curve ball effect'). The Magnus force is considerably smaller than the magnitude of the drag force. It is present only while considering the particle rotation which is not the case in this work. Therefore it is neglected. The Saffman force is due to the shear in the mean flow of carrier gas. It is experienced by the solid particle even if it doesn't rotate. The Saffman force is acting towards the direction of higher slip velocity.

2. Turbulent reacting multiphase flows basics

Due to $\rho/\rho_p \ll 1$ and a very small gradient slip velocity over particle diameter, it is negligible. In addition to above mentioned forces there are other external forces, e.g. electromagnetic force which occurs while a charged particle moves within a magnetic field. It is determined by:

$$\vec{F}_E = q_p \vec{E}_p, \quad (2.39)$$

where q_p and \vec{E}_p denote the particle charge and the magnetic field intensity, respectively. The electromagnetic force may exert an important action on the particle, when the particle mass is very small. It is responsible for the deposition of the dispersed phase and forming thus an electrical filter. In the frame of this work only the gravitation force, is considered, the computed configurations do not exhibit any electrical field.

The considered forces contributing to the motion of particle are then: the drag, gravitation and buoyancy forces. Therefore the equation (2.33) is reduced to:

$$\frac{du_{p,i}}{dt} = \frac{3 C_W}{4 D_p} \frac{\rho}{\rho_p} |\vec{u} - \vec{u}_p| (u_i - u_{p,i}) + \frac{(\rho_p - \rho)}{\rho_p} g_i = \frac{1}{m_p} \sum_i F_i \quad (2.40)$$

2.4 Combustion

The intensive development of mathematical combustion theory began in the first half of the twentieth century. It was originally initiated by military objectives. The definition of combustion in terms of macroscopic kinetics is given in [115], one of the pioneering works in this area: "Combustion is the proceeding of a chemical reaction under condition of progressive self-acceleration, which is, in turn, caused by the accumulation in a system either of heat or catalyzing reaction products". The macroscopic theory of combustion deals with investigation of the role of convection, diffusion and heat exchange and their interaction in chemical reaction processes. The elements of chemical kinetics necessary for further considerations are briefly described in section 2.4.1. Generally speaking, single-phase combustion can be subdivided into two major parts. These include non-premixed or diffusion and premixed combustion that are described in the next sections. Less idealized and more commonly occurring in practice partially premixed combustion is considered next.

2.4.1 Chemical kinetics

The chemical kinetics is the study and research of reactions with respect to reaction rates, formed species, formation of new intermediates etc. The points of interest are basically linked to amounts reacted, formed, and the

speed of their formation, i.e., the rate at which the concentration of reactants and products change. Consider the following example:



Factors ν'_A , ν'_B and ν'_C denote the molar stoichiometric coefficients of species A , B and C . The equation (2.41) states that the chemical reaction involves direct convection from reactant to product. In reality the chemical reaction can have not only one step, but also few steps, that complicate the chemical kinetics and allow many possible reaction mechanisms. The last one specifies at the molecular level how a reaction proceeds and describes in detail exactly what takes place at each stage of a chemical transformation. A complete mechanism must also account for all reactants used, and all products formed. The equation (2.41) is then not enough to describe a chemical reaction and a system of equations arise:

$$\sum_{k=1}^N \nu'_{kj} M_k \rightleftharpoons \sum_{k=1}^N \nu''_{kj} M_k \quad \text{for } j = 1, M, \quad (2.42)$$

where M_k represents the symbol of species k , ν'_{kj} and ν''_{kj} are the molar stoichiometric coefficients of species k in reaction j . The above system of equations must obey the mass conservation given by:

$$\sum_{k=1}^N \nu'_{kj} W_k \rightleftharpoons \sum_{k=1}^N \nu''_{kj} W_k \quad \text{for } j = 1, M, \quad (2.43)$$

here W_k denotes the molecular weight of species k . However the balanced equation (2.43) does not tell us how the reactants become products. The rate of the overall process will be determined by the slowest (highest energy) step in the reaction mechanism. The mass reaction rate $\dot{\omega}_{kj}$ of species k in the reaction j is given by:

$$\dot{\omega}_{kj} = r_j W_k \nu_{kj} \quad \text{with} \quad \nu_{kj} = \nu''_{kj} - \nu'_{kj} \quad (2.44)$$

where r_j represents the rate of progress of reaction j . By considering all M reactions, which take place within a reaction mechanism, the mass reaction rate $\dot{\omega}_k$ is the sum of all produced rates $\dot{\omega}_{kj}$:

$$\dot{\omega}_k = \sum_{j=1}^M \dot{\omega}_{kj} = W_k \sum_{j=1}^M r_j \nu_{kj} . \quad (2.45)$$

The sum of all mass reaction rates $\dot{\omega}_k$ produced for all specie k is given by (2.46) and obeys the law of mass conservation. Then we know the famous principle of Antoine-Laurent de Lavoisier stating: "*Rien ne se perd, rien ne se crée, tout se transforme.*"

2. Turbulent reacting multiphase flows basics

$$\sum_{k=1}^N \dot{\omega}_k = \sum_{j=1}^M \left(r_j \sum_{k=1}^N W_k \nu_{kj} \right) = 0. \quad (2.46)$$

The progress rate r_j of reaction j , which denotes the change of products formation in time can be affected by four factors:

- Concentrations
- Phase of the reactants
- Temperature
- The presence of catalyst

If we plot the concentration of a product forming against time we will get a curve. The tangential slope at any place on that curve would be the instantaneous rate at that moment in time. The reaction rate r_j for a considered reaction j is written [74]:

$$r_j = K_{fj} \prod_{k=1}^N \left(\frac{\rho y_k}{W_k} \right)^{\nu_{kj}} - K_{rj} \prod_{k=1}^N \left(\frac{\rho y_k}{W_k} \right)^{\nu_{kj}}, \quad (2.47)$$

where K_{fj} and K_{rj} are the forward and reverse constants of the reaction rates. $\rho y_k / W_k$ is the molar concentration of species k . The rate constants are difficult to determine and are related to the temperature of the system by what is known as the Arrhenius equation:

$$K_{fj} = A_{fj} T^{\beta_j} \exp\left(-\frac{E_j}{RT}\right) = A_{fj} T^{\beta_j} \exp\left(-\frac{T_{aj}}{T}\right), \quad (2.48)$$

where R is the ideal gas constant (8.314 J/mole.K), T is the temperature in Kelvin with the temperature exponent β_j , E_j is the activation energy in joules/mole, T_{aj} is the activation temperature in K , and A_{fj} is a constant called the frequency factor; which is related to the fraction of collisions between reactants having the proper orientation. The backwards constant rates K_{rj} are calculated using the equilibrium and the forward rates constants:

$$K_{rj} = \frac{K_{fj}}{\left(\frac{P_a}{RT}\right)^{\sum_{k=1}^N \nu_{kj}} \exp\left(\frac{\Delta S_j^0}{R} - \frac{\Delta H_j^0}{RT}\right)} \quad (2.49)$$

where $p_a = 1 \text{ bar}$. The Δ symbols refer to changes occurring when passing from reactants to products in the j^{th} reaction: ΔH_j^0 and ΔS_j^0 are respectively enthalpy and entropy changes for the reaction j . These quantities are obtained from tabulations [74]. The computing of r_j for every reaction necessitate the calculation of forwards and backwards

constants i.e. the knowledge of all variable: frequency factors A_{fj} , temperature exponents β_j and the activation energy E_j . The huge number of variables and parameters required for the computation of r_j makes the tasks very complex. Using a detailed mechanism in the frame of numerical combustion leads to the resolution of a balance equation for each species included. Consequently it aggravates the tasks for the CFD. In order to use numerical simulation of practical combustion processes, one should use simplified models for the chemical kinetics i.e. the one step reaction mechanism, equilibrium model, Flamelet model or ILDM.

In the first model "one step reaction mechanism" the combustion process in a flame is approximated by a one-step irreversible infinitely fast global reaction (Burke & Schumann, [75]). We know that global reactions do not represent an actual reaction that occurs during combustion and that processes follows many elementary reactions. However global reactions can represent very well what an engineer may want from combustion and to examine the overall stoichiometry. Such engineering approximations to the overall rate of combustion exist and are called *reduced reaction mechanisms*. The equilibrium chemistry model as it is used in the frame of this work refers to a radical: radical A is said to be in a steady-state if its net production rate from the mechanism is approximately zero, i.e. $d[A]/dt \approx 0$. The state of forward and reverse reactions continues to occur at equal rates, but no net change is observed. Hence, by employing the equilibrium model, many species may be eliminated from the reaction rate expressions by relating their concentration to those of other species. The flamelet model provides detailed insight into flame structure by accurately accounting for non-equilibrium, strain and turbulence effects. This approach can be considered as an extension of the "flame sheet" model which assumes infinitely fast chemical reaction as the reaction zone which is an infinitely thin interface. With the equal diffusivity assumption under constant pressure combustion without heat loss, the thermo-chemical properties are determined completely by the local mixing state which is described by the mixture fraction. The flamelet model as proposed by Peters [132] aimed at coupling chemistry with a flow code through tabulating stationary flame solutions. The flamelet solutions are stored in libraries where they are represented in terms of scalars as function of the mixture fraction and the scalar dissipation rate. Maas and Pope [76] proposed a new method for reducing chemical kinetics based on Intrinsic Low-Dimensional Manifolds (ILDM). This approach is based on a local time scale analysis of the Jacobian of the chemical reaction system. During a chemical reaction, some species concentrations will be evolved more quickly than others for an initial period of time. The essence of the behavior of these species is governed by fast time scale terms for the initial period of time. When enough time has passed, the slower time scale terms begin to affect the behavior of the system. As time passes, the slower time scale terms dominate the evolution of each species concentration.

2.4.2 Non-premixed flame

Diffusion flames represent a specific class of combustion problems. The main feature of these flames is that fuel and oxidizer are not mixed before they enter the domain where they are burnt. Mixing brings reactants into the reaction zone where thin layers of burnable mixtures at different equivalence ratios are formed and combustion takes place. Thus, mixing becomes one of the main issues in this type of flames controlling the behavior of the whole combustion system. Combustion occurs only in a limited region, where fuel and oxidizer are adequately mixed. Outside this region the mixture is either too rich (fuel side) or too lean (oxidizer side) for chemical reactions to proceed. In contrast with premixed flames that are considered in the next section, diffusion flames are not able to propagate against the flow. A definite "thickness" can not be assigned to these flames either. Among industrial applications the diesel engine can be mentioned as a typical example for diffusion flame. Combustion in aero-propulsion devices (aero engines) also takes place in diffusion mode. From the design and safety point of view, diffusion flames are simpler because no premixing with a given equivalence ratio is required and they do not propagate. However, their burning efficiency is restricted compared with premixed flames because the mixing or rather the rate of mixing limits the speed at which chemical reactions may proceed. In modern stationary gas turbines these flames are only employed for the piloting (or stabilization) of the main flame mostly in start-up regimes.

The main disadvantage of pure diffusion flames is that they are less affectable in terms of combustion temperature and, consequently, NO_x emissions. The fuel can be diluted with nitrogen or exhaust gases, but the maximal combustion temperature is always achieved in the region of stoichiometric mixture where the greatest NO_x formation rates take place.

Nevertheless, the fundamental understandings as well as modeling details of diffusion combustion phenomena are very important in context of partially premixed flames that actually appear in steady gas turbine combustors. Many modeling aspects concerning diffusion flames are used in the complete model considered in the present work.

Besides the more complex methods like the flamelet [78] or the ILDM approach [77], the simplest approach for the modeling of diffusion flames is the well-known mixture fraction description. As a starting point in the analysis several assumptions are made:

- Equality of diffusion coefficients for all chemical species;
- Equality of heat capacities for all chemical species and their independence on the temperature.

One can introduce a conserved scalar, mixture fraction, as a dimensionless element mass fraction. The mixture fraction variable is defined by [74] as:

$$z = \frac{\dot{m}_F}{\dot{m}_F + \dot{m}_O} = \frac{sy_F - y_O + y_O^0}{sy_F^0 + y_O^0}, \quad (2.50)$$

where s denotes the stoichiometric ratio defined by:

$$s = \frac{\nu_O W_O}{\nu_F W_F}. \quad (2.51)$$

The variables ν_F and ν_O denote the molar stoichiometric coefficients of species F (fuel) and, O (oxidizer) having the mass fraction and mass flux y_F , \dot{m}_F , y_O and \dot{m}_O , respectively.

The mixture fraction changes because of diffusion and convection but not reaction. It has no reaction source term. The transport equation is given by:

$$\frac{\partial \rho z}{\partial t} + \frac{\partial (\rho u_i z)}{\partial x_i} = \frac{\partial}{\partial x_i} \left(\rho D \frac{\partial z}{\partial x_i} \right) \quad (2.52)$$

The simplified description of diffusion flames presented above was first proposed by Shvab and Zeldovich and called Shvab-Zeldovich formalism. It tremendously reduces the modeling demands and allows describing the whole system by means of only one variable. One can represent the idealized one-dimensional diffusion flame structure in terms of the mixture fraction z (see Figure 2.3). If no heat loss because of radiation and no mixing of fuel (or oxidizer) streams with different enthalpies is considered, then the species concentrations, the temperature and the density are all functions of the mixture fraction only: $y_k = y_k(z)$, $T = T(z)$, $\rho = \rho(z)$; while the mixture fraction itself is the function of time and space: $z = z(t, x_i)$.

Real diffusion flames, of course, behave more complicated and feature more complex structure, but this simplified mixture fraction approach provides reasonable results at least for the flow density, temperature and stable species' concentrations. The improved description of radicals can be achieved using more sophisticated models like the flamelet [78] or the ILDM approach [77].

It is essential that using the mixture fraction description of the whole modeling of diffusion flames can be basically decomposed into two sub-problems:

1. **Mixing problem** where equation (2.52) has to be solved with appropriate boundary conditions in order to obtain the mixture fraction field $z(t, x_i)$ as a function of time t and spatial coordinates x_i
2. **Flame structure problem** where the mixture fraction field $z(t, x_i)$ obtained in the previous **mixing problem** is used to reconstruct the

2. Turbulent reacting multiphase flows basics

$y_k = y_k(z)$, $T = T(z)$, $\rho = \rho(z)$ dependencies and, consequently, reproduce the flame structure: $y_k = y_k(t, x_i)$, $T = T(t, x_i)$, $\rho = \rho(t, x_i)$

For taking into account the enthalpy variations one only needs to introduce an additional independent variable, enthalpy h , and to extend the dependencies for the species concentrations, the temperature and the density to $y_k = y_k(z)$, $T = T(z, h)$, $\rho = \rho(z, h)$ (see [116] for details). The transport equation for h has to be solved in this case with appropriate boundary conditions and including some model for radiation.

Different approaches exist for the determination of the flame structure depending on the mixture fraction. The simplest one is proposed by Burke and Schumann [75]. They assumed that the chemistry is infinitely fast, i.e. all chemical time scales are shorter than all time scales of the flow (mixing, diffusion etc.). Moreover the one-step reaction (2.41) runs only in one direction - increasing of products (irreversibility). These two assumptions require that fuel and oxidizer can not exist simultaneously. They must also vanish as the mixture fraction approaches its stoichiometric value.

More sophisticated assumption, which is used in the present work, is that chemistry is infinitely fast but reversibility allows fuel, oxidizer and products to coexist. In other words, all elementary reactions of a complete system (2.42) are in equilibrium state. In this case all species mass fractions can be calculated from the elements' composition, that is exactly given by the mixture fraction, z . It can be either done by using the calculations of minimization of Gibbs' energy (see e.g. Warnatz et al. [117]), or by calculating homogeneous reactors using the CHEMKIN package [137].

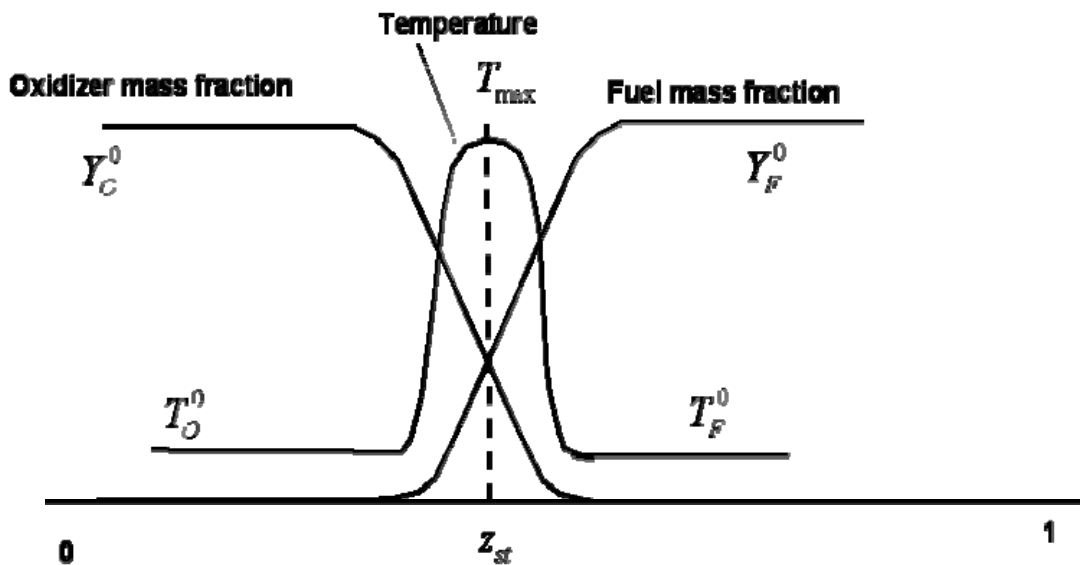


Figure 2.3: One-dimensional structure of a diffusion flame

2.4.3 Premixed flame

Another special class of combustion processes is represented by premixed combustion. Contrary to the diffusion flames considered in the previous section, in premixed flames the fuel and oxidizer are completely mixed on the molecular level before combustion takes place. A schematic representation of an idealized one-dimensional flame is shown in Figure 2.4. This idealized representation is introduced by Zeldovich and Frank-Kamenetsky (see e.g. [115]) in their asymptotic analysis. One can see the development of the gas temperature T along the only considered axis x from minimal value T_0 (reactants) to maximal value T_{\max} (products) and, consequently, the one-dimensional flame structure. Actually the flame front, if it is considered as an interval where significant temperature changes occur, consists of two main zones:

- Preheating zone where the diffusion of heat and mass proceeds very intensively while chemical reactions are not yet running;
- Reaction zone where, in contrast to the preheating zone, chemical reaction rates rapidly grow up first and then go down so that chemistry dominates against diffusion.

Behind the reaction zone a post flame region (or oxidation zone) is located where no significant heat is released and only some slow (in terms of kinetics) reactions occur at the high temperature achieved in the reaction zone. The fundamental issues of Zeldovich-Frank-Kamenetsky-von-Karman (ZFK) asymptotic theory are as follows:

- The reaction zone is located in the high temperature part of the flame and has a temperature nearly equal to T_{\max} ;
- The thickness of the reaction zone δ is approximately one order of magnitude smaller than the thickness of the flame front l_f ;
- The flame front propagates in the reactants' direction with velocity \bar{s} . This velocity is proportional to the square root of the reaction rate (see equation (2.48)) taken at $T = T_{\max}$ and to the thermal diffusivity

$$|\bar{s}|^2 \sim \frac{\lambda}{\rho c_p} \cdot \exp\left(\frac{E}{RT_{\max}}\right), \quad (2.53)$$

that reveals, consequently, the nature of the flame propagation coupled with the kinetics of the heat release and with heat conduction from the hot to the cold gas layers;

- The maximal combustion temperature T_{\max} is equal to the adiabatic temperature of the chemical reaction that, in turn, can be determined independently on the flame propagation theory from thermodynamic equilibrium.

2. Turbulent reacting multiphase flows basics

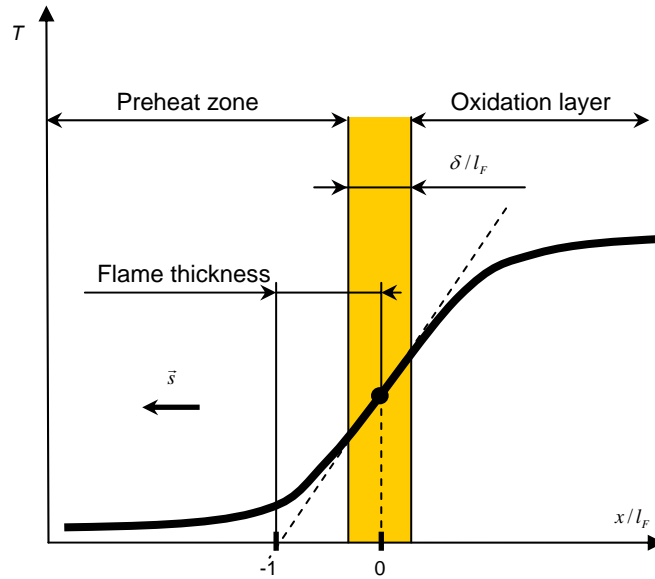


Figure 2.4: Schematic illustration of the structure of laminar and stationary flame

In spite of lots of simplification and assumptions introduced in ZFK asymptotical thermal propagation theory, it helps to understand the fundamental mechanism. Namely that the flame propagation is caused by diffusive processes and the gradients, necessary for diffusion, are sustained by the chemical reaction. This fact is common for all premixed flames independently on the flow regime: laminar or turbulent.

First, it is the laminar burning velocity (called by some authors the laminar flame speed) which is defined as a flow velocity necessary to keep a laminar premixed flame in the steady state (no propagation in reactants' direction). It is also directed normal to the flame front from products (burnt) to reactants (unburnt). The laminar burning velocity can be determined analytically under certain assumptions (ZFK theory [115], Williams [118] etc.). However, these assumptions lead to quantitatively poor results especially for rich flames. More accurate results may be obtained either from one-dimensional computations using detailed chemistry or from experiments. Actually the laminar burning velocity for a given fuel is only a function of the fuel/oxidizer ratio (equivalence ratio ϕ), pressure and the initial temperature of reactants. The laminar burning velocity decreases with increasing pressure and it increases with increasing temperature of the fresh gases. The values of the laminar burning velocity used in the present work are those measured in [119] for a methane/air combustion system at pressure $p = 1 \text{ bars}$ and fresh mixture temperature $T = 298 \text{ K}$. The measured values (points) and the fitted curve (line) are presented in Figure 2.5. Here, the equivalence ratio ϕ is converted into the mixture fraction z according to

$$z = \frac{\phi z_{st}}{1 - z_{st}(1 - \phi)}, \quad (2.54)$$

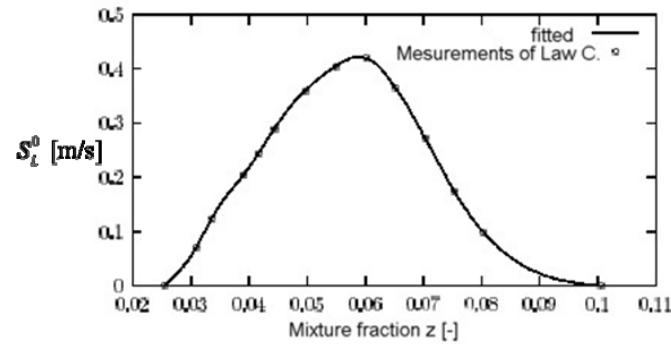


Figure 2.5: Laminar burning velocity for methane/air system at $p=\text{bar}$, $T_0=298\text{K}$

where z_{st} is the stoichiometric mixture fraction value corresponding to the complete consumption of reactants or $\phi=1$ and calculated for the global reaction (2.41) as

$$z_{st} = \frac{1}{1 + \frac{\nu'_O W_O Y_F}{\nu'_F W_F Y_O}} \quad (2.55)$$

The left and the right boundaries in Figure 2.5 (mixture fraction values at which $s_L^0=0$) correspond to the so called flammability limits. Beyond these limits, the mixture is either too lean or too rich for reactions to proceed.

Second, it is the maximal flame temperature that may be achieved behind the flame front. In the case of adiabatic combustion, that is considered in the present work, this is the adiabatic flame temperature that, similarly to the species mass fraction for diffusion flame (see previous section), may be computed for given elements' composition (given by the mixture fraction) from the thermodynamical equilibrium (see Warnatz et al. [117]). If radiation has to be considered, then the maximal flame temperature has to be corrected corresponding to the enthalpy loss.

Another important aspect is that the fuel consumption and the main products formation take place in the narrow reaction zone, but for the pollutant formation, both the reaction zone and the post flame region is important. Due to the fact that the post flame region is significantly larger than the reaction zone and consequently the residence time, there is much longer, the importance of this region for the "slowly" formed species (e.g. NOx) is even greater than that of the reaction zone.

2.4.4 Partially premixed flame

The non-premixed and premixed regimes of combustion discussed in the previous sections are actually separated in terms of mixing. However, in technical applications, that also include stationary gas turbines, there are

2. Turbulent reacting multiphase flows basics

very few situations when one of these combustion regimes appears in its pure form. More often a combination of non-premixed and premixed combustion modes takes place featuring the so-called partially premixed combustion phenomenon. The definition of partially premixed combustion given by Peters in [78] is as follows "... If the fuel and oxidizer enter separately, but partially mix by turbulence before combustion, the turbulent flame propagates through a stratified mixture. Such a mode of combustion has traditionally been called partially premixed combustion ...". In partially premixed flames the equivalence ratio ϕ of the fresh gas mixture directly in vicinity of the flame front is still located within the flammability limits but cannot be a priori specified like in perfectly premixed flames because of the additional mixing processes (not mandatory turbulent) appearing before combustion proceeds. Therefore, the equivalence ratio ϕ changes. These changes directly influence the flame propagation process. If the equivalence ratio varies only within the lean region ($z < z_{st}$), the complete fuel consumption occur in the flame front. But if the mixture includes rich values of ϕ then the premixed flame is accompanied by an additional diffusion flame in the post flame region where the remaining fuel oxidizes. This type of flames is called triple flame. An example of a triple flame may be a lifted jet diffusion flame schematically shown in Figure 2.6. One observes that depending on the nozzle exit velocity, the diffusion flame structure may be destroyed. I.e. at a sufficiently low nozzle exit velocity value a diffusion flame is attached to the nozzle. But increasing the exit velocity leads to stretching and finally disruption of the flame. Consequently, the flame lifts, the reactants mix above the nozzle without reaction to proceed, and a premixed flame stabilizes downstream within the jet. The stabilization appears at those points where the equilibrium between the flow velocity and the burning velocity (that depends on the local mixture) is achieved. In the region with rich (lean) mixture a rich premixed flame is stabilized. The fuel which is not consumed in the rich premixed flame diffuses across the flame into the post flame region and oxidizes building an additional diffusion flame along the stoichiometric mixture surfaces ($z = z_{st}$). Thus, three flame zones can be distinguished at one spatial location: lean premixed, rich premixed and diffusion flame. The location of the flame stabilization depends on the nozzle exit velocity and is characterized by the lift-off height. The lift-off height increases with increasing jet exit velocity but it can not exceed a critical value at which the flame is completely blown out.

In real gas turbine combustors the situation is even more complicated. The flow is more complex, featuring different recirculation zones and gradients in different directions. The fuel is usually injected into a compact mixing chamber where it is mixed with the oxidizer. It is very important to accurately predict the mixing and flame stabilization processes for the construction of the burner.

Partially premixed flames represent a very nice example of highly complicated phenomena where fluid dynamics mixing and combustion

interact strongly influencing each other. Therefore, the importance of their understanding and possible prediction can not be emphasized enough [134].

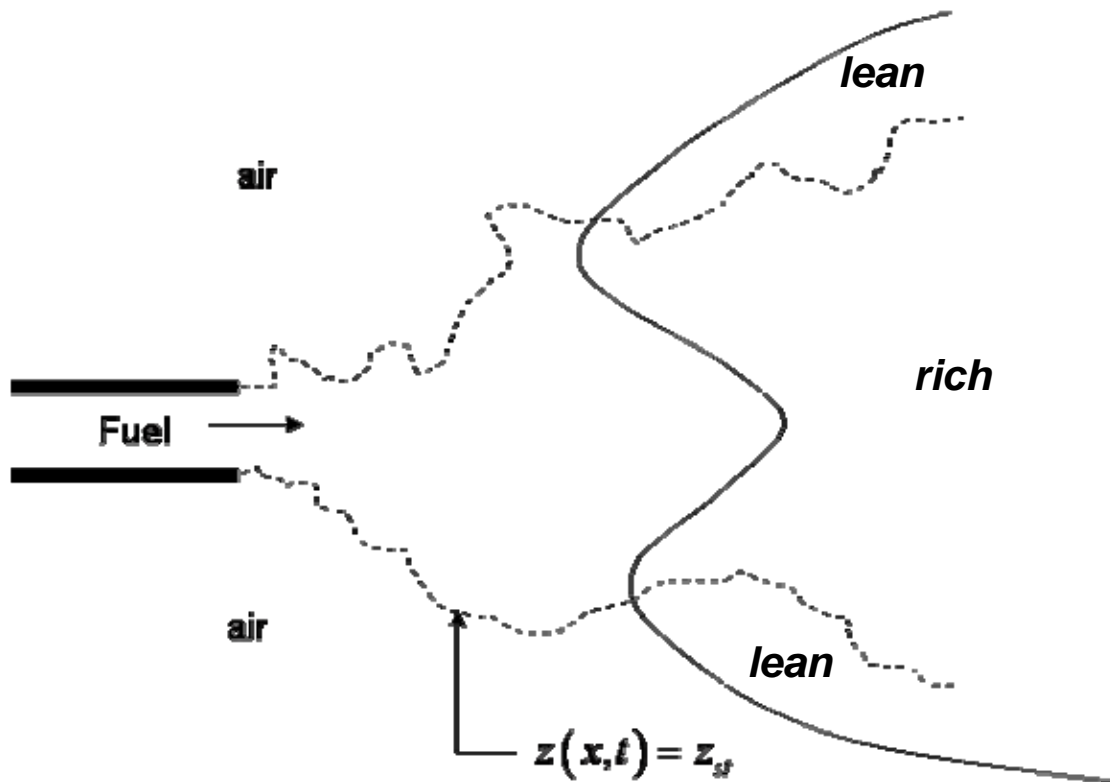


Figure 2.6: Lifted jet diffusion flame

3 Eulerian-Lagrangian modeling approach

In this Chapter the Eulerian-Lagrangian approach, as introduced in section 2.3, is applied for the computation of reactive multiphase flows in the frame of this thesis. First, the turbulence modeling for the continuum phase will be presented. Then the two ways coupling between particles/droplets and the carrier phase is introduced. Thereafter, two different spray evaporation models are presented. Finally the modeling of turbulent spray combustion involving the turbulence modeling for reactive flow, based on primitive variables, is outlined.

3.1 Turbulence modeling for non-reacting flows

Turbulence is associated with high Reynolds number. It is an irregular and random flow process which is independent of fluid, i.e. turbulence is a manifestation of flow and not of the fluid. It describes the chaotic fluid properties (velocity, density, concentration etc.) fluctuation within the flow, so it exhibits a large range of scale structures varying from the so called large scales to very small scales which are generated by the vortex stretching mechanism [101]. Turbulence is highly dissipative; therefore it needs a source of energy to be maintained. It is also a three-dimensional continuum phenomenon [84].

In order to prescribe turbulence, Osborne Reynolds showed, hundred years ago [81], that by taking a time average of the Navier Stokes equations, fluctuations in the flow introduced additional stress gradients (these stress terms are represented by the last variables in the equations (2.7) and (2.14)). Focused on the mean flow description, turbulence modeling aims, therefore, at representing these stresses as realistically as possible. As a result Reynolds-averaged Navier Stokes equations, (RANS) or Favre-Averaged Navier-Stokes (FANS) equations can be solved numerically. In the following a first and a second order turbulence model, as they are used within this work, will be introduced.

3.1.1 First order turbulence modeling

Boussinesq proposed the first assumption [79] for the description of the unknown Reynolds stresses by introducing the correlation (3.1), and thus gave rise to the first order turbulence modeling.

$$-\overline{u_i u_j} = \nu_t \left(\frac{\partial \overline{u_i}}{\partial x_j} + \frac{\partial \overline{u_j}}{\partial x_i} \right) - \frac{2}{3} k \delta_{ij}, \quad (3.1)$$

3.1 Turbulence modeling for non-reacting flows

where ν_t represents the eddy viscosity and $k = 1/2 \overline{u_i' u_i'}$ is the turbulent kinetic energy. The Reynolds stress tensor modeled by means of the velocity gradients, can be justified for applications with a flow dominant direction, e.g. turbulent channel or shear flow. In 1974 Launder and Spalding introduced the famous $k-\varepsilon$ two equation turbulence models [80], where the turbulent eddy viscosity ν_t is related to k and ε , through the following semi-empirical expression:

$$\nu_t = C_\mu \frac{k^2}{\varepsilon}, \quad (3.2)$$

where C_μ is a constant model, k and ε are determined by their respective coordinate-invariant semi-empirical transport equations. For the turbulent kinetic energy:

$$\frac{\partial k}{\partial t} + \frac{\partial}{\partial x_i} (\overline{u_i k}) = \underbrace{-\frac{\partial}{\partial x_i} \left[\overline{u_i \left(\frac{u_j' u_j'}{2} + \frac{p'}{\rho} \right)} \right]}_{\text{turbulent transport}} - \underbrace{\overline{u_i u_j} \frac{\partial \overline{u_i}}{\partial x_j}}_{\text{production}} - \underbrace{\overline{\nu \frac{\partial u_i'}{\partial x_j} \frac{\partial u_i'}{\partial x_j}}}_{\text{dissipation } \varepsilon}. \quad (3.3)$$

The production term represents the rate at which the turbulent kinetic energy is transferred from the mean flow to the turbulence whereas the dissipation term represents the rate at which the turbulent kinetic energy is converted into thermal energy. Equation (3.3) should contain the term involving the molecular diffusion representing the diffusion of turbulent kinetic energy caused by the fluid's natural molecular transport process, but since this term is very small compared to turbulent transport, it is neglected. The unsteady term and convection diffusion are exact while turbulent transport, production and dissipation involve unknown correlations which have to be modeled.

The turbulent transport in (3.3) is modeled according to gradient approach, using the following equation [83]:

$$\overline{u_i \left(\frac{u_j' u_j'}{2} + \frac{p'}{\rho} \right)} = -\frac{\nu_t}{\sigma_k} \frac{\partial k}{\partial x_i}, \quad (3.4)$$

where σ_k is a closure coefficient.

For the determination of dissipation of turbulent kinetic energy (last term in equation (3.3)), the following transport equation has to be solved:

3 Eulerian-Lagrangian modeling approach

$$\begin{aligned}
 \frac{\partial \varepsilon}{\partial t} + \frac{\partial}{\partial x_i} (\overline{u_i \varepsilon}) = & \underbrace{-2\nu \left(\frac{\partial u'_i}{\partial x_j} \frac{\partial u'_k}{\partial x_j} + \frac{\partial u'_j}{\partial x_i} \frac{\partial u'_j}{\partial x_k} \right) \frac{\partial \overline{u_i}}{\partial x_k}}_{\text{production due to mean velocity gradient}} - \underbrace{2\nu \overline{u'_k} \frac{\partial u'_i}{\partial x_j} \frac{\partial^2 \overline{u_i}}{\partial x_k \partial x_j}}_{\text{production due to mean velocity gradient curvature}} \\
 & \underbrace{-2\nu \frac{\partial u'_i}{\partial x_k} \frac{\partial u'_i}{\partial x_l} \frac{\partial u'_k}{\partial x_l}}_{\text{production due to vortex stretching}} - \underbrace{-\nu \frac{\partial}{\partial x_k} \left(\overline{u'_k} \frac{\partial u'_i}{\partial x_l} \frac{\partial u'_i}{\partial x_l} + 2 \frac{\partial p'}{\partial x_l} \frac{\partial u'_k}{\partial x_l} \right)}_{\text{turb. transport } T_\varepsilon} - \underbrace{2\nu^2 \frac{\partial^2 u'_i}{\partial x_k \partial x_l} \frac{\partial^2 u'_i}{\partial x_k \partial x_l}}_{\text{destruction } D_\varepsilon} \quad (3.5)
 \end{aligned}$$

The equation (3.5) describing the variation of turbulent kinetic energy dissipation is much more complicated than the one of turbulent energy. It involves several new unknown double and triple correlations of velocity fluctuations, pressure and velocity gradients. The production, turbulent transport term T_ε and dissipation term D_ε are modeled by

$$P_\varepsilon = -C_{\varepsilon 1} \frac{\varepsilon}{k} \overline{u'_i u'_j} \frac{\partial \overline{u_i}}{\partial x_j}, \quad (3.6)$$

$$T_\varepsilon = -\frac{\partial}{\partial x_i} \left(\frac{\nu_t}{\sigma_\varepsilon} \frac{\partial \varepsilon}{\partial x_i} \right), \quad (3.7)$$

$$D_\varepsilon = -C_{\varepsilon 2} \frac{\varepsilon^2}{k}. \quad (3.8)$$

The different closure coefficients which were calibrated for homogenous shear flow conditions [129] are given in Table 3.1

C_μ	σ_k	σ_ε	$C_{\varepsilon 1}$	$C_{\varepsilon 2}$
0.09	1.0	1.3	1.44	1.92

Table 3.1: Closure coefficients for the k - ε model

By introducing equations (3.4) and (3.6)-(3.8) into (3.3) and (3.5) respectively, the modeled new equations for turbulent kinetic energy and its dissipation yield to:

$$\frac{\partial k}{\partial t} + \frac{\partial}{\partial x_i} (\overline{u_i k}) = \frac{\partial}{\partial x_i} \left(\frac{\nu_t}{\sigma_k} \frac{\partial k}{\partial x_i} \right) - \overline{u'_i u'_j} \frac{\partial \overline{u_j}}{\partial x_i} - \varepsilon \quad (3.9)$$

$$\frac{\partial \varepsilon}{\partial t} + \frac{\partial}{\partial x_i} (\overline{u_i \varepsilon}) = -\frac{\partial}{\partial x_i} \left(\frac{\nu_t}{\sigma_\varepsilon} \frac{\partial \varepsilon}{\partial x_i} \right) - C_{\varepsilon 1} \frac{\varepsilon}{k} \overline{u'_i u'_j} \frac{\partial \overline{u_j}}{\partial x_i} - C_{\varepsilon 2} \frac{\varepsilon^2}{k} \quad (3.10)$$

3.1 Turbulence modeling for non-reacting flows

Using the eddy viscosity approach, one can model the production term (second term in the RHS of equation (3.9)) as

$$-\overline{u_i u_j} \frac{\partial \overline{u_j}}{\partial x_i} = \nu_t \left(\frac{\partial \overline{u_i}}{\partial x_j} + \frac{\partial \overline{u_j}}{\partial x_i} \right) \frac{\partial \overline{u_j}}{\partial x_i}, \quad (3.11)$$

and close both transport equations for k and ε . The $k-\varepsilon$ turbulence model (or, in general, eddy viscosity models) has the disadvantages of being isotropic and unable to account for curvature effects. In order to overcome these weaknesses, non-linear formulations such as the Algebraic Reynolds Stress Model (ASM) [127] or the Explicit Algebraic Reynolds Stress Model (EASM) [128] have been introduced. At a high level of modeling, second order models have been considered as presented in the following section.

3.1.2 Second order turbulence modeling

The Boussinesq hypothesis, used for the first order turbulence modeling, may not be suitable for industrial configurations which often involve complex flow geometry and difficult flow conditions involving strong three-dimensional effects, such as flows with sudden changes in mean strain rate, flows with significant streamline curvature or boundary-layer separation. This weakness can potentially be removed using second order turbulence models. However, there is a significant price to pay in modeling difficulties and computational costs for these improvements [128].

The exact differential equation describing the behavior of the Reynolds-stress tensor, $\tau_{ij} = -\rho \overline{u_i' u_j'}$, in the incompressible flow case is:

$$\underbrace{\frac{\partial}{\partial t} \left(\overline{u_i' u_j'} \right)}_{\text{unsteady term}} + \underbrace{\frac{\partial}{\partial x_k} \left(\overline{u_k u_i' u_j'} \right)}_{\text{convective term}} = \frac{\partial}{\partial x_k} \left(\underbrace{-\overline{u_k u_i' u_j'} - \frac{1}{\rho} \overline{p' u_i'} \delta_{jk} - \frac{1}{\rho} \overline{p' u_j'} \delta_{ik}}_{\text{turbulent transport}} \right) \quad (3.12)$$

$$\underbrace{-\overline{u_i' u_k'} \frac{\partial \overline{u_j}}{\partial x_k} - \overline{u_j' u_k'} \frac{\partial \overline{u_i}}{\partial x_k}}_{\text{production}} + \underbrace{\frac{p'}{\rho} \left(\frac{\partial \overline{u_i}}{\partial x_j} + \frac{\partial \overline{u_j}}{\partial x_i} \right)}_{\text{pressure strain } \Pi_{ij}} - \underbrace{2\nu \frac{\partial \overline{u_i}}{\partial x_k} \frac{\partial \overline{u_j}}{\partial x_k}}_{\text{viscous dissipation } \varepsilon_{ij}}$$

The unknown terms in equation (3.12) are: the turbulent transport, the pressure strain correlation and the dissipation. All of these terms denote naturally a tensor form. In order to provide any guidance for the modeling of these unknown terms, experimentalists can not deliver any data for these variables. Therefore a lot of pioneering efforts have been made within the second order turbulence modeling [127] [128]. Rotta [81] was the first researcher to accomplish the closure of the Reynolds-stress

equation in 1951. Lumley (1978) [129] developed a method to satisfy the realizability in turbulence modeling.

The turbulent transport term was among others modeled by Launder et al. [82] with the following approximation:

$$-\overline{u'_k u'_i u'_j} - \frac{1}{\rho} \overline{p' u'_i} \delta_{jk} - \frac{1}{\rho} \overline{p' u'_j} \delta_{ik} = \frac{2}{3} C_s \frac{k^2}{\varepsilon} \frac{\partial \overline{u'_i u'_j}}{\partial x_k}, \quad (3.13)$$

where C_s is a scalar closure coefficient ($C_s \approx 0.11$).

The pressure strain correlation Π_{ij} is of the same order as a production term [83] and includes pressure fluctuation. In order to model this term, first the Poisson equation (3.14) has to be solved. It follows from taking the divergence of the Navier-Stokes equation (2.2) and subtracting the time-averaged equation from the instantaneous equation (2.7).

$$-\frac{1}{\rho} \frac{\partial^2 p'}{\partial x_k \partial x_k} = 2 \frac{\partial \overline{u'_l}}{\partial x_k} \frac{\partial u'_k}{\partial x_l} + \frac{\partial^2}{\partial x_k \partial x_l} \left(u'_k u'_l - \overline{u'_k u'_l} \right). \quad (3.14)$$

For solving the Poisson equation, one uses the Green's function which, neglecting a surface integral (playing only a significant role near the solid boundary), leads to

$$-\frac{p'(x)}{\rho} = \frac{1}{4\pi} \int_V \left(2 \frac{\partial \overline{u'_l}}{\partial x_k} (x^*) \frac{\partial u'_k}{\partial x_l} (x^*) + \frac{\partial^2}{\partial x_k \partial x_l} \left[u'_k u'_l (x^*) - \overline{u'_k u'_l} (x^*) \right] \right) \frac{dV(x^*)}{|x-x^*|} \quad (3.15)$$

The terms with (x^*) are related to values at $x^* = x + r$, where r represents the distance between the point of pressure fluctuation $p'(x)$ and the cell having dV as volume. The integration is carried out over the r space.

Multiplication of the both sides of equation (3.15) by $\frac{\partial u'_i}{\partial x_j}$, taking this factor inside the integral and subsequent averaging lead to

$$\begin{aligned}
 -\frac{\overline{p' \frac{\partial u'_i}{\partial x_j}}}{\rho} = \frac{1}{4\pi} \int_V \left(\underbrace{2 \frac{\partial \bar{u}_l}{\partial x_k}(x^*) \frac{\partial u'_k}{\partial x_l}(x^*) \frac{\partial u'_i}{\partial x_j}(x)}_{\text{Rapid part}} \right. \\
 \left. + \underbrace{\frac{\partial^2 u'_k u'_l}{\partial x_k \partial x_l}(x^*) \frac{\partial u'_i}{\partial x_j}(x)}_{\text{slow part}} \right) \frac{dV(x^*)}{|x - x^*|} , \quad (3.16)
 \end{aligned}$$

where the slow part does not contain the mean velocity gradient and is, therefore, responsible for the return to isotropy of initially anisotropic turbulence once the mean velocity gradient vanishes. It is therefore often called return part. The rapid term contains the mean velocity gradient and can dominate in a flow field with rapidly evolving velocity field.

By assuming quasi-homogeneity for the mean velocity gradient $\frac{\partial \bar{u}_l}{\partial x_k}$, the latter is taken outside the integral in the so called rapid term:

$$\begin{aligned}
 -\frac{\overline{p' \frac{\partial u'_i}{\partial x_j}}}{\rho} = \frac{1}{2\pi} \frac{\partial \bar{u}_l}{\partial x_k}(x) \int_V \left(\underbrace{\frac{\partial u'_k}{\partial x_l}(x^*) \frac{\partial u'_i}{\partial x_j}(x)}_{\text{rapid part}} \right) \frac{dV(x^*)}{|x - x^*|} \\
 + \int_V \underbrace{\frac{\partial^2 u'_k u'_l}{\partial x_k \partial x_l}(x^*) \frac{\partial u'_i}{\partial x_j}(x)}_{\text{slow part}} \frac{dV(x^*)}{|x - x^*|} \quad (3.17)
 \end{aligned}$$

By modeling the return and the rapid part separately, Launder et al. [82] assumed no direct dependence of the mean strain rate on the return part. Jones [103] proposed the collective modeling of the two parts acknowledging however that the resulting model will not behave correctly in the limit of a suddenly imposed mean strain field occurring in the so called rapid distortion limit (RDT). This fact, however, does not affect the final form of the model of Jones [103]. The most models proposed for the pressure-strain correlation have a similar algebraic form, thus, neglecting any history or non-local effects:

$$\Pi_{ij} = \frac{1}{\rho} \left(\overline{p' \frac{\partial u'_i}{\partial x_j}} + \overline{p' \frac{\partial u'_j}{\partial x_i}} \right) = A_{ij} + \underbrace{M_{ijkl} \frac{\partial \bar{u}_k}{\partial x_l}}_{\Pi_{ij}^L} . \quad (3.18)$$

3 Eulerian-Lagrangian modeling approach

The first tensor A_{ij} is related to the slow part. It is modeled as a function of the anisotropy tensor, b_{ij} :

$$A_{ij} = a_0 b_{ij} + a_1 \left(b_{ik} b_{kj} - \frac{1}{3} II \delta_{ij} \right), \quad (3.19)$$

where the anisotropy tensor is defined as:

$$b_{ij} = \frac{\overline{u'_i u'_j}}{2k} - \frac{1}{3} \delta_{ij}, \quad (3.20)$$

and II represents the second invariant of the anisotropy tensor which is given by:

$$II = b_{ij} b_{ji}. \quad (3.21)$$

Variables a_0 and a_1 denote coefficients, which are most generally functions of anisotropy tensor invariants. Rotta [81] postulated that the slow pressure strain term, is given by:

$$A_{ij} = -C_1 \varepsilon \left(\frac{\overline{u'_i u'_j}}{k} - \frac{2}{3} \delta_{ij} \right), \quad (3.22)$$

where C_1 denotes a closure constant obtained from fitting of numerical results to measurements [81]. The rapid pressure strain term was modeled by several researchers as Launder, Reece and Rodi [82]. They have closed this term on the basis of kinematical considerations as follows:

$$\begin{aligned} \Pi_{ij}^L = & -2C_1 \varepsilon b_{ij} + C_2 \overline{u'_k u'_l} \frac{\partial \overline{u'_k}}{\partial x_l} + C_3 \left(\overline{u'_j u'_k} \frac{\partial \overline{u'_i}}{\partial x_k} + \overline{u'_i u'_k} \frac{\partial \overline{u'_j}}{\partial x_k} \right) \\ & + C_4 k \left(\frac{\partial \overline{u'_i}}{\partial x_j} + \frac{\partial \overline{u'_j}}{\partial x_i} \right) - \left(\frac{3}{2} C_2 + C_3 \right) \left(\overline{u'_j u'_k} \frac{\partial \overline{u'_k}}{\partial x_i} + \overline{u'_i u'_k} \frac{\partial \overline{u'_k}}{\partial x_j} \right). \end{aligned} \quad (3.23)$$

More recent work has been achieved by Jones and Musonge [84] by new calibration of the model constants based on turbulent flow jet. The used closure coefficients are summarized in Table 3.2.

Model	C_1	C_2	C_3	C_4
LRR	1.5	-0.582	0.764	-0.182
Jones	3.0	-0.44	0.46	-0.23

Table 3.2: Closure coefficients for LRR and Jones Musonge models

The dissipation term in equation (3.12) is modeled using the Kolmogorov hypothesis of local isotropy which assumed to occur at the smallest scales:

$$\varepsilon_{ij} = \frac{2}{3} \varepsilon \delta_{ij}, \quad (3.24)$$

where ε is described using the balance equation for the turbulent kinetic energy dissipation is given by:

$$\frac{\partial \varepsilon}{\partial t} + \frac{\partial}{\partial x_i} (\overline{u_i \varepsilon}) = \frac{\partial}{\partial x_i} \left(C_\varepsilon \frac{k}{\varepsilon} \overline{u_i u_j} \frac{\partial \varepsilon}{\partial x_i} \right) - C_{\varepsilon 1} \frac{\varepsilon}{k} \overline{u_i u_j} \frac{\partial \overline{u_j}}{\partial x_i} - C_{\varepsilon 2} \frac{\varepsilon^2}{k}, \quad (3.25)$$

where the production term is now computed by means of the solution obtained from (3.12). The coefficient C_ε equals 0.15., whereas $C_{\varepsilon 1}$ and $C_{\varepsilon 2}$ are given in Table 3.1.

3.2 Carrier phase and two way coupling

Performed simulations within this thesis consider a fully two way coupling, i.e. taking into account the presence of particles/droplets on the carrier phase. This involves interactions in momentum, turbulence quantities, energy and mass conservation. In this chapter, first the two ways coupling (for non evaporating droplets) with respect to different modulation models will be introduced. Thereafter, the influence of the turbulence of carrier gas on the particles (in terms of dispersion model) will be illustrated.

The influence of the dispersed phase on the fluid motion can be treated as an extra force exerted on the carrier gas when the particles/droplets have much larger density than surrounding fluid, as it is the case in the present work. Thus, the momentum transfer from the dispersed phase to the carrier phase is included by adding the reaction force against the surface force acting on the particle/droplet to the Navier-Stokes equation (2.2). This model is known as force coupling model or particle-source-in-cell (PSI-Cell) model proposed by Crowe et al. [97].

In general, the additional source terms $\overline{S_{\psi,p,s}}$ in (2.6) and (2.9) which characterize the direct interaction of mass, momentum, energy and species between solid particle and carrier gas are summarized in Table 3.3. Source terms of turbulent quantities will be introduced in the following two sections. The variable ψ may represent the mean value of mass density, velocity components (u, v, w), enthalpy/temperature T , turbulent kinetic energy k , turbulent dissipation rate ε , components of the deviatoric part of the Reynolds stress tensor R_{ij} (anisotropy tensor components) and chemical species mass fraction ($O_2, CO_2, \text{vapor fuel } y$,

etc), respectively. \bar{u} , \bar{v} and \bar{w} are the mean gas phase (axial, tangential and transversal) velocity components. \bar{u}_p , \bar{v}_p and \bar{w}_p represent the three velocity components of the droplet respectively. N_p is the number of real particles represented by one numerical droplet, V_{ijk} is the cell volume.

\dot{Q}_i represents the heat flux into the particle/droplet and g is the gravitation. \dot{m}_p is the droplet mass flow cross a CV per second. Δt is the Lagrangian integration time step. For the turbulent kinetic energy, its dissipation and the Reynolds Stress components, source terms will be explained in detail in the following section.

ψ	$\bar{S}_{\psi,p,s}$
1	0
\bar{u}	$-\sum_p \frac{\dot{m}_p N_p}{V_{i,j,k}} [(u_p^{t_n+\Delta t} - u_p^{t_n}) - g_x \Delta t]$
\bar{v}	$-\sum_p \frac{\dot{m}_p N_p}{V_{i,j,k}} [(v_p^{t_n+\Delta t} - v_p^{t_n}) - g_y \Delta t]$
\bar{w}	$-\sum_p \frac{\dot{m}_p N_p}{V_{i,j,k}} [(w_p^{t_n+\Delta t} - w_p^{t_n}) - g_z \Delta t]$
T	$-\sum_p \frac{N_p}{V_{i,j,k}} (\dot{Q}_i)$
y	0

Table 3.3: Source terms due to the presence of solid particles

3.2.1 Turbulence modulation modeling

The turbulence of the carrier phase can be affected by the presence of the dispersed phase, particularly if the particle concentration is high enough. The presence of particles/droplets in flows may cause distortion of streamlines. Thus it modifies the velocity gradients due to shear forces between different phases. Vice versa, the generated wakes behind a particle/droplet can produce a damping effect of the drag force on the dispersed phase. This phenomenon, known as turbulence modulation, is extremely complex. Even though a lot of work is done in this area, it remains still not completely understood at present.

As mentioned in the introduction, it was experimentally observed that the energy spectrum of the turbulent field with particles is modified [17].

3.2 Carrier phase and two way coupling

Turbulence modulation is based on the perturbation of the flow field which can affect the dynamics of turbulence structure behind particles/droplets, and, so, turbulent transfer mechanisms. In [25] authors mentioned a criterion to differentiate between small and large particle by comparing the diameter to the turbulent length scale. The turbulence modification was described as follow:

- Attenuating effect for $\frac{D_p}{l_t} < 0.1$
- Enhancing effect for $\frac{D_p}{l_t} > 0.1$

where l_t denotes the turbulent length scale as defined in equation (2.21).

In a different analysis of Hetsroni [28], a particle Reynolds number (see section 2.3.2) was introduced to classify turbulence modification. In this view, turbulence production is due to detachment of eddies created in the wake of the particles (vortex shedding). Hereby, the production of turbulent kinetic energy is expected for values of $Re_p > 400$.

To account for this interaction numerically within a Lagrangian-Eulerian approach few models have been developed and tested. In general, these models differ upon correlations between fluid velocities and particle concentrations and velocities.

Within this chapter three models (standard model [92], Crowe model [87] and the thermodynamically consistent model [35]), which are used in the frame of this work will be introduced.

The so called standard modulation model stems from Shuen et al. [85] and is obtained by time averaging the Navier Stokes equations. Following this procedure for the turbulent quantities, the source term resulting from the Reynolds-averaging procedures is given for the Reynolds stress tensor as follows [35]:

$$\overline{S_{R_{ij}}} = \overline{u_j S_{u_i,p}} + \overline{u_i S_{u_j,p}} - \overline{u_j} \overline{S_{u_i,p}} - \overline{u_i} \overline{S_{u_j,p}} \quad (3.26)$$

In case of $k-\varepsilon$ turbulence model, the source term reduces to:

$$\overline{S_k} = \overline{u_i S_{u_i,p}} - \overline{u_i} \overline{S_{u_i,p}} \quad (3.27)$$

where $R_{ij} = \overline{u'_i u'_j}$ and $k = \frac{1}{2} \overline{u'_i u'_i}$ with $u'_i = u_i - \overline{u_i}$ expressing the fluctuating component of the continuous phase velocity. The dissipation source term is computed by equation (3.28), see [92],

$$S_\varepsilon^{k-\varepsilon} = C_{\varepsilon,3}^{k-\varepsilon} \frac{\varepsilon}{k} S_{k,p} \quad (3.28)$$

For Reynolds stress components R_{ij} , the source term for the dissipation rate is computed by:

$$S_{\varepsilon}^{RS} = c_{\varepsilon,3}^{RS} \frac{\varepsilon}{k} S_{k,p}^{RS}. \quad (3.29)$$

The constants $c_{\varepsilon,3}^{k-\varepsilon}$ and $c_{\varepsilon,3}^{RS}$ are set to 1.87 within this thesis. They are derived from experimental data in the literature [93]. These constants, however, depend on particles/droplets diameter and dispersed phase concentrations [94].

The second modulation model used in the frame of this thesis is the turbulence modulation model of Crowe [87]. Crowe studied the turbulence modulation problem and proposed many models to account for this phenomenon [6], [25]. His latest model, published in 2000, is based on energy balance [87]. The energy production and dissipation due to the presence of particles is deduced from the recent experimental data in a channel and pipes (Kulick et al, [88], Hosokawa et al., [89] and Savolainen et al., [90]). He started with the equation for the mechanical energy of the carrier phase and performed the averaging procedures. This approach yields an equation which reduces results for the simplified flow. This approach provides a correlation which is supported by trends observed in experimental results. The correlations describing source terms for $k-\varepsilon$ turbulence model developed by Crowe [87] in the frame of Eulerian-Eulerian approach and then transformed by Lain et al. [91] to Eulerian-Lagrangian notation are given by:

$$\overline{S_k} = \overline{u_{p,i} S_{u_i,p}} - \overline{u_i S_{u_i,p}} \quad (3.30)$$

Analogical prescription is done, also by Lain et al. [92], for the computation of source terms for the Reynolds stress tensor which are given by:

$$\overline{S_{R_{ij}}} = \overline{u_{p,j} S_{u_i,p}} + \overline{u_i S_{u_j,p}} - \overline{u_{p,j} S_{u_i,p}} - \overline{u_i S_{u_j,p}} \quad (3.31)$$

The modeling of source term for the dissipation of the turbulent kinetic energy is performed in the standard manner given in equations (3.28) and (3.29).

3.2.2 Thermodynamically modulation modeling

The third modulation model describing turbulence modification, also used in the frame of this thesis, stems from Sadiki and Ahmadi [86]. The model considers enhancement and decreasing of turbulence intensity depending on particle/droplet diameters. Following an Eulerian approach, Sadiki and Ahmadi [86] derived a first approximation of the extra term for the

3.2 Carrier phase and two way coupling

turbulent kinetic energy based on the exploitation of the second law of thermodynamics as:

$$\overline{\rho^f} S_{k,p} = \sum_{\alpha=1}^n s_1^\alpha D_0^\alpha (\overline{u_i^\alpha} - \overline{u_i^f})(\overline{u_i^\alpha} - \overline{u_i^f}) + 2 \sum_{\alpha=1}^n D_0^\alpha (k^\alpha - k^f) \quad (3.32)$$

where $k^\alpha = k_p = \frac{1}{2} \overline{u_{pi}' u_{pi}'}$ and $k^f = k = \frac{1}{2} \overline{u_i' u_i'}$ are the turbulent kinetic energy of the dispersed phase (α) and the gas phase (f), respectively. In this polydispersed multiphase flows description only the drag force has been considered, so that the coefficient D_0^α is proportional to the drag coefficient c_D , while $0 < s_1^\alpha < 1$ [86]. Equation (3.32) can be recast in the following form:

$$S_{k,p} = \frac{\alpha_p \rho_p}{\tau_p (c_D)} \left\{ \alpha' \left[\left| \overline{u_i^\alpha} - \overline{u_i^f} \right|^2 + (\overline{u_i'^\alpha u_i'^\alpha} - \overline{u_i'^f u_i'^f}) \right] - (\overline{u_i'^f u_i'^\alpha} - \overline{u_i'^f u_i'^f}) \right\} \quad (3.33)$$

where α' is a model coefficient related to s_1^α according to [86]. For a mono-dispersed case ($\alpha=1$) and if $\alpha'=1$, the first two terms in (3.33) obviously correspond to the production term derived by Crowe [87] based on the energy balance:

$$S_{k,p} = \frac{\alpha_p \rho_p}{\tau_p (c_D)} \left\{ \left| \overline{u_i} - \overline{u_{pi}} \right|^2 + (\overline{u_{pi}' u_{pi}'}) - \overline{u_i' u_{pi}'} \right\} \quad (3.34)$$

with

$$\tau_p (c_D) = \frac{4 \rho_p D_p^2}{3 \mu Re_p c_D} \quad (3.35)$$

where α_p is the volume fraction of the particles, τ_p the particle response time scale and μ the dynamic viscosity. Re_p and c_D in this report are given by:

$$Re_p = \frac{\rho D_p \left| \vec{u} - \vec{u}_p \right|}{\mu} \quad (3.36)$$

and
$$c_D = \frac{24}{\text{Re}_p} \left(1 + \frac{1}{6} \text{Re}_p^{2/3} \right) \quad (3.37)$$

The first contribution in equations (3.33) and (3.34) takes into account the so-called wake induced turbulence. It reflects the conversion of mechanical energy by the drag force into turbulent kinetic energy. The second term represents the redistribution of the kinetic energy between phases. The last term in equations (3.33) and (3.34) is responsible for the gas phase dissipation of the induced turbulence. However, the numerical analyses from the literature have shown that the energy balance alone is not able to account for the evolution of a physical process along with the dissipation mechanism. In a Lagrangian notation one gets after a short but cumbersome transformation of (3.33) [35]:

$$S_{k,p} = \alpha' \left(\overline{u_{pi} S_{u_i,p}} - \overline{u_i S_{u_i,p}} \right) + (1 - \alpha') \left(\overline{u_{pi} S_{u_i,p}} - \overline{u_{pi} S_{u_i,p}} \right) + \left(\overline{u_i S_{u_i,p}} - \overline{u_i S_{u_i,p}} \right) \quad (3.38)$$

in which $S_{u_i,p} = -\frac{m_p}{V\tau_p} (u_i - u_{pi})$, with $\frac{m_p}{V} = \alpha_p \rho_p$, expresses the particle source term in the momentum equation (see Table 3.3). This term may include other force contributions, if necessary. The relation (3.38) can be further transformed in two ways. By combining the first two production terms, the following useful expression emerges:

$$S_{k,p} = \beta \left(\overline{u_{pi} S_{u_i,p}} - \overline{u_i S_{u_i,p}} \right) + \left(\overline{u_i S_{u_i,p}} - \overline{u_i S_{u_i,p}} \right) \quad (3.39)$$

where
$$\beta = \alpha' + \frac{(1 - \alpha') \left(\overline{u_{pi} S_{u_i,p}} - \overline{u_{pi} S_{u_i,p}} \right)}{\left(\overline{u_{pi} S_{u_i,p}} - \overline{u_i S_{u_i,p}} \right)}. \quad (3.40)$$

The quantity β denotes a modified model coefficient to be determined. A similar modified model coefficient can also be encountered in the well known modeling of diffusion terms in the transport equation of the Reynolds stress tensor anisotropy [84]. The first term in (3.39) features a production behavior while the second one has a dissipation performance. As demonstrated in Groh et al. [53], the expression (3.39) is able to account for both the dissipation and the production of the gas phase turbulence induced by small particles and big particles, respectively. In the calculations in [53], a value $\beta = 0.5$ has been used. Furthermore, the expression (3.38) can also be rearranged in the following form

3.2 Carrier phase and two way coupling

$$S_{k,p} = \gamma \left[\overline{S_{u_i,p}} (\overline{u_{pi}} - \overline{u_i}) \right] + (\overline{u_i S_{u_i,p}} - \overline{u_i} \overline{S_{u_i,p}}) \quad (3.41)$$

where

$$\gamma = \alpha' + \frac{(\overline{u_{pi} S_{u_i,p}} - \overline{u_{pi}} \overline{S_{u_i,p}})}{\overline{S_{u_i,p}} (\overline{u_{pi}} - \overline{u_i})}. \quad (3.42)$$

The quantity γ is a new modified parameter to be determined. Other contributions accounting for the phase change in the extra term of the k-equation have been considered and can be found in [86]. Focusing on the equation of the dissipation rate of the kinetic energy, we use in a standard manner the proportionality to S_{kp} ($S_{k,p}^{RS}$) as introduced in equations (3.28) and (3.29).

The value used for the model parameters in equations (3.28) and (3.29) was 1.87 (in accordance to [53]). The limits of its validity have been discussed in [92].

To account for the indirect interaction process in the transport equations of the Reynolds stress components, the term corresponding to (3.39) has the following form:

$$S_{R_{ij},p} = \beta \left(\overline{u_{pi} S_{u_j,p}} + \overline{u_{pj} S_{u_i,p}} - \overline{u_i} \overline{S_{u_j,p}} - \overline{u_j} \overline{S_{u_i,p}} \right) + \left(\overline{u_i S_{u_j,p}} + \overline{u_j S_{u_i,p}} - \overline{u_i} \overline{S_{u_j,p}} - \overline{u_j} \overline{S_{u_i,p}} \right) \quad (3.43)$$

3.2.3 Dispersion modeling

The dispersion quantifies the instantaneous fluid velocity (including fluctuations) seen by the particles and its effect on the particles/droplets distribution. Therefore, when using fluid turbulence statistical models, a key question of the dispersed phase flow modeling is the description of the fluid turbulence along the particle trajectories. This can be adequately done using a stochastic Lagrangian process, in terms of the computed fluid turbulent variables, to generate the instantaneous fluid velocity in the discrete particle dynamic equation.

As pointed out by several authors, the interaction of particles with turbulent eddies leads to preferential concentration effects that can change drastically the mass flow distribution of dispersed phase. Consequently these effects enhance the inhomogeneity of species, e.g. vapor concentration. The model used in the frame of this thesis is the so called Markov-sequence dispersion model. The latter is based on the Markov assumption noting that the fluid fluctuation on the parcel location depends only on the immediately previous time step and no longer history. Figure 3.1 shows the development of particle trajectory and fluid element streamline which are located at the moment t_n at the same location. After one time step Δt , the particle and fluid element change their positions. However, they do not overlap because of drag and

external forces acting on the particle. The Markov sequence model is based on the following two steps for the computation of the fluid element instantaneous fluctuation along the particle trajectory:

- The evolution of the fluid element velocity fluctuation along the stream line is determined using the Lagrangian correlation factor:

$$u_i^F(t_{n+1}) = u_i^F(t_n) \cdot R_{L,i}(\Delta t) + \sigma_i \sqrt{1 - R_{L,i}^2(\Delta t)} \cdot \xi_i(t_n) \quad (3.44)$$

- The fluid element velocity fluctuation located at the particle position u_i^p is correlated with the fluid element location using the Eulerian correlation factor:

$$u_i^p(t_{n+1}) = u_i^F(t_{n+1}) \cdot R_{E,i}(\Delta r) + \sigma_i \sqrt{1 - R_{E,i}^2(\Delta r)} \cdot \zeta_i(t_n) \quad (3.45)$$

The Lagrangian and Eulerian correlation factors defined by equations (3.46) and (3.47) denote the time and spatial correlation functions respectively, as presented in equations (2.19) and (2.22) in chapter 2:

$$R_{L,i}(\Delta t) = \frac{\overline{u_i'(t)u_i'(t+\Delta t)}}{\sqrt{u_i'^2(t)}\sqrt{u_i'^2(t+\Delta t)}}, \quad (3.46)$$

$$R_{E,i}(\Delta r) = \frac{\overline{u_i'(t)u_i'(t+\Delta r)}}{\sqrt{u_i'^2(t)}\sqrt{u_i'^2(t+\Delta r)}}. \quad (3.47)$$

The product of both correlation factors (Lagrangian $R_{L,i}(\Delta t)$ and Eulerian $R_{E,i}(\Delta r)$) yields to a new coefficient which can be used to compute the fluctuation of the fluid element at the particle location [93]:

$$R_{p,i}(\Delta t, \Delta r) = R_{L,i}(\Delta t) \cdot R_{E,i}(\Delta r), \quad (3.48)$$

$$u_i^p(t_{n+1}) = u_i^p(t_n) \cdot R_{p,i}(\Delta t, \Delta r) + \sigma_i \sqrt{1 - R_{p,i}^2(\Delta t, \Delta r)} \cdot \chi_i(t_n). \quad (3.49)$$

The turbulent flow in many configurations, however, is rather not homogenous. Thus the flow develops stress gradients which are responsible for the enhancement of the pressure gradient. Therefore droplets are immigrating to locations having low pressure, i.e. low turbulent intensity, once common dispersion models valid for isotropic and homogeneous turbulence are used [96]. To avoid these phenomena in the frame of the Markov-sequence dispersion model used in this work, a drift correction term has to be considered following [96].

The final expressions for the fluid fluctuations at particle location (fluctuation seen by dispersed phase) are then calculated by:

$$u_i^p(t_{n+1}) = u_i^p(t_n) \cdot R_{p,u}(\Delta t, \Delta r) + \sigma_u \sqrt{1 - R_{p,u}^2(\Delta t, \Delta r)} \cdot \zeta_u(t_n) + (1 - R_{p,u}(\Delta t, \Delta r)) T_{L,u} \frac{\partial u_i'}{\partial y} \quad (3.50)$$

3.2 Carrier phase and two way coupling

$$v'^p(t_{n+1}) = v'^p(t_n) \cdot R_{p,v}(\Delta t, \Delta r) + \sigma_v \sqrt{1 - R_{p,v}^2(\Delta t, \Delta r)} \cdot \zeta_v(t_n) + (1 - R_{p,v}(\Delta t, \Delta r)) T_{L,v} \frac{\partial v'^p}{\partial y} \quad (3.51)$$

$$w'^p(t_{n+1}) = w'^p(t_n) \cdot R_{p,w}(\Delta t, \Delta r) + \sigma_w \sqrt{1 - R_{p,w}^2(\Delta t, \Delta r)} \cdot \zeta_w(t_n) \quad (3.52)$$

where $\zeta_u(t_n)$, $\zeta_v(t_n)$ and $\zeta_w(t_n)$ note Gaussian random variables. For the Lagrangian correlation factor, an exponential approach was considered:

$$R_{L,i}(\Delta t) = \exp\left(-\frac{\Delta t}{T_{L,i}}\right), \quad (3.53)$$

where $T_{L,i}$ represents the Lagrangian integral time scale as it is calculated for $k-\varepsilon$ turbulence model by $T_{L,i} = c_T k / \varepsilon$. When using Reynolds stress models, $T_{L,i}$ is determined (for all direction, x , y and z) by:

$$T_{L,i} = c_T \frac{\sigma_i^2}{\varepsilon}, \quad (3.54)$$

where the constant c_T equals 0.3 and σ_i^2 denotes $\overline{u'_i u'_i}$. The Eulerian correlation factor $R_{E,i}(\Delta r)$ is computed using longitudinal and transversal correlation functions $f(\Delta r)$ and $g(\Delta r)$ according to [95]

$$R_{E,i}(\Delta r) = (f(\Delta r) - g(\Delta r)) \frac{\Delta r_i \Delta r_j}{\Delta r^2} + g(\Delta r) \delta_{ij} \quad (3.55)$$

The longitudinal and transversal correlations functions $f(\Delta r)$ and $g(\Delta r)$ are computed using the following expression:

$$f(\Delta r) = \exp\left(-\frac{\Delta r}{L_E}\right) \quad (3.56)$$

$$g(\Delta r) = \left(1 - \frac{\Delta r}{2L_E}\right) \exp\left(-\frac{\Delta r}{L_E}\right), \quad (3.57)$$

where L_E represents a simplified turbulent length scale which is determined by:

$$L_E = c_L T_L \sigma. \quad (3.58)$$

T_L is computed according to equation (3.54) and c_L represents a model constant set to 3.0 as given in [96].

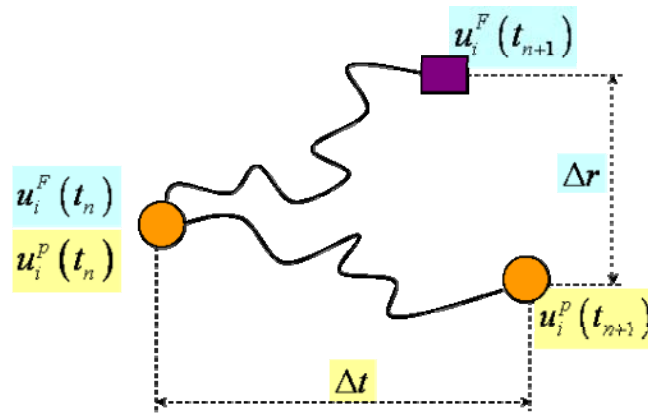


Figure 3.1 time evolution of particle trajectory and fluid element stream line

Obviously many dispersion models were used in the literature. One of the most common is the model proposed by Gosman and Ioannides [139] which was based on stochastic approach. In this model, it is assumed that the gas turbulence is constructed by a consecutive sequence of characteristic turbulent eddies on the trajectory of each individual drop. Each interacting eddy can be either static or in motion and interacts with a drop only during a limited interaction time period. This general approach is central to all eddy lifetime models, the most widely used tool for calculations of drop/turbulence interaction.

3.3 Spray evaporation modeling

In many devices, as it is the case in this work, fuels are liquid droplets and are sprayed as fine droplets into a combustion chamber. Therefore the evaporation represents a decisive process of the fuel preparation in such devices, like gas turbine combustors. Numerous theoretical studies in literature have been carried out for the description of droplet evaporation. In this section two evaporation models, used in the frame of this thesis, will be introduced. The first one is the so-called uniform temperature model by Abramson and Sirignano [33]. This model represents an equilibrium evaporation model based on the film thickness theory, whereas the second one is a non equilibrium evaporation model developed by Langmuir and Knudsen (see [30] and [31]). Accordingly, two time scales characterizing the turbulence and the thermodynamics of the vaporization will be introduced along with a new dimensionless number to characterize the turbulence droplet vaporization interaction regimes.

3.3.1 Concept of the droplet evaporation models

In order to ensure a mathematical description of the evaporation process, one should reduce the complexity of the theoretical description. Thus the following basic assumptions and simplifications are made [112]:

3.3 Spray evaporation modeling

- One component model is considered, so that we solely deal with the so-called infinite conductivity model.
- Droplets are assumed to be spherical.
- Secondary atomization and coalescence of droplets are neglected as we concentrate on the dilute spray region. In other words simple elastic collisions between droplets and wall are assumed without any kind of film formation [12].
- We neglect the influence of the surface tension and assume a uniform pressure around the droplet.
- Uniform physical properties of the surrounding fluid and liquid-vapor thermal equilibrium on the droplet surface.
- The ambient air is not soluble in the droplet fluid.
- Chemical reactions and radiation are not considered.

In order to simplify the modeling of the evaporation process, the evaporation process is subdivided into three spatial zones (Figure 3.2):

- The ambient gas phase, which represents the region infinitely far from the droplet. The temperature and vapor concentration are those of the carrier phase.
- The droplet interior
- The liquid/gas interface, which represents the governing transport processes. In this region one observes radial mass diffusion, heat convection and conduction as well as forced convection.

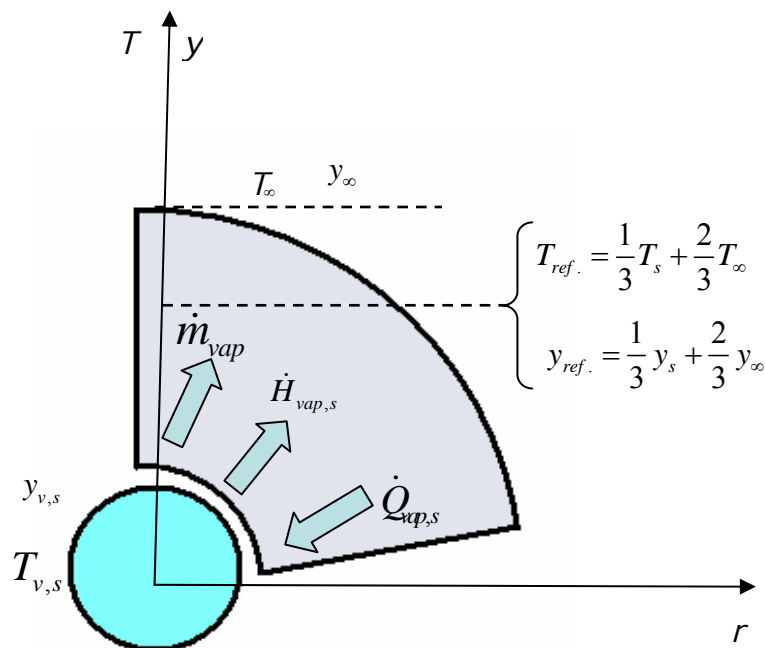


Figure 3.2: schematic description of evaporation

The transport processes linked to the forced convection from the gas flow around the droplet, (located at the liquid/gas interface as presented above), is the fundamental difficulty in the development of practical evaporation models. For solving this problem, one has to start from an isolated droplet in a stagnant gas atmosphere with spherical symmetric transport of mass and energy. The effect of forced convection is then taken into account by means of empirical correlation factors (modified Nusselt and Sherwood numbers), as they will be introduced later on.

3.3.2 The Uniform Temperature model

The Uniform Temperature model (equilibrium) as it is used in the frame of this work (UT model) does not consider any temperature variation in the interior of the droplet (homogenous temperature). However, the temperature variation has an unsteady behavior and is accompanied with mass transition [42]. As this model does not account for the gradient at the interior of the droplet, droplets are not discretized. Therefore this model does not require high computing time. The UT model describes the evolution of the droplet temperature and diameter, i.e. evaporation rate and energy flux through the liquid/gas interface (Figure 3.2).

The vaporization rate $\dot{m}_{p,v}$ is calculated by considering the mass transfer around the droplet following [98] and [99]:

$$\dot{m}_{p,v} = 2\pi r_p \overline{\rho_m} \overline{D_m} Sh^* \frac{\ln(1+B_M)}{B_M} \quad (3.59)$$

where r_p is the droplet radius, $\overline{\rho_m}$ and $\overline{D_m}$ are the averaged values of the mixture density and binary diffusion coefficient throughout the film, respectively. B_M represents the Spalding's mass transfer number defined by

$$B_M = \frac{y_s - y_\infty}{1 - y_s}, \quad (3.60)$$

in which y_s is the surface vapor mass fraction and y_∞ is the vapor mass fraction far from the droplet. In particular y_s depends on the vapor relative pressure which itself depends on the droplet surface temperature.

$$y_s = \frac{v_{s,eq}}{v_{s,eq} - (1 - v_{s,eq})\theta_2} \quad (3.61)$$

where θ_2 is the ratio of molecular weights. The molar mass fraction $v_{s,eq}$ is related to the saturation pressure through the Clausius-Clapeyron equation. Therefore it is referred to as an equilibrium model.

The accuracy of the evaporation rate depends strongly on the determination of the values of $\overline{\rho_m}$ and $\overline{D_m}$. Physical properties of the air vapor mixture (in the gaseous film around the droplet) are determined

3.3 Spray evaporation modeling

using the reference temperature and mass fraction. They are calculated using the Simpson or Sparrow & Gregg "1/3 rule" [99], from which the best accuracy of these quantities have been obtained (see Figure 3.2). The droplet radius is obtained from the equation of the diameter evolution for each droplet by:

$$\frac{dD_p}{dt} = -\frac{2\dot{m}_{p,v}}{\pi\rho_L D_p^2} - \frac{D_p}{3\rho_L} \frac{\partial\rho_L}{\partial T_p} \frac{dT_p}{dt}, \quad (3.62)$$

where ρ_L is the liquid density, D_p the droplet diameter and T_p the droplet temperature. Effects of convection on the vaporization and the heat flux rate are taken into account by means of semi-empirical correlations such as those for the drag coefficient, the Sherwood number and the Nusselt number.

The quantity Sh^* denotes the modified Sherwood number which includes the effects of the Stefan flow. It is defined by

$$Sh^* = 2 + \frac{Sh_0 - 2}{F_M} \quad (3.63)$$

where $Sh_0 = 1 + (1 + Re_p Sc_p)^{1/3} f(Re_p)$ (3.64)

Sh_0 accounts for the bulk convection of a non-evaporating spherical droplet. Re_p is the droplet Reynolds number and Sc_p is the Schmidt number while $f(Re_p)$ is an empirical function defined as $f(Re_p) = Re_p^{0.77}$ and F_M is a correction factor, which takes into consideration the relative change of the mass film thickness due to the droplet evaporation process:

$$F_M = F_M(B_M) = (1 + B_M)^{0.7} \ln \frac{(1 + B_M)}{B_M}. \quad (3.65)$$

The evaporation is coupled with the droplet energy/heating in (3.62) where the droplet temperature variations is described by

$$\frac{dT_p}{dt} = -\frac{6\dot{Q}_l}{\rho\pi c_{pL} D_p^3}, \quad (3.66)$$

where c_{pL} denotes the heat capacity coefficient of the liquid and \dot{Q}_l the heat flux rate penetrating into the droplet. The latter is calculated similarly to the evaporation rate and related to it by:

$$\dot{Q}_l = \dot{m}_{p,v} \left(\frac{c_{pm}(T_\infty - T_p)}{B_T} - h_v(T_p) \right), \quad (3.67)$$

where $h_v(T_p) = r(T_p) + \dot{Q}_l / \dot{m}_{p,v}$ expresses the effective latent heat of vaporization. It is a function of temperature and varies with the considered liquid. $r(T_p)$ is the true latent heat of vaporization and B_T is the Spalding heat transfer number expressed by

$$B_T = \frac{\overline{c_{p,v}}(T_\infty - T_p)}{r(T_p) + \dot{Q}_l / \dot{m}_{p,v}}, \quad (3.68)$$

and is related to the mass transfer number B_M by

$$B_T = (1 + B_M)^\phi - 1, \quad (3.69)$$

where

$$\phi = \frac{c_{p,v}}{c_{p,m}} \frac{Sh^*}{Nu^*} \frac{1}{Le}. \quad (3.70)$$

The variable ϕ depends on the thermo-physical properties, the Lewis number Le , and the modified Sherwood and Nusselt numbers (Sh^* and Nu^*). The modified Nusselt number in (3.70) is defined by:

$$Nu^* = 2 + \frac{Nu_0 - 2}{F_T} \quad (3.71)$$

where

$$Nu_0 = 1 + (1 + Re_p Pr)^{1/3} f(Re_p). \quad (3.72)$$

Nu_0 expresses the Nusselt number for a non-evaporating spherical droplet with $f(Re_p)$ as defined above. Pr is the Prandtl number and F_T is a correction factor which accounts for the change of the temperature within the film thickness due to the droplet evaporation process:

$$F_T = F_T(B_T) = (1 + B_T)^{0.7} \ln \frac{(1 + B_T)}{B_T}. \quad (3.73)$$

In (3.70) c_{pv} and c_{pm} are the heat capacity coefficients of vapor and mixture, respectively. Between Nu_0 and the modified Nusselt numbers Nu^* the relationship (3.71) is considered. No correction to the drag coefficient due to the evaporation process has been taken into consideration for. The gas viscosity in the droplet Reynolds number near the droplet has been estimated at a well defined reference state of temperature and vapor mass fraction according to the averaging "1/3 rule".

3.3.3 The Non-equilibrium evaporation model

In case of non-equilibrium evaporation model [30], the molar mass fraction, here denoted by $v_{s,neq}$, used for the calculation of vapor mass fraction on the droplet surface in equation (3.61), is determined by the following relation

3.3 Spray evaporation modeling

$$v_{s,neq} = v_{s,eq} - \left(\frac{L_K}{d/2} \right) \beta_L \quad (3.74)$$

where

$$\beta_L = - \left(\frac{3 \text{Pr}_G \tau_d}{2} \right) \frac{\dot{m}_{p,v}}{m_p} \quad (3.75)$$

represents the half of the blowing Peclet number. Pr_G is the Prandtl number, L_K represents the Knudsen length and τ_d is the particle relaxation time. The Lagrangian equation describing the transient temperature of a single droplet is given by:

$$\frac{dT_p}{dt} = \frac{f_2 \text{Nu}}{3 \text{Pr}_G} \left(\frac{\theta_1}{\tau_p} \right) (T_G - T_p) + \left(\frac{h_v}{c_{p,l}} \right) \frac{\dot{m}_{p,v}}{m_p} \quad (3.76)$$

where θ_1 denotes the ratio of the gas heat capacity to that of the liquid phase. The function f_2 is given by:

$$f_2 = \frac{- \left(\frac{3 \text{Pr}_G \tau_p}{2} \right) \frac{\dot{m}_{p,v}}{m_p}}{e^{- \left(\frac{3 \text{Pr}_G \tau_d}{2} \right) \frac{\dot{m}_{p,v}}{m_p}} - 1} \quad (3.77)$$

The droplets evaporation influences interactions between carrier gas and dispersed phase by means of mass, momentum, temperature, turbulence quantities, and species concentration. This effect is captured by the introduction of additional source terms $\overline{S}_{\psi,p,v}$ (equations (2.6)-(2.9), (2.13)-(2.16)) which are similar to those introduced for solid particles. Evaporation source terms are summarized in Table 3.4 (for both evaporation models). $\overline{S}_{u_i,m}$ represents the gas momentum flux ejected by the droplet during its vaporization, $\overline{S}_{\rho,m}$ is the mass which is released by the droplet into the fluid because of vaporization, and $\dot{m}_{p,v}$ represents the mean value of the evaporation rate in a control volume (CV). Remaining variables are the same as they were introduced above.

ψ	$\overline{S}_{\psi,p,v}$
1	$-\sum_p \frac{\dot{m}_{p,v}}{V} N_{i,j,k}$

\bar{u}	$\sum_p \frac{\dot{m}_{p,v} N_p}{V_{i,j,k}} u_p^{t_n}$
\bar{v}	$\sum_p \frac{\dot{m}_{p,v} N_p}{V_{i,j,k}} v_p^{t_n}$
\bar{w}	$\sum_p \frac{\dot{m}_{p,v} N_p}{V_{i,j,k}} w_p^{t_n}$
T	$\sum_p \frac{\dot{m}_{p,v} N_p}{V_{i,j,k}} (c_{p,v} T_p - h_v)$
y	$-\sum_p \frac{\dot{m}_{p,v} N_p}{V_{i,j,k}}$
k	$\overline{u_i S_{u_i,m}} - \overline{u_i} \overline{S_{u_i,m}} + \frac{1}{2} \left(\overline{u_i^2 S_{\rho,m}} - \overline{u_i}^2 \overline{S_{\rho,m}} \right)$
R_{ij}	$\overline{u_i S_{u_j,m}} - \overline{u_i} \overline{S_{u_j,m}} + \overline{u_j S_{u_i,m}} - \overline{u_j} \overline{S_{u_i,m}} +$ $\left(\overline{u_i u_j S_{\rho,m}} - \overline{u_i} \overline{u_j} \overline{S_{\rho,m}} \right)$
ε	$c_{\varepsilon,3}^{k-\varepsilon} \frac{\varepsilon}{k} S_{k,p,v}; \quad c_{\varepsilon,3}^{RS} \frac{\varepsilon}{k} S_{k,p,v}^{RS}$

Table 3.4: Source terms due to the presence of evaporating droplets

3.3.4 Turbulence-droplets interaction regimes

In view of describing the process interaction regimes in configuration under study, in the following study we are going to define the time scales characterizing the turbulence and the thermodynamics of vaporization. To define the adequate turbulence time scale, we follow [47] by considering the fraction of turbulence energy that effectively contributes to the turbulent mass and heat transfer. By doing so, we implicitly eliminate the so-called Frössling effect which accounts for the influence of the mean relative velocity. Thus, the relevant turbulence time scale appears to be that of eddies having a length scale equal to, or smaller than the instantaneous droplet diameter. As time scale characterizing the thermodynamics of vaporization, a residence time of the fuel vapor within the film thickness around the droplet can be used. This evaporation time depends on the droplet diameter, the diffusion coefficient, and the transfer number B_M .

As an approximation, this can be estimated as the ratio between the film thickness δ and the Stefan velocity or the radial blowing velocity v_r

3.3 Spray evaporation modeling

$$t_{ed} = \frac{(D_p^2 l_t)^{1/3}}{\sigma} \quad (3.78)$$

$$t_v = \frac{\delta}{v_r} \quad (3.79)$$

In (3.78) l_t is the turbulent length scale whereas σ represents the velocity fluctuation calculated by $\sigma^2 = 2/3 k$. The velocity in (3.79) is determined using the evaporation rate also defined as

$$\dot{m}_{p,v} = 4\pi r_p^2 v_r, \quad (3.80)$$

while the film thickness is calculated according to:

$$\delta_M = \frac{D_p}{Sh^* - 2} \quad (3.81)$$

To derive a measure of the relative importance of these time scales, a vaporization Damkohler number, defined as the ratio between the turbulence time scale and the vaporization time scale, is introduced (equation (3.82)). It characterizes the turbulence-droplet vaporization interaction regimes.

$$Da_v = \frac{t_{ed}}{t_v} \quad (3.82)$$

It turns out that in case of $Da_v > 1$ turbulence augmentation enhance evaporation rate, whereas for $Da_v \leq 1$ the opposite phenomenon takes place, namely the rate of evaporation is reduced.

3.4 Turbulent spray combustion modeling

In many engineering devices, the liquid fuel is not only evaporated, but also burned. Thereby combustion takes place after fuel evaporation and occurs only where vapor and air meet. Flames where fuel and oxidizer are initially separate are called non-premixed flames. They form, because of their safety, a very large percentage of combustion practice. Since the work done in the frame of this thesis deals with non-premixed flame, only the models describing the non-premixed combustion will be presented.

Turbulent combustion can be accounted for by solving the transport equations of chemical species which describe the convection, diffusion, and reaction sources for each species given by equation (2.15) and rewritten in a Favre averaged form as follow:

$$\frac{\partial(\bar{\rho}\tilde{\psi})}{\partial t} + \frac{\partial(\bar{\rho}\tilde{u}_j\tilde{\psi})}{\partial x_j} = \frac{\partial}{\partial x_j} \left(\bar{\rho}\Gamma \frac{\partial\tilde{\psi}}{\partial x_j} - \overline{\rho u_j \psi} \right) + \tilde{\omega}_{\psi} + \tilde{S}_{\psi,p,s} + \tilde{S}_{\psi,p,v}, \quad (3.83)$$

where $\tilde{S}_{\psi,p,s}$ and $\tilde{S}_{\psi,p,v}$ denotes source terms due to the dispersed phase, whereas $\tilde{\omega}_{\psi}$ is the chemical reaction rate. The Modeling of $\tilde{\omega}_{\psi}$ is the major challenge for the theoretical and numerical combustion in non premixed combustion. For this purpose, the modeling of diffusion flame can be classified into two different strategies [74]:

- Models based on the calculation of the primitive variable: The use of this concept for turbulent combustion permits the calculation the calculation of the temperature and species without solving species and energy transport equations. In this way, It avoids an explicit modeling of the time averaged chemical reaction rates $\tilde{\omega}_{\psi}$. The only variables to solve are related to momentum, mass conservation, mixture fraction, and variance of mixture fraction [74]. This approach, which has been used in the frame of this thesis, will be detailed in the following section.
- Model based on the calculation of reaction rate: In this case, the transport equations for species mass fraction are no longer related to the mixture fraction. Therefore the reaction rates $\tilde{\omega}_{\psi}$ must be modeled. This method requires more computational time than models based on the calculation of primitive variable, since all transport equations for species have to be solved.

In order to analyze the performance of the turbulent non-premixed combustion models, the Favre average has to be applied to the mixture fraction transport equation (2.52) introduced in chapter 2.3. The following section introduces the mixture fraction formalism along with the mixture fraction variance and highlights different terms to model.

3.4.1 Mixture fraction and its variance

Models based on mixture fraction approach are used very often in non-premixed flame calculations. In order to calculate the flame length and its location, one solves the mixture fraction equation and seeks for the stoichiometric value, which indicates the location of the flame. In addition to the Favre-averaged equations of continuity, momentum, and turbulent quantities, a Favre-averaged mixture fraction \tilde{z} equation and a Favre-averaged equation for its variance \tilde{z}''^2 have to be considered. From equation (2.52), the Favre-averaged equation for the mixture fraction can be written as follows [74]:

$$\frac{\partial \bar{\rho} \tilde{z}}{\partial t} + \frac{\partial (\bar{\rho} \tilde{u}_i \tilde{z})}{\partial x_i} = \frac{\partial}{\partial x_i} \left(\rho D \frac{\partial \tilde{z}}{\partial x_i} - \bar{\rho} \tilde{u}_i \tilde{z}'' \right) + \tilde{S}_{\tilde{z},p} \quad (3.84)$$

To obtain the Favre averaged equation for the mixture fraction variance, the following procedure can be used: 1) Multiply the instantaneous z

3.4 Turbulent spray combustion modeling

balance equation (2.52) by z and Favre-average the obtained equation provides a balance equation for \tilde{z}^2 . 2) Multiplying the \tilde{z} balance equation (3.84) by \tilde{z} provides a balance equation for \tilde{z}^2 . 3) Subtract the transport equation of \tilde{z}^2 from the transport equation of \tilde{z}^2 provides the balance equation for the variance of the mixture fraction:

$$\begin{aligned} \frac{\partial \overline{\rho \tilde{z}^2}}{\partial t} + \frac{\partial (\overline{\rho \tilde{u}_i \tilde{z}^2})}{\partial x_i} = & \underbrace{\frac{\partial}{\partial x_i} \left(\overline{\rho D \frac{\partial \tilde{z}^2}{\partial x_i}} \right)}_{\text{molecular diffusion}} + \underbrace{2 \overline{z''} \frac{\partial}{\partial x_i} \left(\overline{\rho D \frac{\partial \tilde{z}}{\partial x_i}} \right)}_{\text{turbulent transport}} - \underbrace{\frac{\partial}{\partial x_i} \left(\overline{\rho u_i'' z''^2} \right)}_{\text{production}} \\ & - \underbrace{2 \overline{\rho D \frac{\partial \tilde{z}^2}{\partial x_i}}}_{\text{dissipation}} + \tilde{S}_{\tilde{z}^2, p} \end{aligned} \quad (3.85)$$

The second RHS term of equation (3.85) represents the turbulent transport and is modeled using a classical gradient assumption:

$$\overline{\rho u_i'' z''^2} = -\overline{\rho} \frac{\nu_t}{S_{ct1}} \frac{\partial \tilde{z}^2}{\partial x_i} \quad (3.86)$$

where ν_t denotes the turbulent viscosity, calculated using a turbulence model and S_{ct1} represents a turbulent Schmidt number, ranging between 0.5 and 1.0. The term $\overline{\rho u_i'' z''}$ is also modeled with the gradient transport assumption:

$$\overline{\rho u_i'' z''} = -\overline{\rho} \frac{\nu_t}{S_{ct2}} \frac{\partial \tilde{z}}{\partial x_i} \quad (3.87)$$

where S_{ct2} represents a turbulent Schmidt number. [74].

The dissipation term (last term in RHS of equation (3.85)) is modeled using the scalar dissipation rate which is defined as follows:

$$\chi = 2D \frac{\partial z}{\partial x_i} \frac{\partial z}{\partial x_i}. \quad (3.88)$$

The scalar dissipation rate controls the mixing and measures the z-gradient towards the flame. It is directly influenced by the strain. In order to relate the scalar dissipation rate (3.88) with the last term in equation (3.85), one can apply the Favre average to the equation (3.88) and obtain:

$$\overline{\rho \tilde{\chi}} = 2 \overline{\rho D \frac{\partial z}{\partial x_i} \frac{\partial z}{\partial x_i}} = \underbrace{2 \overline{\rho D \frac{\partial \tilde{z}}{\partial x_i} \frac{\partial \tilde{z}}{\partial x_i}}}_{\overline{\rho \tilde{\chi}_m}} + 4 \overline{\rho D \frac{\partial z''}{\partial x_i} \frac{\partial z''}{\partial x_i}} + \underbrace{2 \overline{\rho D \frac{\partial z''}{\partial x_i} \frac{\partial z''}{\partial x_i}}}_{\overline{\rho \tilde{\chi}_p}} \quad (3.89)$$

3 Eulerian-Lagrangian modeling approach

$\tilde{\chi}_m$ measures the scalar dissipation rate due to the mean \tilde{z} field while $\tilde{\chi}_p$ measures the scalar dissipation rate due to the turbulent fluctuation of z , i.e. z'' -field. [74] refers that in RANS context the mean gradients are negligible against the fluctuation gradients. Also for a constant density flow, the second term in the RHS of equation (3.89) vanishes (per definition). The total scalar dissipation rate can now be reduced to:

$$\overline{\rho \tilde{\chi}} = 2\rho D \overline{\frac{\partial z}{\partial x_i} \frac{\partial z}{\partial x_i}} \approx 2\rho D \overline{\frac{\partial z''}{\partial x_i} \frac{\partial z''}{\partial x_i}} = \overline{\rho \tilde{\chi}_p} \quad (3.90)$$

The scalar dissipation rate $\tilde{\chi}_p$ plays for the mixture fraction the same role as the dissipation rate of the kinetic energy, ε , for the velocity field [74]. This analogy is used to model $\tilde{\chi}_p$ with the turbulent mixing time $\tau_t = k/\varepsilon$

$$\tilde{\chi}_p = c \frac{\overline{z''^2}}{\tau_t} = c \frac{\varepsilon}{k} \overline{z''^2}, \quad (3.91)$$

where c is a model constant equals 2 [74].

According to all presented modeling and after neglecting the molecular diffusion terms, the final closed equation for mixture fraction variance yields to:

$$\frac{\partial \overline{\rho z''^2}}{\partial t} + \frac{\partial (\overline{\rho u_i z''^2})}{\partial x_i} = \frac{\partial}{\partial x_i} \left(\frac{-v_t}{\rho S_{ct1}} \frac{\partial \overline{z''^2}}{\partial x_i} \right) + 2\overline{\rho} \frac{v_t}{S_{ct2}} \frac{\partial \tilde{z}}{\partial x_i} \frac{\partial \tilde{z}}{\partial x_i} - c\overline{\rho} \frac{\varepsilon}{k} \overline{z''^2} + \tilde{S}_{z''^2,p} \quad (3.92)$$

When droplets vaporization occurs due to the local sources of fuel, the mixture fraction z is not a conserved scalar. It results in two additional source terms ($\tilde{S}_{z,p}$ and $\tilde{S}_{z''^2,p}$) appearing in the transport equation of \tilde{z} and $\overline{z''^2}$. In RANS, the liquid phase is described using a Lagrangian approach. In addition to that the sources of the fuel, leading to mean sources of \tilde{z} , are estimated on an Eulerian mesh from the droplets tracked in the Lagrangian frame. The source terms $\tilde{S}_{z,p}$ and $\tilde{S}_{z''^2,p}$ for the mixture fraction (equation (3.84)) and its variance (equation (3.92)) are given by [50] as follows:

$$\tilde{S}_{z,p} = - \sum_p \frac{\dot{m}_{p,v} N_p}{V_{i,j,k}}, \quad (3.93)$$

and

$$\tilde{S}_{z''^2,p} = \left(- \sum_p \frac{\dot{m}_{p,v} N_p}{V_{i,j,k}} \right) \frac{\overline{z''^2} (1 - 2\tilde{z})}{\tilde{z}}. \quad (3.94)$$

The used parameters are the same as explained in the section 3.2.

3.4.2 Turbulent combustion modeling based on primitive variables

In order to relieve the complexity of modeling, turbulent diffusion flame may be subdivided into two parts. The first one is a mixing problem, describing the homogeneity of fuel-oxidizer mixture, while the second problem is associated with the chemistry or combustion. Based on time scales of mixing and combustion, the description of the system chemistry in case of non-premixed flame, as introduced in the chemical kinetics (chapter 2.4.1), can be summarized in the following three options:

- The flame sheet model: This approach assumes that the chemistry is infinitely fast and irreversible. The fuel and oxidant species never coexist in space and that the reaction is a one step mechanism. This approach is attractive for engineer since it reduces drastically the complexity of turbulence-chemistry interaction because no reaction rate or equilibrium calculations are required. This approach, however, can not predict intermediate species formation or dissociation effects. It is therefore not considered in the calculation in this thesis.
- Equilibrium model: This approach assumes, similarly to the flame sheet model, that the chemistry is very fast. However, it is able to predict the formation of intermediate species and does not require knowledge of detailed chemical kinetic rate data. The mass concentration of each species is related to the mixture fraction by the Gibbs free energy [100].
- Flamelet Model: This model relaxes the infinitely fast chemistry assumption by introducing the scalar dissipation rate as a parameter to describe the degree of departure from the equilibrium state. However, the flamelet approach still relies on the assumption that the time scales for chemical kinetics are much shorter than the time scales of convection and diffusion. Under this condition of time scales, the combustion chemistry reaches a quasi-steady state and adjusts immediately to local flow conditions, i.e. strain and stretch of the flame. Given the distributions of both mixture fraction and the scalar dissipation rate, one can obtain density, temperature, and species concentrations from the so called flamelet library by an interpolation scheme.
- ILDM mechanism: As introduced in chapter 2, in this model it is assumed that the fastest reactions can be decoupled from the slow ones (in general all time scales affect each species evolution). Then, the decoupled fast reactions (those that are faster than the flow time scales) can be ignored while those with slow time scales are tracked using progress variables. When the slowest and fastest time scales of a solution differ by several orders of magnitude, the most important information about the system behavior is often contained in the terms of the solution with the slower time scales. The main

consequence is that chemical evolution associated with detailed kinetics scheme can be reduced to chemical processes having time scale slower than the flow time scales. The problem of ILDM is the large amount of storage needed for the tabulations of species values concentrations at given states of the system in terms of the other variables [77].

The first three models introduced above are based on the mixture fraction modeling formalism. Thus they have the advantage of reducing the chemistry to two conserved transport equations. All scalar variables (species mass fraction, density, and temperature) are linked to the mixture fraction. For a given *instantaneous* value of mixture fraction at any point of the adiabatic flow field, one can compute the *instantaneous* values of species mole fractions, density, and temperature as turned out from the flamelet, equilibrium or flame sheet chemistry model. However, the instantaneous relationship in the context of RANS is not computed. In addition to that, the prediction of turbulent reacting flow is achieved using the Favre-averaging method. Therefore one should take into consideration the fluctuation of the mixture fraction and its effect on the combustion along with turbulence-chemistry dependency. In the frame of this work, the interaction of turbulence and chemistry is accounted for with a probability density function (PDF) which has a presumed form. For engineering purposes, a widely used PDF is the so called β presumed probability density function which depends not only on the mean value of the variable but also on its second moment (variance). The PDF which describes the temporal fluctuations of mixture fraction z in a turbulent flow provides the time averaged values of species mass fractions and temperature (if adiabatic) by: [74]

$$\overline{\rho \tilde{\psi}_i} = \int_0^1 \rho \psi_i p(z) dz, \quad \tilde{\psi}_i \in \{\text{species mass fraction, Temp.}\} \quad (3.95)$$

The β function PDF is given by:

$$p(z) = \frac{z^{a-1} (1-z)^{b-1}}{\int_0^1 z^{a-1} (1-z)^{b-1} dz}, \quad (3.96)$$

where

$$a = \tilde{z} \left[\frac{\tilde{z}(1-\tilde{z})}{\tilde{z}^2} - 1 \right] \quad (3.97)$$

and

$$b = \frac{a}{\tilde{z}} - a \quad (3.98)$$

3.4 Turbulent spray combustion modeling

In case of flamelet approaches, also used in this work, the scalar dissipation rate allows to characterize the flame structure. The Favre averaged temperature or mass fraction concentration are evaluated as following [74]:

$$\overline{\rho \tilde{\psi}_i} = \int_0^1 \rho \psi_i(z, \tilde{\chi}) p(z) dz \quad (3.99)$$

Figure 3.3 shows the dependence of averaged scalar $\tilde{\psi}_i$ on the mixture fraction, the chemistry model and the turbulence-chemistry interaction which is represented by the probability distribution function [135].

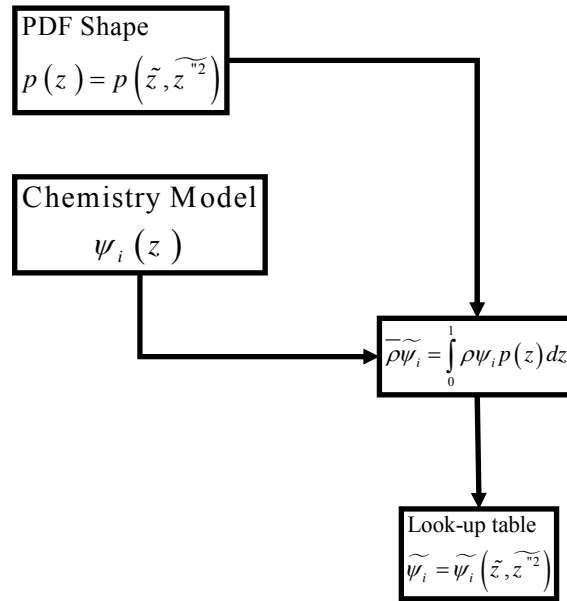


Figure 3.3: Dependence of Averaged Scalars $\tilde{\psi}_i$ on \tilde{z} , \tilde{z}''^2 and the Chemistry Model (Adiabatic, Single-Mixture-Fraction Systems) from [135]

Figure 3.4 notes the schematic procedure for a presumed PDF method for infinitely fast irreversible chemistry [74]. The computing starts with solving the mean values for momentums, turbulence quantities, mixture fraction and its variance, then for each point of the flow field having the couple $(\tilde{z}, \tilde{z}''^2)$ corresponds unique density, mean temperatures and species mass fractions (equation (3.95)).

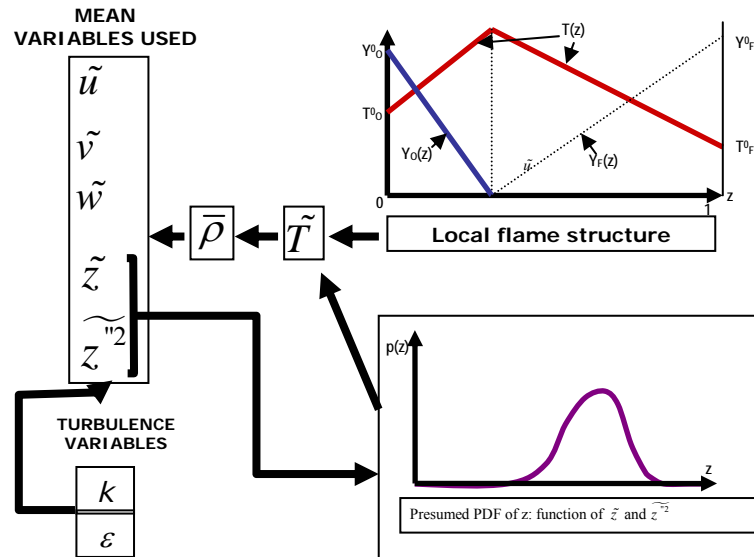


Figure 3.4: Presumed PDF method for infinitely fast irreversible chemistry [74]

3.4.3 Turbulence modeling for reacting flows

The differences between reactive and non reactive flows modeling consists of the density variation. For isothermal flows, the density is considered as constant whereas in case of reactive flow the density is a function of temperature and species. The Favre-averaging process performed on Navier-Stokes transport equations (equation (2.14)) contains terms which correspond to the convective transport of momentum and scalar due to the fluctuating component: Reynolds stresses $\overline{\rho u_i'' u_j''}$ and scalar turbulent fluxes $\overline{\rho u_j'' \psi''}$. To close these terms, there are different alternatives which depend on hypothesis and degree of modeling, i.e. first moment order or second moment order [134].

First order turbulence modeling:

Similar to chapter 3.1.1, these models are based on the addition of isotropic eddy viscosity ν_t to the molecular viscosity of the fluid. The turbulent Reynolds stresses $\overline{\rho u_i'' u_j''}$ are described using the viscous tensor expression valid for Newtonian fluids:

$$\overline{\rho u_i'' u_j''} = -\mu_t \left(\frac{\partial \tilde{u}_i}{\partial x_j} + \frac{\partial \tilde{u}_j}{\partial x_i} - \frac{2}{3} \delta_{ij} \frac{\partial \tilde{u}_k}{\partial x_k} \right) + \frac{2}{3} \tilde{\rho} \tilde{k} \quad (3.100)$$

The turbulent kinetic energy and its dissipation (in case of $k-\epsilon$ turbulence model) are key variables in the definition of the turbulent flow. The turbulent kinetic energy is defined by:

$$\tilde{k} = \frac{1}{2} \overline{u_i'' u_i''} \quad (3.101)$$

3.4 Turbulent spray combustion modeling

The turbulent viscosity μ_t is estimated (in case of $k-\varepsilon$ turbulence model) as:

$$\mu_t = \bar{\rho} C_\mu \frac{\tilde{k}}{\tilde{\varepsilon}} \quad (3.102)$$

Following the same approach as in chapter 3.1.1, the transport equations for the turbulent Favre-averaged variables \tilde{k} and $\tilde{\varepsilon}$ used to compute turbulent non-premixed flame can be written as:

$$\frac{\partial \bar{\rho} \tilde{k}}{\partial t} + \frac{\partial}{\partial x_i} (\bar{\rho} \tilde{u}_i \tilde{k}) = \frac{\partial}{\partial x_i} \left(\frac{\bar{\rho} \nu_t}{\sigma_k} \frac{\partial \tilde{k}}{\partial x_i} \right) + \mu_t \left(\frac{\partial \tilde{u}_i}{\partial x_j} + \frac{\partial \tilde{u}_j}{\partial x_i} \right) \frac{\partial \tilde{u}_i}{\partial x_j} - \varepsilon \quad (3.103)$$

$$\begin{aligned} \frac{\partial \bar{\rho} \tilde{\varepsilon}}{\partial t} + \frac{\partial}{\partial x_i} (\bar{\rho} \tilde{u}_i \tilde{\varepsilon}) = & - \frac{\partial}{\partial x_i} \left(\frac{\bar{\rho} \nu_t}{\sigma_k} \frac{\partial \tilde{\varepsilon}}{\partial x_i} \right) + \\ & \bar{\rho} \nu_t \left(\frac{\partial \tilde{u}_i}{\partial x_j} + \frac{\partial \tilde{u}_j}{\partial x_i} \right) \frac{\partial \tilde{u}_i}{\partial x_j} C_{\varepsilon 1} \frac{\tilde{\varepsilon}}{\tilde{k}} - C_{\varepsilon 2} \bar{\rho} \frac{\tilde{\varepsilon}^2}{\tilde{k}} \end{aligned} \quad (3.104)$$

The used model constants have the same value as presented in chapter 3.1.1.

Scalar turbulence:

The scalar turbulent flux term in equation (2.15) is modeled also using the Boussinesq approximation as follows:

$$-\overline{\rho u_j \psi} = \frac{\mu_t}{\sigma_\psi} \frac{\partial \tilde{z}^2}{\partial x_i} \quad (3.105)$$

Second order turbulence modeling:

The transport equations for the Reynolds stress components are derived and modeled in the same way as in section 3.1.2 The exact balance equation is given by:

3 Eulerian-Lagrangian modeling approach

$$\begin{aligned}
 \frac{\partial}{\partial t} \left(\overline{\rho u_i'' u_j''} \right) + \frac{\partial}{\partial x_k} \left(\overline{\rho u_i'' u_j'' u_k''} \right) = & \underbrace{\overline{\rho} \left(-\overline{u_i'' u_k''} \frac{\partial \widetilde{u}_j}{\partial x_k} - \overline{u_j'' u_k''} \frac{\partial \widetilde{u}_i}{\partial x_k} \right)}_{\text{production}} - \underbrace{2 \overline{\rho \nu} \frac{\partial u_i''}{\partial x_k} \frac{\partial u_j''}{\partial x_k}}_{\text{viscous dissipation } \varepsilon_{ij}} \\
 & + \underbrace{\frac{\overline{p'}}{\rho} \left(\frac{\partial u_i''}{\partial x_j} + \frac{\partial u_j''}{\partial x_i} \right)}_{\text{pressure strain } \Pi_{ij}} + \frac{\overline{\rho' u_j''}}{\rho} \frac{\partial \overline{p}}{\partial x_i} + \frac{\overline{\rho' u_i''}}{\rho} \frac{\partial \overline{p}}{\partial x_j} \\
 & + \frac{\partial}{\partial x_k} \left(\nu \frac{\partial \left(\overline{\rho u_i'' u_j''} \right)}{\partial x_k} - \underbrace{\left(\overline{\rho u_k'' u_i'' u_j''} + \overline{p' u_i''} \delta_{jk} + \overline{p' u_j''} \delta_{jk} \right)}_{\text{turbulent transport}} \right)
 \end{aligned} \tag{3.106}$$

In the equation (3.106) a new term arises. This term, describing the correlation between density fluctuations and velocity fluctuations, comes out only in case of reacting flow depending on the mean pressure gradient. Jones [101] modeled this new term as:

$$\overline{\rho' u_i''} = -\frac{1}{4.3} \frac{\tilde{k}}{\tilde{\varepsilon}} \overline{u_i'' u_k''} \frac{\partial \overline{p}}{\partial x_k} \tag{3.107}$$

The closure constants and the modeling of remaining unclosed parts are done in the same way as in section 3.1.2 for isothermal flows.

4 Numerical procedure

As presented in chapter 2 and 3, the modeling of reactive multiphase flows consists mainly of ordinary and partial differential equations which can not be solved analytically. The development and analysis of discretization methods for systems of ordinary and partial differential equations and the implementation of the respective algorithms in efficient computer codes are the only way to transform the theoretical work into practical one and thus provide useable results. The problem is then shifted from the continuous mathematics to discrete mathematics. This chapter deals with the used numerical procedure to discretize the governing equations for the carrier phase and the particle/droplet equation of motion for the dispersed phase as well as with the coupling method between both phases. Furthermore the statistical method for properties sampling and the convergence criteria will be introduced.

4.1 Numerical method for the gas phase

The details of the numerical procedure used in this work are the topic of this sub-chapter. Following Ferziger and Peri [125] in general, a numerical solution method includes a mathematical model (that has been already established in the previous chapters), a discretization method, a coordinate and basis vector system, a numerical grid, a finite approximation and a solution method. In the present work the CFD package FASTEST-3D (Flow Analysis Solving Transport Equations Simulating Turbulence 3 Dimensional) was used. The program was originally developed by INVENT Computing GmbH (Erlangen, Germany) and obtained as a source code in the framework of the Collaborative Research Project SFB-568. Consequently, the parts of numerical solution method mentioned above and applied in the present work are those based on the features of FASTEST-3D:

- Finite volume discretization method based on hexahedral control volumes;
- Cartesian coordinate and basis vector system;
- Boundary-fitted non-orthogonal block-structured grid with matching interfaces and collocated variable arrangement;
- Implicit and semi-implicit temporal and first and second order spatial discretization schemes;
- Strongly implicit procedure for the iterative solution of the linearised equation system;
- Full geometrical multigrid solver for convergence acceleration;

- Parallelization based on domain decomposition in space using the MPI message passing library.

The most important details as well as implementation of the boundary conditions are presented and discussed in the following sections.

4.1.1 Finite volume method

The finite volume method is used in the frame of this work to describe the continuous phase. This method is based on the resolution of governing equations in the integral form given by the equation (4.1):

$$\int_V \frac{\partial}{\partial t} (\rho \psi) dV + \int_V \frac{\partial}{\partial x_i} (\rho u_i \psi) dV = \int_V \frac{\partial}{\partial x_i} \left(\Gamma_\psi \frac{\partial \psi}{\partial x_i} \right) dV + \int_V S_\psi dV . \quad (4.1)$$

The quantity ψ represents a conserved variable (velocity component, scalar, etc.), Γ_ψ notes the diffusivity coefficient, S_ψ the sum of all source terms and V the volume of the considered cell. The volume integrals are transformed to area integrals using Gauss' Law:

$$\int_V \frac{\partial}{\partial t} (\rho \psi) dV + \int_\sigma \left(\rho u_i \psi - \Gamma_\psi \frac{\partial \psi}{\partial x_i} \right) n_i d\sigma = \int_V S_\psi dV , \quad (4.2)$$

where σ represents the surface confining the volume V (of the cell) and n_i the unit vector normal to the surface σ . The equation (4.2) is applied for each control volume (CV) of the numerical grid which defines the computational domain where the discrete locations at which the variables are to be calculated (Figure 4.1). The storage of the flow information related to every CV divides the discretization problem into two different arrangements, namely: collocated grid and staggered grid.

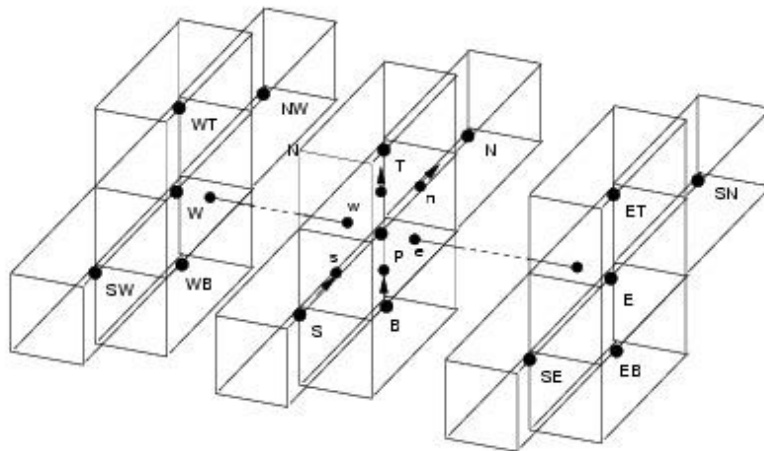


Figure 4.1: Topology and control volume notification

4.1 Numerical method for the gas phase

Collocated grid, as used in this work, is one in which the pressure and velocity variables share the same grid (Figure 4.2). Thus all variables are stored on the same grid point and the same control volume is used for all variables. It is the preferred method for nonorthogonal coordinates. The implementations of collocated grids on nonorthogonal coordinates require regularization to prevent the formation of oscillations because of pressure velocity decoupling [125].

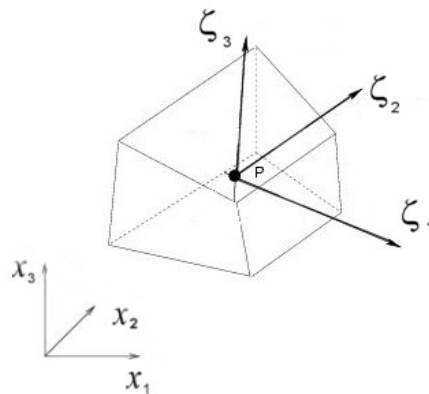


Figure 4.2: Collocated grid

Staggered grid: The scalar variables (pressure, density, total enthalpy, scalar, etc.) are stored in the center of the grid, whereas the normal components of the momentum (velocity) are located at the midpoints of the cell faces (Figure 4.3). Using a staggered grid is the most common way to avoid the pressure-velocity decoupling and thus avoid pressure oscillations [125].

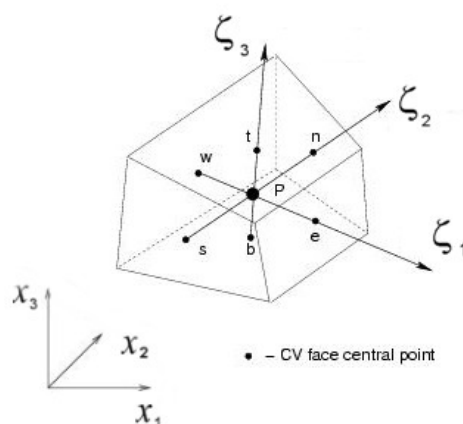


Figure 4.3: Variables arrangement on staggered grid

Now consider a hexahedral control volume with central point denoted as P, having six neighbors CVs: E (east), W (west), N (north), S (south), T (top) and B (bottom) (see Figure 4.1) and sharing common faces with

neighbors: e, w, n, s, t and b, respectively. The final objective within finite volume method is to transform the integral differential equation (4.2) into an algebraic equation of the following form:

$$\underbrace{A_p \psi_p - \sum_{Nb} A_{Nb} \psi_{Nb}}_{\text{implicit part}} = \underbrace{S_p}_{\text{explicit part}} \quad (4.3)$$

Here, the subscript Nb corresponds to the 6 neighbors CVs: W, E, S, N, B, T and A_p , A_{Nb} denote the coefficients belonging to the dependent variable values ψ_p , ψ_{Nb} in the point P , Nb derived from the discretization. All the remaining terms resulting from the discretization that can not be included into the implicit part of (4.3) are treated explicitly and put into the source term S_p on the RHS.

4.1.1.1 Coordinate transformation

Taking into account the non-orthogonality of the grid used, it is plausible to use in each CV and on each CV face a local coordinate system and then to transform the operators (derivatives) from local into the global (Cartesian) coordinate system. In Figure 4.4 a local coordinate system arranged in the CV central point is shown. The basis vectors of the local coordinate system are obtained connecting the CV central point with the central points of the CV's faces.

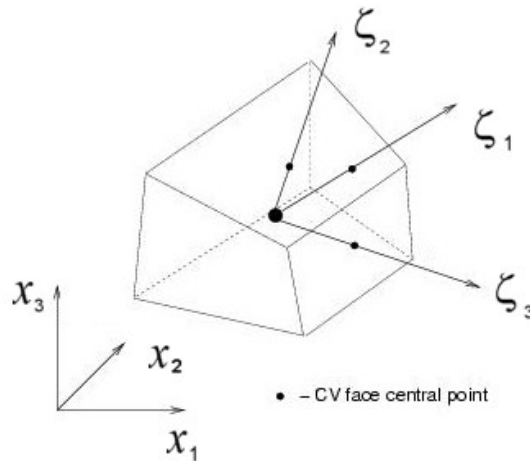


Figure 4.4: Local coordinate system arranged in the CV central point.

The local coordinates are in the following denoted as $(\zeta_1, \zeta_2, \zeta_3)$ while global (Cartesian) coordinates are denoted as (x_1, x_2, x_3) . The transformation

4.1 Numerical method for the gas phase

matrix (for transformation from the global into the local coordinate system) is

$$A = \begin{pmatrix} \frac{\partial x_1}{\partial \zeta_1} & \frac{\partial x_1}{\partial \zeta_2} & \frac{\partial x_1}{\partial \zeta_3} \\ \frac{\partial x_2}{\partial \zeta_1} & \frac{\partial x_2}{\partial \zeta_2} & \frac{\partial x_2}{\partial \zeta_3} \\ \frac{\partial x_3}{\partial \zeta_1} & \frac{\partial x_3}{\partial \zeta_2} & \frac{\partial x_3}{\partial \zeta_3} \end{pmatrix}. \quad (4.4)$$

The derivative of some field variable ψ with respect to Cartesian coordinates can be expressed in terms of the local coordinates according to

$$\frac{\partial \psi}{\partial x_i} = \frac{\partial \psi}{\partial \zeta_j} \frac{\partial \zeta_j}{\partial x_i}. \quad (4.5)$$

The elements of the inverse transformation matrix, A^{-1} , (local to global),

$$A^{-1} = \begin{pmatrix} \frac{\partial \zeta_1}{\partial x_1} & \frac{\partial \zeta_1}{\partial x_2} & \frac{\partial \zeta_1}{\partial x_3} \\ \frac{\partial \zeta_2}{\partial x_1} & \frac{\partial \zeta_2}{\partial x_2} & \frac{\partial \zeta_2}{\partial x_3} \\ \frac{\partial \zeta_3}{\partial x_1} & \frac{\partial \zeta_3}{\partial x_2} & \frac{\partial \zeta_3}{\partial x_3} \end{pmatrix} \quad (4.6)$$

are obtained from the well-known linear algebraic relation:

$$A^{-1} = \frac{1}{J} (A_{adj})^T, \quad (4.7)$$

where $J = \det(A)$ is the Jacobean and (A_{adj}) is the transpose adjoint matrix obtained from matrix A . I.e.

$$\frac{\partial \zeta_j}{\partial x_i} = \frac{1}{J} \left[adj \left(\frac{\partial x_j}{\partial \zeta_i} \right) \right]^T = \frac{1}{J} \beta_{ij} \quad (4.8)$$

and

$$\frac{\partial \psi}{\partial x_i} = \frac{1}{J} \beta_{ij} \frac{\partial \psi}{\partial \zeta_j} \quad (4.9)$$

where β_{ij} is the element of matrix B given by

$$B = \begin{pmatrix} \frac{\partial x_2}{\partial \zeta_2} \frac{\partial x_3}{\partial \zeta_3} - \frac{\partial x_2}{\partial \zeta_3} \frac{\partial x_3}{\partial \zeta_2} & \frac{\partial x_1}{\partial \zeta_3} \frac{\partial x_3}{\partial \zeta_2} - \frac{\partial x_1}{\partial \zeta_2} \frac{\partial x_3}{\partial \zeta_3} & \frac{\partial x_1}{\partial \zeta_2} \frac{\partial x_2}{\partial \zeta_3} - \frac{\partial x_1}{\partial \zeta_3} \frac{\partial x_2}{\partial \zeta_2} \\ \frac{\partial x_2}{\partial \zeta_3} \frac{\partial x_3}{\partial \zeta_1} - \frac{\partial x_2}{\partial \zeta_1} \frac{\partial x_3}{\partial \zeta_3} & \frac{\partial x_1}{\partial \zeta_1} \frac{\partial x_3}{\partial \zeta_3} - \frac{\partial x_1}{\partial \zeta_3} \frac{\partial x_3}{\partial \zeta_1} & \frac{\partial x_1}{\partial \zeta_3} \frac{\partial x_2}{\partial \zeta_1} - \frac{\partial x_1}{\partial \zeta_1} \frac{\partial x_2}{\partial \zeta_3} \\ \frac{\partial x_2}{\partial \zeta_1} \frac{\partial x_3}{\partial \zeta_2} - \frac{\partial x_2}{\partial \zeta_2} \frac{\partial x_3}{\partial \zeta_1} & \frac{\partial x_1}{\partial \zeta_2} \frac{\partial x_3}{\partial \zeta_1} - \frac{\partial x_1}{\partial \zeta_1} \frac{\partial x_3}{\partial \zeta_2} & \frac{\partial x_1}{\partial \zeta_1} \frac{\partial x_2}{\partial \zeta_2} - \frac{\partial x_1}{\partial \zeta_2} \frac{\partial x_2}{\partial \zeta_1} \end{pmatrix}. \quad (4.10)$$

Substitution of the expression for the differential operator (4.9) into equation (4.2) gives

$$\int_V \frac{\partial}{\partial t} (\rho \psi) dV + \int_{\sigma} \left(\rho u_i \psi - \Gamma_{\psi} \frac{\partial \psi}{\partial x_i} \right) n_i d\sigma = \int_V S_{\psi} dV \quad (4.11)$$

4.1.1.2 Discretization of the convective and diffusion terms

The discretization of the convective term is given by:

$$\int_{\sigma} \rho u_i \psi n_i d\sigma = \sum_{k=e,w,n,s} a_k \sigma_k = (\rho u \psi)_e \sigma_e - (\rho u \psi)_w \sigma_w + (\rho u \psi)_n \sigma_n - (\rho u \psi)_s \sigma_s + (\rho u \psi)_t \sigma_t - (\rho u \psi)_b \sigma_b \quad (4.12)$$

The problem now is how to approximate the value ψ at the faces e , w , n , s , t and b . There are three basic discretization schemes.

The first common way is to use linear interpolation **Central Differencing Scheme** (CDS). The value of ψ (e.g. at the east face) is estimated using the neighbors nodes P and E (Figure 4.1).

$$\psi_e = f_x \psi_E + (1 - f_x) \psi_P, \quad (4.13)$$

where f_x is the interpolation function, and for a constant mesh spacing $f_x = 0.5$. The central differencing scheme has a second order accuracy. One can prove this by applying the Taylor series expansion on the point P . The accuracy is proportional to the square of grid width. I.e. if the number of cells within one direction is doubled, the error will be divided by a factor of 4.

The Upwind Differencing Scheme (UDS) assumes that the neighboring cell value for ψ will be convected across the boundary:

$$\psi_e = \begin{cases} \psi_P & \text{if } u_e \geq 0 \\ \psi_E & \text{if } u_e < 0 \end{cases} \quad (4.14)$$

4.1 Numerical method for the gas phase

The main drawback of the upwind scheme is that it is inaccurate and very diffusive, because it is of first order.

The Flux Blending switches between the two, according to the relative size of the convective and diffusive fluxes across the cell face. By resulting in oscillation, one can combine UDC and CDS to calculate the value at the faces e :

$$\psi_e = \underbrace{\psi_e^{UDS}}_I + \gamma \underbrace{(\psi_e^{CDS} - \psi_e^{CDS})}_{II}, \quad (4.15)$$

where $0 \leq \gamma \leq 1$ is factor which scales the manner of flux blending. For $\gamma = 0$, the interpolation is pure CDS whereas for $\gamma = 1$, the interpolation is pure Upwind. Part I of (4.15) is treated implicitly whereas part II is treated explicitly. The flux blending scheme is a good control tool to achieve an optimum between stability and accuracy.

For the diffusive part, a centered difference for the discretization of the normal gradient of the flux on the control volumes faces is used. Thus the diffusive part is discretized by:

$$\left(\frac{\partial \psi}{\partial x} \right)_e = \frac{\psi_E - \psi_P}{x_E - x_P} \quad (4.16)$$

In the frame of this work, all above mentioned schemes for the interpolation of scalar (e.g. ψ_e) at the control volume faces have been applied on different configurations. These numerical schemes reflect the way how information is transported through the faces. It is dependent on the ratio between convection and diffusion, i.e. the Peclet number, which is defined by:

$$Pe = \frac{\rho u_i \Delta x_i}{\Gamma} \quad (4.17)$$

If the Peclet number is small, the transport is dominated by diffusion, which transports information equally in all directions. Contrarily if the Peclet number is large, information is transported in the direction of the velocity field. Having a large Pe is undesired, since it influences the solution convergence very much. The numerical results may contain oscillations due to the fact that while computing the convective term at the node P only the values at E (east) and W (west) nodes are used, but not at the P node. Thus, ψ_P can take any value, i.e. oscillations are allowed.

Other than CDS, UDS, and the flux blending schemes there is a large number of interpolation methods, e.g. Quadratic Upwind Interpolation for Convective Kinematics "QUICK", which is third accurate order. Unfortunately it was not used within this work. A recent review on numerical schemes and their performance can be found in [125] and [126].

4.1.1.3 Time dependent discretization

Unsteady flows have a fourth coordinate direction as time, which must be discretized. The implemented time discretizations within the used code are: First Order Forward Implicit (FOFI), Second Order Forward Implicit (SOFI), Crank Nicolson (CN), and Runge Kutta (RK) [126] methods. The last one (RK) is an explicit method, i.e. there is only one unknown in the discretized equation time level (equation (4.18) for one dimensional convective diffusive problem).

$$\frac{\psi_P^{n+1} - \psi_P^n}{\Delta t} + u \frac{\psi_E^n - \psi_W^n}{2\Delta x} - \Gamma \frac{\psi_E^n + \psi_W^n - 2\psi_P^n}{(\Delta x)^2} = 0. \quad (4.18)$$

From this equation, one can define the *CFL* number. Thus one can also make an instruction for the explicit time discretization method which is valid for RK-method:

$$CFL = \left| u \cdot \frac{\Delta t}{\Delta x} \right| \leq 1, \quad (4.19)$$

this requires:

$$\Delta t < \frac{\Delta x}{u}. \quad (4.20)$$

The FOFI method (also known as implicit Euler method) is applied by discretizing the variable in the time level $n+1$ as follows:

$$\frac{\partial \psi(t_{n+1})}{\partial t} \approx \frac{\psi^{n+1} - \psi^n}{\Delta t_n} = f(\psi^{n+1}) \quad (4.21)$$

For the computed time dependent configuration in this thesis, the FOFI method was chosen. The advantage of using this scheme (fully-implicit technique) is that there is no restriction on time-steps (the implicit Euler method allows arbitrarily large time steps to be taken). However the first order implicit method is no more accurate than the explicit Euler method [126]. The disadvantage is the first order truncation error in time.

The Crank-Nicolson method solves both the accuracy and the stability problem. It is based on central differencing and hence it is second-order accurate in time. The approximation of the time derivative is done on the time point $t_{n+1/2}$ as follows:

$$\frac{\partial \psi(t_{n+1/2})}{\partial t} \approx \frac{\psi^{n+1} - \psi^n}{\Delta t_n} = \frac{1}{2} [f(\psi^{n+1}) + f(\psi^n)] \quad (4.22)$$

4.1.1.4 Pressure velocity coupling

The 3D-incompressible flow is described numerically by three equations of momentum and the continuity. Thus we have four unknowns (u , v , w , and P) and four equations (3 for momentum + 1 for continuity). One should mention here, that the density ρ is not considered as variable, because the flow is incompressible. In other words, the density may change due to variations in temperature and concentration of species, but not due to pressure variations ($\partial\rho/\partial p=0$). The problem is that we do not have any equation for pressure P . In case of compressible flow, i.e. Mach number > 0.3 , the pressure is deduced by the equation of state. Unfortunately, the flows under investigation are incompressible. Therefore we can use the continuity equation as an indirect equation for the pressure. This method is called the SIMPLE (Semi Implicit Method for Pressure Linked Equation) algorithm.

The SIMPLE algorithm is preceded as follows: first the momentum equations are solved, using an "old" pressure to give u^* , v^* , and w^* . In the following we are going to consider only the x -direction with the velocity component u^* , the other two directions can be treated in the same way. The discretized governing equation (4.3) for the u^* velocity component is given by:

$$a_e u_e^* = \sum_{nb} a_{nb} u_{nb}^* + S_{\bar{u}} + (p_W^* - p_P^*) \sigma_e, \quad (4.23)$$

where $S_{\bar{u}}$ represents a source term, σ_e the control volume surface in the east face and a_{nb} are the discretization coefficients related to all faces.

Now we introduce:

$$u_i^{n+1} = u_i^* + u_i^{cor}, \quad p^{n+1} = p^* + p^{cor}, \quad (4.24)$$

where u_i^* have been obtained from the momentum equations, and p^* was obtained from the previous iteration. u_i^{cor} and p^{cor} are the velocity and pressure correction respectively.

Now, velocities u_i^{n+1} are used (corrected) to solve the continuity equation

$$\sum_i (\rho u^{n+1} \sigma)_i = 0 \quad (4.25)$$

Then we use the momentum equations to obtain a relation between u_i^{n+1} and p^{cor} .

$$a_e u_e^{n+1} = \sum_{nb} a_{nb} u_{nb}^{n+1} + S_{\bar{u}} + (p_W^{n+1} - p_P^{n+1}) \sigma_e, \quad (4.26)$$

where nb denotes the neighboring faces. The equation (4.26) provides a relation between u_i^{cor} and p^{cor} as follows:

$$a_p u_p^{cor} = \sum_{nb} a_{nb} u_{nb}^{cor} - \sigma_e (p_W^{cor} - p_P^{cor}) \quad (4.27)$$

Equation (4.27) necessitates the determination of p^{cor} to calculate the corrected velocities. So we use equation (4.25) and deduce the following expression:

$$a_p p_P^{cor} = \sum_{nb} a_{nb} p_{nb}^{cor} - \underbrace{\sum_{nb} (\rho u_i^* \sigma_i)}_{b'} \quad (4.28)$$

The object of the pressure correction equation is to satisfy the continuity equation, i.e. to make the term b' in equation (4.28) vanish and thus determine p^{cor} . Once $(p_W^{cor} - p_P^{cor})$ is calculated, we can compute the new velocities as follows:

$$u_e^{n+1} = u_e^* - \frac{\sigma_e}{a_e - \sum_{nb} a_{nb}} (p_W^{cor} - p_P^{cor}) \quad (4.29)$$

The equation (4.29) includes the term $\sum_{nb} a_{nb}$, which is unknown and therefore it will be set to zero in the frame of the SIMPLE method [125]. Other pressure correction method (SIMPLEC) assumes that $\sum_{nb} a_{nb} u_{nb}^{cor} \approx \sum_{nb} a_{nb} u_e^{cor}$ in (4.27) to get the equation (4.29).

The solution procedure using the SIMPLE method can be summarized as follows:

1. Guess the pressure p^* (or take it from previous step)
2. Solve the Navier-Stokes equations and get u_i^*
3. Solve the pressure correction p^{cor} (equation (4.28))
4. Correct the velocities and pressure (equations (4.24) and (4.29))
5. Repeat Steps 2-4 till convergence.

4.1.2 Boundary conditions

In view of a good representation of a physical system beside the mathematical model and the numerical scheme, properly chosen boundary conditions are of great importance. The imposition of exact boundary and initial conditions is necessary for a unique solution of the underlying partial differential equations [126]. The boundary conditions are those which are imposed by nature and must be satisfied by every Navier-Stokes fluid. They are at the inlet, outlet, wall, symmetry and periodicity-limit. For transient problems, the initial conditions are also to be defined at the time point $t_o = 0s$.

4.1.2.1 Inlet boundary conditions

The inlet boundary conditions for the velocity components (momentum) as well as other scalar variables like temperature and concentration are set by means of Dirichlet. Turbulent quantities, such as k , Reynolds stress components and ε are normally not known. But they must be estimated or they are measured experimentally. The dissipation is set from the equation [126]:

$$\tilde{\varepsilon} = C_{\mu}^{3/4} \frac{\tilde{k}^{3/2}}{L}. \quad (4.30)$$

Based on isotropic turbulence, L represents a characteristic length scale, often set to 10% of the inlet dimension.

4.1.2.2 Wall boundary conditions

Mean velocity components

The solid boundary conditions used in the code are the von Neumann zero gradient scalars (mixture fraction, variance of mixture fraction, mass fraction). The velocities in grid nodes conjoined with the wall are set equal to the wall movement. In the frame of this work they are set to zero in the tangential as well as in the normal direction, because the wall is fixed (equation (4.31)). This condition is also valid for all turbulent quantities.

$$\tilde{u}_i|_{wall} n_i = 0 \quad \tilde{u}_i|_{wall} t_i = 0 \quad (4.31)$$

In the near wall region a boundary layer is formed and the velocity profile slowly increases until it reaches the outer flow velocity. In order to capture this damping effect, wall functions are applied for the velocity components, the turbulent kinetic energy, Reynolds stress components, and the dissipation rate. For finer grids, the cell height in the region near the wall is sufficiently small that wall functions are not necessary to represent the distributions of velocity, turbulence, energy etc. within the boundary layer that forms adjacent to the hull surface. However, due to large grids and long computing times necessary, it is not practical to use the mesh refining method. The wall function, therefore, prescribes a logarithmic velocity profile within the boundary layer as:

$$U^+ = \frac{1}{\kappa} \ln \frac{u_{\tau} y_w}{\underbrace{\nu}_{y^+}} + B, \quad (4.32)$$

where U^+ represents a dimensionless velocity defined as function of velocity tangential to the wall \tilde{u}^t and the so called dynamic or friction velocity u_{τ} which is calculated as:

$$U^+ = \frac{\tilde{u}_t}{u_{\tau}}; \quad u_{\tau} = \sqrt{\frac{\tau_w}{\rho}} = C_{\mu}^{1/4} \sqrt{\tilde{k}} \quad (4.33):$$

The variable y^+ in equation (4.32) values provide information whether wall functions should be used or not. Generally a limit for $y^+ < 11.63$ is considered for which the wall function method is not applied, otherwise wall functions are used for resolving the boundary layer. κ in equation (4.32) represents the Karman constant and is equal to 0.41, whereas B notes an empirical constant set to 5.2. In the viscous sublayer ($y^+ < 11.63$) the velocity $U^+ = y^+$.

Turbulent kinetic energy

In a turbulent boundary layer the turbulent production and dissipation are presumed to be in local equilibrium (see equation (3.9)):

$$\underbrace{P_k}_{\text{production}} = \underbrace{\bar{\rho}\varepsilon}_{\text{dissipation}}, \quad (4.34)$$

where the production term in the k -transport equation in a fully developed boundary layer is given by:

$$P_k = -\bar{\rho}\tau_{12}^L \frac{\partial \tilde{u}_t}{\partial \zeta_2}. \quad (4.35)$$

The variable τ_{12}^L denotes the local tangential Reynolds stress component in a fully developed turbulent boundary layer. In the viscous sublayer the flow is actually laminar and no turbulent production is present. Strictly speaking the turbulent kinetic energy must be set to zero in this region. On the other hand this can cause problems in the numerical solution resulting in discontinuous distributions of k in the near-wall cells. There is, however, another term, that dominates in the viscous sublayer and be taken instead of turbulent production, namely

$$\frac{\partial}{\partial \zeta_2} \left(\mu \frac{\partial k}{\partial \zeta_2} \right). \quad (4.36)$$

The fact that k itself is zero in the viscous sublayer does not force the spatial derivative of k in the wall normal direction to be zero, too. Thus the turbulent production can be replaced by the molecular diffusion of k and the general form of the production term can be rewritten:

$$P_k = \tau_w \frac{\partial \tilde{u}_t}{\partial \zeta_2}, \quad (4.37)$$

Two different formulations of the wall shear stress τ_w and mean velocity gradient (one for viscous sublayer and the other for the fully developed turbulent layer) are necessary. Following formulations can be derived:

1. Viscous sublayer:

The wall shear stress is given by

$$\tau_w = \bar{\rho}u_\tau^2 = -\mu \frac{\partial \tilde{u}_t}{\partial \zeta_2}. \quad (4.38)$$

4.1 Numerical method for the gas phase

Since for the viscous sublayer $U^+ = y^+$

$$u_\tau^2 = -\frac{\mu}{\bar{\rho}} \frac{\tilde{u}_t}{n_p} \quad (4.39)$$

and, consequently,

$$\tau_w = \frac{\mu \tilde{u}_t}{n_p}. \quad (4.40)$$

The mean velocity gradient that must again satisfy $U^+ = y^+$ is given by

$$\left(\frac{\partial \tilde{u}_t}{\partial \zeta_2} \right)_p = \left[\frac{\partial}{\partial \zeta_2} (u_\tau y^+) \right]_p = \left[\frac{\partial}{\partial \zeta_2} \left(\frac{\bar{\rho} u_\tau \zeta_2}{\mu} \right) \right]_p = \frac{\bar{\rho} u_\tau^2}{\mu} = \frac{\tilde{u}_t}{n_p} \quad (4.41)$$

The production term is then deduced to:

$$(P_k)_p = \mu \left(\frac{\tilde{u}_t}{n_p} \right)^2. \quad (4.42)$$

2. Turbulent layer:

The wall shear stress is given by

$$\tau_w = \bar{\rho} u_\tau^2 \quad (4.43)$$

For the determination of u_τ on the one hand the logarithmic law of the wall

$$U^+ = \frac{1}{\kappa} \ln(y^+ e^{\kappa B}) \quad (4.44)$$

resulting in

$$u_\tau = \frac{\kappa \tilde{u}_t}{\ln(y^+ e^{\kappa B})} \quad (4.45)$$

on the other hand the experimental results of fully developed boundary layer

$$u_\tau = C_\mu^{1/4} \sqrt{\tilde{k}} \quad (4.46)$$

are used. Combining (4.45) and (4.46) in one expression for u_τ^2 the wall shear stress becomes

$$\tau_w = \bar{\rho} C_\mu^{1/4} \sqrt{\tilde{k}} \frac{\kappa \tilde{u}_t}{\ln(y^+ e^{\kappa B})} \quad (4.47)$$

The mean velocity gradient can be expressed in terms of u_τ using the same logarithmic law of the wall [125]:

$$\left(\frac{\partial \tilde{u}_t}{\partial n}\right)_p = \frac{u_{\tau,p}}{\kappa n_p} = \frac{C_\mu^{1/4} \sqrt{\tilde{k}_p}}{\kappa n_p} \quad (4.48)$$

Finally, the production term in the control volume is computed as

$$(P_k)_p = \tau_w \left(\frac{\partial \tilde{u}_t}{\partial n}\right) = \frac{\tilde{u}_t \bar{\rho} C_\mu^{1/4} \tilde{k}_p}{n_p \ln(y^+ e^{\kappa B})} \quad (4.49)$$

The turbulent kinetic energy is a scalar and, thus, a frame independent quantity. The production term calculated using the above formulation is substituted as a source term into the k transport equation in near-wall control volumes without coordinate transformation. The diffusive and convective fluxes through the solid boundary are set to zero. The value of the dissipation rate ε_p is taken directly from its transport equation, the correction of which in near wall cells is given below.

Reynolds stress components

The wall functions formulation in the Reynolds stress transport equations is a little bit more complicated but similar to that in the k transport equation. Not only the production and dissipation but also redistribution terms are present. The idea used here is to derive all three types of terms (production, dissipation and redistribution) for the local coordinate system Reynolds stress tensor components τ_{11}^L , τ_{22}^L , τ_{33}^L and τ_{12}^L , transform them into the Cartesian coordinate system and substitute into the corresponding transport equations. Consider three terms on the right hand side of the Reynolds stress transport equation which are significant in the turbulent boundary layer – production, dissipation and redistribution (pressure fluctuation) term. Applying assumptions made above these terms can be reduced to the following form (here the linear modeling form of the pressure-strain correlation adopted by Jones [103] is used):

$$S_{11}^L = -2\bar{\rho}\tau_{12}^L \frac{\partial \tilde{u}_t}{\partial n} + \bar{\rho} \left(c_1 \tilde{\varepsilon} \left(\frac{\tau_{11}^L}{\tilde{k}} - \frac{2}{3} \right) - c_2 \tau_{12}^L \frac{\partial \tilde{u}_t}{\partial n} - c_3 2\tau_{12}^L \frac{\partial \tilde{u}_t}{\partial n} \right) - \frac{2}{3} \bar{\rho} \tilde{\varepsilon} \quad (4.50)$$

$$S_{22}^L = \bar{\rho} \left(c_1 \tilde{\varepsilon} \left(\frac{\tau_{22}^L}{\tilde{k}} - \frac{2}{3} \right) - c_2 \tau_{12}^L \frac{\partial \tilde{u}_t}{\partial n} + \left(\frac{2}{3} c_2 + c_3 \right) 2\tau_{12}^L \frac{\partial \tilde{u}_t}{\partial n} \right) - \frac{2}{3} \bar{\rho} \tilde{\varepsilon} \quad (4.51)$$

$$S_{33}^L = \bar{\rho} \left(c_1 \tilde{\varepsilon} \left(\frac{\tau_{33}^L}{\tilde{k}} - \frac{2}{3} \right) - c_2 \tau_{12}^L \frac{\partial \tilde{u}_t}{\partial n} \right) - \frac{2}{3} \bar{\rho} \tilde{\varepsilon} \quad (4.52)$$

$$S_{12}^L = -\bar{\rho}\tau_{12}^L \frac{\partial \tilde{u}_t}{\partial n} + \bar{\rho} \left(c_1 \tilde{\varepsilon} \left(\frac{\tau_{22}^L}{\tilde{k}} - \frac{2}{3} \right) - c_2 \tau_{12}^L \frac{\partial \tilde{u}_t}{\partial n} + \left(\frac{2}{3} c_2 + c_3 \right) 2\tau_{12}^L \frac{\partial \tilde{u}_t}{\partial n} \right) \quad (4.53)$$

Here, S_{11}^L , S_{22}^L , S_{33}^L and S_{12}^L represent the source terms for the local Reynolds stress components τ_{11}^L , τ_{22}^L , τ_{33}^L and τ_{12}^L respectively. The mean velocity gradient in the wall normal direction is calculated in the same manner as

4.1 Numerical method for the gas phase

for the turbulent kinetic energy equation. All local Reynolds stress components can be directly transformed from the known Cartesian ones.

Dissipation rate

As mentioned above it is assumed that a local equilibrium is reached between the production and the dissipation of the turbulent kinetic energy. Therefore, the ε equation is not solved in the CV next to the wall. Instead the value of ε in the CV central point is set to

$$\varepsilon_p = \frac{C_\mu^{3/4} \tilde{k}_p^{3/2}}{\kappa n_p} \quad (4.54)$$

For the derivation of this formula the same strategy is applied as for the production term for k except no logarithmic law of the wall, but only experimental results for the fully developed boundary layer are used for the determination of the dynamic velocity u_τ because the logarithmic law of the wall has been already utilized by the formulation of production term.

4.1.2.3 Symmetry boundary conditions

Symmetry boundaries can be used to reduce the size of the problem. If we know that there is a plane where the flow field is symmetric then instead of simulating the whole configuration, we can set the appropriate boundary conditions and reduce the problem size. The symmetry boundary conditions are set as follows:

$$\frac{\partial \psi}{\partial n} = 0, \quad \psi = \left(\tilde{u}, \tilde{u}_i \tilde{u}_j \Big|_{i=j}, \tilde{\varepsilon}, \tilde{p}^c, \tilde{\rho}, \tilde{z}, \tilde{z}^2, \tilde{y} \right) \quad (4.55)$$

$$\psi = 0, \quad \psi = \left(\tilde{v}, \tilde{w}, \tilde{u}_i \tilde{u}_j \Big|_{i \neq j} \right), \quad (4.56)$$

where n is the direction normal to the symmetry plane.

4.1.2.4 Periodic boundary conditions

The periodic boundary conditions (between boundary I and II) make the variables at the *boundary I* equal the variables at the *boundary II* conforming to the following equation.

$$\psi(\vec{r}) = \psi(\vec{r} + \vec{L}), \quad (4.57)$$

where \vec{r} is the position vector and \vec{L} is the periodic length vector of the domain considered. The periodic boundary condition corresponds to zero flux. Making the boundaries periodic, this will make the inflow through one of the boundaries equal the outflow through the other.

4.1.3 Solvers

Solution of the linear equation system

The discretization of the governing equations summarized in section by means of the finite volume procedure explained in section results in a system of linear algebraic equations each having a form. This system can be written in matrix notation as

$$A\underline{\Psi} = \underline{S} \quad (4.58)$$

where A is the square coefficient matrix built from the coefficients of the linear equations (4.3) for each CV, $\underline{\Psi}$ is a vector containing the values of the variable Ψ in each CV and \underline{S} is the vector containing the terms on the RHS of (4.3)

The system (4.58) has to be solved by means of an efficient solution method. The coefficient matrix A resulting from (4.3) is sparse, i.e. most of its elements are zero and the non-zero elements lie on a small number of well-defined diagonals (in FASTEST-3D seven diagonals). Advantage should be taken from this structure. Since direct methods like Gauss elimination or LU decomposition do not take this advantage, being quite costly, and since discretization errors are normally much larger than the computer accuracy, there is a clear reason to apply an iterative method. Furthermore, the fully implicitly discretized momentum equations are actually non-linear and can not be solved by means of a direct method. The details of their linearization are discussed in the following section. In an iterative method some initial solution is guessed and then systematically improved. One would have after n iterations an approximate solution of (4.58), $\underline{\Psi}^n$, that is not the exact one. The non-zero residual vector \underline{r}^n (a difference between the left and the right hand side of (4.58)) satisfies the expression

$$A\underline{\Psi}^n = \underline{S} - \underline{r}^n. \quad (4.59)$$

An iterative scheme for the linear system, that should drive the residual to zero, can be written as

$$M(\underline{\Psi}^{n+1} - \underline{\Psi}^n) = B - (M - N)\underline{\Psi}^n \quad (4.60)$$

or

$$M\underline{\delta}^n = \underline{r}^n \quad (4.61)$$

Here, $\underline{\delta}^n = \underline{\Psi}^{n+1} - \underline{\Psi}^n$ is the correction vector which is simultaneously an approximation to the convergence error. Once the computation of $N\underline{\Psi}^n$ is inexpensive and the solution of (4.60) converges rapidly the optimal iterative method is found. For rapid convergence in the solution of (4.60) the matrix M must be as good an approximation to A as possible. For that purpose the *strongly implicit procedure* (SIP), originally proposed by Stone [102] and further developed for the seven diagonal coefficient

4.1 Numerical method for the gas phase

matrix by Leister and Peric [104], is applied in FASTEST-3D. In this method the matrix M is chosen to be equal to the incomplete LU decomposition (ILU):

$$M = LU = A + N. \quad (4.62)$$

In the ILU decomposition the procedure is the same as in standard LU factorization. But for each zero element of the original matrix A a corresponding element of the lower triangular matrix L or the upper triangular matrix U is set to zero too. Even though L and U have the non-zero elements only on the same diagonals as $A(W, E, S, N, B, T, P)$, their product LU has additional non-zero diagonals (SE, NW etc.). Stone [102] found that convergence can be improved by allowing N to have non-zero elements on the diagonals corresponding to all non-zero diagonals of LU . The elements of the matrix N must be defined so that the elements of vector $N\underline{\Psi} \approx 0$ and that the matrix M to be the best approximation to A . This means that the contribution of the terms on the 'additional' diagonals (SE, NW etc.) in N must be nearly cancelled by the contribution of other diagonals (W, E, S, N, B, T, P). Expecting the solution of the elliptic partial differential equations to be smooth, Stone [102] approximated the unknown function values in 'additional' nodes in terms of the known function values at nodes corresponding to the diagonals of A .

Finally, one proceeds as follows. Having a matrix A the elements of N can be found. The elements of M , which are the sum of A and N , do not need to be computed. Instead, the elements of L and U are found in sequential order for the given A and N . Once the elements of L and U are known, the *inner iterations* begin. The system (4.61) can be rewritten as

$$LU\underline{\delta}^n = \underline{r}^n \quad (4.63)$$

or

$$U\underline{\delta}^n = L^{-1}\underline{r}^n = \underline{R}^n. \quad (4.64)$$

Using the advantage of LU decomposition the elements of the vector \underline{R}^n are computed first using (4.64) by marching in the order of increasing CV's index (*forward substitution*). Then the elements of the correction vector $\underline{\delta}^n$ are calculated by marching in the order of decreasing CV's index (*backward substitution*). In addition to that the variable values in the CVs are updated following $\underline{\Psi}^{n+1} + \underline{\Psi}^n = \underline{\delta}^n$. The iterations proceed until the sum over all elements of the residual vector \underline{r}^n becomes lower than some given tolerance.

Solution of steady and unsteady problems

In steady computations a steady state solution of the governing equation system is sought. In this case the time history is of no interest. One can either neglect the unsteady terms in the governing equations or iterate

until the steady equations are satisfied, or march in time without requiring full satisfaction of the equations at each time step.

The iterations within one time step or during steady computations, in which the coefficient matrices and source vectors in (4.3) are updated, are called *outer iterations* in order to distinguish them from the *inner iterations* performed on the linear systems (4.3) with fixed coefficients (in the SIP solver).

The changes in variables after each outer iteration may be significant and particularly at the beginning where they may cause instabilities. In order to reduce this effect the under-relaxation of the variables is applied:

$$\psi^m = \psi^{m-1} + \alpha_\psi (\psi^m - \psi^{m-1}) \quad (4.65)$$

where ψ^m and ψ^{m-1} are the values of the variable ψ after m -th and $(m-1)$ st outer iteration, ψ^{new} is the result of solution of equation (4.3) and the under-relaxation factor α_ψ satisfies $0 < \alpha_\psi \leq 1$.

In unsteady computations (URANS) the time accuracy is required in order to resolve in time e.g. some periodical process. In this case the iterations must be continued within each time step until the entire system of the governing equations is satisfied to within a narrow tolerance.

4.2 Numerical method for the dispersed phase

4.2.1 Solving the equation of motion and time discretization

Since equation (2.40) is ordinary differential equation, it can be solved by using classical numerical methods such as Euler's forward integration method [126]:

$$x_i^{n+1} = x_i^n + \Delta t u_{d,i}^n, \quad (4.66)$$

$$u_{d,i}^{n+1} = u_{d,i}^n + \frac{\Delta t}{m_d} \sum F_i^n, \quad (4.67)$$

where x_i and $u_{d,i}$ denote the parcel location and velocity component respectively. From one given time point (t_n), it is possible to find the next point at a given time step (t_{n+1}) along the same streamline and thus tracking the whole line. The Euler's forward method is fast but strongly depends on the quality of the initial velocity field. In some situations, it may lead to spirals. Then, additional stopping conditions must be added to avoid such situations. Moreover, in zones where the velocity orientation changes, the streamline presents a high curvature and its trajectory is not

4.2 Numerical method for the dispersed phase

necessarily parallel to the initial velocity field. The Euler's method is a simple approach to implement. However, it has a low accuracy, as it is a first order method. If one wishes to compute very accurate solutions or solutions that are accurate over a long interval, then Euler's method (used for the dispersed phase in this work – equation (2.40)-) requires a large number of small steps. (accuracy $\sim dt$), but thus one renders the simulation time impractically long.

Other time integration methods often used in literature are Runge Kutta method [126] and the backward Euler method [126], which are implicit. These methods require the resolution of a linear system per iteration, as well as the storage of the system state added to those required for the system resolution algorithm. These methods are supposed to provide approximate results that are not subject to numerical instability as the time step is increased [126].

As mentioned above, time steps within Euler's forward method, are limited by the conditions for physical processes and numerical stability according the next equation:

$$\Delta t = 0.1 \min(\tau_p, T_E, T_W, T_{CV}), \quad (4.68)$$

where τ_p denotes the particle relaxation time, defined in section 2.3.2, and T_E is the turbulent integral time scale

$$T_E = c_T \frac{k}{\varepsilon}. \quad (4.69)$$

The variable T_W is the time required by a parcel to traverse a turbulent eddy

$$T_W = \frac{L_E}{|\vec{u} - \vec{u}_d|}, \quad \left(L_E = T_E \sqrt{\frac{2}{3} k} \right), \quad (4.70)$$

and the variable T_{CV} represents the time taken by a parcel to cross the entire control volume.

$$T_{CV} = \frac{\Delta x_i}{|u_{d_i}|} \quad (4.71)$$

4.2.2 Statistical sampling

Similarly to the Eulerian part where equations averaged for flow quantities (velocity, mass fraction, temperature, etc) are solved, in the Lagrangian part momentaneous quantities are to be sampled and averaged. Mean values and variances of droplet characteristic variables (velocity components, diameter, temperature, etc.) are evaluated in each cell according to [93]:

$$\overline{\phi_d} = \frac{\sum_{k=1}^{K_d} \left(\sum_{n=1}^{N_{CV}} \phi_{d,i,j,k} N_{d,k} \right)}{\sum_{k=1}^{K_d} N_{CV}} \quad (4.72)$$

$$\overline{(\phi_d)'}^2 = \frac{\sum_{k=1}^{K_d} \left(\sum_{n=1}^{N_{CV}} \phi_{d,i,j,k}^2 N_{d,k} \right)}{\sum_{k=1}^{K_d} N_{CV}} - \left(\overline{\phi_d} \right)^2 \quad (4.73)$$

where K_d is the total number of numerical droplets in a considered cell, N_{CV} represents the number of time steps which a droplet needs while crossing the cell and $N_{d,k}$ is the number of real particles represented by a numerical one.

One should mention here that the total number of particles/droplets within a control volume represents an important factor for the accuracy of statistics of dispersed phase properties. In order to secure smooth distribution of results, the variables $N_{d,k}$ is desired not to exceed 10^3 , as pointed out by [93]. Nevertheless, regions where particles/droplets are not able to reach, due to high shear flow or due to total evaporation, are characterized by non-uniform properties profiles.

The particles/droplets mass concentration within a control volume is computed in the following way:

$$\sigma_d = \sum_{k=1}^{K_d} \left(\sum_{n=1}^{N_{CV}} \frac{m_d N_{d,k}}{\vec{u}_{d,k} \Delta A_j \Delta t_{in}} \right), \quad (4.74)$$

where ΔA_j denoted the cross section area of the considered control volume, Δt_{in} represents a reference time, which specifies the droplets/particles mass flow at the boundary conditions.

4.3 Eulerian-Lagrangian coupling

The Eulerian and Lagrangian equations need to be coupled in order to achieve a numerical solution for multiphase flows. The coupling between continuous and dispersed phases is performed by interchanging flow properties and particles source terms between FASTEST (fluid) and LAG3D (particles/droplets). FASTEST is used to solve the gas phase (see section 4.1), whereas LAG3D is the Lagrangian solver used for the dispersed phase. Different types of E-L coupling can be performed (e.g. steady or unsteady coupling).

4.3.1 Steady state coupling

Figure 4.5 shows the numerical computing procedure, for a steady state problem, in the frame of Eulerian/Lagrangian approach. Such a coupling is achieved through the following 4 steps [93]:

1. Computation of the gas phase till convergence of the steady problem. The particles/droplets source terms are not accounted for.
2. The dispersed phase is tracked in the Lagrangian frame and the particles/droplets source terms are computed for all flow variables in every control volume.
3. Computation of the gas phase under consideration of source terms calculated in step number 2. The first coupling (consideration of source terms) is generally very challenging and a convergence of the carrier phase is often difficult to accomplish. It is therefore some time recommended not to consider 100 % of the source terms value but to under relaxate them to 50 %. (equation 4.68)
4. Track the dispersed phase and compute the new source terms. Steps 2 and 3 are to repeat till convergence of the Eulerian/Lagrangian approach.

The issue of convergence of the Eulerian - Lagrangian coupling has been debated in many papers [44]. It turns out that there are several aspects related to the definition of numerical convergence for multiphase flows, so that selecting proper relaxation and convergence criteria can be difficult for multiphase flows. Being solved, the criteria that depend on the specifics of the problem may change during the evolution of a problem. Unfortunately, there are no universal guidelines for selecting criteria because they depend not only on the physical processes being approximated, but also on the details of the numerical formulation. As an example, one can mention the normalized residual method, as it is used for single phase flow. Nevertheless, this criterion is not appropriated for multiphase. The principal reason is thereby related to the stochastic nature of the Lagrangian procedure and the associated sources terms fluctuations within every coupling between both phases. These fluctuations, as mentioned above, depend naturally strongly on the spatial smoothness of particles/droplets source terms distributions.

In the frame of this work, the convergence of Eulerian-Lagrangian coupling procedure is reached when the fluid properties in the presence of particles/droplets do not change their value from one coupling to the next. The convergence of the Eulerian-Lagrangian coupling is sensitive to the considered total number of the numerical particles/droplets. Computations using high particles/droplets number provide reliable statistical source terms (see equation 4.65-4.67), which in turn enable to get overall fast convergence. On the other side more particles means more computation time for the Lagrangian part.

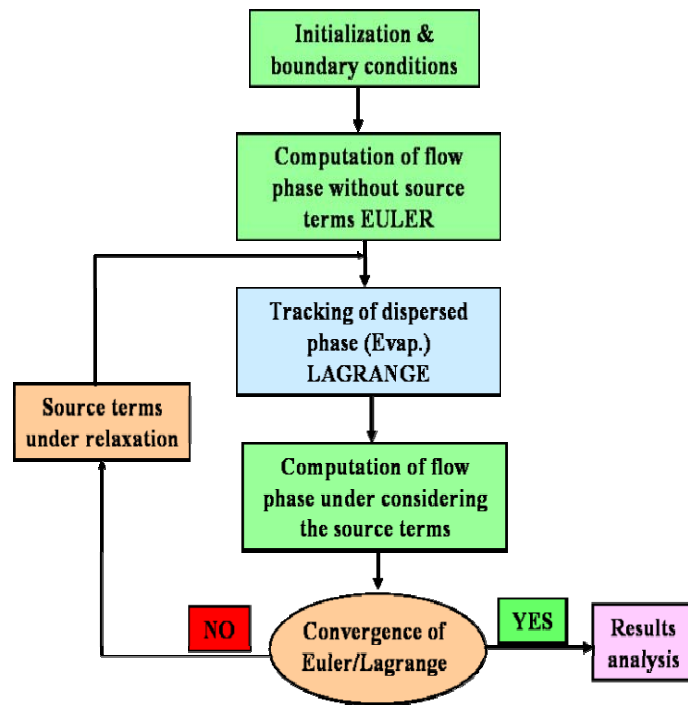


Figure 4.5: Diagram for the numerical coupling between the continuous and dispersed phases in the frame of Eulerian/Lagrangian approach

4.3.2 Under-relaxations of source terms

Numerical methods used to solve the equations for fluid flow and particles/droplets evolution most often employ more iteration procedures which require a criterion that is used to decide when the iterations can be terminated. In many cases, iteration methods are supplemented with relaxation techniques. For example, over relaxation is often used to accelerate the convergence of iteration methods. Under-relaxation is sometimes used to achieve numerically stable results. Kohnen [44] showed in his work that it is mandatory to use under-relaxation factors for the particles/droplets source terms which are introduced in the transport equations of the gas phase.

The under-relaxation of particles/droplets source terms is accounted for using the following expression:

$$S_{\phi,p(\text{considered})}^{i+1} = \alpha S_{\phi,p}^{i+1} + (1-\alpha)S_{\phi,p}^i . \quad (4.75)$$

Here $S_{\phi,p}^{i+1}$ denotes the new computed particles/droplets source terms within the iteration $(i+1)$, whereas $S_{\phi,p}^i$ is the old source terms (previous iteration) and $S_{\phi,p(\text{considered})}^{i+1}$ the source terms account for the carrier phase.

4.3 Eulerian-Lagrangian coupling

The variable α denotes the under-relaxation factor, which vary between zero and one. It is user defined and can not influence the numerical results once convergence reached.

The goal of introducing under-relaxation factors is to enhance the numerical stability and to accelerate the convergence of the Eulerian-Lagrangian coupling. Sommerfeld [93] mentioned that an under-relaxation factor of 0.1 was required for his work to achieve a stable numerical computation and that the total Eulerian-Lagrangian coupling was between 30 and 50 iterations. The experience made within this thesis shows that under-relaxation factors may attain value of 0.8 without affecting the stability of coupling whereas the total number of Eulerian-Lagrangian procedures varies between 12 and 20 iterations.

5 Models validation

This chapter features the configuration as well as the experimental data used to validate different modulation models introduced in chapter 3.2. The experimental results were obtained by the measurement in single- and two-phase flows. Autocorrelation functions were represented in the form of autocorrelation coefficients that made possible direct comparisons between different flows. Details of the experimental setup (see Figure 1.1) can be found in Geiss [120]. The experimental data concerning turbulent kinetic energy were considered as a key quantity to highlight the differences between all used models for the description of the turbulence modulation.

5.1 Configuration and numerical Set up

The configuration consists of a vertical closed wind-tunnel using air as a continuous (carrier) phase and mono-dispersed, non-evaporating particles with diameters ranging from 120 to 480 μm (as dispersed phase) that are seeded to the flow. The used particles are hallow, manufactured from glass which features a good refraction index. They have a density of 2500 kg/m^3 .

The turbulent flow was generated by the means of a turbulence-generating grid having a mesh grid size: $M=12$ mm. According to [121], the system generates a locally isotropic flow behind the grid. The cross-section of the configuration has dimension of 0.2 by 0.2 m (see Figure 5.1). It was assumed that these dimensions guarantee that the flow around the centerline of the test section will be free from influences coming from the walls and boundary layer. This assumption was confirmed by the measurements of radial profiles of the axial velocity of the continuous phase as shown in [121]. The vertical channel (test section) was made of glass plates that provide optical access from two sides of the test section. The latter made the use of Phase-Doppler Anemometry (PDA) possible by allowing for simultaneous measurements of mean velocities and higher moments for both phases, as well as particle diameters. Particle concentration measurements were performed by conventional probe (patternator) techniques [121].

Grid independent solutions are necessary to minimize numerical errors (particularly numerical diffusion) so that the performance assessment of mathematical models can be done appropriately. It is difficult to obtain grid independent solutions with first order (upwind) methods. Therefore the flux blending differencing scheme with $\gamma=0.8$ was applied within this configuration. Grid independent solutions are obtained for mesh that was

5.1 Configuration and numerical Set up

sufficiently refined (74 x 34 x 34 cells in vertical (x-axis), transversal (y) and longitudinal (z) directions, respectively).

The flow conditions for carrier and dispersed phases, which were taken from experimental data are presented in the following section.

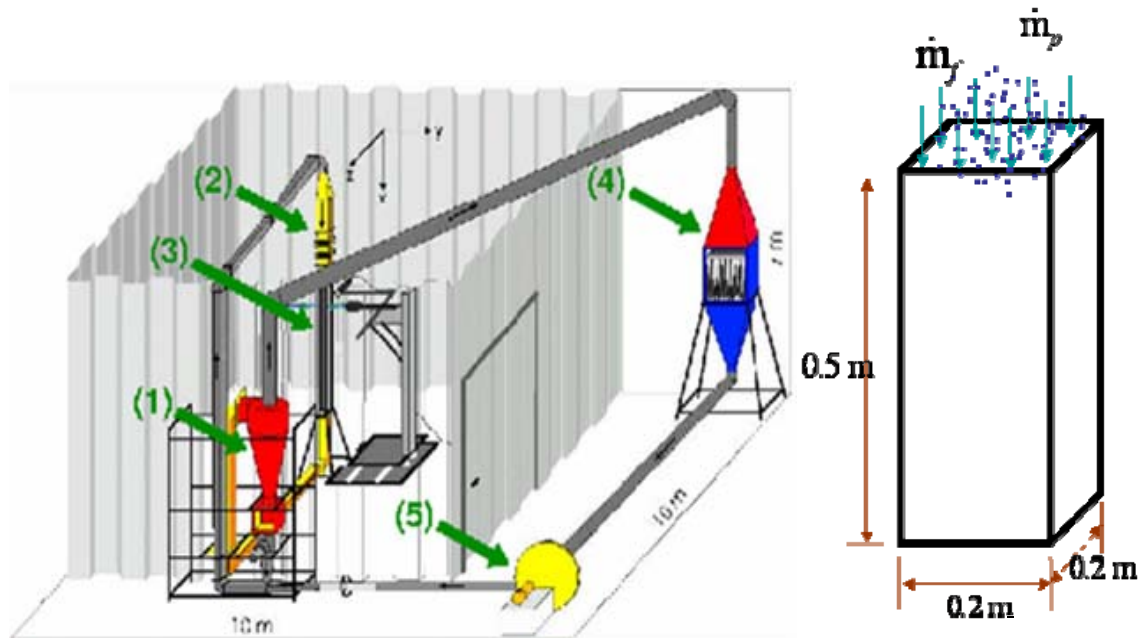


Figure 5.1: Particle-laden vertical channel flow; Left: experimental set up (1 – dosage sluice, 2 – contraction and turbulence generating grid, 3 – cyclone, 4 – filter section, 5 – blower); Right: Computational domain

5.2 Flow conditions

The mean velocity of the continuous phase (without particles) equals 10 m/s, the kinematic viscosity of air is $1.5 \cdot 10^{-5} \text{ m}^2 / \text{s}$ and the half-width of the test section equals 0.1 m. Upon these values, the Reynolds number corresponds to 66667.

The turbulence-generating grid (M=12 mm) provides a fluctuation of the gas phase corresponding to a turbulent kinetic energy about $0.735 \text{ m}^2 / \text{s}^3$. The measured dissipation rate of turbulent kinetic energy is $110.00 \text{ m}^2 / \text{s}^3$.

The particles used within this configuration have three different diameter sizes [120]: $D_p = 120 \mu\text{m}$, $D_p = 240 \mu\text{m}$, $D_p = 480 \mu\text{m}$

The particles were assumed to be spherical and monodisperse. The volume fractions of the different test cases are summarized in Table 5.1. Values presented in this table refer to all results for the axial profiles of the turbulent kinetic energy.

D_p	Volume fraction
$120\mu m$	$8.5 \cdot 10^{-5}$
$240\mu m$	$6.1 \cdot 10^{-4}$
$480\mu m$	$4.1 \cdot 10^{-4}$

Table 5.1: Volume fraction of the dispersed phase

According to Geiss [120], the Kolmogorov length scale of the flow was assumed to be equal to $100\mu m$. It is interesting to analyze two-phase flows with particles having size around the Kolmogorov length scale and others having diameter of an order of bigger magnitude. Geiss also mentioned also in his thesis [120]. that a careful study of axial profiles of the turbulent kinetic energy in the measurements of the flows with $240\mu m$ reveals a very little turbulence augmentation, whereas with $480\mu m$ the turbulence augmentation is very intensive. Therefore, only the effect of particles having $D_p = 120\mu m$ and $D_p = 480\mu m$ will be numerically investigated.

The flow conditions for the carrier phase (gas phase with particles) are given in Table 5.2

$D_p [\mu m]$	120	480
$u [m/s]$	10.00	10.00
$v [m/s]$	0.00	0.00
$w [m/s]$	0.00	0.00
$k [m^2/s^2]$	0.56	1.68
$\varepsilon [m^2/s^3]$	110.00	110.00

Table 5.2: Flow conditions of the carrier phase for measurements with 120 and $480\mu m$

For the dispersed phase, the three velocity components and the corresponding fluctuations are given in Table 5.3.

5.2 Flow conditions

D_p [μm]	120	480
u_p [m/s]	8.40	5.00
v_p [m/s]	0.00	0.00
w_p [m/s]	0.00	0.00
u'_p [m/s]	1.00	1.20
v'_p [m/s]	0.98	1.25
w'_p [m/s]	0.98	1.25

Table 5.3: Particle velocity components at the inlet and the corresponding fluctuations for test cases with diameter 120 and 480 μm

5.3 Results and discussions

In the following, results of simulations performed for turbulent two-phase flows with particles having diameters equal to 120 and 480 μm and volume fraction as introduced in the previous section will be shown. Focus is put on the profiles of the turbulent kinetic energy in order to gain information about the turbulence modulation.

The numerical work has been achieved using three modulation models (standard approach, Crowe model and the thermodynamically consistent model as they were introduced in chapter 3) in order to investigate the dissipation and production of turbulence energy caused by particles in continuous phase.

First computations are carried out without taking into consideration the dispersed phase in order to quantify the agreement between experimental results and numerical simulation. Then, the turbulent kinetic energy will be computed using modulation models (mentioned above). Results are compared respectively with experimental data as well as with these of the gas phase. In all figures x/M represents the distance from the turbulence generating grid divided by the grid width and the measurements shown are taken on the channel centerline.

5.3.1 Standard modulation model

The effect of the continuous phase on the turbulence properties is more complex. From the experimental side, one observes that, for the 120 μm

particles the initial turbulent kinetic energy at $x/M = 10$ (boundary conditions (see Table 5.2)) is reduced by approximately 25%. The decay curve is not however changed by the presence of $120 \mu\text{m}$ particles. This indicates compensation between additional particle-induced dissipation and production of turbulence (Figure 5.2).

For mean particle diameters of $480 \mu\text{m}$ the initial value of turbulent kinetic energy of the continuous phase is increased by approximately a factor of two (see Table 5.2). A much weaker decay of continuous phase turbulence is observed (Figure 5.3). Consequently, particle-induced turbulence production clearly overbalances dissipation. This results in a particle-induced increase of turbulent kinetic energy by a factor of ten at $x/M = 50$ showing the importance of turbulence modification especially for these conditions.

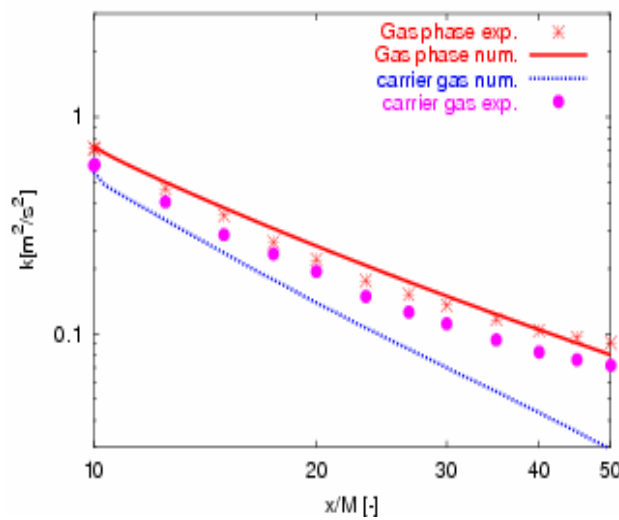


Figure 5.2: Dissipation of turbulence (particle diameter $d=120 \mu\text{m}$)

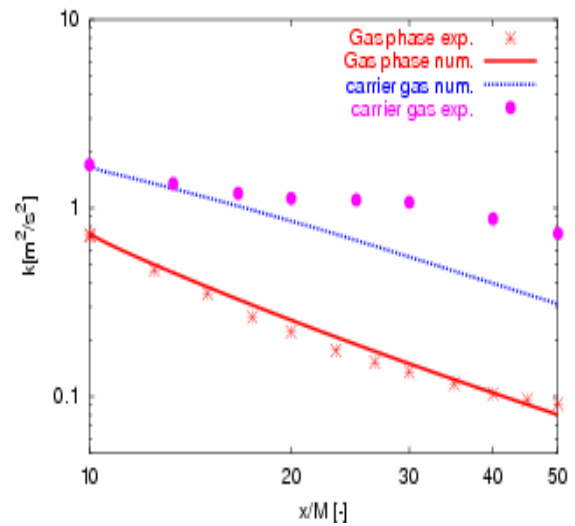


Figure 5.3: Dissipation of turbulence (particle diameter $d=480 \mu\text{m}$)

Figure 5.2 and Figure 5.3 show the influence of dispersed phase diameter distribution on the turbulence properties of the continuous phase resulting from the standard modulation model [92]. Differences in properties of the turbulent kinetic energy are clearly observed. The decay of the dispersed phase turbulence is however, distinctive from small particles of $120 \mu\text{m}$, whereas for particles of $480 \mu\text{m}$ a much less pronounced decay is observed. The particle relaxation time τ_p varies between 0.11 and 1.56 sec for the respective mean particle sizes of 120 and $480 \mu\text{m}$ which imply that big particles respond slowly to velocity modifications. Unfortunately they generate, numerically, dissipation of turbulence. Stokes numbers range between 2.75 and 41.05 for both diameters, so this corresponds well to the diagram presented in Figure 1.1. The standard modulation model, as observed in Figure 5.2 and Figure 5.3 dissipate turbulent kinetic energy for both particles of $120 \mu\text{m}$ and $480 \mu\text{m}$ diameters.

5.3.2 Crowe modulation model

Figure 5.4 and Figure 5.5 show a clear discrepancy between the experimental data and the numerical simulation for the flow with both particles (120 and 480 μm). The trend between x/M equal to 10 and 15 is correctly predicted, but the values of turbulent kinetic energy at the positions in the range of x/M from 15 to 50 are over-predicted by the simulation. The modulation model by Crowe [87] is productive. It is necessary to remark that the boundary conditions are exactly the same for all three simulations of each particle diameters class. Therefore, a quantitative estimation of the effect of the different modeling approaches on the gas turbulent quantities can be well evaluated.

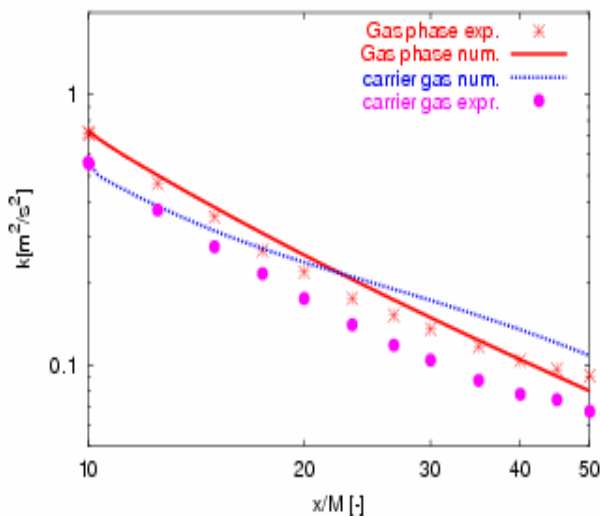


Figure 5.4: Production of turbulence (particle diameter $d=120 \mu\text{m}$)

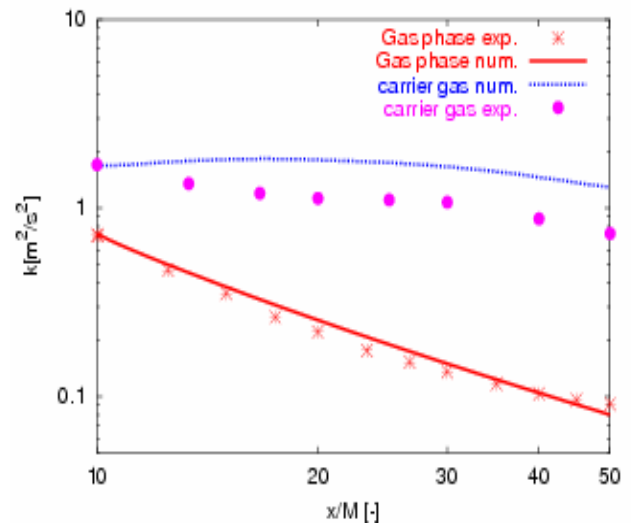


Figure 5.5: Production of turbulence (particle diameter $d=480 \mu\text{m}$)

5.3.3 Thermodynamically consistent modulation model

Figure 5.6 and Figure 5.7 exhibit very good agreement between results obtained using the thermodynamically consistent model [35] and experiment. Particles with diameters 120 μm show turbulence dissipation, whereas particles having diameters 480 μm show augmentation of turbulent kinetic energy.

In the case without particle loading, a very good agreement between experimental and numerical data can be seen. As expected, a decrease and increase of turbulence energy arising from small and big particles are represented by the model by Sadiki and Ahmadi. The suitability in estimating energy production and depletion distinguishes the model of Sadiki & Ahmadi as an appropriate choice for modeling of the turbulence

interaction in turbulent two-phase flows. In the calculations, a value $\beta = 0.5$ in (3.39) has been found to be suitable for this configuration. It must be mentioned that expression (3.40) allows a dynamic determination of the β value. Thereby the variable α' in (3.40) is known using specific particle/droplet properties. In this case, an expression for this variable (α') can be found in [86], making the parameter β configuration dependent. This consideration has not however, been achieved within this thesis.

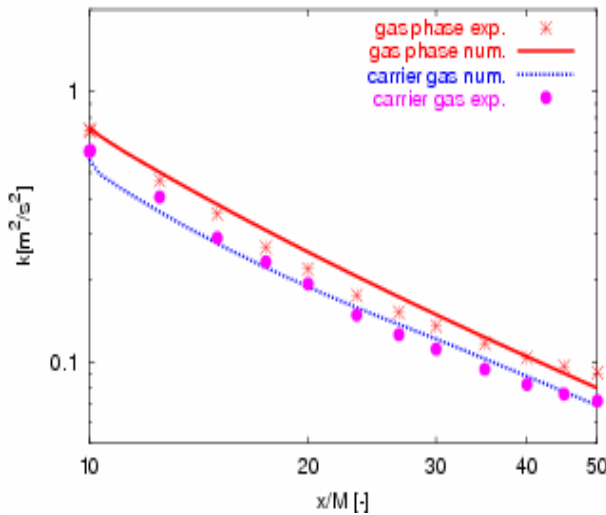


Figure 5.6: Dissipation of turbulence (particle diameter $d=120 \mu\text{m}$)

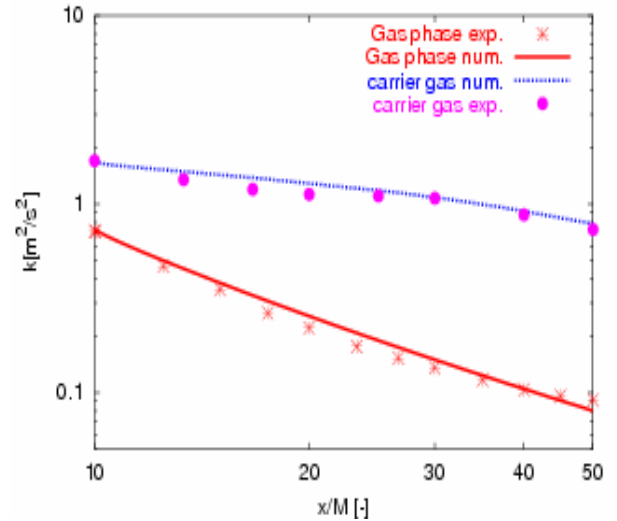


Figure 5.7: Production of turbulence (particle diameter $d=480 \mu\text{m}$)

5.3.4 Particle fluctuations

Figure 5.8 shows the profile of the turbulent kinetic energy for the dispersed phase. At $x/M = 10$ a slight increase of turbulent kinetic energy is apparent. This increase is believed to be due to the particle-grid interaction that is not investigated in this study. The decay of the dispersed phase turbulence is however, distinctive from small particles of $120 \mu\text{m}$. This effect is due to the particle relaxation time τ_p [122]. On the other hand, the differences between experimental and numerical, observed in the profile of the particle kinetic energy, may be originated on the dispersion model, which does not account for the drift term presented in equations (3.50)-(3.52). The drift correction term may attenuate the velocity fluctuation of the gas phase seen by the particles. Additionally, the boundary conditions for the dispersed phase are experimentally very difficult to capture as well as numerically to establish. Therefore, the over prediction of the particle kinetic energy seen in Figure 5.8 may be due to the inlet conditions. The statistics for the properties of the dispersed phase were performed based only on 20,000 trajectories. Therefore one observes no smooth distribution in the curve of the particles turbulent kinetic energy. In order to get smooth curves the total number of particles

should be increased. The particle diameter distribution has not been shown, since the test case dealt with monodisperse phase. As the mean velocities of the carrier phase have been analyzed, results have shown good agreements with experimental data. Particles properties will be analyzed in details within a swirled flow in more complex configuration, as it will be presented in the next chapter.

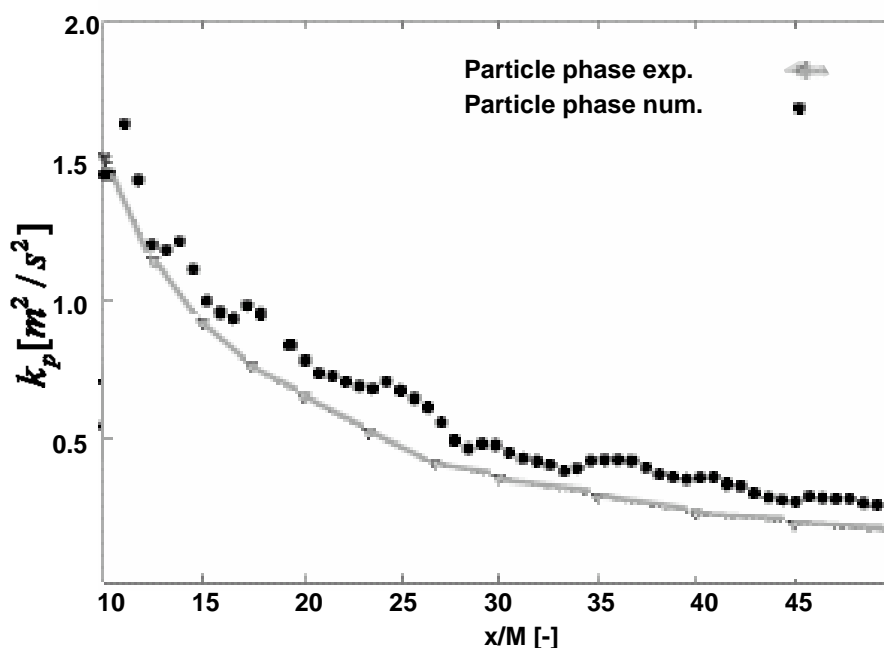


Figure 5.8: Turbulent kinetic energy of the dispersed phase (120 μm) along the channel center line

5.3.5 Some remarks

The present chapter features an investigation of the feedback mechanism of a dispersed on a continuous phase in a turbulent two-phase flow known as turbulence modulation. For this purpose air as continuous and glass beads as dispersed phase have been employed. A vertical orientated wind-tunnel was used to create and study the modification of turbulence without taking care about anisotropy or wall influence.

The numerical work performed with three different modulation models reveals that the obtained results of the turbulent kinetic energy, along the channel center line, using the thermodynamically consistent model accounts better for both the turbulence attenuation and production caused by the presence of small and big particles in the gas phase, respectively. The standard model underestimates the turbulence and features a dissipative behavior either for small (120 μm) or for big (480 μm) particles. In contrast, the model by Crowe is usually productive.

The particle turbulent kinetic energy is over-predicted compared to the experimental data and the profile exhibits no smooth distribution. In order to evade these weaknesses for the following configurations, the total number of particles will be increased and a drift contribution for the dispersion model will be included.

6 Applications

In this chapter applications of the complete model for the simulation of turbulent spray evaporation and subsequently spray combustion are presented and discussed. The different sub-models should reproduce all accruing non-linear physical effects in multi-phase reacting flow. In fact, turbulence influences droplet motions, droplet motions influence turbulence, turbulence influences droplet vaporization rate, droplet evaporation rate influences flame structure, flame structure influences turbulence and evaporation rate.

The systematical model assessment should include computations and comparisons of numerical results to experimental data in different configurations of various complexities. For that reason three different configurations will be simulated. The combination of different sub-models used within three configurations is summarized in Table 6.1.

			Config. I	Config. II	Config. III
Sub-models	Turbulence	k- ϵ	X	X	X
		RSM		X	X
	Turbulence modulation	Standard	X	X	X
		Crowe			
		Thermody. consistent	X		X
	Evaporation	UTM (equi.)		X	X
		Non-equi.		X	X
	Combustion	Equilibrium		X	X
		Flamelet			X

Table 6.1: Model combinations used for the simulations

The first configuration consists of a swirling particulate two-phase flow in a model combustion chamber. It is designed to produce the classical recirculating flow conditions typically observed in gas turbine combustors.

In the second one, which consists of a spray issuing into a co-flowing heated air-stream, we aim to investigate the different evaporation models and the influence of turbulence intensity on the vaporization rate. One key issue within this configuration is to characterize the interaction regimes between turbulence and evaporation processes. The contribution of the drift term effect on the mass and heat transfer will be also pointed out within this configuration.

Finally, an industrial combustion chamber (BR 710) by Rolls-Royce is presented as practical configuration. It contains multiple recirculation zones and different inlet conditions, as well as spray evaporation and subsequent combustion.

6.1 Isothermal swirling particulate two-phase flow

In this section we aim at studying the influence of swirled co-flow on the behavior of dispersed phase such as particle dispersion, velocities and fluctuations of the two-phase flow. For this purpose we choose the configuration, represented in Figure 6.1, as experimentally investigated by Sommerfeld et al. (1991) [124]. It consists of a vertical test section with a downward flow, which is injected to the main chamber from the top. Upon entering the chamber the flow undergoes a sudden expansion followed by series of complex fluid dynamic interactions.

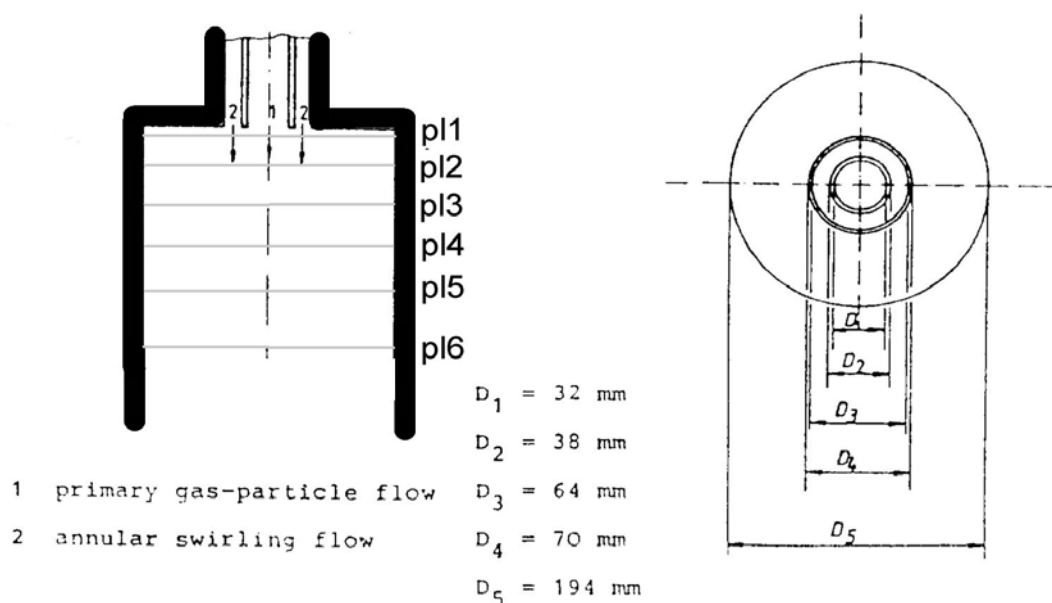


Figure 6.1: Test section of swirling particulate two-phase flow with dimension as published in [124]

6.1 Isothermal swirling particulate two-phase flow

The configuration has a diameter of 194 mm and a length of 500 mm. The annulus of the swirled co-flow has an outer diameter of 64 mm and an inner diameter of 40 mm. Upon leaving the main chamber the flow undergoes into plenum chamber (not shown in figures) in order to eliminate the backlash. The particles are injected into the inlet around the axis of the main jet. They differentiate boundary conditions. The axial stations where cross-sectional PDA measurements were taken at different plane distant from the nozzle exit as shown in Figure 6.1: $p1=3\text{mm}$, $p2=52\text{mm}$, $p3=85\text{mm}$, $p4=112\text{mm}$, $p5=155\text{mm}$ and $p6=195\text{mm}$.

In order to get grid independent solution, 80 % of the discretization scheme was achieved using CDS method. It was very difficult to get convergence with 100 % CDS. The mesh was sufficient refined and the computation was carried out by using a structured grid of approximately 65000 control volumes representing the cylindrical combustor in Figure 6.2. The convergence of the two ways coupling was achieved within 12 coupling iterations.

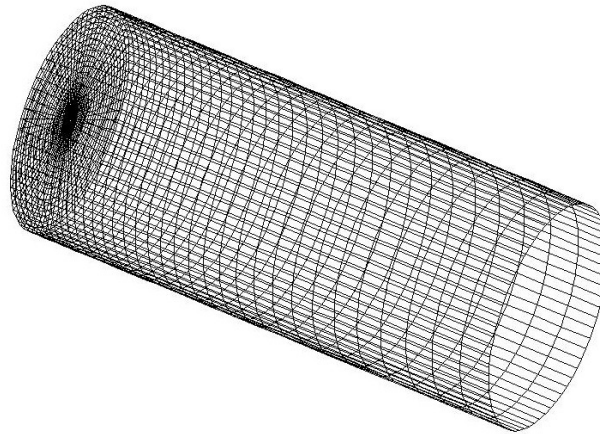


Figure 6.2: computational domain for the isothermal swirling particulate two-phase flows

6.1.1 Flow conditions

The used flow inlet conditions correspond to experimental measurements. The flow rates in the primary and the annular inlet are adjusted to give maximum velocities of 12.5m/s and 18 m/s, respectively. Associated mass flow rates, the flow Reynolds number, the swirl number and the experimental conditions are listed in Table 6.2. The flow Reynolds number was obtained using the total volume flow rate at the inlet and the outer diameter of the annulus. The swirl number was calculated as the ratio of the axial flux of the angular momentum to the axial flux of linear momentum [124], which is obtained by integration across both the primary and annular inlet.

Air flow	
Mass flow rate of primary jet	9.9 g/s
Mass flow rate of secondary jet	38.3 g/s
Inlet Reynolds number (obtained with D=64 mm)	52400
Swirl number	0.47

Table 6.2: Parameters of the flow conditions for the carrier gas

The properties of the glass beads and the particle flow rate are given in Table 6.3. The particles have a smooth surface and are spherical in shape. The mean diameter is 45.5 μm and the loading ratio in the primary jet is 3.4%. Sommerfeld and Qiu [124] provided detailed measurements for the particle size distribution (see Figure 6.3) where 20 000 samples were accounted for. The particles initial conditions were measured 3 mm downstream.

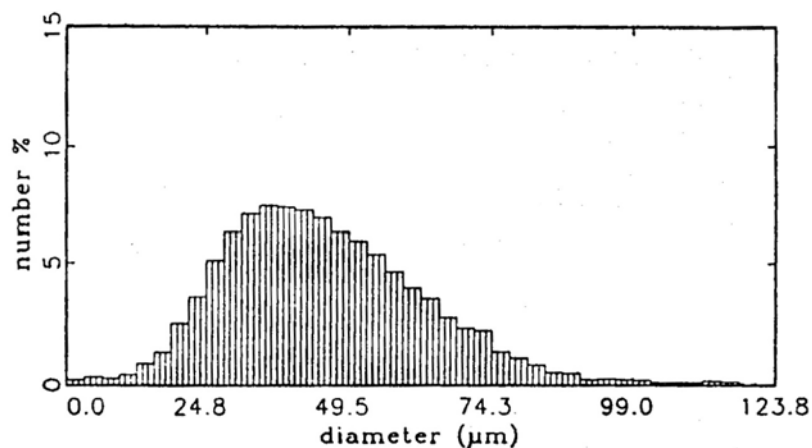


Figure 6.3: Particle size distribution

The numerical simulation was achieved using 75000 parcels, which assured enough statistics to provide plausible results.

Particle parameters	
Particle mass flow rate	0.34 g/s
Particle loading	0.034
Particle mean diameter	45 μm
Particle material density	2500 kg/m^3

Table 6.3: Parameters of the flow conditions for the dispersed phase

6.1.2 Results and discussions

A good prediction of particles evolution properties under turbulent conditions is strongly related to a better capture of the gas-phase turbulent phenomena and associated complex interaction with the dispersed phase. Therefore, first the results for the gas phase are presented.

The mean flow characteristics are featured in Figure 6.4. This figure shows the iso-lines for the axial velocity of gas-phase field. The key features of the flow include the primary and secondary recirculation zones. Due to the convergence problem with RSM, we used the $k-\varepsilon$ model for this calculation. The stagnation point in the core region centered at $x=0.09\text{m}$ approximately and the reattachment point of the secondary recirculation zone at approximately 0.1m do not agree well with experiments. Further results, noting the length of the central recirculation zone ($x=0.35\text{m}$), do not coincide with the measured data (see Figure 6.4-bottom) favorably. The highest negative velocities within the primary recirculation bubble are found at the coordinate $x=0.125\text{m}$.

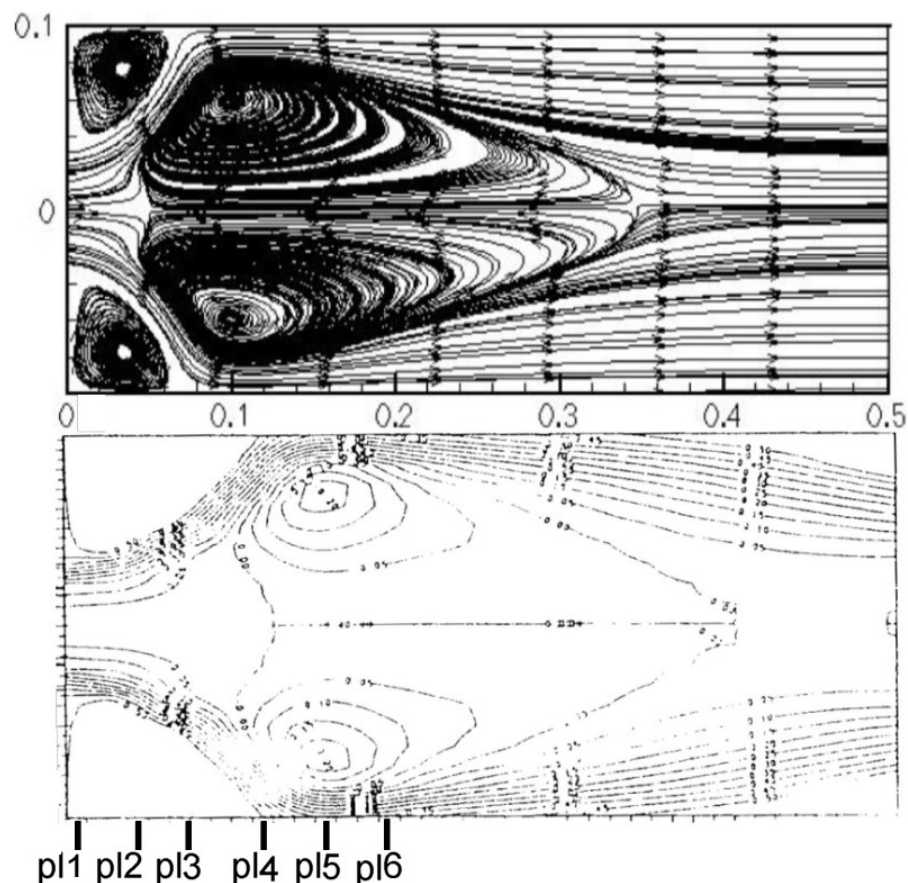


Figure 6.4: Gas-phase stream function: top=simulation; bottom=experiment

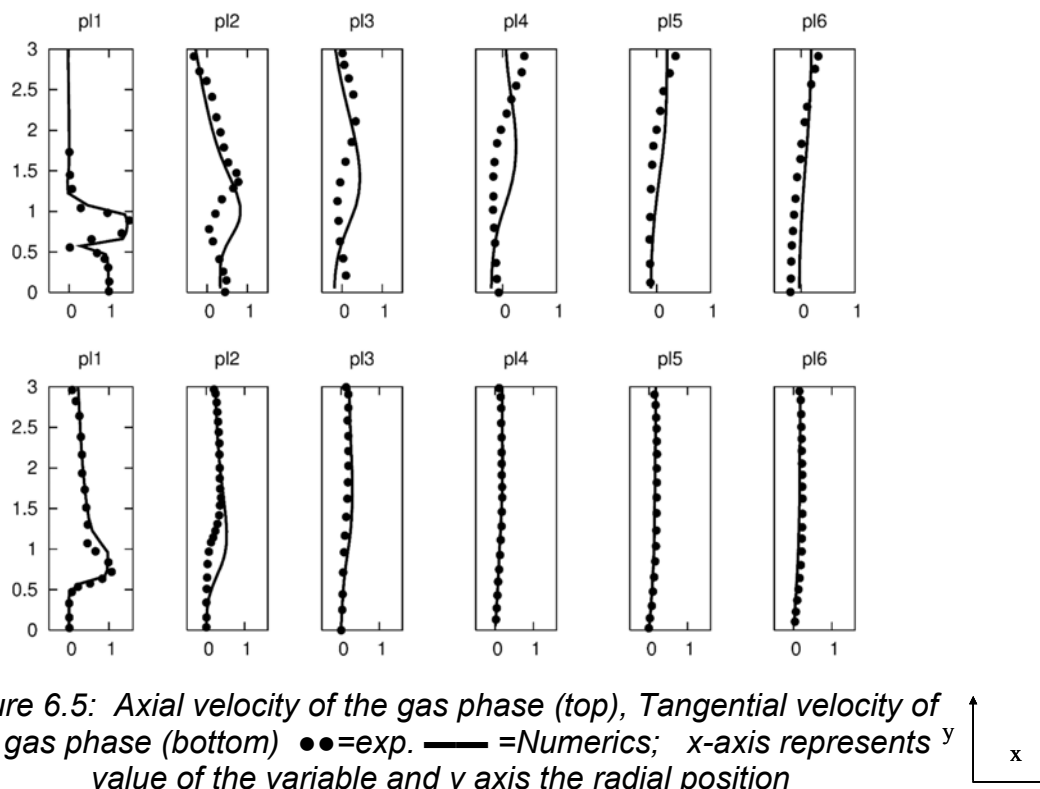


Figure 6.5: Axial velocity of the gas phase (top), Tangential velocity of the gas phase (bottom) ●●=exp. —=Numerics; x-axis represents y value of the variable and y axis the radial position

The computed profiles of mean velocities of the air are shown in Figure 6.5, where pl1, pl2 ... pl6 represent different measurements at plane sections. These results clearly show a good agreement with the experimental data except at the section pl2. This is mainly due to the recirculation induced by the swirl, which is very difficult to predict with the $k-\varepsilon$ model. It was found that the maximum value of tangential velocity near the inlet is 10 m/s and remains constant at 3 m/s away from the inlet. The mean axial velocity profiles, (100 mm away from the nozzle) show that there is a recirculation zone, which is due to the sudden expansion of the geometry. One should mention here that all normalization is based on the values at the boundary conditions.

The profiles of the radial velocity and the turbulent kinetic energy are shown in Figure 6.6. Due to the presence of recirculation zone it is difficult to properly predict turbulence at the recirculation zone by means of $k-\varepsilon$ turbulence model. Nevertheless, the simulation outlines plausible agreements with the experimental data. At this stage, one should mention that, RSM-turbulence models do not provide better results than $k-\varepsilon$ for this configuration. The reason for this may underlies to the big expansion ratio, which equals 3 for the geometry under investigation.

The measurements show higher turbulent intensity in the region close to inlets due to the shear phenomena. The radial velocity in the different planes are very good predicted and found to be almost zero.

6.1 Isothermal swirling particulate two-phase flow

Figure 6.7 shows particle axial velocity and tangential velocity. It displays a good agreement with experimental results except in the range from 50 mm (pl2) to 112 mm (pl4). At these positions the deviation is due to the fact that gas velocity is negative because of the recirculation zone. Particles that initially have about the same velocity as the air flow are not able to follow the rapid expansion and deceleration of the air jets. Therefore they have higher axial velocity, particularly, in the centerline than the air flow. Due to their higher inertia, the larger particles have the larger velocities.

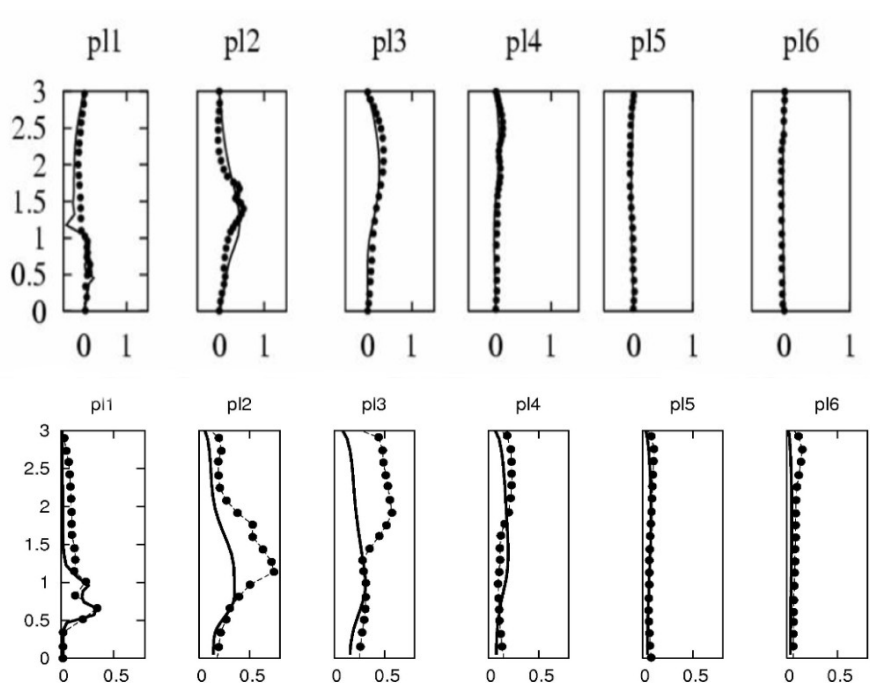


Figure 6.6: Radial velocity component of the gas phase (top) Turbulent kinetic energy of the gas phase (bottom), ▲▲▲=exp. —=Numerics; x axis represents value of the variable and y axis the radial position

Figure 6.8 shows the particle radial velocity and mean diameter in good agreement with experimental data at different axial positions except at pl1, i.e. for lack on statistical samples. In fact, particles are not able to cross the strong air jet on the pl1 section between the radial positions 0.6 to 1.0 at 3 mm which is coming from the inlet, so that no particles could be found in the numerical cells (see Figure 6.8 bottom). This phenomenon may be eliminated by improving the dispersion model, through the consideration of drift correction terms which was not accounted for at this stage of computations.

Furthermore, due to the centrifugal forces, the particles move away from the core. This generates high concentration of the particles on the wall. It must be emphasized here, that it is very difficult to find available experimental data exactly in the vicinity of the particle injection nozzle due to the presence of high loading of particles. To properly represent

accurate inflow boundary conditions for the dispersed phase, which is an actual point of issue [35], one should use Eulerian-Eulerian approach in the vicinity of particles inlet where a very dense two-phase flow is expected.

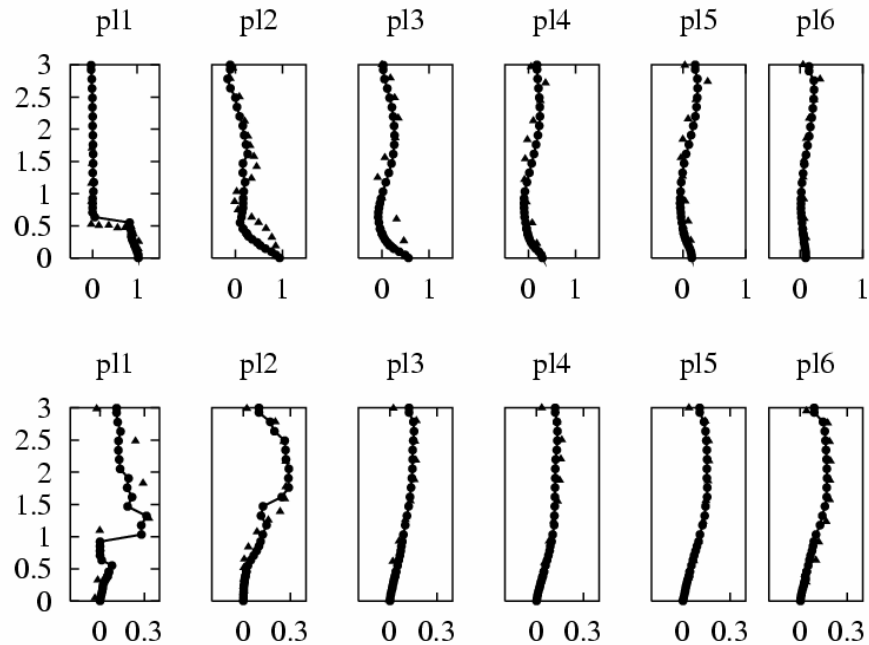


Figure 6.7: Particle axial velocity (top), Particle tangential velocity (bottom) $\blacktriangle \blacktriangle \blacktriangle$ = exp. \bullet = Numerics; x axis represents value of the variable and y axis the radial position

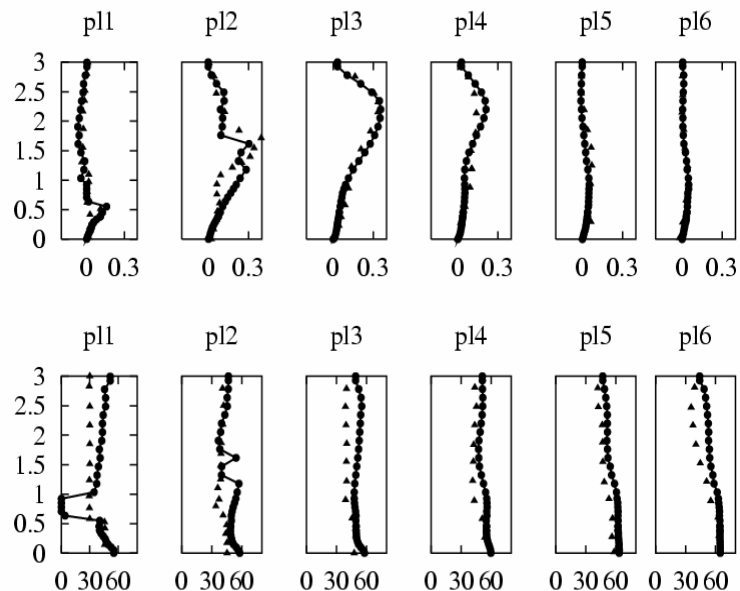


Figure 6.8: Particle radial velocity (top), Particle mean diameter (bottom) $\blacktriangle \blacktriangle \blacktriangle$ = exp. \bullet = Numerics; x axis represents value of the variable and y axis the radial position

6.1.3 Some remarks

As a conclusion, one can affirm that numerical simulation of two-phase flows using k - ε turbulence model can provide acceptable results compared to experimental data. In contrast RSM-turbulence models can not provide better agreements with measurements. The reason for this might be due to the big expansion ratio, which equals 3 for the geometry under investigation. Furthermore, the thermodynamically consistent modulation model provides similar results to these obtained using the standard modulation model. This behavior is expected since used particles have relatively small diameters, which does not exceed 60 μm . Disagreements observed in particle properties close to the nozzle exit might be corrected by improving boundary conditions for the dispersed phase, such as the use of Eulerian-Eulerian approach in the vicinity of the inlet where a very dense two-phase flow is expected.

6.2 Spray issuing into a co-flowing heated air-stream

In this second test case, simulations of two phase flows represented by a spray injected into a co-flowing heated air-stream are presented and discussed. The objective of these simulations is to assess the ability of the equilibrium uniform temperature as well as the non-equilibrium evaporation models to successfully predict the mass transfer and vapor distributions. These numerical investigations are important in order to characterize the interaction regimes between processes that occur during evaporation, namely turbulence and heat transfer. These regimes govern the conditions for the fuel air mixing preparation. For this reason the influence of the turbulence intensity on mass and heat transfer will be particularly investigated. In this regard the influence of the dispersion model on the evaporation rate (vapor concentration and droplet spatial distribution) will be pointed out. For this purpose, the drift correction term will be accounted for.

6.2.1 Configuration description

We have considered the experiments with polydispersed evaporating sprays reported by Sommerfeld et al. [4]. The experimental test case is an axisymmetric, turbulent, two-phase jet. The flow configuration consisted of a pipe with an expansion ratio of three, where heated air was injected through an annulus with 64 mm outer diameter (see Figure 6.9). The nozzle holder had a size of 38 mm, and the test section had a diameter of 198 mm. A two-component phase Doppler anemometry (PDA)

was used to simultaneously measure droplet velocities and diameters and to discriminate gas-phase tracers from the different size-classes of droplets. An isopropanol-alcohol spray liquid was chosen due to its high evaporation rates. Measurements were taken for different flow conditions, such as air flow rate, droplet velocities, droplet diameter distribution and liquid flow rate in order to provide a set of reliable data. Measurements were available in six cross-sections downstream for droplets and carrier phase, namely at: $x=25$, $x=50$, $x=100$, $x=200$, $x=300$ and $x=400$ mm.

This experiment gives a valuable database of polydispersed two-phase flows since initial conditions are detailed for each droplet size class. Those initial conditions are not given right at the injector exit but 3 mm downstream due to measurement technique limitations.

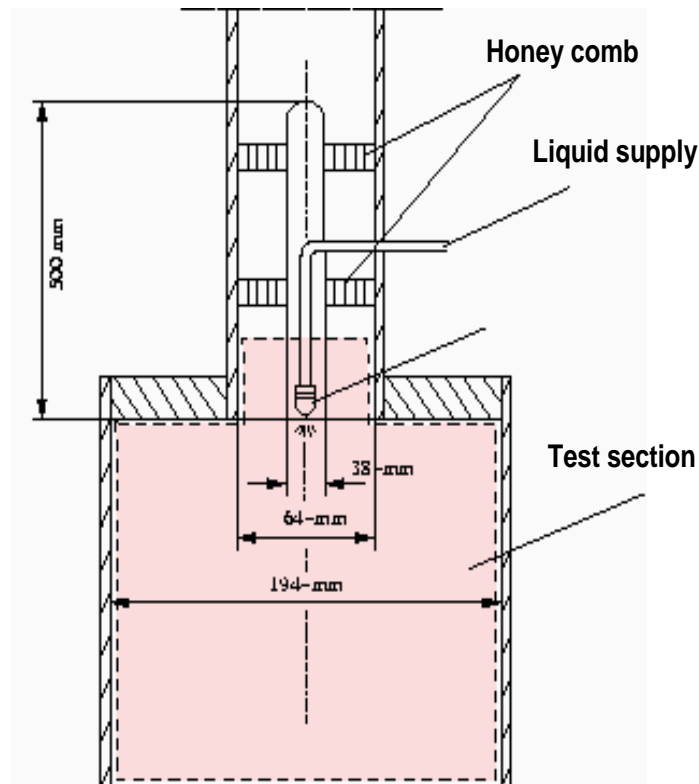


Figure 6.9: Test configuration for spray issuing into a co-flowing heated air-stream

6.2.2 Flow conditions

The first flow considered in the studies was a single phase flow case (i.e. liquid spray is not operated) in order to assess the flow characteristics. The air flow conditions for the single phase were summarized in Table 6.4.

Grid independent solutions were obtained using enough refinements and central differencing scheme. The computational domain for the simulation was represented by a grid having 39 x 29 x 80 cells in axial, radial and

6.2 Spray issuing into a co-flowing heated air-stream

tangential direction, respectively. The grid was generated with an equidistant displacement in the tangential direction, continuously expanded in the axial direction with finest mesh near the inlet and refinement where high velocity gradient were expected in the radial direction (see Figure 6.10).

Air volume flow rate	Air mass flow rate	Maximum air velocity	Air temperature	Flow Reynolds number
(m ³ /s)	(g/s)	(m/s)	(°C)	(-)
0.032	29.0	18.0	100	8577

Table 6.4: Flow conditions for the considered single phase flow

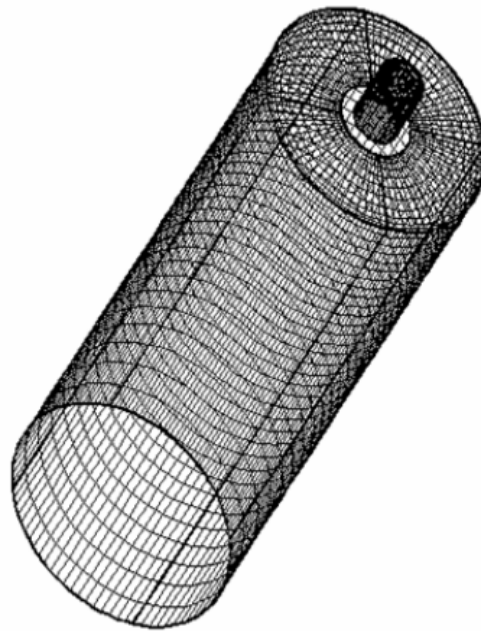


Figure 6.10: Computational domain for the test case of spray evaporation

In case of two-phase flows, the inlet boundary conditions for the carrier phase were given in Table 6.5. The measurements were performed 3 mm downstream for all three velocity components as well as the associated rms values. For more details, Sommerfeld et al. [4] provided detailed profiles at the inlet section for all carrier phase variables.

Air volume flow rate	Air mass flow rate	Maximum air velocity	Air temperature	Flow Reynolds number	Liquid mass flow rate	Liquid temp. at nozzle exit
(m ³ /s)	(g/s)	(m/s)	(°C)	(-)	(g/s)	(°C)
0.034	32.6	18.0	80	10024	0.44	32

Table 6.5: Flow conditions for the considered two phase flows

The spray generated by the hollow-cone pressure atomizer can be split into 8 different of droplet classes. The classes are distinguished by the droplet diameter, start velocities, start locations and rms values. Table 6.6 gives the inlet properties for the different classes. One should mention here that, the mean tangential velocity of the droplet inflow during the simulation were set to zero (not conform to the experimental boundary conditions), since a spray nozzle without swirl was used and, therefore, the measured mean tangential velocity was due to disturbances from the flow at the edge of the nozzle exit. The total liquid mass flow rate and the inlet temperature at the nozzle exit are given in Table 6.5. In order to get statistically reliable results, 75 000 parcel trajectories are calculated every coupling iteration. The increase of parcel number has no influences on the statistical droplets properties.

z	flux	size	Umean	Urms	Vmean	Vrms	Wmean	Wrms
(mm)	(g/m ² /s)	(μm)	(m/s)	(m/s)	(m/s)	(m/s)	(m/s)	(m/s)
0	88.6	18.10	7.698	3.307	0.508	1.452	-0.749	1.037
1	214.5	20.51	10.688	3.674	2.107	0.898	-0.434	0.829
2	952.5	28.22	14.386	3.021	5.054	1.225	-0.243	0.669
3	3080.7	36.54	16.017	2.442	7.785	1.248	-0.120	0.586
4	6321.3	44.61	15.93	2.022	9.766	1.530	-0.034	0.533
5	5664.5	47.47	14.295	2.126	8.740	3.443	-0.001	0.530
6	973.7	37.96	10.436	2.593	6.200	4.569	-0.095	0.606
7	95.0	27.98	6.178	2.835	2.303	3.530	-0.250	0.794

Table 6.6: Flow conditions for the considered dispersed phase

6.2 Spray issuing into a co-flowing heated air-stream

The only missing information is a profile for turbulent dissipation (ε). The distribution of the dissipation rate is therefore estimated using the following expression [55]:

$$\varepsilon = C_{\mu}^{3/4} \frac{k^{3/2}}{0.41 \cdot \Delta r}, \quad (6.1)$$

where $C_{\mu}=0.09$ and Δr is the width of the annulus, i.e. $\Delta r=12\text{mm}$.

6.2.3 Results and discussions

To demonstrate the ability of the equilibrium and non-equilibrium evaporation models combined with $k-\varepsilon$ and RSM turbulence model in predicting spray properties and interaction processes, numerical results are presented and compared with available experimental data. In the following first section a comparison between numerics and experimental data are shown, then a parametric study is presented.

6.2.3.1 Parametric studies

1. Turbulent droplet dispersion

First the capability of the Lagrangian tracking approach to capture the dynamic droplet behavior is evaluated by comparing the calculated droplet velocities with experimental data. The axial droplet velocities are plotted in Figure 6.11 as a function of radial position at different axial positions (100 mm, 200 mm, and 300 mm distant from the inlet). Additional results at other cross sections provide as well good agreement. These results which are obtained with the second order turbulence model (JM) show better agreement with measured values compared to the results with $k-\varepsilon$ model (not shown). The effects of evaporation are also observable by comparing the calculated results with and without considering the evaporation source terms. The evaporation was accounted for by means of the equilibrium evaporation model.

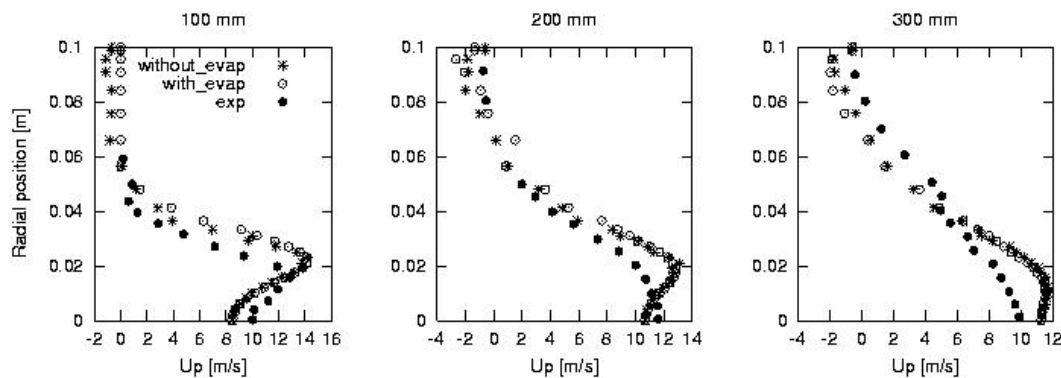


Figure 6.11: Radial profiles of the droplet mean axial velocity at different axial positions

2. Influence of droplets on turbulence

The influence of droplets on the turbulence of the carrier gas is presented in Figure 6.12 at three different cross sections which are located in the first half of the configuration. The effect of droplets is no more observable 200 mm afterwards because of evaporation and droplet dispersion in the entire test section. Results show that the droplets modify the turbulent kinetic energy mainly near the centerline where the droplet density is high. As noted above, the gas turbulence could be reduced since a portion of turbulent kinetic energy is used to disperse the droplets. The turbulent kinetic energy is attenuated as expected, since droplets involved have diameters of about 20-60 μm . Having in mind the fact that coalescence effects among others, are not included in the modeling at this stage of investigation, the deviations around the centerline can be well understood.

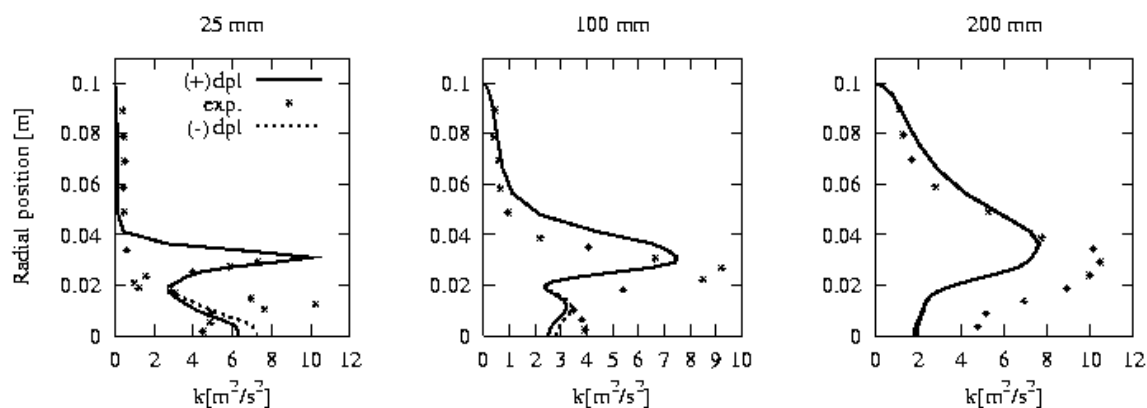


Figure 6.12: Influence of droplet on the turbulence of the carrier gas: profile of the turbulent kinetic energy

3. Effect of droplet evaporation on mass and heat transfer processes

Expressed by (3.59) and (3.62), the mass and heat transfer rates are linked to the time evolution of the droplet diameter and temperature. The influence of the droplet vaporization on mass and heat transfer processes can be therefore characterized by considering the distribution of droplet diameters and droplet mass flux. In Figure 6.13 the radial distribution of the mean droplet diameter, as defined in equation (6.2), is shown at different axial positions ($x=25, 200$ and 300 mm) which were close to inlet, center and outlet regions. The droplet diameter decreases while moving downstream the nozzle exit. The influence of the phase change process is shown by comparing the results calculated with and without evaporation.

$$D_{10} = \frac{\sum_i n_i D_i}{\sum_i n_i} \quad (6.2)$$

The deviations between the numerical calculations and experiments result basically from the lack of coalescence effects along with the primary breakup and the spray formation processes which are not yet included in the modeling. Simulations are performed using the equilibrium evaporation model. At section of 25 mm one observes a zero mean diameter (for radius bigger than 0.03m) while considering the evaporation. This lies to the fact that no droplets are registered within the control volumes.

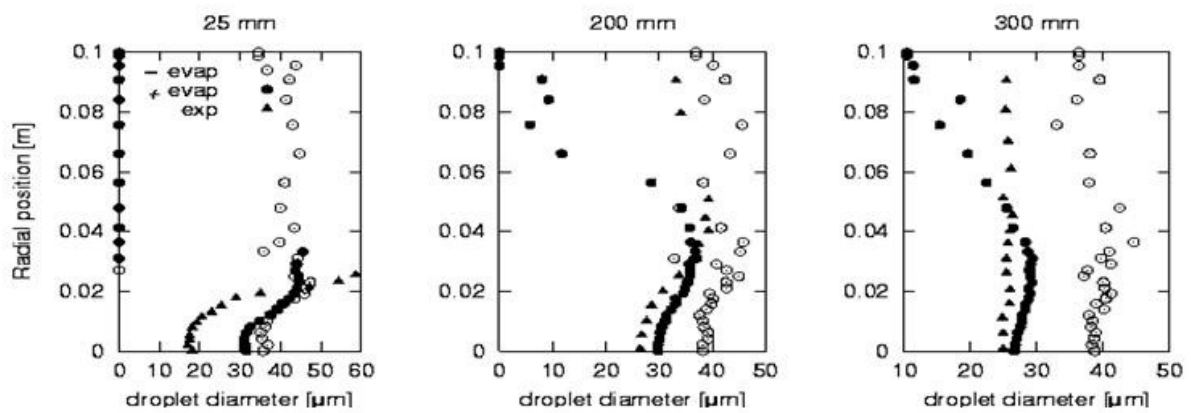


Figure 6.13: Radial distribution of the droplet diameter [m]

The convection processes around the droplets are accounted for by the correlations laws (3.63) and (3.71) where the variation of velocities, temperature or vapor mass fraction, far from the droplet, are introduced in the particle Reynolds number, Prandtl number and Schmidt number respectively. Based on these relations the influence of the turbulence on the modification of the interface transport processes can be studied.

4. Fluctuations of temperature

Numerical parametric study has shown that temperature variation affects the evaporation very strongly. With a relative augmentation of 12.5% corresponding to an increase of the temperature at the injection of 10 °C, one observes an evaporation rate that increases up to 50%. The plots in Figure 6.14 show the mass flux distribution as a function of radial position at axial positions of 300 and 400 mm. The mass flux obviously decreases while the temperature is increased.

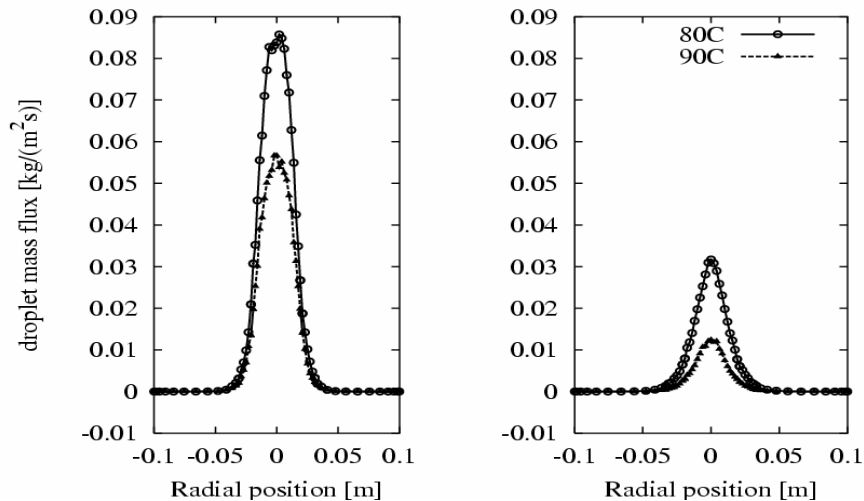


Figure 6.14: Influence of the temperature variation on droplet evaporation at axial position 300 (left) and 400 mm (right)

6.2.3.2 Prediction of the spray evaporation

The Langmuir-Knudsen model as suggested in [30] accounts for the changes of non-equilibrium interfacial transport processes. It implicitly involves the turbulence modifications and may improve significantly the prediction of heat and mass transfer. This fact is demonstrated in Figure 6.15, where a comparison of calculations of the evaporation rate with equilibrium evaporation model (eq.) and non equilibrium evaporation model (neq.) in coupling to the standard modulation model is presented. For the range of droplet involved diameters, results using the non-equilibrium model prescribe better the evaporation rate than equilibrium one. The reference value for the normalization is the evaporation rate at the configuration inlet, i.e. $x = 0.0$ m. One can outline that the investigated configuration involve non-equilibrium evaporation processes. Therefore the model by Langmuir-Knudsen agrees most favorably with the experimental measurement of the droplet mass flux.

Figure 6.16 represents the radial distribution of the droplet mass flux at different axial positions (0.025m, 0.05m, 0.1m, 0.2m, 0.3m and 0.4m far away from the inlet). In accordance with the experiment, the concentration of droplets decreases while moving away from the nozzle due to the evaporation. A comparison between equilibrium and non equilibrium evaporation models reveals that the latter delivers results closer to experimental results. The equilibrium model following Abramson and Sirignano allows almost a constant evaporation rate, which is not enough to give a droplet mass fraction properly.

The estimated evaporation rate using equilibrium model appears higher than non-equilibrium (Figure 6.15) just because of the normalization. Indeed the normalization is applied for each model with respect to its evaporation value at the first computational control volume. The rate of evaporation computed by the Langmuir-Knudsen model is much higher (in

6.2 Spray issuing into a co-flowing heated air-stream

real value) than the one obtained by the model of Abramson & Sirignano. Therefore, Figure 6.15 and Figure 6.16 do not show any contradiction.

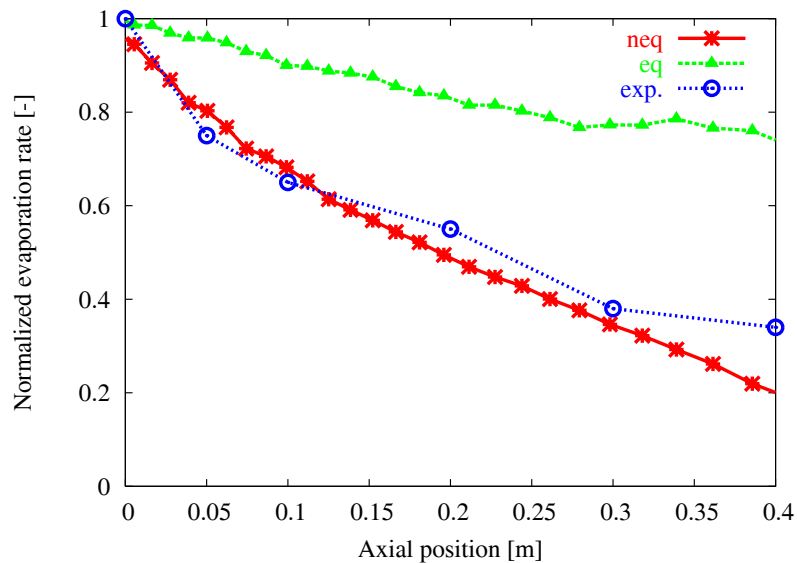


Figure 6.15: Normalized evaporation rate: Comparison between results with equilibrium and Non equilibrium evaporation models

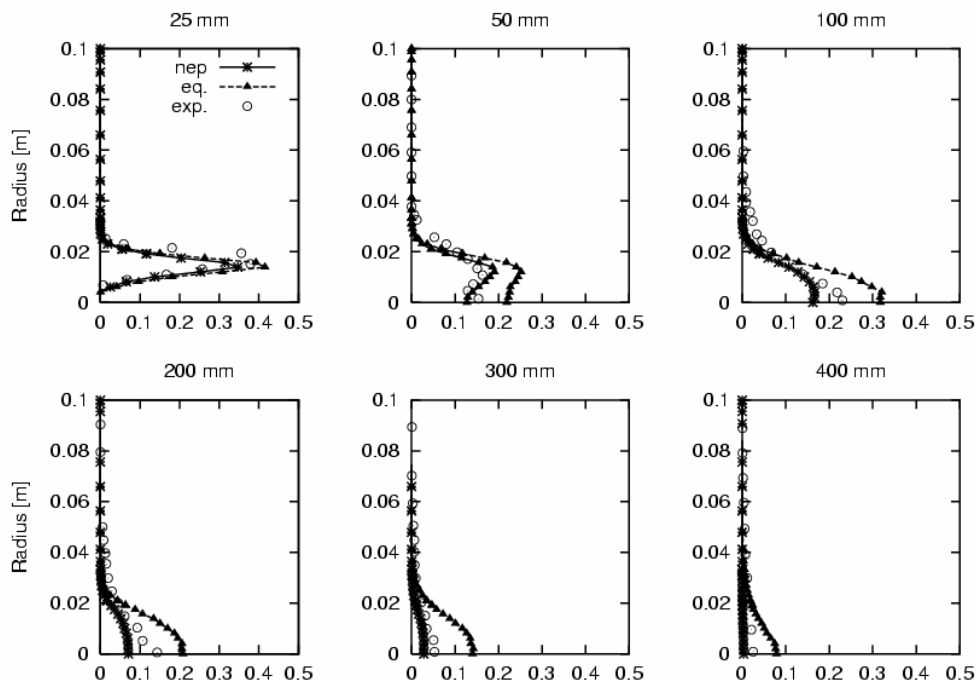


Figure 6.16: Comparison between results with equilibrium and non equilibrium evaporation models. X-axis represents value of the Droplet mass flux $[kg/(m^2s)]$ and y-axis the radial position

6.2.3.3 Turbulence evaporation interaction regimes

Different results demonstrating turbulence effects along with turbulence modulation on mass and heat transfer in evaporating sprays are presented. Figure 6.17 and Figure 6.18 show that by increasing the turbulence intensity, the efficiency of the mass transfer increases, approximately during the first half of the droplet lifetime ($x/D < 3$). The variable x represents the axial length whereas D represents the inlet diameter which equals 64 mm.

The influence of turbulence intensity decreases while the mean droplet diameter decreases, i.e. stream forwards. It must be mentioned that the turbulence effect manifests itself well before the droplet dimensions become comparable to the smallest turbulence eddies. As pointed out in [47], a pure turbulence effect is expected for smaller droplets that are transported by the carrier phase without mean relative velocity while the influence of mean relative velocity may be significant for larger droplets. The reference value for the normalization is set to the value of the evaporation rate resulting from a turbulent kinetic energy boundary condition of 60% of experimental data.

To evaluate the importance of the evaporation process and the gaseous turbulence within the system, let us retrieve and compare the characteristic time scales of the processes involved as introduced in equations (3.78) and (3.79). The first task is achieved through Figure 6.19, while the second is accomplished by means of Figure 6.20. The axial profiles of the process characteristic time scales are plotted in Figure 6.19 where the reference value for the normalization is set to the value of each time scale at $x=0.0$ m. One can observe that a process inversion occurs after the first half of the droplet lifetime at $x=0.25$ corresponding to a critical value of $Da_v=1$, see equation (3.82). This behavior may be affected by the turbulence modulation through changes in the turbulent kinetic energy. Therefore it is wisely indicated to detect its persistency or sensitivity with respect to the turbulent kinetic energy. We then varied turbulent kinetic energy intensities from 60% to 140%, and recorded their effect on the behavior of the evaporation rate along the axial direction in Figure 6.21. This figure confirms the findings from Figure 6.19 and reveals the existence of a limited range for the effects of the turbulence intensity variations (around 40%) out of which the increase or decrease of the turbulence intensity affects no more the efficiency of the mass transfer. Within this sensitive range, it is easy to distinguish two regions separated by the critical value $Da_v=1$. In the first region ($Da_v < 1$), when the turbulence intensity increases, the efficiency of the mass transfer increases, approximately during the first half of the droplet lifetime. According to the findings in Figure 6.20. This influence decreases with decreasing droplet diameter.

6.2 Spray issuing into a co-flowing heated air-stream

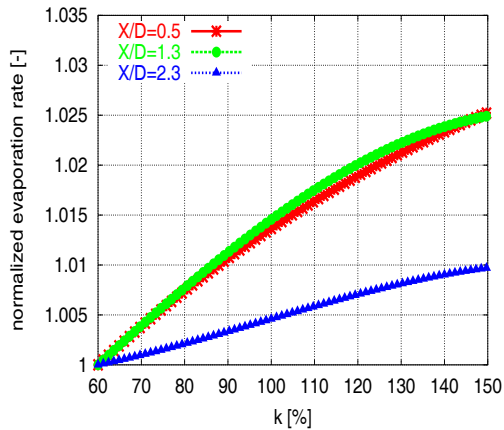


Figure 6.17: Influence of turbulence variation on the first half part of the configuration

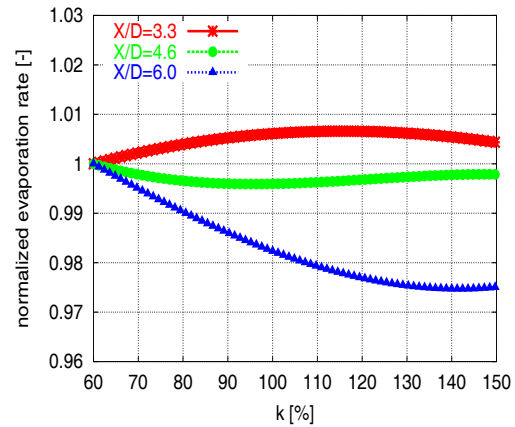


Figure 6.18: Influence of turbulence variation on the second half part of the configuration

Based on the fuel vapor concentration gradient near the droplet surface which is the driving force for evaporation, the beneficial effect of high turbulence intensity near the droplet surface could contribute to the build-up of the fuel vapor concentration gradient by removing the fuel vapor from the surface.

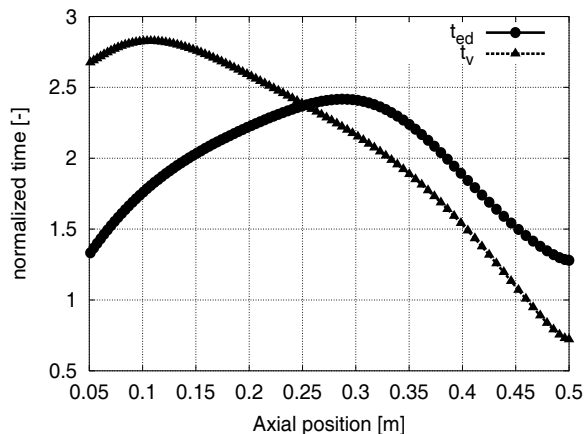


Figure 6.19: Turbulent time scale and time scale characterizing the thermodynamics of vaporization at different axial positions

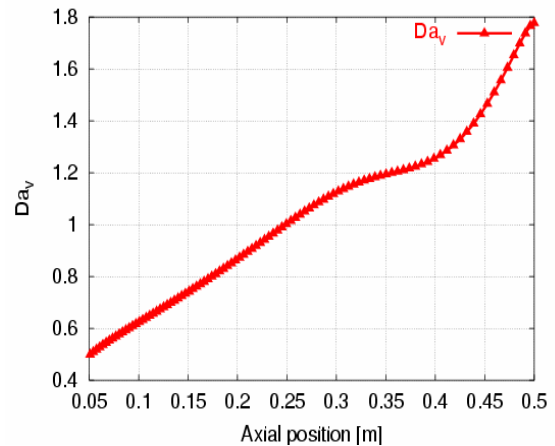


Figure 6.20: Evolution of the vaporization Damkoehler number along the axial position

Consequently, if the residence time of the fuel vapor in the vicinity of the droplet surface is larger than the turbulent time scale, any acceleration of the vapor removal will strongly contribute to an increase in the vaporization rate. Below the critical value, for ($Da_v < 1$) the turbulence energy is able to increase the mass transfer. For higher value ($Da_v > 1$) an inverse phenomenon is observed, namely the increase of the turbulent intensity decreases the vaporization rate. These results which distinguish two characteristic interaction regimes based on a vaporization Damkoehler number agree well with the experimental results in [47].

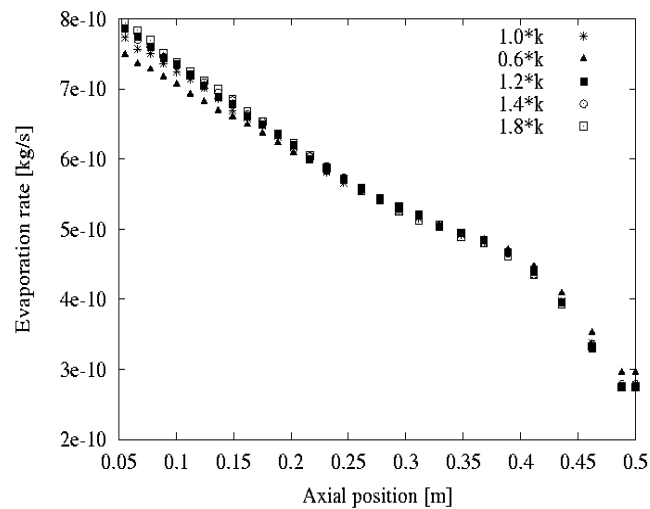


Figure 6.21 Influence of the turbulent intensity on the evaporation rate along the axial direction

One can summarize that for the characterization of turbulence-droplet vaporization interaction regimes, a vaporization Damkoehler number appeared to be useful. To demonstrate the ability of the model combinations used in predicting evaporating spray and droplet properties under turbulent conditions, some representative results calculated by coupling the turbulence model, the equilibrium and non equilibrium evaporation models have been presented. The effect of the turbulence intensity variations seems to be restricted to the region in which the turbulence affects positively the evaporation and heat flux rate.

6.2.3.4 Mixing degree

As mentioned in the introduction, the fuel preparation in gas turbine combustors and in many internal engines strongly depends on fuel-air mixing processes. One of the most relevant operating parameters of such combustion system is the mixture ratio, i.e. the ratio, either locally or overall, in which the fuel and air are present in the system. The mixture ratio can be defined in different ways [74]. In the frame of this work, we used the mixture fraction definition formulated in equation (2.50) and the transport equation (2.52). The question now is how to characterize the influence of the turbulence intensity variation on the mixture ratio along with the mixing degree of the gaseous fuel and air. This can be achieved by means of the so-called Spatial Mixing Deficiency (SMD). According to [123], it is defined as:

6.2 Spray issuing into a co-flowing heated air-stream

$$SMD = \frac{RMS_{plane}(\bar{Y}_i)}{Avg_{plane}(\bar{Y}_i)}, \quad \text{with} \quad Avg_{plane}(\bar{Y}_i) = \frac{1}{m} \sum_{i=1}^m \bar{Y}_i \quad (6.3)$$

and

$$RMS_{plane}(\bar{Y}_i) = \sqrt{\frac{1}{m-1} \sum_{i=1}^m (\bar{Y}_i - Avg_{plane}(\bar{Y}_i))^2} \quad (6.4)$$

In (6.3) $Avg_{plane}(\bar{Y}_i)$ is the average of the mean vapor mass fraction over a plane section having m cells and $RMS_{plane}(\bar{Y}_i)$ its corresponding root mean square. A zero value of SMD indicates perfect mixing at a given plane. Figure 6.22 shows the influence of the turbulence intensity on the mixing process in the combustion chamber at different axial planes located between $x=0$ m and $x=0.4$ m nozzle downstream. A modification of about 6.2 % is observed between $x=0.05$ m and $x=0.225$ m

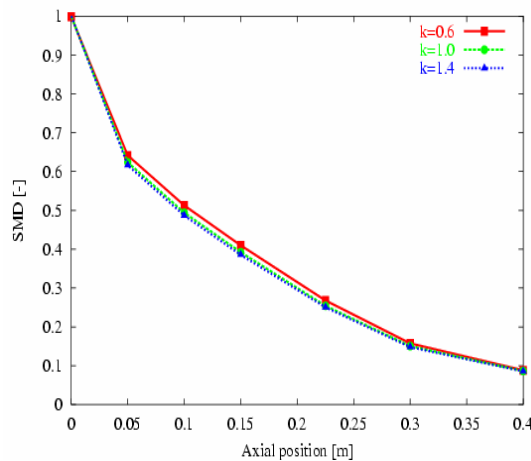


Figure 6.22: Influence of the turbulence intensity through the turbulent kinetic energy, k , on the spatial mixing deficiency (SMD) along the axial direction.

6.2.3.5 Contribution of the drift correction effect to mass and heat transfer

The drift correction term has to be added to the fluid fluctuation velocity on the parcel position along the droplet trajectory. This is only made in this study when the equilibrium evaporation model is used. In the frame of this work, the model developed by Kohnen and Sommerfeld [55], which is based on stress gradient and turbulent time scale, has been accounted for. The drift factor added to the equation (3.49) is given by:

$$v_{drift} = c_{drift} T_L \frac{\partial \sigma^2}{\partial r} \quad (6.5)$$

T_L is the Lagrangian turbulent time scale, which is given in case of $k-\varepsilon$ turbulence model by:

$$T_L = c_T \frac{k}{\varepsilon} \quad (6.6)$$

the constants c_{drift} and c_T are set to 0.25 and 0.3, respectively. The quantity σ^2 represents the velocity variance, and may be calculated using the turbulent kinetic energy by $\sigma^2 = 2/3k$. The variable r represents the radial direction. The expressions for the fluid fluctuations at particle location (fluctuation seen by dispersed phase), used in the frame of this work are calculated by:

$$u'^p(t_{n+1}) = u'^p(t_n) \cdot R_{p,u}(\Delta t, \Delta r) + \sigma_u \sqrt{1 - R_{p,u}^2(\Delta t, \Delta r)} \cdot \chi_u(t_n) + c_{drift} T_{L,u} \frac{\partial u' u'}{\partial y} \quad (6.7)$$

$$v'^p(t_{n+1}) = v'^p(t_n) \cdot R_{p,v}(\Delta t, \Delta r) + \sigma_v \sqrt{1 - R_{p,v}^2(\Delta t, \Delta r)} \cdot \chi_v(t_n) + c_{drift} T_{L,v} \frac{\partial v' v'}{\partial y} \quad (6.8)$$

$$w'^p(t_{n+1}) = w'^p(t_n) \cdot R_{p,w}(\Delta t, \Delta r) + \sigma_w \sqrt{1 - R_{p,w}^2(\Delta t, \Delta r)} \cdot \chi_w(t_n), \quad (6.9)$$

where all used variables remain the same as introduced in section 3.2.3

In the following study, results calculated by using different model combinations, denoted by Eo0 or eq, EwD or eq-drift, NoE or neq for equilibrium evaporation model/Markov-sequence/k-Epsilon, equilibrium evaporation model/Markov-sequence with drift correction/k-Epsilon, and nonequilibrium evaporation model/Markov-sequence/k-Epsilon respectively are presented and compared to experimental data. The objective is thereby to retrieve the effects of the drift correction in comparison to-non-equilibrium effects. Throughout the figures, the radial direction is designed to coincide with the y-axis.

First, the capability of the Lagrangian tracking approach to capture the dynamic droplet behavior is evaluated by comparing the calculated droplet velocities with experimental data. The axial droplet velocities are plotted in Figure 6.23 as function of radial positions at different axial positions. One observes some differences between experimental and numerical results. In particular, at $x \geq 300$ mm the computed droplet axial velocities are about 1.8 m/s higher at the centerline than the measured values. However, it is remarkable that the drift correction factor does not influence the numerical droplet axial velocities.

Figure 6.24 shows the radial droplet velocity at different axial cross sections. The influence of the drift correction factor on the droplet radial velocities is obvious at the last two axial sections. The results with the model combination Eo0 are closer to experimental data, whereas the results obtained using the combination EwD deliver higher values. This is

6.2 Spray issuing into a co-flowing heated air-stream

mainly due to the high value of the turbulent kinetic energy gradient in this region (see Figure 6.12). The drift factor generates a high radial velocity fluctuation which is up to 4 times higher than the fluid mean radial velocity at the parcel location in the region where high gradients of turbulence exist. Figure 6.25 presents the radial fluctuations of droplet at different sections as function of radial positions. One observes that the computed values of the radial velocity fluctuations are overestimated compared to experimental results. Furthermore, the drift factor enhances the droplet fluctuations while the radial velocity itself increases on value.

In Figure 6.26 parcels entries numbers in thousands per cell are plotted along radial positions at different sections. Remarkable differences are observed. From 200 mm onwards the results without drift correction factor show higher values, this lies on the fact that the evaporation rate is smaller than for the two other simulations. At the end of the test section the combination EoN as well as EwD indicates that the majority of droplets are already evaporated. This effect is in particular enhanced in case of EwD model. The droplet concentration represented by the number of parcels entries in Figure 6.26 shows at the last section ($x=400\text{mm}$) that droplets having the minimum diameter (at the center line as depicted in Figure 6.13) are almost evaporated.

In Figure 6.27 the radial distribution of the droplet mass flux is shown at different axial positions. In accordance with the experiment, the concentration of droplets decreases while moving away from the nozzle due to the evaporation. The model EwD provides higher evaporation rates than experimental measurements (see section at 300mm). This is mainly due to higher predicted droplet velocity which in turn induces higher relative velocity between the fluid and the dispersed phase. A comparison between Eo0, EwD and EoN models reveals that the latter (EoN) delivers results closer to experimental results. The equilibrium model following Abramson and Sirignano allows almost a constant evaporation rate, which is not enough to give a droplet mass fraction properly (compare to Figure 6.16).

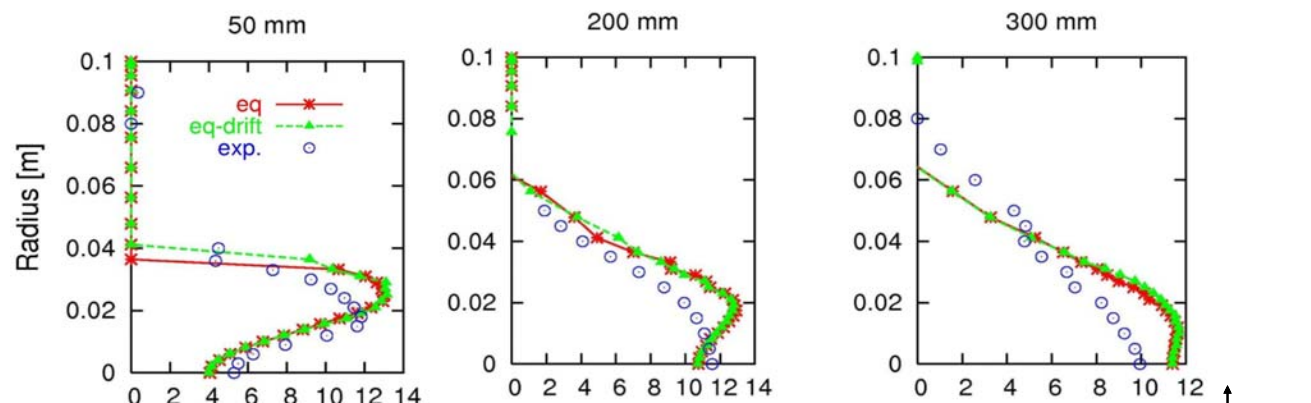


Figure 6.23: Axial droplet velocity at different axial sections far away from the spray nozzle exit. The x-axis stands for axial droplet velocity [m/s]

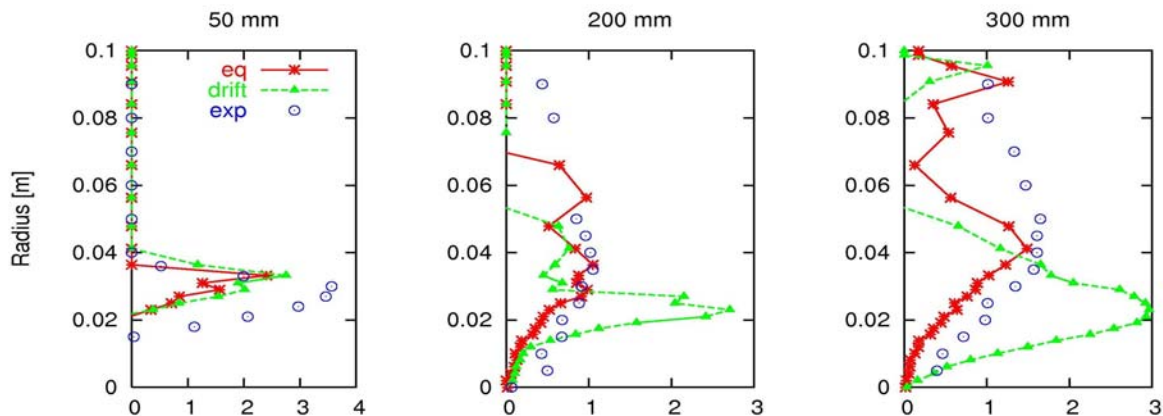


Figure 6.24: Radial droplet velocity at different axial sections far away from the spray nozzle exit. The x-axis stands for radial droplet velocity [m/s]

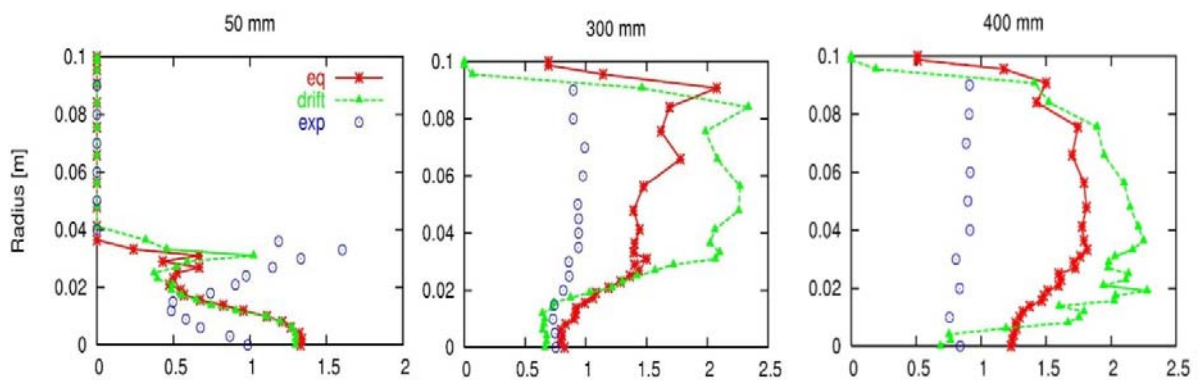


Figure 6.25: Radial droplet velocity fluctuation at different axial sections far away from the spray nozzle exit. The x-axis stands for radial droplet velocity fluctuation [m/s]

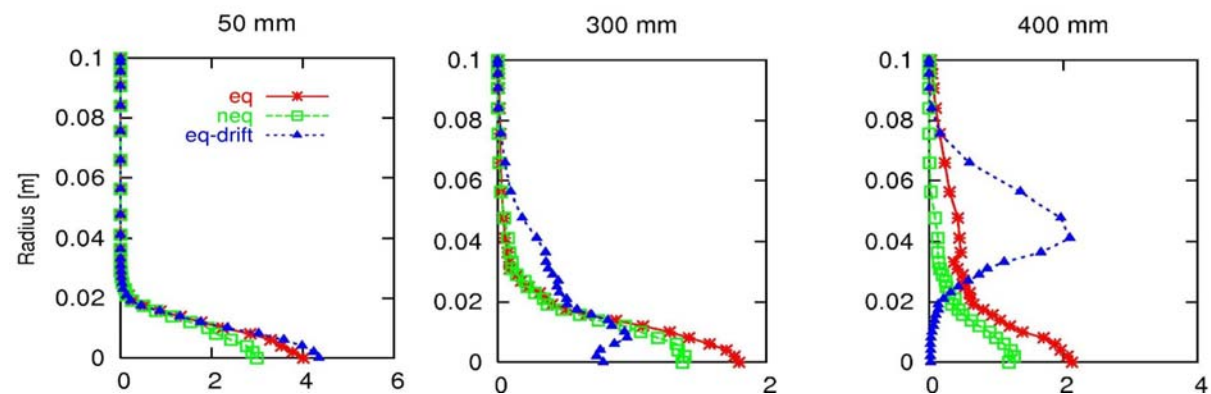


Figure 6.26: Numbers of parcels entries in thousands per cell along the radial position at different axial sections far away from the spray nozzle exit. The x-axis stands for numbers of parcels entries [1000 entries/CV]

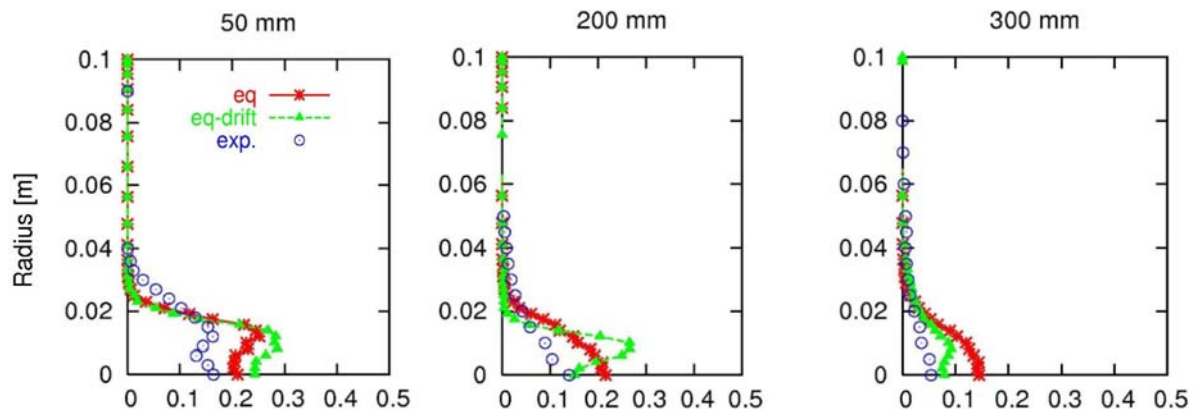


Figure 6.27: Droplet mass flux at different axial sections far away from the spray nozzle exit. The x-axis stands for droplet mass flux [$\text{kg}/(\text{m}^2\text{s})$]. Comparison between the combination Eo0 (equilibrium) and EwD (equilibrium drift correction factor)

Conclusion: The ability of the model combinations used in predicting evaporating spray and droplet properties under turbulent conditions has been investigated. It results that the combination EwD predicted higher evaporation rates than experimental measurements. This was mainly due to the higher droplet velocity which in turn induced higher relative velocity between fluid and the dispersed phase. Simulations have in particular shown that results using EoN model agreed most favorably with the experimental measurement of the droplet mass flux. The consideration of the advanced dispersion models that are able to account well for anisotropic turbulence and vortex structures inherent to complex turbulent two phase flows may improve the rate of evaporation, it can be considered as future work.

6.3 Spray combustion in complex configuration: gas turbine engine combustor

RANS based simulations of gas turbine combustion chamber are the subject of the present section. The configuration is used for the assessment of the complete spray combustion model. This gas turbine chamber is characterized by a complex geometry having multiple recirculation zones and reattachment points. Different thermodynamic processes, such as spray evaporation, fuel-air mixing and subsequent combustion make the test case extremely complex and pose an important challenge for the modeling. Thus, it is of great interest to evaluate the performance of all combined sub-models within such configuration. Understanding reacting flow characteristics as well as droplet behavior

near the injector is, most notably, very crucial for gas turbine engine design. Unfortunately, up to the date there is no effective method and instrument to measure detailed flow properties inside the combustion chamber under the engine operating condition and of the real engine configuration. Moreover, it is too expensive and costly to conduct hot fire tests for all preliminary design concepts. Therefore, in addition to experimental studies the spray combustion engine design community has been making tremendous efforts to understand the injection and combustion phenomena by developing analytical and numerical design tools.

In this section, we focus on the two-phase turbulent combusting flow in an annular combustor from RRD (Rolls-Royce Aero Engines Deutschland). This configuration has been already numerically investigated by Smiljanovsky et al. [131]. Their simulations, however, were performed using only standard $k-\varepsilon$ turbulence model, equilibrium evaporation model and equilibrium chemistry without accounting for the turbulence modulation. Besides these models, we also investigated the effect of the Reynolds Stress models (Jones Musonge) for turbulence combined with equilibrium and flamelet chemistry approaches. Moreover different turbulence modulation models as well as equilibrium and non-equilibrium evaporation models have been considered. Simulations were performed using an assumed shape of probability density function to prescribe the turbulence-combustion interaction

6.3.1 Configuration description

The Rolls Royce BR710 annular combustor is fired by 20 burners consisting of an air blast atomizer, 3 concentric co-swirling air circuits, and fuel atomizer in shear layers of the inner two air streamers. For the numerical simulation only one sector of 18 degrees has been modeled (Figure 6.28) to model computational combustion. The single dome sector of 18° span includes swirler, which was accounted for by inlet boundary conditions, fuel nozzle on the inlet and a set of primary and secondary openings on the outer and inner walls (Figure 6.28).

Figure 6.29 shows the overall mesh for the single annular combustor without fuel injector containing about 350 000 control volumes. The grid of the gas-turbine combustor sector has 99 multiply-connected domains, i.e., they consist of several separate flow-paths that interact with each other. Hexahedral cells were used to generate the mesh. The boundaries specified at inlets are highlighted with green color (Figure 6.28). They include heatshields, starter and Z-ring cooling air as well as primary and secondary air mixing ports.

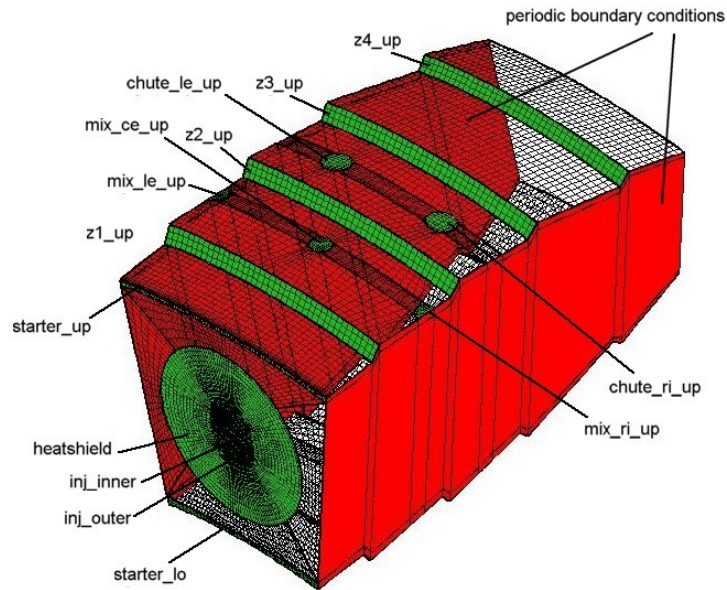


Figure 6.28: Single annular combustor geometry and inlets

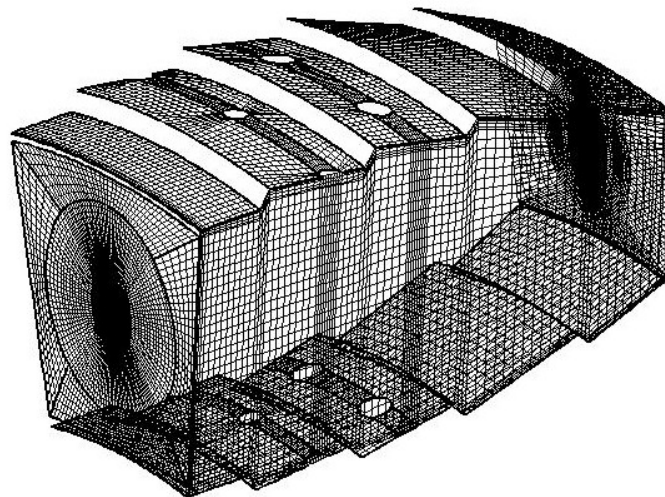


Figure 6.29: Single annular combustor mesh

6.3.2 Flow conditions

The inlet boundary conditions for the combustion chamber corresponded to scaled take off conditions. The pressure was scaled to $P_{inl}=1241$ kPa according to experimental data carried out in a full annular combustor rig. The corresponding temperature $T_{inl}=842$ K. The mass flow boundary conditions for the gas phase were provided by measurements and estimated by an in house code from Rolls Royce. The air mass flow rates, by reason of secrecy, cannot be published.

The fuel injector exists of three different air swirlers, inner, outer and dome air swirler [131]. Each one is defined primarily by its effective area and its swirl angle. Additional swirling air is introduced by the heatshield inlets. The circumferential velocities are simply determined using the swirler vanes turning angles and the constant axial velocities, which are calculated from cold flow rig test measurements. Swirlers were not accounted for during computation, since no geometrical data was available. Therefore boundary conditions at the inlets were imposed by velocities profiles provided by Rolls Royce.

Inlet conditions for the turbulent kinetic energy are calculated using a turbulence intensity of 10% of the resultant velocity through an inlet. For the Reynolds Stress Model, only main diagonal components were considered. For these terms also a turbulence intensity of 10% is applied, i.e. $u'/\bar{u}=0.1$. Tangential components of the Reynolds stress tensor are set to zero. The distribution of the dissipation rate is estimated using the expression (6.1). Here the turbulent length scale was assumed to be equal to the holes' diameter or inlet's opening.

The mixture fraction boundary conditions are set to zero at all inlets ($\tilde{z}=0$), since the injected air do not contain any fuel and the variation of mixture fraction is originated only to the vapor produced by droplets. Even though the fuel is entirely supplied by the liquid droplets, chemical reactions are assumed to occur only in the gaseous phase, far enough from the liquid interface. Consequently, fuel droplets play the role of vapor source terms for the gaseous medium. The mixture fraction variance was set to 0.25 at swirlers and heatshield in order to obviate combustion at the fuel atomizer. The remaining inlets have a zero boundary condition ($\widetilde{z''^2}=0$). The turbulent Schmidt number is set to 0.5. For the simulation of only one sector of the annular ring combustor, periodic boundary should be used. Therefore one has applied this condition on the two side planes (see Figure 6.28).

As mentioned above, the combustor is operated with liquid kerosene at a pressure of 12.0 bars. However, kerosene is a multi-component fuel which typically consists of a mixture of about 10 hydrocarbons such as n-dodecane, alkyl derivatives of benzene, naphthalene and derivatives of naphthalene which is therefore difficult to model. Thus we have used a substitute spray model with dodecane $C_{12}H_{26}$ as fuel in order to prescribe evaporation. Dodecane has a higher vapor pressure and a lower initial distillation temperature as compared with kerosene. Thus, it is relatively non-volatile and can reproduce the thermodynamical characteristic of kerosene [130]. For combustion processes, kerosene is modeled with decane $C_{10}H_{22}$.

Given the air mass flow rate, the fuel mass flow is determined by the Air to Fuel mass Ratio (AFR), which equals $AFR=40.7$. Fuel boundary conditions are usually unknown and are very difficult to estimate.

In order to understand the complex two-phase flow, measurements are applied for cold flow conditions in which the droplet size and velocity distribution are measured as close to the fuel injector-combustor-interface as possible. Later, they are used as boundary conditions for the fuel spray model in the calculations. The droplets have a mean diameter of $20 \mu\text{m}$. They are introduced into the gas phase at discrete circumferential injection points ranging from 4 to 6 mm at the fuel lip radius. The temperature of the fuel droplets is set to $T_{\text{fuel}} = 300\text{K}$, the axial, tangential and radial velocity equal 30.0 m/s, 10.0 m/s and 10.0 m/s respectively, whereas the corresponding velocity fluctuations are 3.0 m/s, 5.0 m/s and 5.0 m/s respectively. The initial spray parameters specified by velocity boundary conditions give a spray injection angle of 28° .

For simplification of the Lagrangian approach, the primary atomization as well as the spray formation is not going to be considered within this work. So we will track discrete particles of liquid fuel, which are supposed to evaporate in the carrier phase.

6.3.3 Results and discussion

In this section we aim at giving an assessment about different models combinations including multiphase flows, evaporation, combustion and turbulence modulation, used to predict spray combustion. Results from these models combinations should be used to suggest a reliable complete model, which is able to provide predictions of main flow and combustion properties useful for the design of combustor. Measurements are carried out in a 360° full-annular combustor rig. A sampling probe is located in the combustor exit plane measuring gas concentrations in radial positions. They are 11.7, 31.43, 51.38, 71.07, and 89.97 percent of the exit duct height as presented in Figure 6.30. Two main aspects will be emphasized with respect to non-premixed combustion, namely equilibrium and flamelet chemistry. Simulations were performed at the first stage in a steady state calculation. Thereafter unsteadiness was considered for the carrier phase.

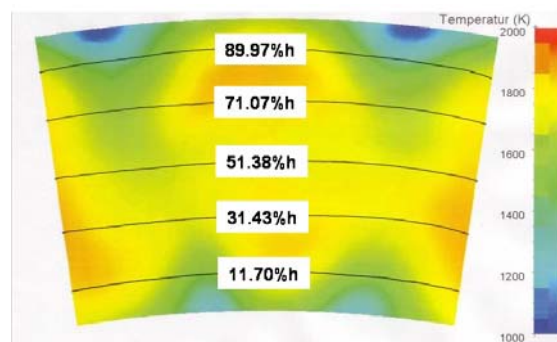


Figure 6.30: Location where measurements were carried out at the combustor exit.

6.3.3.1 Equilibrium chemistry

Because the air is highly turbulent in the combustor, the resulting flow field, as shown in Figure 6.31 and Figure 6.32, is very complex. The numerical results concerning axial-, radial-velocity and turbulent kinetic energy using $k-\varepsilon$ and Reynolds Stress Model (Jones Musongé) are plotted in Figure 6.33 - Figure 6.38. Since there is no experimental data for this cross section, it is difficult to validate the flow field at the symmetry plane. Nevertheless, one observes a larger recirculation zone calculated with RSM turbulence model compared to $k-\varepsilon$. Differences are also observable on the axial velocity at the combustor exit. Both models predicted nearly the same plot for the radial velocity. Differences are observable only in regions closed to the inlet where the flow is highly swirled. One observes in the axial velocity plots that the air film coming from the z-rings which are used to protect and cool the metallic shield in the primary and secondary zones, did not cover the entire outer part of the combustor. Note that all z-inlets represent multi-perforated wall. In order to accurately describe air injection through these cooling z-rings, it would be necessary to calculate each little air jet blowing from the drilled surface, but this method is obviously computationally too expensive. As an alternative solution one can apply a porous wall boundary condition, where the prescribed mass flux at the wall remains unchanged compared to a standard inlet condition. Unfortunately, the porous wall boundary condition is not available in the used code, i.e. the velocity components are adapted to satisfy the mass flux. The momentum flux is, therefore, not satisfied, due to the fact that the velocity entering the computational domain is much higher than the velocity based upon the surface averaged mass flow rate. This assumption could result in an important boundary condition since the total mass flux through all z-rings equals 35.19 %, which represent a considerable amount. Thereby it could exhibit an important influence on the flow field.

Figure 6.37 and Figure 6.38 show plots of the Turbulent Kinetic energy (TKE). It can be seen that the maximum value of TKE is located in the centerline of the injector fuel plane where jets entering with 140 m/s through the mix-openings (see Figure 6.28) are going to meet. The predicted TKE by RSM model is higher than $k-\varepsilon$ turbulence model, particularly in the second zone of the combustor where different jets are interacting. Contours of the turbulent kinetic energy suggest that small turbulent scales occur close to the combustor exit, whereas in the first zone of the flow field length scales are larger. Based on this observation, we perform parametric study on the influence of the swirl number at the inlet in order to enhance the turbulence intensity in the near fuel injector and thus seek optimum operating conditions.

6.3 Spray combustion in complex configuration: gas turbine engine

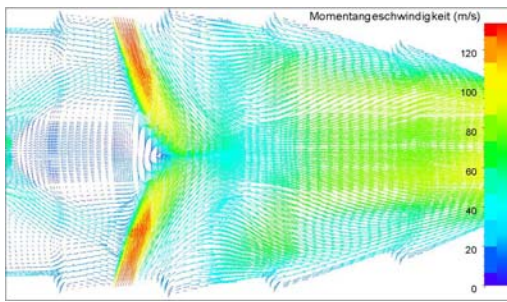


Figure 6.31: Velocity vectors in the fuel injector plane ($k-\varepsilon$ model)

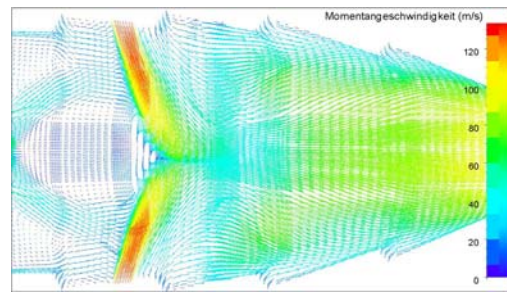


Figure 6.32: Velocity vectors in the fuel injector plane (RSM(JM) model)

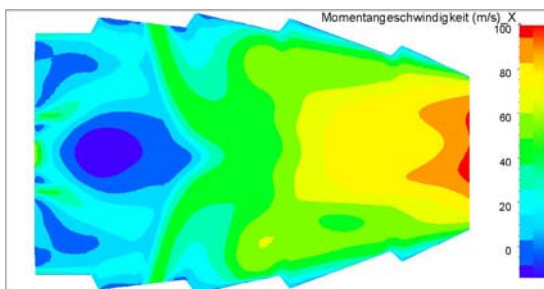


Figure 6.33: Axial velocity in the fuel injector plane ($k-\varepsilon$ model)

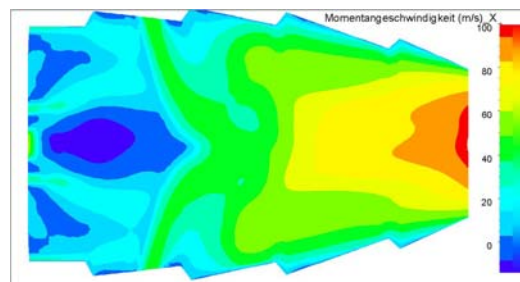


Figure 6.34: Axial velocity in the fuel injector plane (RSM(JM) model)

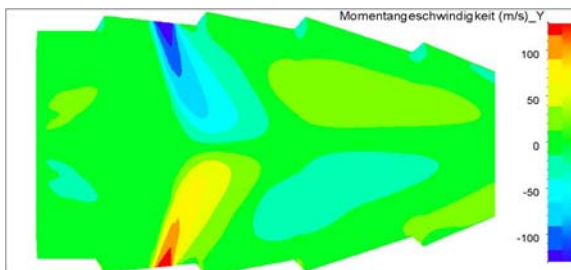


Figure 6.35: Radial velocity in the fuel injector plane ($k-\varepsilon$ model)

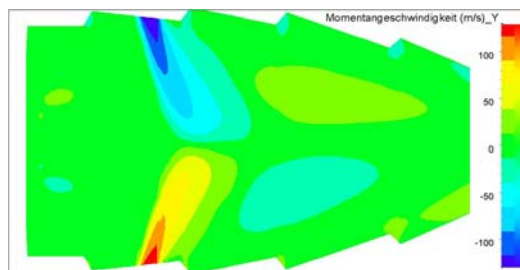


Figure 6.36: Radial velocity in the fuel injector plane (RSM(JM) model)

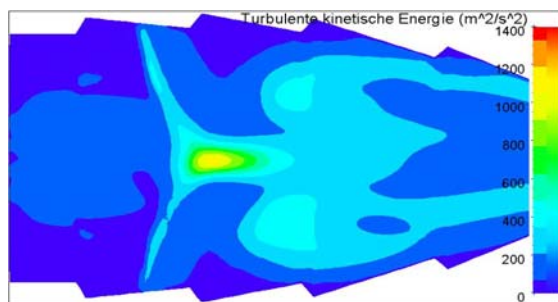


Figure 6.37: Turbulent kin. energy in the fuel injector plane ($k-\varepsilon$ model)

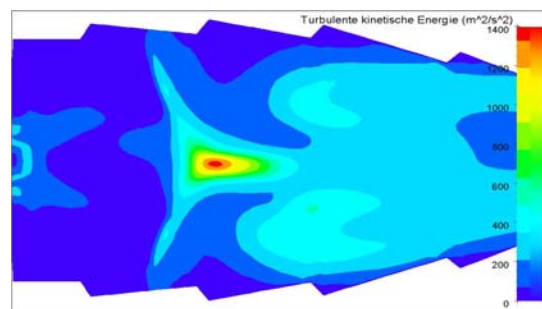


Figure 6.38: Turbulent kin. energy in the fuel injector plane (RSM(JM) model)

Concerning the spray behavior, one observes that droplets are nearly completely evaporated when they reach the first z-ring as shown in Figure 6.39 and Figure 6.40. Results using RSM model show higher evaporation rate than $k-\varepsilon$ model. The spray seems to be deeply influenced by the carrier phase flow near the atomizer exit since its momentum is quite high in this region.

One notices that the spray opening angle computed using $k-\varepsilon$ turbulence model is less than RSM where droplets are dragged away by the gas flow towards the external wall.

Contour plots of the mixture fraction and temperature at the symmetry plane as well as the temperature traverse at the combustor exit are presented in Figure 6.41 - Figure 6.46. The local mixture, in the first part of the combustion chamber, is rich but rapidly mixes with air coming from mix-opening, which is perforated on the external wall.

The turbulent mixing between air and fuel is enhanced by the swirl effect. On the other hand, the air flows coming from the chute openings (see Figure 6.28) have a strong influence on the internal aerodynamics. Indeed they have opposite tangential velocities, which interact with the jets coming from the mix-openings (see Figure 6.28) and thus provoking regions that propagate till combustor exit. Results calculated using $k-\varepsilon$ model are similar to the RSM model. Some differences are seen in the second part of the combustion chamber where the mixture fraction predicted using RSM is higher than the one computed with $k-\varepsilon$ model.

Temperatures are function of the mixture fraction and its variance ranging from values of the inlet air temperature to equilibrium temperature. Close to the nozzle exit, despite low mixture fraction, the temperature remains below the stoichiometric value because of the cooling effect of the evaporating spray. The flame position indicated by the stoichiometric value of mixture fraction shows how close the flame can come to the liner wall, and gives a hint about the 3D geometry of the flame surface (Figure 6.43 and Figure 6.44).

The result of the combustion and mixing process which is represented by the temperature traverse at the combustor exit, as shown in Figure 6.45 and Figure 6.46, points out a remarkable difference between $k-\varepsilon$ and RSM turbulence models. The last one exhibits a smoother distribution of the temperature, whereas $k-\varepsilon$ shows higher values and hot spots about 2000K. These spots stem from the incomplete mixing process between the hot combustion products and the secondary air jets (predicted by $k-\varepsilon$ model). Furthermore low temperature values closed to the liner wall are visible, because of the z-rings cooling. The stoichiometric mixture fraction is very small in the used C10H22 diffusion flame, ($\tilde{z}_{st} = 0.063$). Due to this low stoichiometric mixture fraction value, small errors in the mixture fraction prediction will cause larger errors in the concentration and temperature field.

6.3 Spray combustion in complex configuration: gas turbine engine

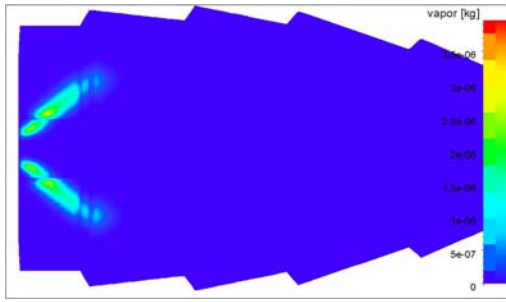


Figure 6.39: Vapor concentration in the fuel injector plane ($k-\varepsilon$ model)

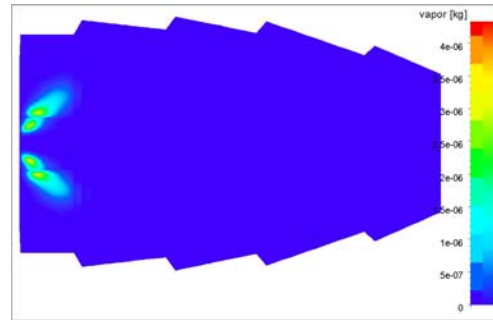


Figure 6.40: Vapor concentration in the fuel injector plane (RSM(JM) model)

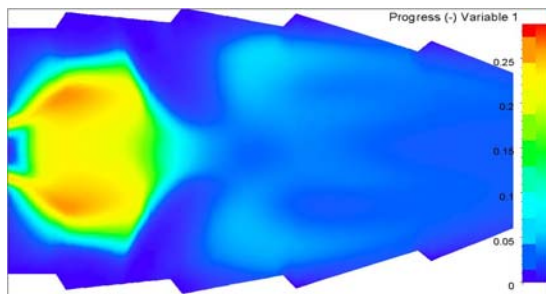


Figure 6.41: Mixture fraction in the fuel injector plane ($k-\varepsilon$ model)

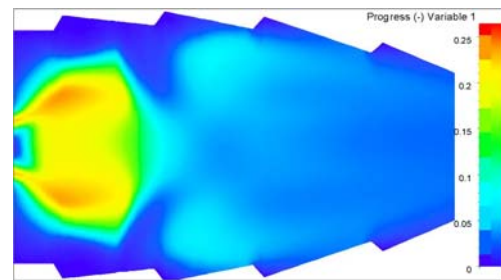


Figure 6.42: Mixture fraction in the fuel injector plane (RSM(JM) model)

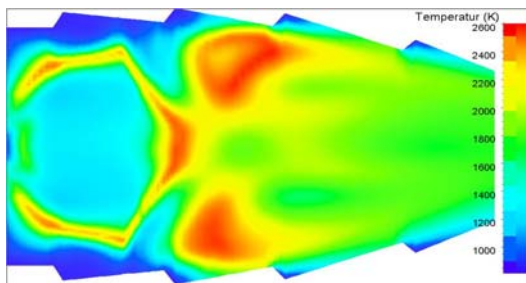


Figure 6.43: Temperature in the fuel injector plane ($k-\varepsilon$ model)

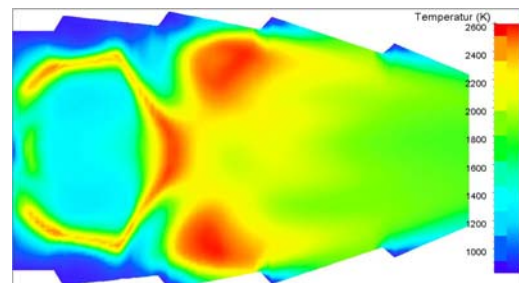


Figure 6.44: Temperature in the fuel injector plane (RSM(JM) model)

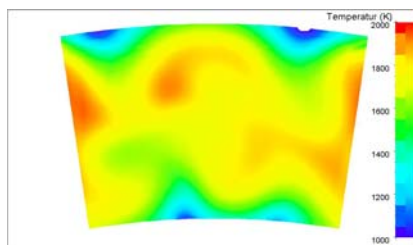


Figure 6.45: Temperature traverse at the combustor exit ($k-\varepsilon$ model)

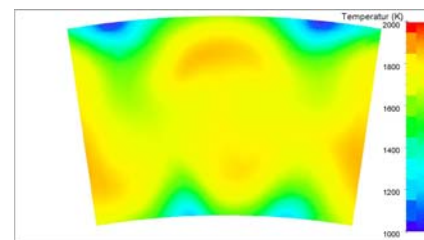


Figure 6.46: Temperature traverse at the combustor exit (RSM(JM) model)

For design process, typically the combustor exit temperature pattern, in terms of the Temperature Distribution Factor (RTDF), is required. The RTDF parameter is used as a measure of the uniformity of the gaseous temperature profile presented to the gas turbine vanes. It is defined as follows:

$$RTDF(r) = \frac{T(r) - T_{avg}}{T_{avg} - T_{inl}}, \quad (6.10)$$

where $T(r)$ is the tangentially averaged mean temperature in the exit plane, written as

$$T(r) = \frac{1}{2\pi} \int_0^{2\pi} \tilde{T}(r, \theta) d\theta. \quad (6.11)$$

T_{avg} and T_{inl} are the surface averaged temperature in the exit plane and inlet temperature, respectively.

Figure 6.47 shows the variation of the non-dimensional RTDF calculated using $k-\varepsilon$ and RSM models versus percentage of the combustor exit duct height. The numerical results are compared to experimental measurements. From the test results three curves are shown, the minimum temperature for a constant radius T_{min} , the circumferential average temperature for a constant radius T_{mean} , and the maximum temperature for a constant radius T_{max} . The numerical results with both turbulence models ($k-\varepsilon$ and RSM) predicted well the RTDF distribution, which lied between the minimum and maximum curves. The CFD results show the typical parabolic shape with almost constant curvature as the measurements. The RTDF features a lower temperature on the wall border of the combustor due to the penetration of the cooling air. Therefore, parametric study concerning modification of air mass flow distribution should be done in order to investigate how to reduce temperature differences at the exit and thus improve the combustor design.

The predicted RTDF ranges between 12% and -24%, which would represent an acceptable combustor exit temperature profile in an engine application. The RTDF computed using RSM model shows a good agreement with test results in the upper part of the combustor exit duct height whereas in the lower part, $k-\varepsilon$ turbulence model predict the most favorable results.

Figure 6.48 - Figure 6.52 show a detailed comparison of CFD results computed using $k-\varepsilon$ and RSM models with the test data and a commercial CFD-Tool where simulation results were published in [131]. The measured exit temperature is plotted at 5 radial duct height positions, as mentioned before, for two sectors of 36° . First one can observe that the periodicity behavior is captured well by the calculation. In Figure 6.48, which represents the radial position closest to the inner liner, the maximum predicted temperature by $k-\varepsilon$ turbulence model is about 100 K higher

6.3 Spray combustion in complex configuration: gas turbine engine

than experimental data, especially at the interface of two sectors, whereas RSM model yields a temperature difference of 70 K. The temperature over prediction is due to the fact that the combustion model does not consider energy exchanges through the wall or heat losses due to radiations. Figure 6.49 and Figure 6.50 notice that predicted temperature using RSM model has less modifications and agree better than $k-\varepsilon$ model compared to test data. The commercial CFD-Tool predicted high temperature variations compared to FASTEST code (Figure 6.50). In Figure 6.51 and Figure 6.52 the RSM turbulence model exhibits lower temperature distribution than $k-\varepsilon$. This is originated to the fact that RSM model provided better air-fuel mixing as seen in the temperature contour plots at the traverse (Figure 6.46). Furthermore, one observes that FASTEST results agree better with experimental measurements than the commercial CFD-Tool.

In general, deficiencies of temperature details are remarkable, especially where mixing is not well predicted. Nevertheless, the quantitative periodic behavior of numerical predictions and experimental results are basically in agreement. The predicted RTDF distributions are satisfactory and provide plausible results compared with measurements, i.e. CFD results are quite promising.

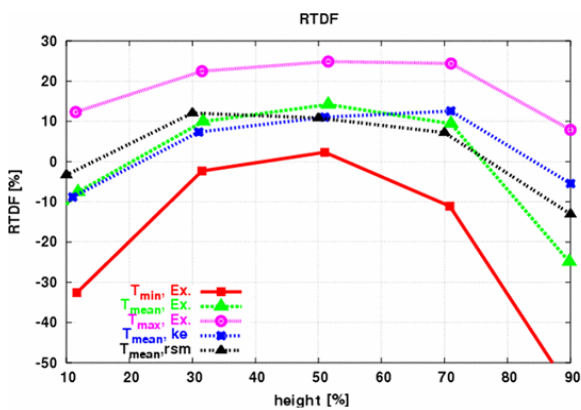


Figure 6.47: Radial distribution of the RTDF: comparison between num. results and measurements

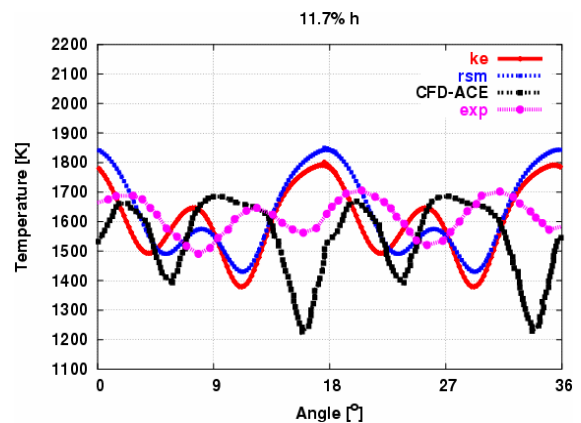


Figure 6.48: Temperature vs. angle for 11.70% of the duct height

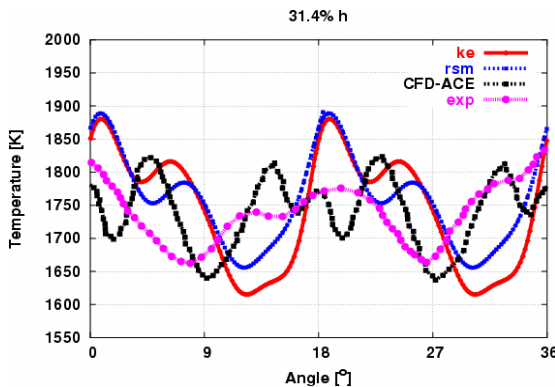


Figure 6.49: Temperature vs. angle for 31.43% of the duct height

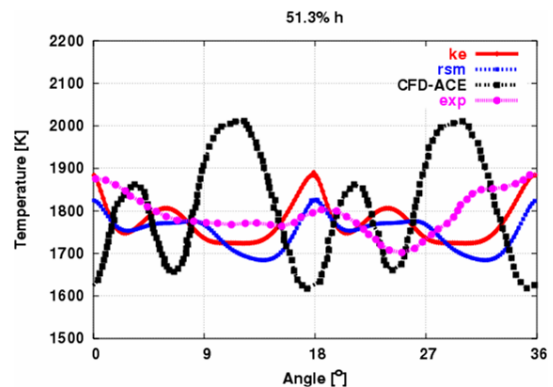


Figure 6.50: Temperature vs. angle for 51.38% of the duct height

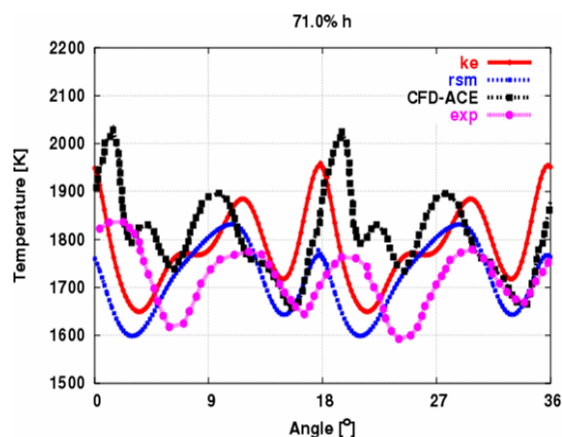


Figure 6.51: Temperature vs. angle for 71.07% of the duct height

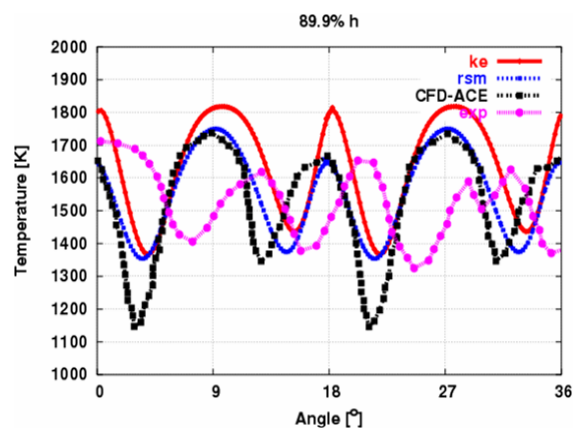


Figure 6.52: Temperature vs. angle for 89.97% of the duct height

Effect of modulation modeling on the RTDF prediction

The results in Figure 6.53 and Figure 6.54 show the influence of turbulence modulation modeling on the Radial Temperature Distribution Factor (RTDF) using the standard modulation model and the thermodynamically consistent model by Sadiki & Ahmadi [86], respectively. The injected fuel droplets have a mean diameter of $20\ \mu\text{m}$, i.e. used particles are small compared to turbulent length scales, which range between $100\ \mu\text{m}$ close to inlets and $20\ \text{mm}$ in the recirculation zone (see Figure 6.55). The fact that the smallest turbulent length scales are 5 times bigger than the mean droplet diameter ensures the dissipative behavior of the dispersed phase. Since they have a negative sign, the computed source terms of the droplets added to the balance equation of the turbulent kinetic energy confirm this theory.

As mentioned in the section 6.3.2 (Flow conditions) the used Air-Fuel Ratio (AFR) for take off conditions equals 40.7. I.e. the mass loading of multiphase flows, as defined in the second chapter, is 2.45%, which represents a low loading. However droplets are located more close to the nozzle exit, where spray is going to be injected. Thus, the droplet mass loading can be very large at this region so that momentum exchange between dispersed phase and gas results in a significant modulation of the turbulence.

The numerical simulations have shown that the modulation of the flow turbulence due to the presence of droplets using the standard model can provide in cells with high mass loading a huge negative values for the source terms. Thus, on the one hand, the standard model can significantly modify the prediction of the behavior of the turbulent kinetic energy and give rise to convergence problems. On the other hand, the thermodynamically model computed also negative values for the source terms of the turbulent kinetic energy, which confirms the dissipative behavior of the two ways coupling, but the source terms distribution was smooth and does not feature huge values.

6.3 Spray combustion in complex configuration: gas turbine engine

It can be seen in Figure 6.53 that the standard model clearly affects the temperature distribution on the combustor exit, whereas the thermodynamically model does not. This is due to following two reasons, which indeed are applied for both models:

- 1) The spray injection is far away from the combustor exit
- 2) The droplets are rapidly evaporated due to the high temperature and small droplet diameters

The thermodynamically modulation model tends to provide an acceptable agreement with experimental data of the temperature distribution at the exit (see Figure 6.54). In addition the numerical convergence is achieved in an easier way than simulations using the standard model.

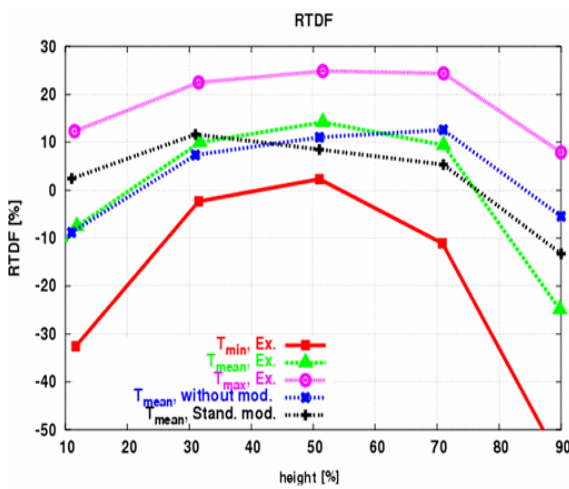


Figure 6.53: Radial distribution of the RTDF: effect of standard modulation modeling

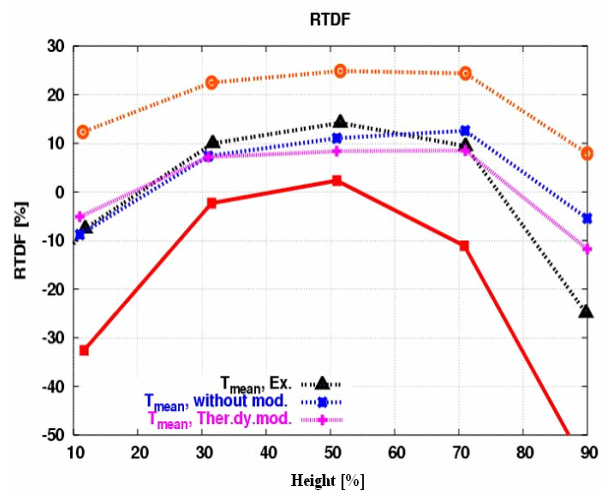


Figure 6.54: Radial distribution of the RTDF: effect of thermodynamically consistent modulation modeling by Sadiki & Ahmadi

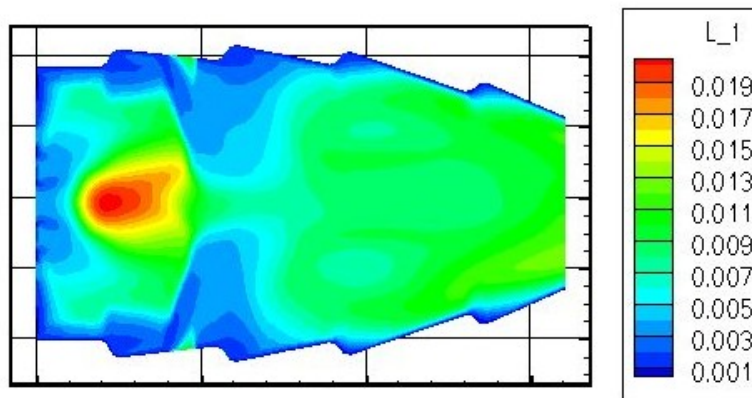


Figure 6.55: Contour plot of the turbulent length scale in the injector fuel plane

Effect of evaporation models on combustion prediction

In Figure 6.56 and Figure 6.57 one can observe slight differences in temperature profile due to the different evaporation model contributions. Close to the fuel injector nozzle where gas inlet velocities rise to 130 m/s, droplets are subjected to high relative velocity ($Re_p = 323$). Consequently the dispersed phase faces rapid thermodynamical variations. Droplets, therefore, do not have enough time to attain a thermodynamical state. So phase transition occur in a non-equilibrium way. The non-equilibrium evaporation conditions are derived from the large temperature and surface pressure variation of the droplets. Nevertheless, the model by Langmuir-Knudsen [31] does not exhibit important change compared to the equilibrium evaporation model by Sirignano [34]. Figure 6.58 shows the computed fuel vapor concentration obtained using non-equilibrium model. One can observe that droplets exceed the first z-cooling ring, which is not the case with the equilibrium model (compare to Figure 6.39). The evaporation rate is, therefore, smaller estimated by the equilibrium model. For this reason the temperature distribution, at the combustor exit, is over predicted by the non-equilibrium model (see Figure 6.56 and Figure 6.57). It appears that both models provide similar results for the temperature distribution. This is due to the Knudsen thickness in the non-equilibrium contribution $2L_K\beta_L/d$ (see equation (3.74)), which yields the deviation from the equilibrium state. It is generally relatively small for droplets at high pressure as it is the case within this configuration. In fact, the Knudsen layer thickness is given by:

$$L_K = \frac{\mu_G \sqrt{2\pi T_d R / W_v}}{\alpha_e S_{c_G} P_G}, \quad (6.12)$$

where α_e is the molecular accumulation coefficient (assumed equal to unity), T_d the droplet temperature, μ_G the carrier phase viscosity, W_v the molecular weight of vaporized fuel, R the universal gas constant, S_{c_G} the gas Schmitt number and P_G denotes the total pressure, which reign in the combustion chamber. As introduced in the section "flow conditions", P_G equals $12.41 \cdot 10^6 \text{ Pa}$, which makes the Knudsen thickness about 12 times smaller than in case of evaporation at atmospheric conditions. The high pressure in the combustor is thus responsible for the small deviation of the equilibrium state.

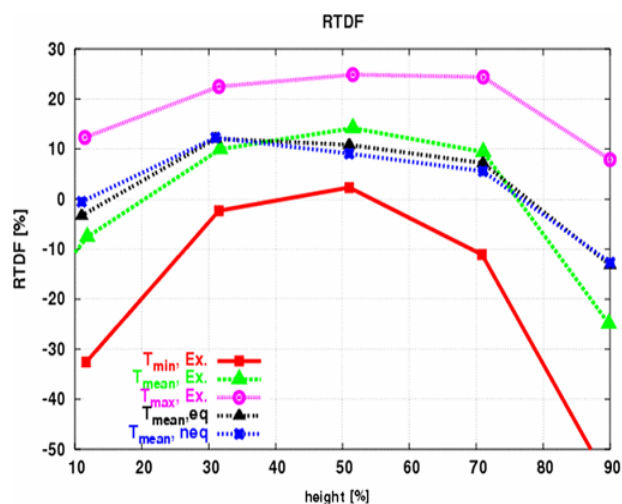


Figure 6.56: Radial distribution of the RTDF: contribution of equilibrium and non-equilibrium evaporation models

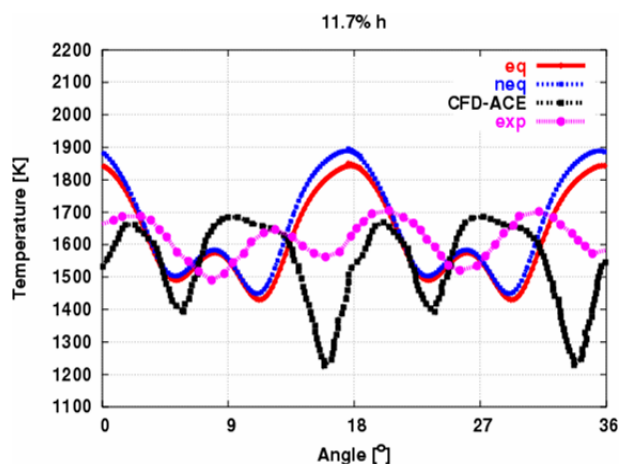


Figure 6.57: Temperature profile vs. angle for 11.70% of the duct height: comparison between equilibrium and non-equilibrium evaporation models

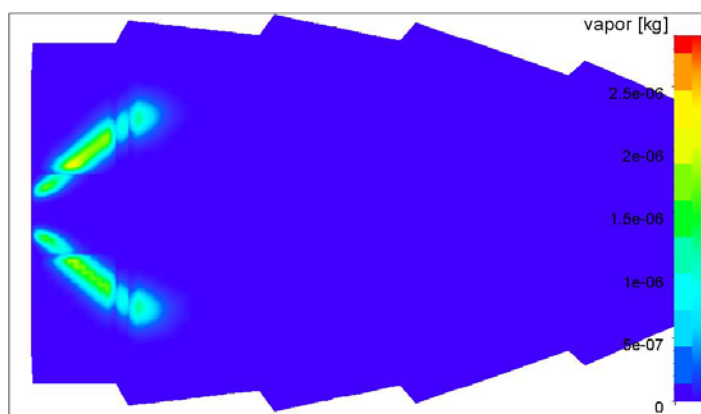


Figure 6.58: Vapor concentration in the fuel injector plane obtained with non-equilibrium evaporation model

6.3.3.2 Flamelet chemistry

In order to investigate the effect of the deviation from equilibrium chemistry on the prediction of combustion and mixing properties, we apply within this section, the flamelet chemistry model. For this purpose, flamelet look up tables have been incorporated according to Figure 3.3. These look up tables have been created using CHEM1D code, which was kindly provided by de Goey [133]. The used reaction mechanism involves 63 species and accounts for 315 reactions. The essential feature of the flamelet approach is that the scalar dissipation rate χ (see equation (3.88)) appears explicitly as a parameter in the model. The scalar

dissipation rate determines the rate of molecular mixing in the flow and quantifies the departure from equilibrium.

Using multiple flamelets allows accounting for spatial variations of the scalar dissipation rate which is especially important in this test case, since the complex configuration includes fuel rich and lean zones, and regions of very high shear due to recirculations. The computational domain has been, therefore, divided into three regions having different scalar dissipation rates (see Figure 6.59), each of them corresponds to one flamelet table. The number of flamelet sets in the flamelet library is therefore equal to 3. The highest value for the scalar dissipation rate is located close to the fuel nozzle exit because of the high variance of the mixture fraction. The numerical simulations were achieved using non-equilibrium evaporation model, $k-\varepsilon$ turbulence model and thermodynamically consistent modulation model.

Figure 6.60 shows the contour plot of the mixture fraction, which reveals no remarkable differences compared to equilibrium chemistry (Figure 6.41). The reason behind this lies on the negligible density variation, which was computed using flamelet or equilibrium models. The same density as well as the same boundary conditions provides similar velocity field and thus no differences on the mixture fraction distribution. In contrast computations including the flamelet turbulent combustion model predict a lower peak reaction temperature and a more gradual temperature decrease than predictions using equilibrium chemistry. Figure 6.61 and Figure 6.62 show the temperature contour plot in the fuel injector plane and at the combustor exit obtained using the flamelet tables. One can clearly observe the differences in the first part (rich zone) of the combustor (Figure 6.61) compared with equilibrium model (Figure 6.43). For the rich zone, two tables having scalar dissipation rate of 68.431 s^{-1} and 459.07 s^{-1} provide about 300 K less than the equilibrium model. Moreover, the flame front in the rich zone appears close to the wall and exhibits a wide margin.

One should mention that local extinction events did not occur since the local value of the mixture-fraction dissipation rate remains below the critical quench value which corresponds to a strain rate of 9300 s^{-1} .

A contour plot of the temperature traverse is shown in Figure 6.62. Results obtained with flamelet tables do not differ from those of equilibrium model due to the fact that non-equilibrium effects manifest themselves mainly at the stoichiometric ($\tilde{z}_{st}=0.063$) values [74], whereas at the combustor exit, the mixture fraction reveals a value usually smaller than 0.03. Thus the radial temperature distribution factor at the combustor exit shows almost the same profile compared to equilibrium chemistry model (see Figure 6.63). Peters wrote in his paper [132] "The outer flow field acts upon the flamelet structure only through the scalar dissipation rate at stoichiometric mixture". Temperature distributions

6.3 Spray combustion in complex configuration: gas turbine engine

computed using flamelets model can be, therefore, considered as plausible.

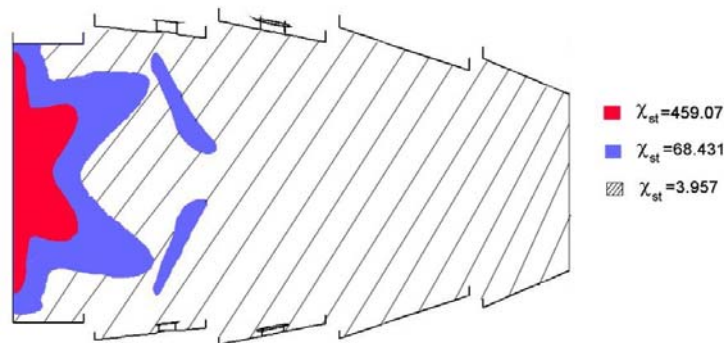


Figure 6.59: Repartition of scalar dissipation rate over the computational domain

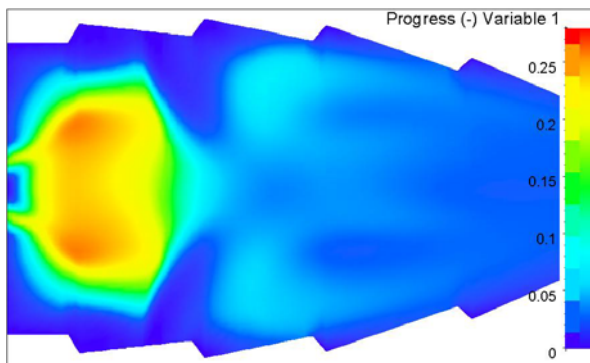


Figure 6.60: Mixture fraction in the fuel injector plane obtained with flamelet model

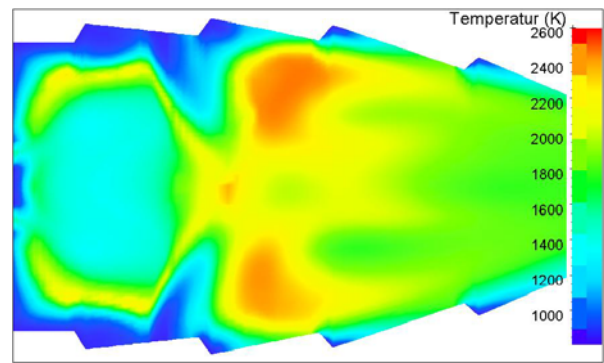


Figure 6.61: Temperature variation in the fuel injector plane using flamelet model

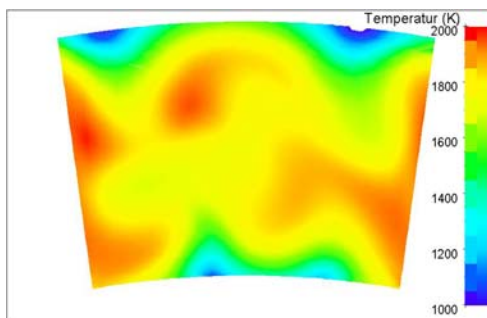


Figure 6.62 Temperature traverse at the combustor exit using flamelet model

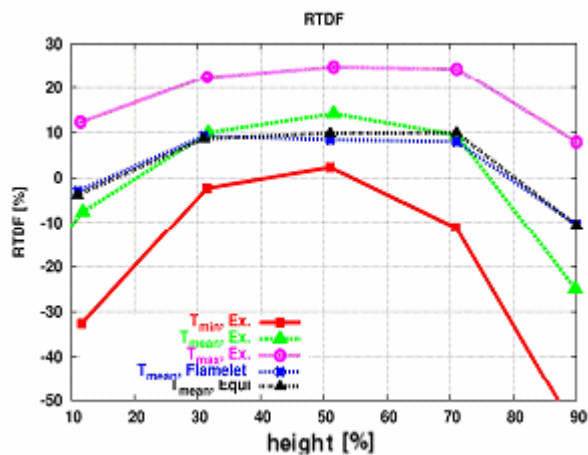


Figure 6.63: Radial distribution of the RTDF; comparison between flamelet and equilibrium models

6.3.3.3 Unsteady RANS

As pointed out in Figure 6.48 - Figure 6.52, experimental data have shown a high dependency of the mean temperature at the combustor exit of the sector angle, which may be induced by coherent structures. Therefore, it is of great importance to capture transient effects of the three dimensional reacting flow. For this purpose unsteady computations were carried out using the standard $k-\varepsilon$ turbulence model as well as the Reynolds stress model.

Transient computations of turbulent multiphase flows in the frame of Eulerian Lagrangian approach is generally achieved by exchanging of data within every time step [44], i.e. droplets are tracked, not from injection to outlet or until complete evaporation, but during the same step considered for the carrier phase. This procedure of Eulerian Lagrangian coupling necessitates that the source terms in transient equations, which characterize the particle-fluid interaction, should be calculated, averaged and substituted every time step. Thus, the unsteady computations of multiphase flows require high computational costs.

In the frame of this work unsteadiness is accounted for only for the gas phase, while droplets are tracked from the start point until complete evaporation. Unsteady Eulerian Lagrangian coupling, as outlined above, demands a huge implementation input. Therefore, this task is referred to as a future work. However, a first attempt toward this investigation is provided in this section. To this end, time dependent terms are included into the governing equations of the carrier phase.

During the unsteady flow simulations, two monitoring points at different radial and axial positions within the recirculation zone, as shown in Figure 6.64 were controlled. In order to increase the accuracy, time dependent terms in the governing equations were carried out using an implicit second order accurate scheme. A convergence solution could be attained for a time step of $5 \cdot 10^{-4}$ s in about 30 iterations.

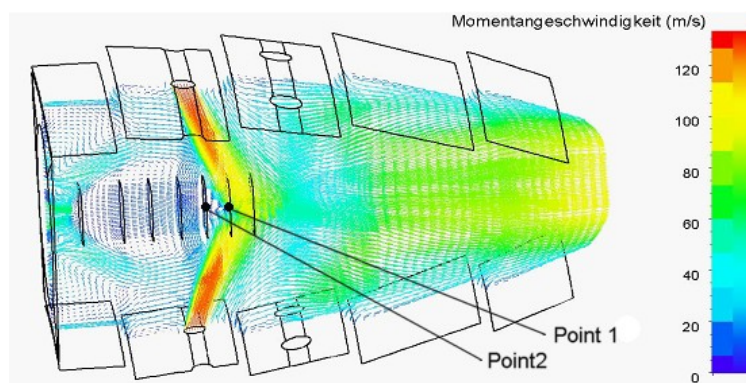


Figure 6.64: Monitoring points for the unsteady computation

Applying the standard k - ϵ model, the transient simulation led to a steady state flow solutions. The velocity results shown that in the center of the used combustion chamber, a strong recirculation region was obtained. This region is, however, a steady state and symmetrical. The k - ϵ model was found to be inadequate in representing the complex time dependent turbulent structure of multiphase reacting flows, due to the strong dissipation introduced by the turbulent viscosity. The same notices were mentioned by Maltsev [134] within his work showing that the standard k - ϵ model showed damping of the coherent fluctuations. Hereby one can deduce that k - ϵ turbulence model, in the frame of this configuration with a resolution of 350 000 cells, was not suitable for unsteady problems. It does not distinguish between the resolved unsteady vortex structure and the averaged turbulence.

With the application of Reynolds Stress Model (by mean of pressure strain correlations of Jones [103]), one obtains a much lower dissipation than the standard k - ϵ model. As a consequence unsteady velocity oscillations could be captured. One should mention here that for the discretization of convective terms of momentum equations the upwind scheme was not suitable, since tests performed show that the 1st order upwind scheme is very diffusive and should be avoided. In contrast, flux blending spatial discretizations (with $\gamma=0.7$) were found to be far more accurate than the upwind schemes. Figure 6.65 - Figure 6.68 show the axial, tangential, radial and absolute velocity monitored at point 1, respectively. One can clearly observe that the Reynolds Stress model provided stable velocity oscillations. It can be also noticed that the resolved mean flow structures which are primarily larger than the modeled turbulent eddies exhibit an unsteady character. Moreover, the RSM approach revealed the same oscillation frequency of 200 Hz for all velocity components. Figure 6.69 shows the absolute flow velocity captured at the monitoring point 2 as function of time. Also point 2 exhibits a clear periodical character.

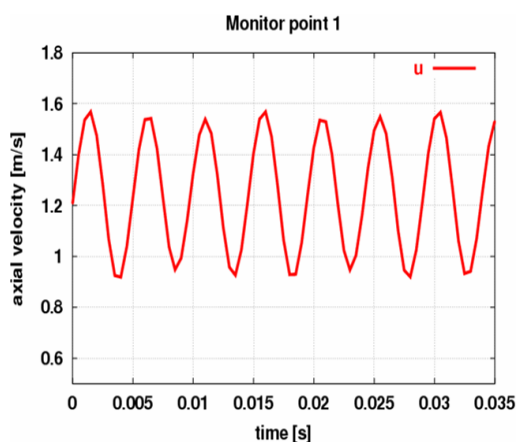


Figure 6.65: Axial velocity as function of time at monitoring point 1

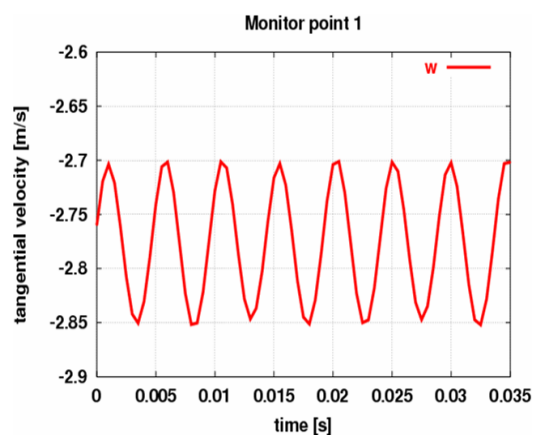


Figure 6.66: Tangential velocity as function of time at monitoring point 1

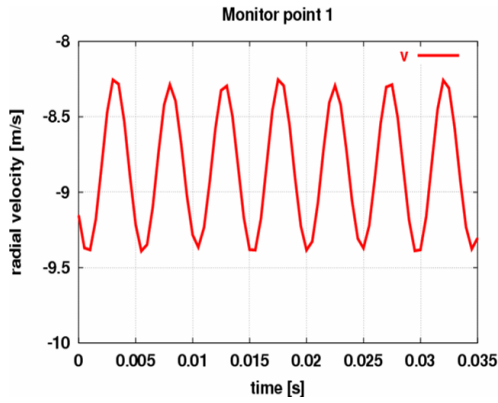


Figure 6.67: Radial velocity as function of time at monitoring point 1

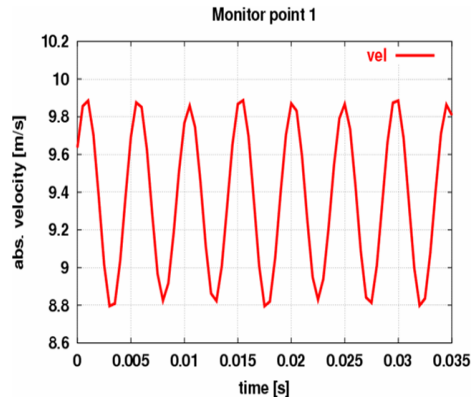


Figure 6.68: Absolute velocity as function of time at monitoring point 1

The presence of large unsteady structures resolved in the URANS computations requires some special treatment when evaluating the time averaged quantities that have to be further compared to the experimental data. In Figure 6.70 an idealized representation of the time evolution of a scalar at some spatial location x is shown. In the presence of a coherent motion the instantaneous scalar can be decomposed as

$$\psi(x, t) = \underbrace{\bar{\psi}(x) + \hat{\psi}^*(x, t)}_{\hat{\psi}(x, t)} + \psi'_{ph}(x, t), \quad (6.13)$$

where $\bar{\psi}$ is the time averaged scalar, $\hat{\psi}$ the phase averaged scalar (resolved directly in URANS), ψ^* the deviation of the phase averaged from the time averaged scalar and ψ'_{ph} is the remaining random fluctuating contribution (modeled in URANS) that is not included in the coherent part. Having the time series of the phase averaged scalar $\hat{\psi}$, obtained directly from the RANS computations, the time averaged mean scalar is obtained from the simple averaging over all samples as

$$\bar{\psi} = 1/N \sum_{k=1}^N \hat{\psi}_k. \quad (6.14)$$

Here, N denotes the number of samples. This procedure was followed in order to obtain the time averaged radial temperature distribution factor (RTDF) at the combustor exit obtained by transient computations.

Figure 6.71 shows the contour plot of the temperature traverse. One observes obvious differences between the unsteady averaged temperature obtained with URANS and results of steady computation shown in Figure

6.3 Spray combustion in complex configuration: gas turbine engine

6.46. The temperature contour plot calculated with URANS features a smooth variation. The arithmetic mean temperature at the exit has the normalized value of 199.16 % which is very close to the experimental measurements having a normalized value of 199.64 %. The time averaged radial temperature distribution factor (RTDF) is presented in Figure 6.72. Here, the numerical simulations show also plausible results. The measurements exhibit a symmetrical profile, which is well predicted by the numerical computations.

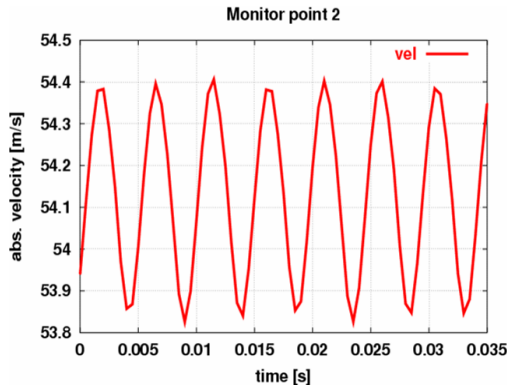


Figure 6.69: Absolute velocity as function of time at monitoring point 2

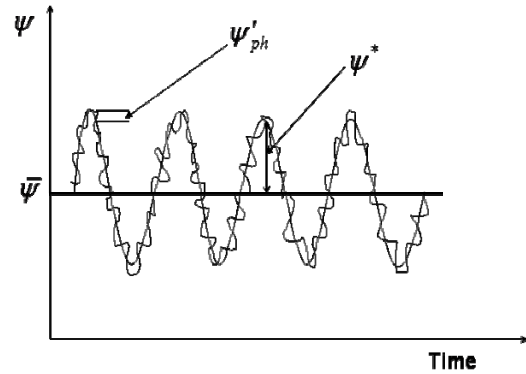


Figure 6.70: Idealized representation of resolved and non-resolved velocity fluctuations in URANS

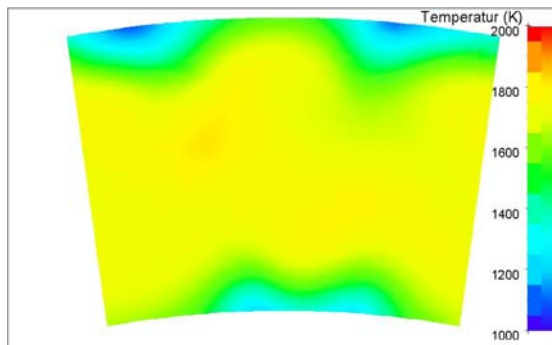


Figure 6.71: Temperature traverse at the combustor exit

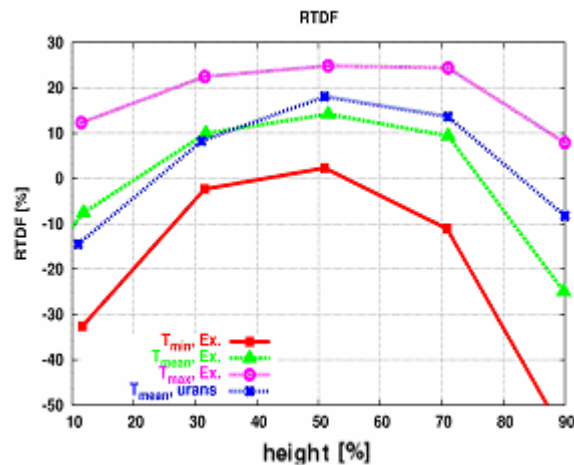


Figure 6.72: Radial distribution of the RTDF

As a conclusion it clearly appears for a moderate resolution of the flow system, that the unsteady RANS simulations using Reynolds Stress Models are generally able to capture the large vortex dynamics and the associated velocity oscillations, whereas the standard $k-\epsilon$ model failed to reproduce the unsteady flow character. Nevertheless, the unsteady multiphase-flows combustion in the frame of Eulerian Lagrangian

approach should be considered also for the dispersed phase. However such multiphase flows simulations are coupled with high data transfer, which require high memory allocation. Another problem for unsteady computations of complex combustion chamber is that the flow contains a large range of frequencies. In order to resolve the high frequencies sufficiently accurate a small computational step has to be chosen. This, however, results in very long computational times when also low frequency phenomena have to be resolved.

7 Conclusion

The work presented in this thesis resulted in the development and application of different mathematical sub-models to describe the physics of turbulent reacting spray typical for gas turbine combustors. The resulting complete models were formulated in the Eulerian-Lagrangian context and include the following elements:

- Emphases were primarily put on the interaction between solid particles and turbulence seeking a correct prediction of turbulent quantities in turbulent two phase flows. The investigation of the feedback mechanism of particles on the continuous phase within the turbulent two-phase flow which is known as turbulence modulation, was carried out in a vertical orientated wind-tunnel. Air was used as a continuous phase whereas glass beads built the dispersed phase.

The numerical work was performed with three different modulation models. Computations reveal that the obtained results of the turbulent kinetic energy along the channel center line using the thermodynamically consistent model, reproduce well both the turbulence attenuation and production. Indeed, the standard model underestimates the turbulence. This model is dissipative for small ($120\mu\text{m}$) and big ($480\mu\text{m}$) particles, whereas the model by Crowe is overall productive. Compared to the experimental data, the particle turbulent kinetic energy is over-predicted. Future work can focus on the way how to determine dynamically the model coefficients of the thermodynamically consistent modulation model.

- The study of the isothermal swirling particulate two-phase flow [124] has shown the influence of the swirled co-flow on the behavior of the dispersed phase in particular particle dispersion, velocities and fluctuations of the carrier phase. A good prediction of particles evolution properties under turbulent conditions was observed. It must be emphasized here, that it is very difficult to find available experimental data exactly in the vicinity of the particle injection nozzle due to the presence of high loading of particles. To properly represent accurate inflow boundary conditions for the dispersed phase, which is an actual point of issue, one should use the Eulerian-Eulerian approach in the vicinity of particles inlet where a very dense two-phase flow is expected.
- In order to assess the ability of the equilibrium uniform temperature as well as the non-equilibrium evaporation models to successfully predict the mass transfer and vapor distributions, the test case measured by Sommerfeld et al. [4], which consists of spray issuing into a co-flowing heated air stream, has been numerically

investigated. For that purpose spray evaporation models have been developed, integrated in FASTEST/LAG3D code and subsequently applied. The computations were achieved using a fully two-way coupling process. A systematical study of the interaction processes including turbulence, turbulence modulation, mass and heat transfer has been satisfactory carried out. Simulations showed that non equilibrium model agree most favorably with experimental measurements of the droplet mass flux.

In order to characterize the turbulence-droplet vaporization interaction regimes, a vaporization Damkohler number (Da_v) has been introduced. Numerical results have demonstrated that in case of $Da_v > 1$ turbulence augmentation enhances the evaporation rate, whereas for $Da_v \leq 1$ the opposite phenomenon takes place, namely the rate of evaporation is reduced.

In addition to some parametric studies, the effect of a correction drift term in the dispersion model and its influence on the prediction of the evaporation rate as well as the vapor concentration and droplet spatial repartitions were investigated. It appeared that the use of drift correction term provided higher evaporation rates than experimental measurements. This was mainly due to higher droplet velocities which in turn induced higher relative velocity between fluid and the dispersed phase and thus enhanced the rate of evaporation.

- The spray combustion was studied in a complex industrial configuration, which consists of a single annular combustor that was experimentally measured by Rolls-Royce Deutschland. Simulations were performed using $k-\varepsilon$ as well as Reynolds Stress model (Jones Musonge) for turbulence, an assumed shape of probability density function to prescribe turbulence combustion interaction and different models describing the turbulence modulation. Equilibrium and a flamelet chemistry approaches were used.

Results showed that predicted RTDF distributions are satisfactory and provide plausible results compared with measurements, i.e. CFD results were quite promising. The quantitative periodic behavior of numerical predictions and experimental results were basically in agreement. However, deficiencies of temperature details were remarkable especially where mixing is not well predicted. Due to the low stoichiometric mixture fraction ($\tilde{z}_{st} = 0.063$), small errors in the mixture fraction prediction have caused larger errors in the temperature field. The use of the thermodynamically consistent modulation model allows an acceptable behavior of the temperature distribution compared to the standard modulation model. Furthermore, with the thermodynamically consistent model, it was easier to achieve numerical convergence than using the standard model. On the other hand, both evaporation models (equilibrium and non-equilibrium) provided similar results for the temperature

distribution. This was originated in the high pressure of the combustion chamber, which in turn provided a small value for the Knudsen thickness responsible for the deviation of the equilibrium state. It is therefore advisable to develop appropriate models which account for evaporation under high pressure.

Numerical computations including the flamelet turbulent combustion model predicted a lower peak reaction temperature and a more gradual temperature decrease than predictions using equilibrium chemistry. For the rich zone two tables having scalar dissipation rate of 68.431 s^{-1} and 459.07 s^{-1} provided about 300 K less than the equilibrium model. Moreover, the flame front in the rich zone appeared closer to the wall and exhibited a wide margin.

First unsteady RANS simulations were performed using Reynolds Stress Model, which was able to capture the large vortex dynamics and the associated velocity oscillations. The standard k- ϵ model, however, failed to reproduce the unsteady flow character (for the used grid resolution). URANS provided better agreement with experimental data in predicting the radial temperature distribution factor (RTDF) than steady RANS calculations. Nevertheless the unsteady multiphase-flows computation in the frame of Eulerian Lagrangian approach should be considered also for the dispersed phase. The couplings between both phases for unsteady turbulent spray combustion (in terms of interface source terms) demand, however, a high memory allocation and expensive computational time.

As final conclusion one can reiterate that the combination of the following sub-models: thermodynamically consistent model for the turbulence modulation, Langmuir-Knudsen non-equilibrium model for the evaporation, Reynolds Stress Model for the turbulence and flamelet model for the chemistry establish a reliable complete model that seems to allow a better description of reactive multi-phase flow studied in the frame of this work.

8 Bibliography

- [1] Buenos Aires, Weltenergiekonzern 2001
- [2] Kuo, K., Recent Advances in Spray Combustion: Spray Combustion Measurements and Mode Simulation, vol. II, AIAA, Inc., 1996
- [3] Sato Y. (1996) Turbulence structure and modeling of dispersed two-phase flows. Keio: Ph.D. thesis, Keio University, Japan.
- [4] Sommerfeld, M., Qiu, H.H., Rüger, M., Kohnen, G., Spies, P.J., Müller, D., (1993), "Spray evaporation in turbulent flow", Proceedings of the 2nd Int. Symp. on Engineering Turbulent Modeling and Measurements, Florence, Italy, 31 May - 2 June, pp. 935-945
- [5] Elghobashi SE (1994) On predicting particle-laden turbulence flows. Appl Sci Res 52:309–329
- [6] Crowe CT, Troutt TR, Chung JN (1996) Numerical models for two-phase turbulent flows. Annu Rev FluidMech 28:11–43
- [7] Elghobashi SE, Truesdell GC (1993) On the two-way interaction between homogeneous turbulence and dispersed solid particles. I: turbulence modification. Phys Fluids A 5(7):1790–1801
- [8] Michaelides EE, Stock DE (1989) Turbulence modification in dispersed multiphase flows (FED-Vol 80).ASME, New York
- [9] Owen PR (1969) Pneumatic transport. J Fluid Mech 39:407–432
- [10] Parthasarathy RN, Faeth GM (1990a) Turbulence modulation in homogeneous dilute particle-laden flows. J Fluid Mech 220:485–514
- [11] Parthasarathy RN, Faeth GM (1990b) Turbulent dispersion of particles in self-generated homogeneous turbulence. J Fluid Mech 220:515–537
- [12] Varaksin AY, Zaichik LI (2000) Effect of particles on the carrier flow turbulence. Thermophys Aeromech 7:237–248
- [13] Lei K, Taniguchi N, Kobayashi T (2000) LES of particle-laden turbulent channel flow considering SGS coupling. Trans JSME B 66(651):2807–2814
- [14] Chandok SS, Pei DCT (1972) Particle dynamics in solid-gas flows in a vertical pipe. Prog Heat Mass Transfer 6:465–474
- [15] Meada M, Hishida K, Furutani T (1980) Optical measurements of local gas and solid velocity in an upward flowing dilute gas-solid suspension. Proc. Polyphase Flow and Transport Technology, Century 2-ETC, San Francisco, pp 211–216
- [16] Durst F (1982) Review – combined measurements of particle velocities, size distributions, and concentrations. J Fluid Eng–T ASME 104:284–296
- [17] Tsuji Y, Morikawa Y, Shiomi H (1984) LDV Measurements of an air-solid two-phase flow in a vertical pipe. J Fluid Mech 139:417–434
- [18] Modarress D, Tan H, Elghobashi S (1984) Two-component LDA measurement in a two-phase turbulent jet. AIAA J 22(5):624–630
- [19] Solomon ASP, Shuen J-S, Zhang Q-F, Faeth GM (1985a) Structure of nonevaporating sprays, Part I: Initial conditions and mean properties. AIAA J 23(10):1548–1555
- [20] Solomon ASP, Shuen J-S, Zhang Q-F, Faeth GM (1985b) Structure of nonevaporating sprays, Part II: Drop and turbulence properties. AIAA J 23(11):1724–1730

Bibliography

- [21] Mostafa AA, Mongia HC, McDonnell VG, Samuelsen GS (1989) Evolution of particle-laden jet flows: a theoretical and experimental study. *AIAA J* 27(2):167–183
- [22] Park CJ, Chen L-D (1989a) Experimental investigation of confined turbulent jets, Part I: Particle-laden flow data. *AIAA J* 27(11):1506–1510
- [23] Park CJ, Chen L-D (1989b) Experimental investigation of confined turbulent jets, Part II: Single-phase data. *AIAA J* 27(11):1511–1516
- [24] Schreck S, Kleis SJ (1993) Modification of grid-generated turbulence by solid particles. *J Fluid Mech* 249:665–688
- [25] Gore RA, Crowe CT (1989) Effect of particle size on turbulent intensity. *Int J Multiphas Flow* 15:279–285
- [26] Kulick JD, Fessler JR, Eaton JK (1994) Particle response and turbulence modification in fully-developed channel flow. *J Fluid Mech* 277:109–134
- [27] Hardalupas Y, Taylor AMKP, Whitelaw JH (1989) Velocity and particle-flux characteristics of turbulent particle-laden jets. *P Roy Soc Lond A Mat* 426:31–78
- [28] Hetsroni G (1989) Particles-turbulence interaction. *Int J Multiphas Flow* 15:735–746
- [29] Oefelein J.C., Aggarwal S.K.: toward a unified high pressure drop model for spray simulation, center for turbulence research, Proceedings of summer program 2000, pp. 193-205
- [30] Miller R.S., Harstad K., Bellan J.: Evaluation of equilibrium and non-equilibrium evaporation models for many droplet gas liquid flow simulation, *Int. J. of Multiphase flow*, 24 pp. 1025-1055, 1998.
- [31] Bellan, J., Harstad, K., 1987: Analysis of the convective evaporation of nondilute clusters of drops. *Int. J. Heat Mass Transfer* 30 (1),125-136.
- [32] Prommersberger k, Stengele J, Dullenkopf K, Himmelsbach J and Wittig S “Investigations of droplet evaporation at elevated pressures“ Collaborative Research Center 167, September 1998 Karlsruhe, Germany
- [33] Sirignano W. A.:”Fluid dynamics of sprays” 1992 Freeman Scholar Lecture *J. Fluids Engng.* Vol. 115, pp. 345-378. 1993
- [34] Abramson B. and Sirignano W.A.: droplet vaporization Model for Spray Combution Calculations, *Int. J. Heat Mass Transfer*, Vol 32, pp. 1605-1618, 1989
- [35] Chrigui, M., Ahmadi, G., Sadiki, A., “Study on Interaction in Spray between Evaporating Droplets and Turbulence Using Second Order Turbulence RANS Models and a Lagrangian Approach”, *Progress in Computational Fluid Dynamics*, Special issue, 2004
- [36] Zamuner, B., Gilbank, P., Bissieres, D., Berat, C., “Numerical Simulation of the reactive two-phase flow in a kerosene/air tubular combustor”, *Aerospace Sci. and Tech.*, Vol. 6, pp.521-529, 2002
- [37] Krebs, W., Gruschka, U., Fielenbach, C., Hoffmann, S., “CFD-analysis of reacting flow in an annular combustor” , *Progress in Computational Fluid Dynamics*, Vol.1, Nos 1/2/3, pp. 104-116, 2001
- [38] Rachner, M., Becker, J., Hassa, C., Doer, R., “Modeling of atomization of a plain liquid jet in cross flow at gas turbine conditions”, *Sci. And Technology*, (6), pp. 495-506, 2002.
- [39] Burger, M., Klose, G., Schmehl, R., Giebert, D., Koch, R., Wittig, S., “A combined Eulerian and Lagrangian method for prediction of evaporating sprays”, *Proceeding of the 46th ASME Turbo Expo*, June 04-07, 2001, New Orleans, Louisiana, USA, 2001-GT-19046.
- [40] Chiu, H.H., “Advances and challenges in droplet and spray combustion I. Toward a unified theory of droplet aerochemistry”, *Progress Energy Combustion Sci.* 26, 381-416, 2000.

Bibliography

- [41] Faeth G. M.: Evaporation and combustion of sprays: Progress in energy and combustion science, Pergamon Press, 9:1-76, 1983
- [42] Law C. K.: Unsteady droplet vaporization with droplet heating. *Combustion and Flame*, 26: 17-22, 1976
- [43] Sommerfeld, M. and Qiu, H. H. "Experimental studies of spray evaporation in turbulent flows." *International Journal of Heat and Fluid Flow*, Vol. 19, 10-22 (1998)
- [44] Kohnen, G. R ger M. and Sommerfeld M. "Convergence behavior for numerical calculations by the EULER/LAGRANGE Method for strongly coupled phases." FED-Vol185, Numerical Methods in Multiphases Flows ASME 1994
- [45] Berlemont A., Grancher M.S., Gouesbet G.: On the Lagrangian simulation of turbulence influence on droplet evaporation. *Int. J. Heat Mass Transfer* 34 (11) 2805-2812, 1991
- [46] Sornek, R.J., Dobashi, R., Hirano, T., "Effect of Turbulence on Vaporization, Mixing, and Combustion of Liquid-fuel Sprays", *Combustion and Flame* 120:479-491, 2000.
- [47] G kalp, I., Chauveau, C., Simon, O., Chesneau, X., "Mass transfer from Liquid fuel droplets in turbulent flow", The combustion Institute 1992.
- [48] Sharif, M.A.R., Wang, Y.K.E., "Evaluation of the Performance of the three turbulence closure models in the prediction of confined swirling flows", "Computers and Fluids", 24, n1, pp. 81-100, 1995.
- [49] Klose, G., Schmehl, R., Meier, R., Meier, G., Koch., R., Wittig, S., "Evaluation of advanced two-phase flow and combustion models for predicting low emission combustors", Proc. of ASME Turbo Expo 2000, May 8th-11th, Munich, Germany, 2000
- [50] Hollmann, C., Gutheil, E., "Flamelet-Modeling of Turbulent Spray Diffusion Flames based on Laminar Spray Flame Library", *Combust. Sci. and Tech.*, Vol. 135, pp. 175-192, 1998
- [51] Sankaran, V., Menon, S., "LES of spray combustion in compressible high Reynolds number swirling flows", Proc. of the 2nd International Symp. on Turbulence and Shear Flow Phenomena, Stockholm, Sweden, 2001
- [52] Bellan, J., "Perspectives on Large Eddy Simulation for Sprays", *Issues and Solutions, Atomization and Sprays*, Vol. 10, pp. 409-425, 2000.
- [53] Groh, B., Chrigui, M., Stojanovi, Z., Sadiki, A., Dreizler, A., Janicka, J., "Validation of second order moment turbulence models using Large eddy simulation and experiments for turbulent two-phase flows", 3th Conf. of Turbulent Shear Flow Phenomena, Japan, 2003
- [54] Melheim; J., Horender S. and Sommerfeld M. „Modeling of the vortex-structure in a particle-laden mixing-layer“ Proceeding of FEDSM 2005, ASME 2005 , Houston, TX, USA, June 19-23, 2005
- [55] Kohnen G. und Sommerfeld M. "Numerische Berechnung verdampfender Spr hnebel" *Chemische Technik* 50 (1998) Heft 5 pp:225-234
- [56] Dekena M. and Peters N.: "Combustion Modeling with the G-Equation" *Oil & Gas Science and Technology* *Rev. IFP*, Vol. 54 (1999), No. 2, pp. 265-270
- [57] Borghi. Turbulent combustion modeling. *Prog. Energy Combust. Sci.*, 14:245-292, 1988
- [58] Pope, S.B., *Prog. Energy Combust. Sci.*, 11:119-192, 1985.
- [59] Lindstedt, R.P., Louloudi, S.A., and Vaos, E.M., *Proc. Combust. Inst.*, 28:149-156, 2000.
- [60] Reveillon J. AND Vervisch L. "Accounting for spray vaporization in turbulent combustion modeling" Center for Turbulence Research Proceedings of the Summer Program 1998
- [61] Keh-Chin Cang „Turbulent Flow Computations in Combustors" *Proc. Natl. Sci. Council. ROC(A)* Vol. 24, No. 6, 2000. pp. 413-421

Bibliography

- [62] Mashayek F. 1999 "Simulations of reacting droplets dispersed in isotropic turbulence" AIAA J.37 1420-25
- [63] Faeth, G. M. "Spray combustion phenomena" 26th International Symposium on Combustion. The Combustion Institute, Pittsburg 1996, p.1593
- [64] Liu Z., Zheng C. and Hzou L. "A joint model for turbulent spray evaporation/Combustion" Proceedings of the Combustion Institute, Volume 29, 2002/pp. 561-568
- [65] Simonin, O., 1996. Continuum Modeling of Dispersed Turbulent Two-phase Flows. In VKI lectures: Combustion in Two-phase Flows, Jan 29-Feb. 2.
- [66] Domelevo K. & Sainsaulieu L. 1997 "A numerical method for the computation of the dispersion of a cloud of particles by a turbulent gas flow field". J. Comput. Phys. 133, pp 256-278.
- [67] Xiang, W., and S. Zhen, The bivariate spline approximate solution to the hyperbolic equation with variable coefficients, J. Comput. Math., 10, 112–128, 1992.
- [68] Boussinesq, J.V.: Sur la resistance d'une sphere solide. C.R. Hebd. Seanc. Acad. Sci. Paris, Vol. 100, 935 (1885)
- [69] Techen C.M., "mean value and correlation problems connected with the motion of small particles suspended in a turbulent fluid", Dissertation, University of Technology, Delft, Netherlands, 1947
- [70] Hansell D., Kennedy I.M. and Kollmann W., "A simulation of particle dispersion in a turbulent jet", Int. J. Multiphase flows, 18 (1992), S. pp. 559
- [71] Morsi S. A. and Alexander A. J. "An investigation of particle trajectories in two phase flow systems", J. Fluid Mech., 55 (1972), pp. 193-208
- [72] Clift R.C., Grace R. and Weber M.E. "Bubbles, drops and particles", Kluwer Academic 1978
- [73] Odar F. and Hamilton W.S. "foces on a Sphere accelerating in a viscous fluid", J. Fluid Mech., 18 (1964), pp. 302-314
- [74] Poinot T. and Veynante D. "Theoretical and numerical combustion" ISBN 1-930217-05-6 R.T. Edwards, Inc. Philadelphia USA
- [75] Burke, S.P. and T.E.W. Schumann, "Diffusion Flames", Industrial Engineering Chemistry, Vol. 20, pp. 998-1004, 1928.
- [76] Maas, U. and Pope, S. B., "Implementation of Simplified Chemical Kinetics Based on Intrinsic Low-Dimensional Manifolds", Twenty-Fourth Symposium (International) on Combustion, 1992, The Combustion Institute, Pittsburgh, pp.103-112.
- [77] Maas, U. and Pope, S., "Simplifying Chemical Kinetics: Intrinsic Low-Dimensional Manifolds in Composition Space," Combustion and Flame, 88:239-264, 1992.
- [78] Peters N., "turbulent combustion" Cambridge university press 2000 ISBN 0-521-66082-3
- [79] Boussinesq, J.: Theorie de l' ecoulement tourbillant. Mem. Acad. Sci., 23:46, 1877.
- [80] Launder, B. E. und D. B. Spalding: The Numerical Computation of Turbulent Flow. Comp. Meth. Appl. Mech. Eng., 3: 269-289, 1974.
- [81] Rotta J. C. "Statistische Theorie nichthomogener Turbulenz", Zeitschrift für Physik, Vol. 129, pp.547-572
- [82] Launder B: E., Reece, G.J. and Rodi, W. "Progress in the development of a Reynolds-Stress Turbulence Closure" Journal of Fluid Mechanics, 1975 Vol.68, Pt.3, pp. 537-566
- [83] David C. Wilcox "Turbulence modeling for CFD" DCW Industries, Inc. La Canada, California 1993, ISBN 0-9636051-0-0

Bibliography

- [84] Jones, W.P. and Musonge, P., 1988, Closure of the Reynolds stress and scalar flux equations, *Phys. Fluids* 31:3589-3604.
- [85] Shuen, J.S. , Solomon, A.S.P., Zhang, Q.F. & Faeth, G.M. "A theoretical and experimental study of turbulent particle-laden jets." NASA Contractor report 168293 (1983)
- [86] Sadiki A. and Ahmadi G.: Modeling of chemically active multiphase turbulent flows on rational extended thermodynamics. *Advances in Turbulence IX, ETC9, U.K.2002.*
- [87] Crowe, C. T., 2000. On models for turbulence modulation in fluid-particle flows. *Int. J. Multiphase Flow* 26, 719-727.
- [88] Kulick, J. D., Fessler, J. R. & Eaton, J. K., 1994. Particle response and turbulence modification in fully developed channel flow. *J. Fluid Mech.* 277, 109-134.
- [89] Hosokawa, S., Tomiyama, A., Morimura, M., Fujiwara, S. & Sakaguchi, T, 1998. Influences of relative velocity on turbulent intensity in gas-solid two-phase flow in a vertical pipe. *Proc. Int. Conf. Multiphase Flow (CD-ROM), Paper 279, 1-7.*
- [90] Savolainen, K. & Karvinen, R., 1998. The effect of particle on gas turbulence in a vertical upward pipe flow. *Proc. 3rd Int. Conf. Multiphase Flow (CD-ROM), Paper 627, 1-6.*
- [91] Lain, S., Bröder, D., Sommerfeld, M. 2000. „numerical modeling of the hydrodynamics in a bubble column using the Euler-Lagrange approach.“ *Proc. On Int. Symp. On Multiphase Flow and Transport Phenomena, Antalya, Turkey.*
- [92] Lain, S. and Sommerfeld M. "Turbulence modulation in dispersed two-phase flow laden with solids from a Lagrangian perspective" *Int. J. heat and fluid flow*" 2002
- [93] Sommerfeld M. "Modellierung und numerische Berechnung von partikelbeladenen turbulenten Strömungen mit Hilfe des Euler/Lagrange-Verfahrens." *Shaker Verlag Aachen 1996. ISBN 3-8265-1951-5*
- [94] Squires K.D. & Eaton J.K "On the modeling of particle-laden turbulent flows", 6th workshop on two-phase predictions, proceedings, ed. By Sommerfeld, *Bilateral Seminars of the international bureau, Vol. 14, Forschungszentrum Jülich GmbH, 220-229 (1993)*
- [95] Karman Th. And Howarth, L. "On the statistical theory of isotropic turbulence", *Proc. Roy. Soc. London, Vol. A 164, pp. 192-215, (1938)*
- [96] Sommerfeld, M. Kohnen, G. and Rüger, M. "Some open questions and inconsistencies of Lagrangian particle dispersion models", *proc. Ninth Symp. On Turbulent Shear Flow, Tokyo, Japan, Paper 5.1, 1993*
- [97] Crowe, C. T., Sharma, M. P. & Stock, D. E., 1977. The particle-source-in-cell (PSICELL) model for gas-droplet flows. *ASME Trans. J. Fluids Eng.* June.
- [98] Park J. H., Yoon Y., Hwang S. S.: Improved Tab-Model for Prediction of Spray Droplet Deformation and Breakup, *atomization and Sprays*, 12, (2002) 387-402
- [99] Berlemont A., Grancher M.S. and Gouesbet G.: Heat and mass transfer coupling between vaporizing droplets and turbulence using a Lagrangian approach. *J. of. Heat and Mass Transfer Vol.38 (1995) 3023-3034*
- [100] Kuo Y. "Principles of Combustion." John Wiley and Sons, New York, 1986.
- [101] Jones W.P. "Models for turbulent flows with variable density and combustion" *Prediction method for turbulent flows, Band 1979-02. Von Karman Institute for fluid dynamics, 1979*
- [102] Stone, L. H. "Iterative solution of implicit approximations multidimensional partial differential equations" *SIAM J. Numer. Anal. Vol.5, No. 3, pp. 530-558, 1968*
- [103] Jones W. P.: In P.A. Libby and F. A. Williams, editors, "Turbulent Reacting Flows", pp. 309-374. *Academic Press, London, San Diego, New York, 1994.*

Bibliography

- [104] Leister H. J. and Peric M.: "Vectorized strongly implicit solving procedure for seven-diagonal coefficient matrix". *Int. J. Numer. Meth. Heat Fluid Flow*, vol. 4, pp. 159-172, 1994
- [105] Sadiki A., Chrigui M., Janicka J. and Maneshkarimi M. R. "modeling and Simulation of effects of turbulence on vaporization, mixing and combustion of liquid fuel sprays" *Journal of Flow, Turbulence and Combustion*, 2005 (in print)
- [106] Sommerfeld, M. "Validation of a stochastic Lagrangian modeling approach for inter-particle collisions in homogeneous isotropic turbulence" *Int. J. of. Multiphase flow*, 27, pp. 1829-1858. (2001)
- [107] Liu, Z. H., Zheng, C. G., and Zhou, L.X. 2001 "A second order moment monte carlo model for simulating swirling gas particle flows" *Powder Technology*, 120, pp. 216-222
- [108] Melheim, J., Horender S., Sommerfeld M. " Modeling of the vortex structure in a particle laden mixing layer" *Proceeding of FEDSM2005 ASME Fluid Engineering Division Summer Meeting and Exhibition Houston, TX, USA, June 19-23, 2005*
- [109] Sankaran and Menon „LES of spray combustion in swirling flows " *J. Turbulence* 3 (2002) 011 PII: S1468-5248(02)32369-5
- [110] Matthews B. W., Fletcher A.J. and PARTRIGE C. T. "Particle flow modeling on spiral concentrators: Benefits of dense media for coal processing" *Second international conference on CFD in the minerals and process industries" CSIRO, Melbourne, Australia 1999*
- [111] Tardy P.; Quintard M. "Solving stiff mass transfers in compositional multiphase flow models: Numerical stability and spurious solutions" : *Computational Geosciences*, 1999, vol. 3, no. 2, pp. 161-183(23)
- [112] Chrigui M. and. Sadiki A.: "Effects of Turbulence Modulation on Mass and Heat Transfer: 3D-Numerical Prediction Based on Coupled Advanced Models for Turbulence and Evaporation" *4th Int. Symp. On Turbulence, Heat and Mass Transfer*, October 12-17, Antalya, Turkey
- [113] Chrigui M., Schroth G., Sadiki A., Janicka J.: *Numerical Prediction of Coal Particles Evolution Behavior in Swirled Flow with and without Combustion using an Euler-Lagrangian Coupling*, ISCC, 2003, China
- [114] Stojanovic Z., Chrigui M., Sadiki A., Dreizler A., Geiß S. and Janicka J.: *Experimental Investigation and Modeling of Turbulence Modification in a dilute Two-Phase Turbulent Flow*, 10th Workshop on Two-Phase Flow Predictions, Merseburg, Deutschland, 2002
- [115] Frank-Kamenstsky D.A.: "Diffusion and heat exchange in chemical kinetics" *Moscow*, third edition 1987
- [116] Krieger G. C.: "Untersuchung zur Hydroxylradikal- und Stickoxidbildung in turbulenten Wasserstoffdiffusionsflammen mittels Wahrscheinlichkeitsdichte-funktionen PhD thesis, Darmstadt University of Technology, VDI-Verlag, 1999
- [117] Warnatz J., Maas U. and Dibble R.W.: "combustion" *Springer Verlag*, 1996
- [118] Williams F.A.: "combustion theory" *Benjamin Cummings*, 1985
- [119] Law C.K, Peters N. and Rogg B.: "Reduced kinetic mechanisms for finite-volume schemes, pp. 15-26" *Springer Verlag Berlin-Heidelberg*. 1993
- [120] Geiss, S. "Über die Turbulenzmodulation turbulenter partikelbeladener nichtreagierender Zweiphasenströmung", *VDI Verlag* 2002
- [121] Stojanovic Z. "Investigation of turbulent dilute non-reacting gas-solid two-phase flows" *VDI Verlag Nr. 461* (2003)

Bibliography

- [122] Crowe C T (1993) Modeling turbulence in multiphase flow. In: Engineering Turbulence Modeling and Experiments 2 (ed Rodi; Martelli), pp. 899 – 913, Elsevier Science Publishers B. V.
- [123] Priere, C., Gicquel, L.Y.M., Kaufmann, P., Krebs, W. and Poinso, T., „ Large Eddy Simulation predictions of mixing enhancement for jets in cross flows, Journal of Turbulence 5, 005, 1-24 (2004)
- [124] Sommerfeld M., Qiu H. H.: Detailed measurements in a swirling particulate two-phase flow by a phase-Doppler anemometer. Int. J. Heat and Fluid Flow. Vol 12, No 1, March 1991
- [125] Ferziger J.H. and Peric M.: “Computational Methods for Fluid Dynamics” (second edition). Springer Verlag, Berlin, Heidelberg, 1999
- [126] Schäfer M.: “Numerik im Maschinenbau” ISBN 3-540-65391-0, Springer Verlag Berlin, 1999.
- [127] Gatski T. B. and Speziale C. G., “On Explicit Algebraic Stress Models for Complex Turbulent Flows”, J. of Fluid Mech., Vol. 254, 1993, pp. 59-78.
- [128] Wallin S., “Engineering turbulence modeling for CFD with a focus on explicit algebraic Reynolds stress models”, Doctoral Thesis, Norstedts Tryckeri AB, Stockholm, Sweden, 2000.
- [129] Lumley J L “Computational modeling of turbulent flows” 1978 Adv. Appl. Mech.18 123-76
- [130] Technical review aviation fuels. Chevron Business and Real Estate Services Creative Center, San Ramon, California. Aviation Fuels Technical Review (FTR-3) 2000 Chevron Products Company, A division of Chevron U.S.A. Inc.
- [131] Smiljanovski V. and Brehm N. "CFD liquid spray combustion analysis of a single annular gas turbine combustor" ASME paper 99-GT-300 1999
- [132] Peters N., “Laminar Diffusion Flamelet Models in Non-Premixed Turbulent Combustion”, Progr. Energy Combust. Sci., Vol. 10, 1984, p. 319-339.
- [133] De Goey L. P. H. Chem1D, 2005. TU Eindhoven
- [134] Maltsev A. “Towards the development and assessment of complete CFD models for the simulation of stationary gas turbine combustion processes” Dissertation vom Fachbereich Maschinenbau TU-Darmstadt 2003
- [135] Fluent user guide, version 6.0
- [136] Chrigui M.; Sadiki A.; Janicka J. and Maneshkarimi M.:”CFD-Analysis of conjugate effects of turbulence and swirl intensity on spray combustion in a single gas turbine combustor” ASME TURBO EXPO 2004; 14-17 June 2004 | Vienna, Austria
- [137] Kee R.J., Rupley F.M. and Miller J.A.: “CHEMKIN-II: A FORTRAN Chemical Kinetics Package for the Analysis og Gas-phase Chemical Kinetics, Sandia National Laboratories, Livermore, CA 94551, SAND89-8009B, 1991.
- [138] Prommersberger, K., G. Maier, and S. Wittig (1998). Validation and Application of a Droplet Evaporation Model for Real Aviation Fuel, Proceedings of NATO-RTO Meeting on Gas Turbine Engine Combustion, Emissions and Alternative Fuels, Lisbon, Portugal, 12-16 October.
- [139] Gosman, A.D. and Ioannides, E., J. Energy, 7(6), 482- 490, 1983